ТЕХНІКА ТА ЕНЕРГЕТИКА

Засновник:
Національний університет біоресурсів і природокористування України

Рік заснування: 2010

*Рекомендовано до друку та поширення
через мережу Інтернет Вченою радою
Національного університету біоресурсів і природокористування України
(протокол № 1 від 11 серпня 2022 р.)*

**Свідоцтво про державну реєстрацію
друкованого засобу масової інформації**
серії КВ № 25126-15066 ПР від 17 лютого 2022

Журнал входить до переліку наукових фахових видань України

Категорія «Б». Галузь наук – Технічні.
Спеціальність: 131 – «Прикладна механіка», 133 – «Галузеве машинобудування»
(Наказ Міністерства освіти і науки України від від 17 березня 2020 року № 409)

**Журнал представлено у міжнародних наукометричних базах даних,
репозитаріях та пошукових системах**: Index Copernicus International,
Google Scholar, Фахові видання України,
Національна бібліотека України імені В. І. Вернадського,
AGRIS, BASE, Academic Resource Index ResearchBib

Адреса редакції:
Національний університет біоресурсів і природокористування України
вул. Героїв Оборони, 15, м. Київ, 03041, Україна
E-mail: info@technicalscience.com.ua
www: https://technicalscience.com.ua/uk

MACHINERY & ENERGETICS

Founder:
National University of Life and Environmental Sciences of Ukraine

Year of foundation: 2010

Recommended for printing and distribution
via the Internet by the Academic Council
of National University of Life and Environmental Sciences of Ukraine
(Minutes No. 1 of August 11, 2022)

Certificate of state registration
of the print media
Series KV No. 25126-15066 PR of February 17, 2022

The journal is included in the list of Professional Scientific Publications of Ukraine
Category “B”. Branch of sciences – Technical.
Specialty: 131 – “Applied mechanics”, 133 – “Branch mechanical engineering
(Order of the Ministry of Education and Science of Ukraine of March 17, 2020, No. 409)

The journal is presented international scientometric databases, repositories and scientific systems: Index Copernicus International,
Google Scholar, Professional publications of Ukraine,
Vernadsky National Library of Ukraine, AGRIS, BASE,
Academic Resource Index ResearchBib

Editors office address:
National University of Life and Environmental Sciences of Ukraine
03041, 15 Heroiv Oborony, Kyiv, Ukraine
E-mail: info@technicalscience.com.ua
www: https://technicalscience.com.ua/en

Редакційна колегія

Віталій Лисенко	Доктор технічних наук, професор, Національний університет біоресурсів і природокористування України, Київ, Україна
Володимир Решетюк	Кандидат технічних наук, доцент, Національний університет біоресурсів і природокористування України, Київ, Україна
В'ячеслав Адамчук	Доктор технічних наук, професор, університет МакГілл, Монреаль, Канада
Вячеслав Братішко	Доктор технічних наук, старший науковий співробітник, Національний університет біоресурсів і природокористування України, Київ, Україна
В'ячеслав Ловейкін	Доктор технічних наук, професор, Національний університет біоресурсів і природокористування України, Київ, Україна
Євгеній Афтанділянц	Доктор технічних наук, професор, Національний університет біоресурсів і природокористування України, Київ, Україна
Юрій Яцкевич	Доктор технічних наук, професор, Університет Британської Колумбії, Ванкувер, Канада
Зиновій Ружило	Кандидат технічних наук, доцент, Національний університет біоресурсів і природокористування України, Київ, Україна

Vitalii Lysenko	Full Doctor in Technical Sciences, Professor, National University of Life and Environmental Sciences of Ukraine, Kyiv, Ukraine
Volodymyr Reshetiuk	PhD in Technical Sciences, Assistant Professor, National University of Life and Environmental Sciences of Ukraine, Kyiv, Ukraine
Viacheslav Adamchuk	Full Doctor in Technical Sciences, Professor, McGill University, Montreal, Canada
Viacheslav Bratishko	Full Doctor in Technical Sciences, Senior Research Associate, National University of Life and Environmental Sciences of Ukraine, Kyiv, Ukraine
Viacheslav Loveykin	Full Doctor in Technical Sciences, Professor, National University of Life and Environmental Sciences of Ukraine, Kyiv, Ukraine
Evgeniy Aftandilianz	Full Doctor in Technical Sciences, Professor, National University of Life and Environmental Sciences of Ukraine, Kyiv, Ukraine
Yurii Jazkevych	Full Doctor in Technical Sciences, Professor, University of British Columbia, Vancouver, Canada
Zynovii Ruzhylo	PhD in Technical Sciences, Assistant Professor, National University of Life and Environmental Sciences of Ukraine, Kyiv, Ukraine

ЗМІСТ

CONTENTS

Machinery & Energetics
Vol. 13, No. 3. 2022

Journal homepage:
https://technicalscience.com.ua/en

UDC 631.363.5
DOI: 10.31548/machenergy.13(3).2022.9-16

Elchyn Aliiev[1,2*], Volodymyr Dudin[2], Mykola Linko[2]

[1]Institute of Oil Cultures of the National Academy of Agrarian Sciences of Ukraine
69055, 1 Institutskaya Str., Soniachne, Zaporizhzhia region, Ukraine

[2]Dnipro State Agrarian and Economic University
49600, 25 Serhii Efremov Str., Dnipro, Ukraine

Physico-Mathematical Apparatus for Numerical Modelling of Feed Expander

Abstract. The productivity of the feed preparation line and its technical and economic efficiency are affected by the design and technological parameters of the equipment. The geometry of the expander screw and its operating modes are no exception. To reduce the specific energy consumption of the expander, it is necessary to establish its rational design and operating parameters. This can be done using analytical calculation methods that consider the mechanisms of movement and destruction of solid substances. Modelling using the discrete element method is becoming increasingly common to describe the movement of solid components in granulators, extruders, or expanders. The purpose of the study is to improve the physical and mathematical apparatus of movement of solid feed components in the screw channel of the feed expander and develop a method for its numerical modelling. Numerical modelling was performed using a model of the movement of a multiphase Euler mixture with a split flow in three-dimensional space. In this case, the motion was subject to an admissible two-layer k-ε model of turbulence and the multiphase equation of state. The physical and mathematical apparatus for the movement of solid feed components in the screw channel of the feed expander was improved, which is the basis for the numerical modelling technique in the Star-CCM+ software suite, based on the fact that the conglomerate of feed components is represented as a package of spherical particles. In this case, the pressure force must be compensated by the total force of contact interaction of particles with each other and the wall. Preliminary numerical modelling of the process of expanded feed preparation was performed in the Star-CCM+ software suite. The practical significance lies in the fact that the improved physical and mathematical apparatus and the developed method of numerical modelling of the feed expander operation process allow substantiating its design and regime parameters to ensure low specific energy consumption without losing the quality of the technological process

Keywords: feed expansion, simulation, discrete element method, Star-CCM+, pressure, velocity vector field, density

Article's History: Received: 08.04.2022; Revised: 25.07.2022; Accepted: 11.08.2022

INTRODUCTION

The choice of the technological mode of feed preparation, as a rule, is based on conducting comprehensive studies that identify the nature of changes in the structure and properties of both individual components of raw materials and the feed value of the processed material.

The science of animal feeding has accumulated a large amount of experimental data on the effects of various nutrients, essential amino acids, vitamins, macro- and microelements, antibiotics, hormones, enzymes, and other components on the metabolism and efficiency of feed use. These data serve to further improve the theory and practice of animal feeding in agriculture. They ensure the realisation of the genetic potential of animal productivity. The more efficient the level of feeding, the higher the productivity of animals and the lower the feed consumption per unit of production [1; 2].

With conventional animal feeding, most of the feed is produced on farms. The use of feed in unprocessed form leads to low digestibility. It is known that animals convert only 20-25% of feed energy into products. The task of feed preparation is to reduce these losses by increasing the digestibility of feed [3; 4].

This problem can be solved by subjecting the feed to complex processing in one machine, to carry it out quickly and continuously (to make compositions of several

Suggested Citation:
Aliiev, E., Dudin, V., & Linko, M. (2022). Physico-mathematical apparatus for numerical modelling of feed expander. *Machinery & Energetics,* 13(3), 9-16.

*Corresponding author

components, mix, compress, heat, cook, sterilise, almost simultaneously), which, in the end, affects production cost.

To date, mixed feed and feed additives must meet the requirements of veterinary and sanitary standards [5]. The microflora of manufactured products is determined not only by the quality of raw materials used, but also by the way the production process is conducted, the level of its automation. The main reason for the deterioration of feed quality indicators is microorganisms. They contribute to the development of various unfavourable processes – self-heating, the appearance of a sharp smell, and colour changes [6]. The development of microorganisms can lead to a complete loss of the original properties of mixed feed and make it unsuitable for feeding to farm animals and poultry. The solution of these tasks is possible in machines for deep feed processing: extruders or expanders. The use of expansion technology improves the quality and digestibility of feed, eliminates harmful components for nutrition, and reduces the energy intensity of feed production.

Processing and preparation of feed involve a certain set of influences of the working bodies of technical means on the environment, which is a variety of feed materials with significantly different properties. Therefore, the real performance indicators of machines can be considered only in connection with the physical and mechanical properties and quality of feed.

The geometry of the expander screw has a great influence on the capacity of the extended feed preparation line, and on their quality, and, therefore, is crucial for technical and economic efficiency [7]. To save specific energy costs, there are various analytical calculation methods that consider the mechanisms of movement and destruction of solid substances, so there is no need to conduct long-term experiments by trial and error. There are many assumptions and simplifications that need to be made to obtain an analytical solution; for example, the assumption that feed components form a solid layer that flows at a uniform rate [8]. Modelling using the discrete element method (DEM) is becoming increasingly common for describing solids moving in granulators, extruders, or expanders, since relative displacements between particles are possible [9-11]. The DEM simulation model is used for the virtual design of experiments and allows getting a large database for evaluating the effectiveness of the technological process.

LITERATURE REVIEW

For a better understanding and discussion of the presented problem, some analysis of the theoretical prerequisites for the movement of solids in single-screw granulators, extruders, and expanders is given.

Many approaches to describe the motion of solids in a single-screw granulator, extruder, or expander that have been known so far can be reduced to the concept of the model by W.H. Darnell and E.A.J. Mol [12]. In this model, it is assumed that the pellets behave like a solid block and flow through the helical channel as a solid layer in the block flow. Various pressure and friction forces act on this solid layer, which allow calculating the direction of movement based on the balance of forces and moments. Since then, modelling, especially forces, has been discussed in detail and adapted in many scientific studies.

The above analytical model for describing the motion of solids based on physical and mathematical considerations temporarily ceased in the early 2000s, as numerical modelling based on the discrete element method (DEM) appeared. This was made possible primarily by improving the performance of a personal computer. DEM developed by P.A Cundall and O.D.J. Strack [13] was originally developed for modelling molecular dynamics and has since found wide application in technological processes, mechanical engineering, and geotechnics.

The main advantage of DEM modelling is that it is necessary to make fewer preliminary assumptions about the behaviour of bulk material particles. The basis of DEM is the representation of particles as spheres or particles consisting of several spheres. To calculate the interaction of these particles with other particles or geometries, they are not connected, but virtual overlap is used. Depending on this overlap and boundary conditions, contact models calculate contact forces in the normal and tangential directions. These forces are then used to solve conservation-of-momentum equations and calculate new quantities of motion. When these motion values are integrated at the modelling stage, new particle positions appear, and thus new virtual overlaps appear, and the calculation cycle begins again [14; 15].

Due to the good suitability of DEM for describing the movement of solids in granulators, extruders, or expanders, this method is used to evaluate existing analytical calculation approaches. The main weak point of analytical models is that they never deviate from the assumption of block flow. Moreover, for this reason, the calculation of structural and technological parameters of a screw of complex design may be inaccurate.

The purpose of the study is to improve the physical and mathematical apparatus of movement of solid feed components in the screw channel of the feed expander and develop a method for its numerical modelling.

MATERIALS AND METHODS

The analysis of the movement of solid feed components in the screw channel of the expander is based on the dynamics of movement of solid particle systems by the discrete element method (DEM). Solid feed components, as discrete elements, are fed into the screw channel through the hopper. The flow in the hopper is usually carried out by gravity, although in certain circumstances it is necessary to create additional effort. This study does not address this issue. After the feed components enter the screw channel of the expander, they begin to move along a horizontal line in a spiral. Due to the reduced geometric dimensions of the screw channel, the feed components are compacted to form a solid layer or conglomerate, which is then transported to the forming nozzle.

To consider the physical and mathematical apparatus of movement of solid feed components in the screw channel of the expander, a corresponding calculation scheme is drawn up (Fig. 1). Fig. 1 shows the following geometric parameters of the expander: cylinder diameter D_b, screw shaft diameter D_s, screw channel depth h, screw pitch t, screw-cylinder gap δ, screw channel width b, screw spiral angle φ, and screw winding width *e*.

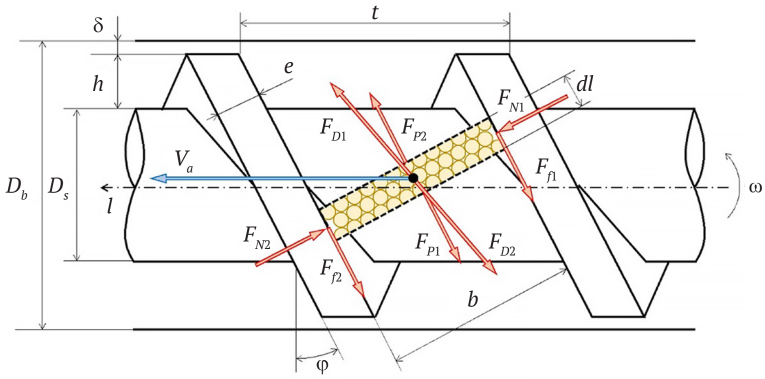

Figure 1. Design scheme of movement of solid feed components in the screw channel of the expander
Source: developed by the authors based on [16-18]

As noted above, its geometric parameters change along the length of the expander screw. According to studies [16-18], to "ensure the quadratic (or, as a special case, linear) nature of changes in the parameters of the screw, namely, the cross-sectional area of the screw channel, the area and volume of the channel along the length of the screw, it is sufficient to provide a linear change in two geometric parameters of the screw, namely, the width of the screw channel (screw pitch) and its depth", that is

$$\begin{cases} t = t_0 + k_b dl, \\ h = h_0 + k_h dl. \end{cases} \quad (1)$$

where t – current screw pitch, m; t_0 – initial screw pitch, m; h – current screw channel depth, m; h_0 – initial screw channel depth, m; k_b – "coefficient of change of screw pitch by its length" [16]; k_h – "coefficient of change of the screw channel depth by its length" 16]; dl – minimum pitch along the length of the screw channel, m.

Next, the study considers all the forces acting on a conglomerate of feed components during its transportation and compaction (Fig. 1). These forces are considered at the macro level (excluding DEM) under the assumption that the conglomerate of feed components is continuous and homogeneous. Thus, according to Fig. 1, the following forces act on a conglomerate of feed components:

– normal reaction forces between the conglomerate of feed components and the side walls of the screw F_{N1}, F_{N2};

– friction forces between the conglomerate of feed components and the side walls of the expander screw F_{f1}, F_{f2};

– friction force between the conglomerate of feed components and the screw F_{D1};

– friction force between the conglomerate of feed components and the cylinder F_{D2};

– normal force from pressure F_{P1}, F_{P2}.

In studies [16-18], the differential equilibrium equation of the conglomerate element of feed components was solved and the dependence of pressure changes along the length of their movement along the expander channel was obtained. The dependence of the pressure created on the element of the conglomerate of feed components obtained by V.V. Bratishko [16-18] does not consider its structure. Considering a conglomerate of feed components as a dense package of spherical DEM particles (Fig. 2), the pressure force must be compensated by the total force of contact interaction of particles with each other and the wall.

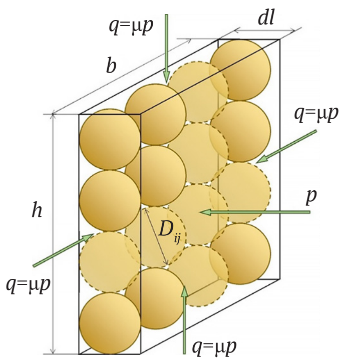

q – lateral pressure, Pa;
p – pressure in the granulator channel, Pa;
h – current screw channel depth, m;
b – screw channel width, m;
μ – lateral pressure coefficient;
dl – minimum pitch along the length of the screw channel, m;
D_{ij} – ij particle diameter

Figure 2. Dense packing of spherical particles of solid feed components in the screw channel of the expander
Source: compiled by the authors

Pressure force F_p is calculated from the geometric parameters of the screw and the number of particles N in the force field in the elementary volume of an element of a conglomerate of feed components:

$$F_p = \frac{q\pi\left(D_b^2 - D_s^2\right)}{4N}, \tag{2}$$

where q – lateral pressure, Pa; D_b – cylinder diameter, M; D_s – screw shaft diameter, m; N – number of particles.

Number of particles N in the unit volume of an element, a conglomerate of components can be calculated as follows

$$N = N_b N_h = \left\lfloor \frac{b}{\langle D_{ij} \rangle} \right\rfloor \left\lfloor \frac{h}{\langle D_{ij} \rangle} \right\rfloor, \tag{3}$$

where N_b – number of particles along the channel width; N_h – number of particles along the channel depth; D_{ij} – ij particle diameter; $\langle\ \rangle$ – average value function; $\lfloor\ \rfloor$ – function for determining the largest integer that is less than or equal to the number in parentheses.

To determine forces of contact interaction of feed components with each other , a suitable scheme for calculations is drawn up (Fig. 3)

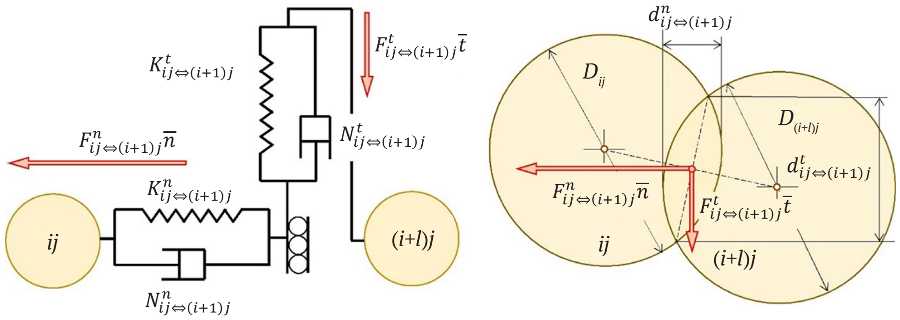

Figure 3. Design scheme of forces of contact interaction of feed components with each other
Source: compiled by the authors

According to the Hertz-Mindlin spring-damper contact Model [19], the total force of contact interaction of feed components with each other is determined as follows

$$\overline{F}^c_{ij\Leftrightarrow(i+1)j} = F^n_{ij\Leftrightarrow(i+1)j}\overline{n} + F^t_{ij\Leftrightarrow(i+1)j}\overline{t}, \tag{4}$$

where $\overline{F}^c_{ij\Leftrightarrow(i+1)j}$ – force of interaction between particles ij and $(i+1)j$, N; $F^n_{ij\Leftrightarrow(i+1)j}$ – normal component of the force between particles ij and $(i+1)j$, N; $F^t_{ij\Leftrightarrow(i+1)j}$ – tangential component of the force between particles ij and $(i+1)j$, N; $\overline{n}, \overline{t}$ – unit vectors of normal and tangential direction, respectively.

The normal component of the force is determined by the following equation:

$$F^n_{ij\Leftrightarrow(i+1)j} = -K^n_{ij\Leftrightarrow(i+1)j} d^n_{ij\Leftrightarrow(i+1)j} - N^n_{ij\Leftrightarrow(i+1)j} V^n_{ij\Leftrightarrow(i+1)j}, \tag{5}$$

where $K^n_{ij\Leftrightarrow(i+1)j}$ – normal coefficient of stiffness of the elastic component, kg/s^2;

$$K^n_{ij\Leftrightarrow(i+1)j} = \frac{4}{3} E_{ij\Leftrightarrow(i+1)j} \sqrt{d^n_{ij\Leftrightarrow(i+1)j} R_{ij\Leftrightarrow(i+1)j}}; \tag{6}$$

$N^n_{ij\Leftrightarrow(i+1)j}$ - normal damping coefficient of the damping component, kg/s;

$$N^n_{ij\Leftrightarrow(i+1)j} = \sqrt{\left(5K^n_{ij\Leftrightarrow(i+1)j} M_{ij\Leftrightarrow(i+1)j}\right)} N_{n\ \ damp}. \tag{7}$$

According to research [18], the tangential component of a force is defined as

$$F^t_{ij\Leftrightarrow(i+1)j} = -K^t_{ij\Leftrightarrow(i+1)j} d^t_{ij\Leftrightarrow(i+1)j} - \\ -N^t_{ij\Leftrightarrow(i+1)j} V^t_{ij\Leftrightarrow(i+1)j} \tag{8}$$

if $\left|K^t_{ij\Leftrightarrow(i+1)j} d^t_{ij\Leftrightarrow(i+1)j}\right| < \left|K^n_{ij\Leftrightarrow(i+1)j} d^n_{ij\Leftrightarrow(i+1)j}\right| C_{fs}$, where C_{fs} – statistical coefficient of friction between feed component particles. Otherwise, the tangential component of the force is determined by the following equation:

$$F^t_{ij\Leftrightarrow(i+1)j} = \frac{\left|K^n_{ij\Leftrightarrow(i+1)j} d^n_{ij\Leftrightarrow(i+1)j}\right| C_{fs} d^t_{ij\Leftrightarrow(i+1)j}}{\left|d^t_{ij\Leftrightarrow(i+1)j}\right|}; \tag{9}$$

where $K^t_{ij\Leftrightarrow(i+1)j}$ – tangential stiffness coefficient of the elastic component, kg/s^2;

$$K^t_{ij\Leftrightarrow(i+1)j} = 8G_{ij\Leftrightarrow(i+1)j} \sqrt{d^t_{ij\Leftrightarrow(i+1)j} R_{ij\Leftrightarrow(i+1)j}}\ ; \tag{10}$$

$N^t_{ij\Leftrightarrow(i+1)j}$ - tangential attenuation coefficient of the damper component, kg/s;

$$N^t_{ij\Leftrightarrow(i+1)j} = \sqrt{\left(5K^t_{ij\Leftrightarrow(i+1)j} M_{ij\Leftrightarrow(i+1)j}\right)} N_{t\ \ damp}\ ; \tag{11}$$

N_{ndamp}, N_{tdamp} – normal and tangential attenuation coefficients, respectively

$$N_{ndamp} = \frac{-\ln(C_{nrest})}{\sqrt{\pi^2 + \ln(C_{nrest})^2}}; \tag{12}$$

$$N_{tdamp} = \frac{-\ln(C_{trest})}{\sqrt{\pi^2 + \ln(C_{trest})^2}}\ ; \tag{13}$$

$R_{ij\Leftrightarrow(i+1)j}$ - equivalent radius of two particles ij and $(i+1)j$, m;

$$R_{ij\Leftrightarrow(i+1)j} = \frac{1}{\dfrac{2}{D_{ij}} + \dfrac{2}{D_{(i+1)j}}}; \tag{14}$$

$M_{ij\Leftrightarrow(i+1)j}$ - equivalent mass of two particles ij and $(i+1)j$, kg;

$$M_{ij\Leftrightarrow(i+1)j}=\frac{1}{\frac{1}{M_{ij}}+\frac{1}{M_{(i+1)j}}};\qquad(15)$$

$E_{ij\Leftrightarrow(i+1)j}$ - equivalent Young's modulus of two particles *ij* and (*i*+1)*j*, Pa;

$$E_{ij\Leftrightarrow(i+1)j}=\frac{1}{\frac{(1-\nu_{ij}^2)}{E_{ij}}+\frac{(1-\nu_{(i+1)j}^2)}{E_{(i+1)j}}};\qquad(16)$$

$G_{ij\Leftrightarrow(i+1)j}$ - equivalent shear modulus of two particles *ij* and (*i*+1)*j*, Pa;

$$G_{ij\Leftrightarrow(i+1)j}==\frac{1}{\frac{2(2-\nu_{ij})(1+\nu_{ij})}{E_{ij}}+\frac{2(2-\nu_{(i+1)j})(1+\nu_{(i+1)j})}{E_{(i+1)j}}};\qquad(17)$$

M_{ij}, $M_{(i+1)j}$ – masses of particles *ij* and (*i*+1)*j*, kg; $d^n_{ij\Leftrightarrow(i+1)j}$, $d^t_{ij\Leftrightarrow(i+1)j}$ – virtual overlap of particles *ij* and (*i*+1)*j* in normal and tangential directions, m [19]; D_{ij}, $D_{(i+1)j}$ – effective diameters of particles *ij* and (*i*+1)*j*, m; E_{ij}, $E_{(i+1)j}$ – Young's modules of particles ij and (*i*+1)*j*, Pa; ν_{ij}, $\nu_{(i+1)j}$ – Poisson coefficients of particles *ij* and (*i*+1)*j*; $V^n_{ij\Leftrightarrow(i+1)j}$, $V^t_{ij\Leftrightarrow(i+1)j}$ – normal and tangential components of the relative velocity of the particle surface at the contact point, m/s.

When feed component particles interact with equipment walls, equations (14)-(15) are valid with the following assumption $D_{wall}=\infty$ and $M_{wall}=\infty$. Substituting, (14)-(15) turn into

$$R_{ij\Leftrightarrow wall}=\frac{D_{ij}}{2},\ M_{ij\Leftrightarrow wall}=M_{ij}.\qquad(18)$$

According to Fig. 2 and considering expressions (2)-(5), a system of equilibrium equations is obtained:

$$\begin{cases}\mu p\dfrac{\pi(D_b^2-D_s^2)}{4\left\lfloor\frac{b}{\langle D_{ij}\rangle}\right\rfloor\left\lfloor\frac{h}{\langle D_{ij}\rangle}\right\rfloor}=\sum\limits_{j=1}^{\left\lfloor\frac{h}{\langle D_{ij}\rangle}\right\rfloor}F^n_{1j\Leftrightarrow wall}+\sum\limits_{i=2}^{\left\lfloor\frac{b}{\langle D_{ij}\rangle}\right\rfloor-1}\sum\limits_{j=1}^{\left\lfloor\frac{h}{\langle D_{ij}\rangle}\right\rfloor}F^n_{ij\Leftrightarrow(i+1)j}+\\ +\sum\limits_{j=1}^{\left\lfloor\frac{h}{\langle D_{ij}\rangle}\right\rfloor}F^n_{\left\lfloor\frac{b}{\langle D_{ij}\rangle}\right\rfloor j\Leftrightarrow wall}+\sum\limits_{i=1}^{\left\lfloor\frac{b}{\langle D_{ij}\rangle}\right\rfloor}F^t_{i1\Leftrightarrow wall}+\sum\limits_{i=1}^{\left\lfloor\frac{b}{\langle D_{ij}\rangle}\right\rfloor}\sum\limits_{j=2}^{\left\lfloor\frac{h}{\langle D_{ij}\rangle}\right\rfloor-1}F^t_{ij\Leftrightarrow(i+1)j}+\sum\limits_{i=1}^{\left\lfloor\frac{b}{\langle D_{ij}\rangle}\right\rfloor}F^t_{i\left\lfloor\frac{h}{\langle D_{ij}\rangle}\right\rfloor\Leftrightarrow wall},\\ \mu p\dfrac{\pi(D_b^2-D_s^2)}{4\left\lfloor\frac{b}{\langle D_{ij}\rangle}\right\rfloor\left\lfloor\frac{h}{\langle D_{ij}\rangle}\right\rfloor}=\sum\limits_{i=1}^{\left\lfloor\frac{b}{\langle D_{ij}\rangle}\right\rfloor}F^n_{i1\Leftrightarrow wall}+\sum\limits_{i=1}^{\left\lfloor\frac{b}{\langle D_{ij}\rangle}\right\rfloor}\sum\limits_{j=2}^{\left\lfloor\frac{h}{\langle D_{ij}\rangle}\right\rfloor-1}F^n_{ij\Leftrightarrow(i+1)j}+\\ +\sum\limits_{i=1}^{\left\lfloor\frac{b}{\langle D_{ij}\rangle}\right\rfloor}F^n_{i\left\lfloor\frac{h}{\langle D_{ij}\rangle}\right\rfloor\Leftrightarrow wall}+\sum\limits_{j=1}^{\left\lfloor\frac{h}{\langle D_{ij}\rangle}\right\rfloor}F^t_{1j\Leftrightarrow wall}+\sum\limits_{i=2}^{\left\lfloor\frac{b}{\langle D_{ij}\rangle}\right\rfloor-1}\sum\limits_{j=1}^{\left\lfloor\frac{h}{\langle D_{ij}\rangle}\right\rfloor}F^t_{ij\Leftrightarrow(i+1)j}+\sum\limits_{j=1}^{\left\lfloor\frac{h}{\langle D_{ij}\rangle}\right\rfloor}F^t_{\left\lfloor\frac{b}{\langle D_{ij}\rangle}\right\rfloor j\Leftrightarrow wall}.\end{cases}\qquad(19)$$

The system of equations (21) together with the dependences (1)-(20) and the dependence of V.V. Bratishko [16-18] of the pressure distribution in the helical channel is very difficult to solve analytically due to the presence of a large number of variables that change over time. Therefore, having put this system as a physical and mathematical apparatus in the Star-CCM+ software suite, the study proceeds to consider the numerical modelling method. The study used the software "Simcenter STAR-CCM+ Academic Pack", the license holder of which is Dnipro State Agrarian and Economic University.

RESULTS AND DISCUSSION

Before performing numerical modelling, a 3D expander grid model was constructed using a surface grid generator, polyhedral cells, and a cell extruder.

Geometric dimensions and the generated grid with a base cell size of 0.005 m are shown in Fig. 4. The geometric dimensions of the expander elements are selected from a righteous analysis of existing structures [20; 21], considering their minimisation for reproducing small-sized laboratory equipment.

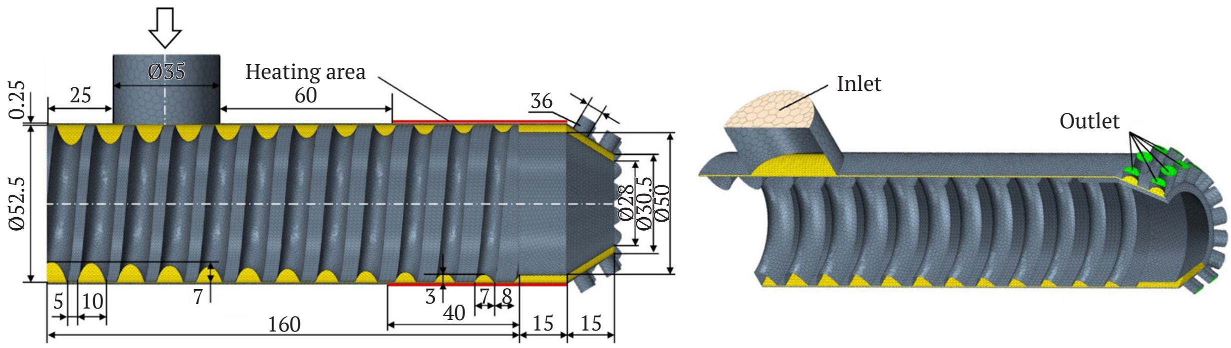

Figure 4. 3D expander model mesh in Star-CCM+

Source: compiled by the authors

The simulation was performed using gradients in 3D space, a model of split flow motion of a multiphase Euler mixture (MMP) using an acceptable two-layer k-ε turbulence model, and a multiphase equation of state. The simulation is non-stationary implicit. Heat-conducting processes followed the multiphase temperature model. The simulation was performed in the field of gravity. The gravity vector is as follows: (0; 0; -9.81) m/s^2.

Physical models for simulating the movement of feed components in the expander in the Star-CCM+ software suite are: a three-dimensional space model, an implicit non-stationary model, a physical model of a single-component gas (air), a real gas (air) model, a model of k-ε turbulence of air flow, an isothermal energy equation, a model of the Navier-Stokes equation averaged over Reynolds, a flow model – separate, boundary and gradient methods, a multiphase Lagrange model of the medium, a multiphase interaction model, discrete elements model (DEM), and the field of gravity.

Feed components are defined as Lagrange phases: density – constant; presence of pressure gradients; particle resistance model; DEM particles – spherical, single-component, and solid.

For example, soybean seeds were chosen as feed components. According to preliminary laboratory studies, soybean seeds have the following physical, mechanical and rheological properties: density – 700 kg/m^3; Young's modulus – 0.2 MPa; Poisson's coefficient – 0.2; normal recovery coefficient – 0.5; resting friction coefficient – 0.58; tangent recovery coefficient – 0.5; rolling resistance coefficient – 0.3; seed diameter – 0.01 m [22]. The Hertz-Mindlin contact interaction model is based on the interaction between the components: normal reduction coefficient – 0.5; rest friction coefficient – 0.58; tangent reduction coefficient – 0.5. The medium in which the components move is air with the following properties: dynamic viscosity – 1.85508·10^{-5} Pa·s; Prandtl's turbulent number – 0.9. Medium temperature – 293 K; medium pressure – 101,325 Pa. Gravity acceleration – 9.8 m/s^2.

The limit parameters selected are as follows. The upper plane of the feed neck (inlet) is represented by a model of the mass flow of feed components, which flows to the screw by gravity under the influence of gravity. The holes of the forming nozzle (outlet) are represented by a free flow of the mixture, the physical parameters of which are formed as a result of modelling.

The screw rotates around its own axis at a constant frequency of 120 rpm.

The solver in Star-CCM+ is selected non-stationary implicit in time increments of 0.01 s. First-order time discretisation. The maximum number of iterations per unit of time is 10, which ensures the necessary convergence of the result. The simulation time is 60 seconds.

As a result of the simulation of the expander operation, the pressure distribution (relative to atmospheric) in the cavity between the screw and the cylinder was obtained (Fig. 5). Fig. 5 clearly shows that the pressure increases along the screw axis in the direction of movement of the multiphase mixture. The increase in pressure is explained by a decrease in the volume of the cavity along the screw axis. At the outlet of the forming nozzle holes, the pressure value is 14.2±0.02·10^5 Pa.

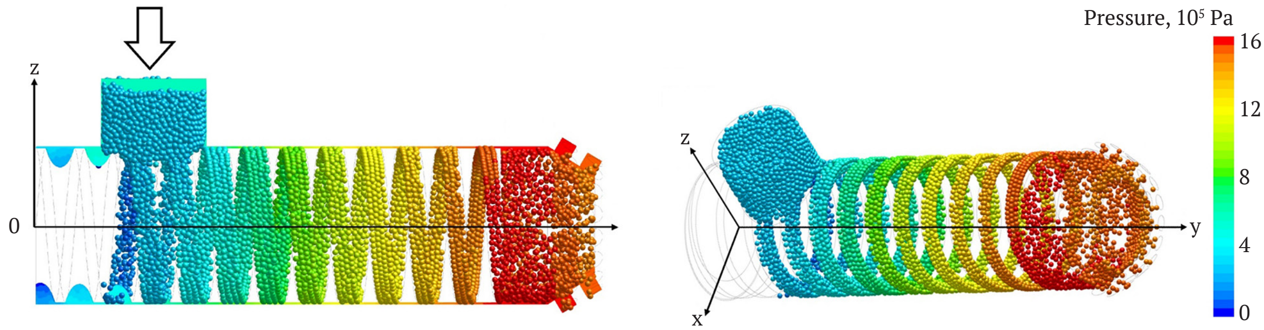

Figure 5. Pressure distribution (relative to atmospheric) in the screw channel of the expander
Source: compiled by the authors

The presented findings in the form of numerical data and visualisation of the technological process of feed expanding confirm the theoretical studies by R. Guy [7], J.L. White and H. Potente [8], V.V. Bratishko [18]. In turn, the results of experimental studies [13; 23] confirm the nature of the pressure distribution (relative to atmospheric) in the screw channel of the expander. This allows asserting the adequacy of the developed physical and mathematical apparatus for numerical modelling of the feed expander in the Star-CCM+ software suite. That is, in further studies to substantiate the range of rational design and regime parameters of the feed expander, provided that the required pressure is provided at the outlet of the forming nozzle holes, a full-fledged numerical experiment can be carried out using generally accepted experimental planning methods.

CONCLUSIONS

The physical and mathematical apparatus of movement of solid feed components in the screw channel of the expander was further developed, which is the basis for the method of numerical modelling of the feed expansion process in the Star-CCM+ software suite. Preliminary numerical simulation of the process of expanded feed preparation is carried out in the Star-CCM+ software suite, which determines as research criteria: pressure in the cavity between the screw and the expander cylinder, the obtained density, the expander performance, the vector field of feed component velocities in the screw channel. The following factors should be selected as research factors: supply of feed components, screw rotation speed, screw diameter, length, and pitch, and the coefficient of change in screw pitch and depth along its length.

In the future, based on the results of numerical modelling using the method of planning multi-factor experiments, it is necessary to establish regularities in the influence of research factors on criteria in the form of second-order regression equations. Further, as a result of solving the compromise problem according to the research criteria, it is necessary to establish rational design and mode parameters of the feed expander. After that, it is planned to test the obtained theoretical regularities experimentally on an experimental feed expander installation

REFERENCES

[1] Khokhrin, S.I. (2002). *Feed and animal feeding*. Saint Petersburg: Lan publishing house.

[2] Polishchuk, V.Yu., Korotkoe, V.G., & Zubkova, T.M. (2003). *Design of extruders for the agro-industrial complex*. Ekaterinburg: Ural Branch of the Russian Academy of Sciences.

[3] Yegorov, B.V., Voyetska, O.E., & Lapinska, A.P. (2011). Modern trends in the production of compound feed for pigs. *Scientific Works of Odessa National Technological University*, 40(1), 76-80.

[4] Yegorov, B.V., & Khorenzhy, N.V. (2004). Technological basis of batch technology for the production of compound feed for cattle. In *Ukraine. Compound feed – 2004* (pp. 70-72). Kyiv: National University of Bioresources and Nature Management of Ukraine.

[5] Law of Ukraine No. 2264-VIII “On Feed Safety and Hygiene”. (2021, Murch). Retrieved from https://zakon.rada.gov.ua/laws/show/2145-19#Text.

[6] Egorov, B.V., Makarynskaya, A.V., Savchenko, S.N., & Paulina, Ya.B. (2004). The quality of the filler is the quality of the premix. *Cereal Products and Compound Feed*, 3, 37-40.

[7] Guy, R. (2001). *Extrusion cooking: Technologies and applications*. Sawston: Woodhead Publishing.

[8] White, J.L., & Potente, H. (2003). *Screw extrusion. Science and Technology*. Munich: Hanser Publishers.

[9] Simon, K.N. (2016). *Numerical modeling of the wood pelleting process*. Esbjerg: Aalborg University Esbjerg.

[10] Estanislao, O.R. (2009). *Numerical simulations of reactive extrusion in twin screw extruders* (Doctoral thesis, University of Waterloo, Waterloo, Canada).

[11] Lewandowski, A., & Wilczyn´ski, K. (2022). Modeling of twin screw extrusion of polymeric materials. *Polymers*, 14, article number 274. doi: 10.3390/polym14020274.

[12] Darnell, W.H., & Mol, E.A.J. (1956). Solids conveying in extruders. *SPE Journal*, 12(4), 20-29.

[13] Cundall, P.A., & Strack, O.D.L. (1979). A discrete numerical model for granular assemblies. *Géotechnique*, 29, 47-65.

[14] Aliev, E. B., Bandura, V. M., Pryshliak, V. M., Yaropud, V. M., Trukhanska, O. O. (2018). Modeling of mechanical and technological processes of the agricultural industry. *INMATEH – Agricultural Engineering*, 54(1), 95-104.

[15] Aliev, E.B., & Labatiuk, Yu.M. (2017). Numerical modeling of mechanical and technological processes of agro-industrial production. Modern problems of improvement of technical systems and technologies in animal husbandry. *Kharkiv National Technical University of Agriculture named after P. Vasylenko*, 180, 67-71.

[16] Bratishko, V.V. (2013). Research of the geometric parameters of the feed granulator screw with the base of the channel in the form of a part of a circle. *Kharkiv National Technical University of Agriculture named after P. Vasylenko*, 132, 415-420.

[17] Bratishko, V.V. (2012). Study of the effect of geometric parameters of the working bodies of the fodder granulator on the intensity of the granulation process. In *Technical progress in animal husbandry and fodder production* (pp. 7-9). Glevakha: National Scientific Center “Institute of Mechanization and Electrification of the Power State”.

[18] Bratishko, V.V. (2014). Model of pressure change in the channel of the granulator screw. In *Technical progress in agricultural production* (pp. 130-131). Glevakha: National Scientific Center “Institute of Mechanization and Electrification of the Power State”.

[19] Johnson, K.L. (1987). *Contact mechanics*. Cambridge: Cambridge University Press.

[20] Moscicki, L. (2003). Effect of screw configuration on quality and SME value of corn extrudate. *Teka Commission of Motorization Power Industry in Agriculture*, III, 182-186.

[21] Sapa, V.Yu. (2009). Improving the design and regime parameters of the expander (Doctoral thesis, Orenburg State Agrarian University, Orenburg, Russia).

[22] Aliev, E.B., & Shevchenko, I.A. (2017). Research of aerodynamic properties of oilseeds. *Herald of Agrarian Science*, 769(3), 63-65.

[23] Bulhakova, A. (2022). Mass spectrometric studies of valine molecules by electron shock in the gas phase. *Scientific Herald of Uzhhorod University. Series “Physics”*, 51, 9-17.

Ельчин Бахтияр огли Алієв[1,2],
Володимир Юрійович Дудін[2], Микола Олександрович Лінко[2]

[1]Інститут олійних культур Національної академії аграрних наук України
69055, вул. Інститутська, 1, с. Сонячне, Запорізька обл., Україна

[2]Дніпровський державний аграрно-економічний університет
49600, вул. Сергія Єфремова, 25, м. Дніпро, Україна

Фізико-математичний апарат чисельного моделювання експандера кормів

Анотація. На продуктивність лінії приготування кормів і на її техніко-економічну ефективність впливають конструктивно-технологічні параметри обладнання. Не винятком є геометрія гвинта експандера і режими його роботи. Для зменшення питомих енерговитрат експандера необхідно встановити його раціональні конструктивно-режимні параметри. Це можна зробити використовуючи методи аналітичного розрахунку, які враховують механізми руху і руйнування твердих речовин. Моделювання з використанням методу дискретних елементів набуває все більшого розповсюдження для опису руху твердих компонентів в грануляторах, екструдерах або експандерах. Метою дослідження є удосконалення фізико-математичного апарата руху твердих компонентів корму у гвинтовому каналі експандера кормів і розробка методики його чисельного моделювання. Чисельне моделювання проводилося із застосуванням моделі руху розділеної течії багатофазної ейлерової суміші у тривимірного просторі. При цьому рух підпорядковувався допустимої двошарової k-ε-моделі турбулентності і багатофазного рівняння стану. Було проведено удосконалення фізико-математичного апарата руху твердих компонентів корму у гвинтовому каналі експандера кормів, яке покладено в основу методики чисельного моделювання в програмному пакеті Star CCM+, базувалося на тому, що конгломерат компонентів корму представляється у вигляді упаковки сферичних частинок. При цьому сила тиску повинна компенсуватися сумарною силою контактної взаємодії частинок між собою і стінкою. Проведено попереднє чисельне моделювання процесу експандованого приготування кормів в програмному пакеті Star CCM+. Практична значимість полягає в тому, що удосконалений фізико-математичного апарата і розроблена методика чисельного моделювання процесу роботи експандера кормів дозволяє обґрунтувати його конструктивно-режимні параметри для забезпечення низьких питомих енерговитрат без втрати якості виконання технологічного процесу

Ключові слова: експандування кормів, симуляція, метод дискретних елементів, Star CCM+, тиск, векторне поле швидкостей, щільність

Machinery & Energetics
Vol. 13, No. 3. 2022

Journal homepage:
https://technicalscience.com.ua/en

UDC 631.354.022
DOI: 10.31548/machenergy.13(3).2022.17-24

Oleksandr Banniy[*], Pavlo Popyk, Dmytro Savko

National University of Life and Environmental Sciences of Ukraine
03041, 15 Heroiv Oborony, Kyiv, Ukraine

Failure Analysis of the Segment Finger Bar Mower and Force Interaction of the Blade Segment with the Plant Stem

Abstract. Scientific observations on the quality and reliability of combine harvesters have shown that of all the delays of equipment, 32...35% of the total operating time, technical failures account for 17.4...19.8%. Most of the failures were observed with the failure of combine parts, mechanical transmissions, hydraulic systems, etc. Quantitative analysis of harvester failures has shown that most failures occur in the operation of the cutting device, namely the finger bar mower. The working hypothesis is that it is possible to increase the reliability of the cutting device of harvesting machines in ordinary operating conditions and in the event of sudden failures by applying a coating on the blade segment, without significantly changing its geometric parameters, and performing notches that ensure both a decrease in the mass of the segment and its destruction without plastic deformation when foreign objects enter the cutting zone. The main problem of the reliability of segments of cutting device, harvesting equipment, is the cutting edge of the blade, which wears out and deforms during operation. From the above, it follows that the purpose of the study is to improve the reliability of segment finger bar mower machines by improving the mechanical properties of segments, these investigations are relevant and of practical interest. The study includes the use of mathematical probability and reliability theory, analysis, and a systematic approach to provide an analytical description of the operation of a cutting device segment. The consequence of this scientific investigation is an analysis of failures and malfunctions of the machinery, presented graphically, a diagram of how a plant stem segment is cut and the forces acting on the stem and the segment during the cutting process are depicted. These materials have scientific and informative content that would be of interest to engineers and scientists in the process of research and production of cutting device segments

Keywords: segment type cutting device, equipment reliability, harvesting equipment header, grain harvesting equipment, header failure, blade segment edge angle

Article's History: Received: 09.03.2022; Revised: 20.07.2022; Accepted: 11.08.2022

INTRODUCTION

A combine harvester is a complex technical system [1; 2], consisting of a large number of parts, components, and aggregates. Each node and mechanism does its own specific job. Contrary to this, one of the defining features of the machine's efficiency is its reliability [3].

The reliability of harvesting equipment is understood as the ability of equipment and its components to perform certain tasks [4], maintain operating parameters and conditions of their use due to maintenance, repair, storage, and transportation.

Currently, there is a tendency to reduce the total number of agricultural machinery and increase the average load on machinery by more than 2 times [5; 6]. All this is the reason for the decrease in its reliability and the increase in downtime conditioned by technical reasons.

Both Ukrainian and foreign researchers have not been able to solve the problem of sudden failures associated with foreign objects getting into the cutting zone.

The purpose of this study is to improve the reliability of the finger bar mower by improving the segment parameters.

The theoretical model of the formation of parametric failure as a result of the size of the working surfaces of the segment blade in contact with the stem material and depending on the rate of damage to its working surfaces is of scientific value. Theoretical model for improving the durability of a cutting device blade segment by creating a wear-resistant coating.

Suggested Citation:
Banniy, O., Popyk, P., & Savko, D. (2022). Failure analysis of the segment finger bar mower and force interaction of the blade segment with the plant stem. *Machinery & Energetics,* 13(3), 17-24.

[*]Corresponding author

The originality of this study is to increase the reliability of the cutting device of harvesting machines.

The conducted studies of the reliability of combine harvesters showed that 17.4...19.8% of total delays (inefficiencies) of the technique, representing 32...35% of the working time is due to a technical malfunction. According to the results of studies, the actual failure time of combine harvesters in Ukraine is 3...70 hours, and the readiness factor is 0.85...0.97, respectively. Most often, malfunctions occur in the harvesting part, mechanical gears, hydraulic systems, working bodies of the thresher, electrical and control devices (Fig. 1) [7].

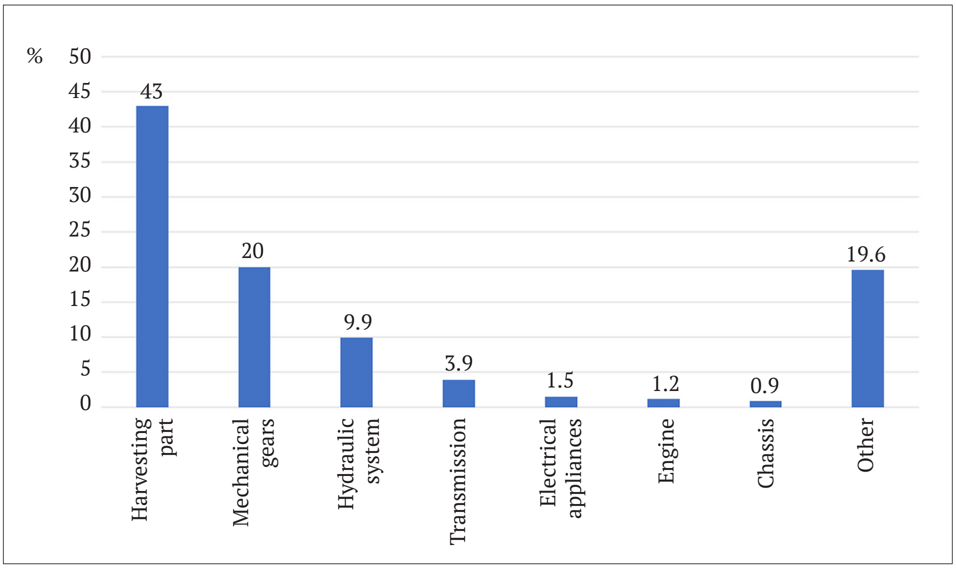

Figure 1. Distribution of combine harvester failures

Source: [7]

Quantitative analysis of malfunctions of combine parts showed that the maximum number of failures belongs to the parts of the cutting device, that is, to segments and counter-cutting parts and fingers (Fig. 2) [7]. Notably, the failure of counter-cutting parts and fingers mainly occurs as a result of force contact of segments deformed under the influence of foreign bodies in the cutting zone [8].

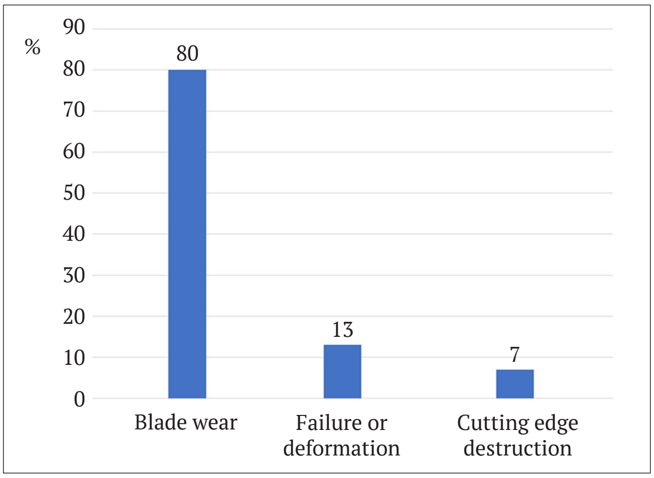

Figure 2. Main types of malfunctions

Source: [7]

Wear of the cutting edge of the blade segments of the cutting machine, their geometric deformation or destruction due to accidents, and loosening of attachment to the knife bar are the main failures of the cutting machine.

THEORETICAL FRAMEWORK

Wear of the blade segment usually occurs as a result of friction during the cutting of the plant stem (Fig. 3). When the blade moves together, the lower cutting edge of segment 1 interacts with the plant stem and the counter-cutting plate 3. In this regard, the wear of the lower part of the segment is significantly greater in relation to the upper part. As a result of wear, the sharpening angle of the blade β and the sharpness of the blade edge δ change, which leads to a decrease in the reliability of the cutting device. There is a possibility of foreign objects (stones, parts of agricultural machinery, etc.) entering the cutting zone when using harvesting equipment on poorly mown and uneven areas of the field due to the flatness of cereals and grass.

The segment curved in the vertical plane when the blade moves back and forth collides with the elements of the finger, destroys it and destroys itself.

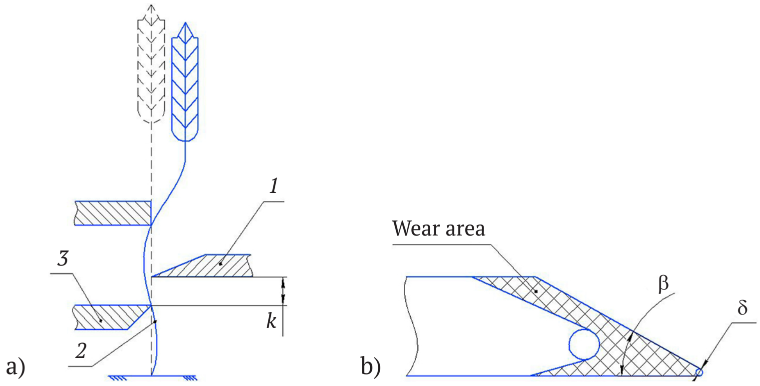

Figure 3. Graphic representation of the operation of the cutting device segment
a) interaction of the blade segment with the plant stem: b) wear of the blade segment.
1 – segment; 2 – plant stem; 3 – anti-cutting plate; *k* – gap in the cutting blades

Segments fail and break off on the back side near the fasteners, the counter-cutting parts of the finger quickly wear out and sometimes break at the edge (Fig. 4). All these processes lead to an increase in the time of repairing the combine and eliminating the malfunction. However, both Ukrainian and foreign manufacturers of grain harvesting machines could not fully solve the problem of preventing foreign objects from entering the working bodies, and therefore, protecting them from emergency failures [9].

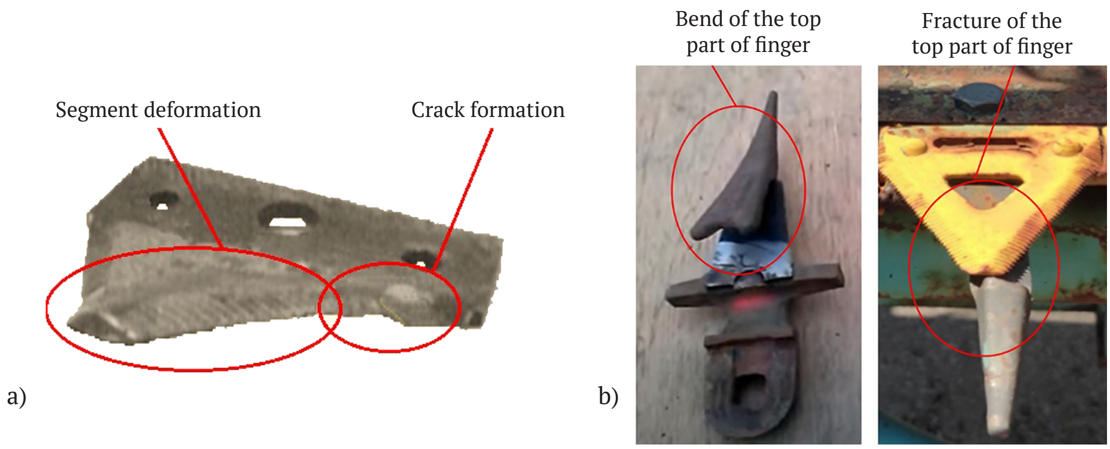

Figure 4. Result of sudden failure: a) damage to the segment; b) damage to the finger elements

Thus, the analysis of the information under study indicated that the weakest component in harvesting machines is the cutting device segment.

MATERIALS AND METHODS

The study involves the use of the theory of probability and reliability, mathematical analysis, and a systematic approach that provides an analytical description of the operation of the cutting device segment, standard bench and operational testing methods on modern equipment, and experimental planning methods, mathematical statistics for processing the results obtained.

RESULTS AND DISCUSSION

A certain amount of energy A needs to be spent to destroy the stem of the plant under the edge of the blade A_{blade} and overcome the resistance forces A_{res} caused by plant deformation [10; 11]:

$$A=A_{blade}+A_{res}, \tag{1}$$

The first term of this expression is characterised by the strength properties of the material, which are estimated by such an indicator as the ultimate strength σ_{ult}. The ultimate strength does not depend on the method of impact on the processed material and the parameters of the cutting tool and is determined by the properties of the material itself:

$$A_{blade}=f(\sigma_{ult}). \quad (2)$$

The second term considers the properties of the plant material, the parameters of the cutting tool, and the operating modes:

$$A_{res}=f(\delta, \beta, h_{cmp}, h_{layer}, l, \mu, E, \tau, v_s, k, s_{bend}, b), \quad (3)$$

where δ – blade edge sharpness, m; β – blade sharpening angle, deg; h_{cmp} – compression of the material preceding destruction, m; h_{layer} – thickness of the cut layer, m; l – length of the blade that came into contact with the material, m; μ – Poisson's ratio; E – elasticity modulus of the material, MPa; b – distance from the top of the finger to the segment blade, m; k – gap between the segment and the anti-cutting plate, m; v_s – segment speed, m/s; s_{bend} – amount of bending of the stem, m; τ – time of impact of the cutting tool on the stem, s.

Thus, the implementation of the cutting process is possible provided that the force P applied to the blade would contribute to the occurrence of a destructive contact stress on its edge σ_d, exceeding the tensile strength of the material $\sigma_d>\sigma_{ult}$, and the destruction itself occurred with minimal deformation of the material $(s_{bend}, h_{cmp})\to min$.

According to [12], to cut the stem of a plant with a segment of the cutting device, it is necessary that it overcomes the resistance force of the blade entering the material P_{cr}, the bending resistance force of the stem P_{bend} and the inertia force of the stem P_{cin}:

$$P=P_{cr}+P_{bend}+P_{cin}. \quad (4)$$

When cutting, the plant stem rests on two supports, the upper part of the finger (support 1) and the anti-cutting plate (support 2), so it can be represented as a beam that rests freely on two supports (Fig. 5).

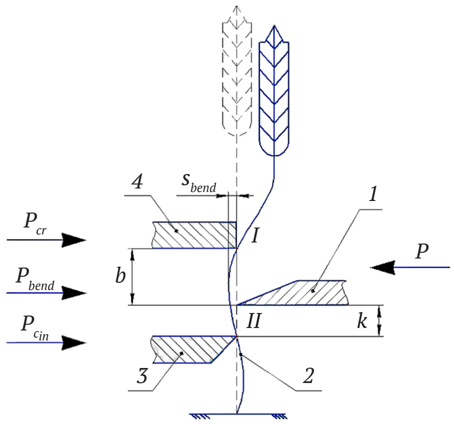

Figure 5. Stem cutting diagram 1 – segment; 2 – stem; 3 – anti-cutting plate; 4 – upper part of the finger

Then the bending resistance of the stem is determined by the following equation:

$$P_{bend}=\frac{3s_{bend}EJ}{bk^2\left(1-\frac{k}{b}\right)^2}, \quad (5)$$

where s_{bend} –amount of bending of the stem, m; E – elastic modulus of the stem, MPa; J – polar moment of inertia of the transverse stem, m4; b – distance from the top of the finger to the blade segment, m; k – gap between the segment and the anti-cutting plate, m.

The moment of inertia of the stem [13] is determined by the equation:

$$P_{c_{in}}=\frac{17m_{I-II}v_H}{35\tau}, \quad (6)$$

where m_{I-II} – weight of the stem of section 1-2, kg; v_H – segment speed, m/s; τ – time of impact of the cutting tool on the stem, s.

According to [14], when a single-face blade is deepened into a layer of material, forces act on it (Fig. 6 and 7): P_{blade} – resistance to destruction under the edge of the blade, directed opposite to the movement of the blade; P_{comp} – compression forces of the blade material that have a vertical direction and act on the edge of the blade; P_{res} – force of resistance of the material to compression by the blade, also directed opposite to the movement of the blade:

$$P_{cr}=P_{blade}+(P_{comp}+P_{res}). \quad (7)$$

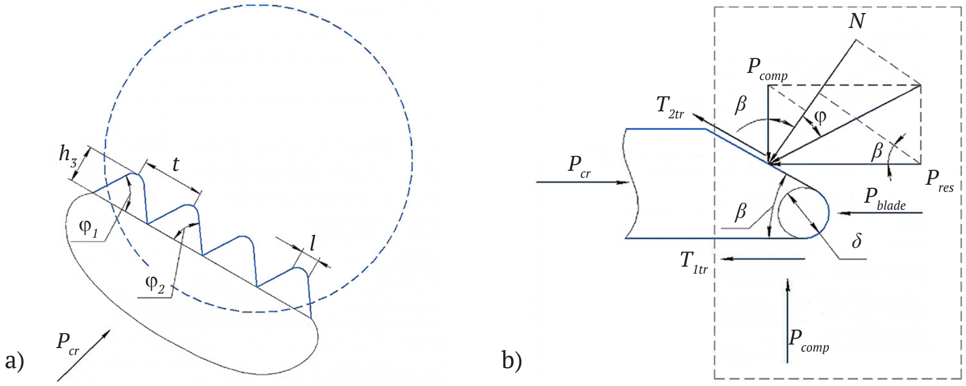

Figure 6. Force interaction of the blade with the plant stem a) forces acting on the blade; b) forces acting on the chamfer of the blade T_{1tr}, T_{2tr} – friction forces, N – normal power

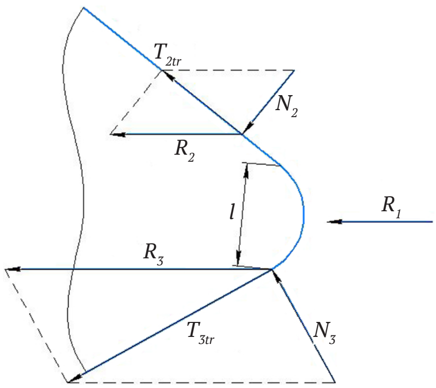

Figure 7. Forces acting on the notch of the blade segment. T_{2tr}, T_{3tr} – friction forces, R_1, R_3, R_l – resultant forces, N_1, N_3 – normal forces

In the transformed form, equation (7) has the form:

$$P_{cr} = l\delta\sigma_d + \frac{E}{2}\cdot\frac{h_{cmp}^2 l}{h_{layer}} \left[tg\beta + f\,sin^2\beta + \mu\left(f + cos^2\beta\right)\right]. \tag{8}$$

where δ – sharpness of the blade edge, m. σ_d – destructive contact stress, $\frac{H}{m^2}$; l – length of the blade in contact with the material, m; E – elasticity modulus of the material, MPa; h_{cmp} – compression of the material preceding destruction, m; h_{layer} – thickness of the cut material layer, m; μ – Poisson's ratio [15]; f – coefficient of friction of the cut fibres of the stem against the edges of the wedge; β – blade sharpening angle, deg.

The first part of equations (7 and 8) reflects the processes occurring on the edge of the blade, and the second part reflects its chamfer. Considering the fact that the blade segment has a notch, the amount of force P_{blade} will depend on its geometric parameters and the number of blades that come into contact with the stem, the latter is determined by the diameter of the stem to be cut, d_cmp and notch spacing t_H. Then equation (7) will take the form:

$$P_{cr} = \frac{d_{cmp}}{t_H}\left(P_{blade} + \frac{E}{2}\cdot\frac{h_{cmp}^2 l}{h_{layer}} tg\beta + f\,sin^2\beta + \mu\left(f + cos^2\beta\right)\right]\right). \tag{9}$$

where d_{cmp} – diameter of the cut stems, m; t_H – notch spacing of the blade segment, m; P_{blade} – resistance to destruction of the stem under the edge of the blade, N; E – elastic modulus of the material, MPa; h_{cmp} – compression of the material preceding destruction, m; h_{layer} – thickness of the cut material layer, m; μ – Poisson's ratio; f – coefficient of friction of the cut fibres of the stem against the edges of the wedge; β – blade sharpening angle, deg.

To calculate the force acting from the stem of the cut plant on the notch P_{blade}, it is assumed that the specific pressure of the plant mass is distributed evenly over the surface of the tooth section.

Under the influence of normal forces N_2 and N_3, friction forces occur on the side faces of the tooth T_{2tr}, T_{2tr}. Forces R_2 and R_3 accordingly are the resultant forces N_2, N_3 and T_{2tr}, T_{3tr}.

$$R_2 = T_{2tr} + N_2, \tag{10}$$

$$R_3 = T_{3tr} + N_3. \tag{11}$$

Then

$$P_{blade} = R_1 + R_2 + R_3, \tag{12}$$

where R_1 – force acting on the top of the tooth, *N*.

Force R_1 can be represented as the product of the contact area of the tooth with the stem F_k for destructive contact stress σ_p:

$$R_1=\sigma_p F_k=\sigma_p \delta l, \tag{13}$$

where δ – sharpness of the blade edge, m; *l* – length of the tooth tip, m.

Size of normal forces N_2 and N_3 is determined by the equations:

$$N_2 = \sigma_p \delta \frac{h_3}{\sin \varphi_1}, \tag{14}$$

$$N_3 = \sigma_p \delta \frac{h_3}{\sin \varphi_2}, \tag{15}$$

where φ_1 and φ_2 – angles of inclination of the side faces of the tooth, deg; h_3 – notch tooth height, m.

Tangential friction forces can be found by equations:

$$T_{2tr}=fN_2, \tag{16}$$

$$T_{3tr}=fN_3, \tag{17}$$

where *f* – coefficient of friction between the notch and the plant stem.

Total cutting force P_blade of fibre stem by tooth notch:

$$P_{blade} = \sigma_p \delta l + \sigma_p \delta \frac{h_3}{\sin \varphi_1} + \sigma_p \delta \frac{h_3}{\sin \varphi_2} + f \sigma_p \delta \frac{h_3}{\sin \varphi_1} + f \sigma_p \delta \frac{h_3}{\sin \varphi_2} = \sigma_p \delta \left[l + h_3(1+f)\left(\frac{1}{\sin \varphi_1} + \frac{1}{\sin \varphi_2}\right)\right]. \tag{18}$$

Substituting the values of all opposing forces P_{cr}:

$$P_{cr} = \frac{d_{cmp}}{t_H}\left(\sigma_p \delta \left[l + h_3(1+f)\left(\frac{1}{\sin \varphi_1} + \frac{1}{\sin \varphi_2}\right)\right] + \frac{E}{2d_{cmp}} h_{cmp}^2 l tg\beta + f \frac{\mu E}{2d_{cmp}} h_{cmp}^2 l + f\left(\frac{E}{4d_{cmp}} h_{cmp}^2 l tg\beta \sin 2\beta + \frac{\mu E}{2d_{cmp}} h_{cmp}^2 l \cos^2 \beta\right)\right). \tag{19}$$

Converting the resulting equation:

$$P_{cr} = \frac{d_{cmp}}{t_H} \sigma_p \delta \left[l + h_3(1+f)\left(\frac{1}{\sin \varphi_1} + \frac{1}{\sin \varphi_2}\right)\right] + \left(\frac{E h_{cmp}^2 l}{2d_{cmp}} \cdot \frac{E h_{cmp}^2 l}{2d_{cmp}} [tg\beta + f \sin^2 \beta + \mu(f + \cos^2 \beta)] + \frac{3 s_{bend} EJ}{bk^2 \left(1-\frac{k}{b}\right)^2} + \frac{17 m_{I-II} v_H}{35\tau}\right). \tag{20}$$

where d_{cmp} – diameter of the cut stems, m; t_H – notch spacing of the blade segment , m; σ_p – breaking contact stress, N/m^2; δ – sharpness of the blade edge, m; *l* – length of the tooth tip, m; h_3 – notch tooth height, m; *f* – coefficient of friction of the cut fibres of the stem on the wedge boundary; φ_1, φ_2 – angles of inclination of the side faces of the tooth, deg; *E* – elasticity modulus of the material, MPa; h_{cmp} – compression of the material preceding destruction, m; *β* – blade sharpening angle, deg; μ – Poisson's ratio; s_{bend} – amount of bending of the stem, m; *J* – polar moment of inertia of the transverse stem, m^4; *b* – distance from the top of the finger to the segment blade, m; *k* – gap between the segment and the anti-cutting plate, m; m_{I-II} – weight of the stem on the section 1-P, kg; v_H – segment speed, m/s; *τ* – time of impact of the cutting tool on the stem, s.

This expression reflects and defines the main parameters that affect the process of destruction of the stem when cutting it with a segment of the cutting device: constructive – *β*, δ, t_H, *l*, h_3, φ_1, φ_2; physical and mechanical – *E*, μ, *f*, σ_p, and operation mode – d_{cmp}, h_{cmp}, *τ*, v_H, *k*, *b*.

The first term of equation (20) defines phenomena that directly lead to the destruction and splitting of the material under the action of notch teeth and can be characterised as useful. The second defines phenomena associated with the deformation of plant material in the direction of movement of the blade, which negatively affect the reliability indicators of the cutting process, such as energy intensity and cut purity.

Determining the optimum shape of cutting device components has been the work of many researchers, who have subsequently laid the foundation for the standardisation of segments and finger plates in harvesting machines.

In [16], the advantage of an oblique cut over an end cut is substantiated, including the cutting speed, angles of inclination and sharpening of the blade, and the height of the cutting part of the segment. In particular, P.V. Sysolin found that in the cutting device of harvesting machines, when the knife speed is less than 3.4 m/s, cutting takes place on the principle of scissors. Similar experiments were conducted by professor V.I. Duganets [17]. The researcher also concluded that at low knife speeds, it is necessary that the plants are pressed by the segment against the anti-cutting plate. In [18], the width of the front part of the segment, both with a smooth and notched blade, is substantiated, and the value of the angles of clamping of steppe grasses is determined.

The study [19] is devoted to substantiating the optimal thickness of the cutting tool. It provides recommendations for choosing the optimal thickness of the blade and its strength. The researcher notes that if there is an angle between the direction of movement of the knife and its rear plane, the thickness of the knife does not play a role, since the rear plane of the knife loses contact with the mass layer, while contact with the front plane increases.

Studies by the researchers have shown that productive cutting can improve stem use and lead to energy savings. The authors of this study investigated the mechanical properties of the plant stem and the angle of inclination of the blade in relation to the cut stems. It was observed that the shear stress decreases from the lower part of the body to the upper part, and the shear force and energy in the lower part are significantly higher than in other regions, due to cross-sectional parameters. Cutting plant stems in high or low humidity conditions can save energy. As the blade angle increases, the cutting force decreases. However, the specific cut energy first decreased, and then gradually increased with increasing angle of inclination of the blade segment.

However, the authors do not provide a theoretical substantiation for the conditions for cutting plant raw materials by sliding. In addition, the studies do not show the influence of plants on the segment of the cutting machine from the standpoint of preserving the strength that is lost during the operation of the segment, which is affected by thermal energy from friction processes, chemical effects on the surface of the blade and the knife itself, which is affected by moisture released during mowing (stem juice). As a result, its reliability is lost and its service life is reduced.

CONCLUSIONS

As a result of the study, the distribution of failures of harvesting equipment and the main types of its malfunctions were highlighted. A diagram of the operation of the cutting device segment is constructed and it is also determined that a certain amount of energy A must be spent to destroy the plant stem under the edge of the blade. Using a graphical representation of the stem cutting scheme, the distribution of forces acting on the segment is constructed and, as a result, the cutting force of the stem is calculated. The analysis of the process of operation of the cutting device of harvesting machines from the standpoint of considering it as a complex system, the lowest elements of which in its hierarchical scheme are the working surfaces of the segment, determined their intended purpose in terms of increasing its reliability in case of gradual wear, reducing material costs, and restoring working capacity in case of sudden failures. The mathematical dependences of cutting resistance forces and power consumption for the cutting device drive are clarified, which determined the areas for improving its reliability by preserving the shape parameters and properties of the blade segment notch during a given period of operation.

In further studies of the finger bar mower, the possibilities of improving the reliability and operability of segments by strengthening them on the surface will be considered, since they are subjected to chemical corrosion during operation, which leads to their failure.

REFERENCES

[1] Boyko, A.I., Novytskyi, A.V., & Bannyi, O.O. (2011). Assessment of risks of failure of complex equipment. *Bulletin of Kharkiv National Technical University of Agriculture named after P. Vasylenko*, 122, 241-249.

[2] Pavlyuk, R.V. (2011). Distribution of failures and time for their elimination between systems of grain harvesters. *A Collection of Scientific Works of the Ukrainian National Academy of Sciences*, 48, 9-14.

[3] Ying, L., Zhuohuai, G., & Yisong, C. (2021). Development and test of frequency subsection regulation system for combine harvester header cutter. *INMATEH. Agricultural Engineering*, 65(3), 283-292.

[4] Novytskyi, A.V., & Ruzhilo, Z.V (2012). Logical-probabilistic model of the reliability of complex equipment. *Collection of Scientific Works of the Vinnytsia National Agrarian University*, 2(66 (11)), 33-37.

[5] Dumenko, K.M. (2011). New ways of increasing the reliability of grain harvesting machines. *Design, Production and Operation of Agricultural Machines*, 41(1), 315-320.

[6] Senchuk, I.I. (2018). Peculiarities of the transformation of the resource potential of agrarian enterprises. *Ukrainian Journal of Applied Economics*, 3(4), 29-34.

[7] Pavlyuk, R.V., & Lebedev, A.T. (2011). Distribution of failures and time for their elimination between systems of grain harvesters. *Izvestiya Gorskogo GAU*, 48(1), 153-156.

[8] Domuschi, D.P., Pozhar, O.Ya., & Lipin, A.P. (2018). Theoretical and experimental studies on determining the production conditions of harvesting grain crops using technological complexes. *Agrarian Bulletin of the Black Sea Coast*, 90, 213-221.

[9] Barabash, G.I., & Mikulina, M.O. (2021). The influence of the width of the harvester on the indicators of the use of the grain harvester. In *Technical support of innovative technologies in the agro-industrial complex: A collection of abstracts of reports on the materials of the 1st International scientific and practical conference of young scientists* (pp. 53-54). Melitopol: Dmytro Motornyi Tavria State Agrotechnological University.

[10] Mazury, M.P. (Ed.). (2020). *Fundamentals of the theory of cutting materials*. Lviv: Novy Svit-2000.

[11] Voytyuka, D.G. (Ed.). (2005). *Agricultural machines. Basics of theory and calculation*. Kyiv: Vyshcha shkola.

[12] Bosoy, E.S. (1967). *Cutting devices of harvesting machines*. Moscow: Mashinostroenie.

[13] Kurylo, V.L., & Pryshlyak, V.M. (2019). Theory and practice of stem cutting in agricultural machine design technologies and formation of professional competencies of the future agricultural engineer. *All-Ukrainian Scientific and Technical Magazine "Technology, Energy, Transport of Agricultural Industry"*, 105(2), 10-17.

[14] Malakov, O.I. (2018). The current state of the technical level of machines for mowing grass for hay. *Technology, Energy, Transport of Agricultural Industry*, 101(2), 139-144.

[15] Kutsenko, A., Bondar, M., & Pryshliak, V. (2018). *Mechanics of materials: Theory and problems*. Kyiv: Center for Educational Literature LLC.

[16] Rud, A., Moshenko, I., Iliyashik, V., Morozov, A., Sysolin, P., Rybak, T., & Salo, V. (2016). Analysis of headers and attachments for grain harvesters and features of their use in soybean and rapeseed harvesting. *Bulletin of the Lviv National Agrarian University: Agricultural Engineering Research*, 20, 187-198.

[17] Ilyashik, V.V., Duganets, V.I., & Moshenko, I.O. (2016). Analysis of the designs of FLEX headers and their adaptation to work with CLAAS grain harvesters for harvesting soybeans. *Collection of Scientific Works of PDATU*, 24, 48-56.

[18] Ivanyshyn, V.V., Iliyashik, V.V., & Duganets, V.I. (2017). Analysis of designs of headers and attachments for grain harvesters and features of their use in harvesting leguminous crops and rapeseed. *Collection of Scientific Works of PDATU*, 26(2), 54-63.

[19] Babii, A.V. (2017). Increasing the cutting efficiency of stem crops. In *All-Ukrainian scientific and practical conference "Equipment and technologies of modern mechanical engineering"* (pp. 4-6). Ternopil: Ternopil National Technical University named after Ivan Pulyu.

Олександр Олександрович Банний, Павло Сергійович Попик, Дмитро Олегович Савко

Національний університет біоресурсів і природокористування України
03041, вул. Героїв Оборони, 15, м. Київ, Україна

Аналіз відмов сегментно-пальцевого ріжучого апарату та силова взаємодія леза сегмента зі стеблом рослини

Анотація. Наукові спостереження за якістю і надійністю зернозбиральних комбайнів показали, що з усіх затримок техніки, що становлять 32…35 % загального часу роботи, технічних відмов припадає на частку 17,4…19,8 %. Більшість відмов спостерігалося з виходом з ладу деталей комбайна, механічних трансмісій, гідросистеми та ін. Кількісний аналіз відмов жатки показав, що найбільше відмовлень виникає в роботі органів ріжучого апарату, а саме сегментно пальцевого різального апарата. Робоча гіпотеза полягає в тому, що підвищити надійність ріжучого апарату збиральних машин у рядових умовах експлуатації та при виникненні раптових відмов можливо за рахунок нанесення покриття на лезо сегмента, без істотної зміни його геометричних параметрів, та виконанням просічок, що забезпечують як зниження маси сегмента, так і його руйнування без пластичної деформації при попаданні до зони різання сторонніх предметів. Головним проблемою надійності сегментів різального апарату, збиральної техніки, є ріжуча кромка леза, яка зношується та деформується в процесі експлуатації. З сказаного вище випливає, що мета дослідження цілеспрямована на підняття надійності сегментно-пальцевих різальних апаратів за рахунок покращення механічних властивостей сегментів, дані дослідження є актуальними та становлять практичний інтерес. Дослідження включають використання математичної теорії ймовірності та надійності, аналізу та системного підходу для забезпечення аналітичного опису роботи сегмента різального апарату. Наслідком даного наукового матеріалу є розбір відмов та несправностей техніки, який подано у графічній формі, а також зображено схему зрізу сегментом стебла рослини та сили які діють на стебло та сегмент під час зрізу. Ці матеріали мають науково-інформативне наповнення, яке буде цікаве інженерам і науковцям у процесі дослідження та виробництва сегментів машин для різання

Ключові слова: ріжучий апарат сегментного типу, надійність техніки, жниварка збиральної техніки, зернозбиральна техніка, відмова жатки, кут кромки леза сегмента

Machinery & Energetics
Vol. 13, No. 3. 2022

Journal homepage:
https://technicalscience.com.ua/en

UDC 621.3.067
DOI: 10.31548/machenergy.13(3).2022.25-33

Viktor Kaplun*, Roman Chuienko, Svitlana Makarevych

National University of Life and Environmental Sciences of Ukraine
03041, 15 Heroiv Oborony Str., Kyiv, Ukraine

Investigation of Energy Parameters of a Compensated Asynchronous Motor in the Mode of Repeated Short-Term Starts

Abstract. The study is devoted to energy efficiency management of induction motors with a short-circuited rotor of low and medium power and is a continuation of the development of the theory of compensated asynchronous motors. The purpose of the study is to substantiate the influence of the capacitance value of the internal capacitive reactive power compensation of an asynchronous motor in starting mode. The performed mathematical modelling of the compensated asynchronous motor allowed investigating quasi-transient electromagnetic processes considering the spatial and temporal orientation of the currents of the main and additional windings of the stator and rotor phases of the compensated asynchronous motor. Achieving this goal is based on establishing the regularities of the influence of the value of the compensating capacitance on the energy characteristics of a compensated asynchronous motor during its start-up and reaching the nominal electromagnetic moment on the rotor shaft. Numerical modelling is performed at the 30o spatial shift angle of the phase axes of the main and additional phase windings of the stator of a compensated asynchronous motor. This ensures that the currents of the main and additional windings of the CAM stator are equal. As the numerical experiment showed, changing the value of the compensation capacitance gives an idea of the conditions for ensuring the normal excitation mode of such an electric device. Ensuring normal excitation during the start-up of a compensated asynchronous motor leads to changes in the energy parameters of the machine – minimising power losses in the windings and reactive power consumption by the motor and increasing its power factor. It is established that the value of the compensation capacitance required to ensure the normal excitation mode during start-up and the steady-state normal mode of a compensated asynchronous motor differ. As a result of modelling, it was found that in order to ensure an energy-efficient starting mode and acceleration to the nominal slip, the value of the compensating capacity of an asynchronous motor should be almost 5 times greater than for a steady-state nominal mode. The results of these studies can be useful for improving the energy efficiency of micro power grids that operate small-and medium-power asynchronous motors

Keywords: energy efficiency, medium-power motors, reactive power, internal capacitive compensation, compensating capacity, starting mode

Article's History: Received: 21.03.2022; Revised: 25.07.2022; Accepted: 11.08.2022

INTRODUCTION

This study is devoted to the further development of the theory of improving the energy efficiency of three-phase power consumption systems with asynchronous motors with a short-circuited rotor (AM) [1].

For special-purpose electric drives, the operating modes of asynchronous motors of which require a large number of repeated-short-term starts, a complex transient process is characteristic, which is accompanied by a significant increase in total currents and power losses, since in the slip range from 1 to the nominal slip s_n the stator current significantly exceeds the nominal values. For induction motors of general industrial design, from the moment of start-up to the critical slip, the power factor is 0.2 … 0.5 [2]. During the start-up process, an asynchronous motor is a large inductive load that causes additional flows in the reactive power microgrid, which significantly affects energy losses in the power consumption system.

The less reactive power the AM consumes from the network, the higher the energy efficiency indicators

Suggested Citation:
Kaplun, V., Chuienko, R., & Makarevych, S. (2022). Investigation of energy parameters of a compensated asynchronous motor in the mode of repeated short-term starts. *Machinery & Energetics,* 13(3), 25-33.

*Corresponding author

of the electric machine complex will have without significantly affecting the normal operation of other consumers. The lower the total currents of the stator winding during start-up under load, the shorter the acceleration time of the motor and heating of its windings and, as a result, the reduction of electricity losses.

The theory of starting modes concerns asynchronous motors for industrial purposes and considers the conditions for reducing the voltage of the electrical network and reducing the electromagnetic moment [3]. Conventional methods of limiting inrush currents include reactor start-up [4], start-up with switching windings from a star to a triangle [5], start-up using frequency converters [6] to a large extent allow solving the problems of the starting mode from the standpoint of considering the electromechanical processes of the machine itself. However, the use of these methods does not solve the problem of significantly reducing the power factor of the microgrid in which such asynchronous machines operate.

In the studies [7; 8] the basic principles of developing methods for improving the characteristics of three-phase asynchronous motors with a short-circuited rotor are formulated, which use design improvements based on the use of the effect of internal capacitive reactive power compensation. The main scientific results devoted to solving such problems are given in [8].

It is the use of internal capacitive compensation that can significantly affect the energy performance of start-up modes of asynchronous machines with a short-circuited rotor without the use of additional power equipment and without significant design changes to the machine itself, providing conditions for improving the energy efficiency of the entire microgrid.

LITERATURE REVIEW

The consumption of reactive power by an asynchronous motor negatively affects its technical and economic indicators; in particular, it reduces its power factor, both during start-up and in other operating modes. In addition, the exchange of reactive power between the AM stator winding and the power supply leads to increased losses in all sections of the microgrid. Various approaches and technical solutions are proposed to reduce the consumption of reactive power by AM. In particular, in [9; 10], it is proposed to connect a three-phase capacitor bank in parallel to the AM stator winding, the capacity of which must be calculated to compensate for the reactive power consumed by the motor in idle mode. In [11], it is noted that the parameters of AM undergo the greatest change during start-up. Inrush AM currents, which have a significant reactive component, lead to a voltage failure in the supply network. During the start-up process, the reactive power of the AM varies widely. To compensate for it, it is proposed to connect a three-phase adjustable capacitor bank in parallel to the AM stator winding and change its capacity in accordance with changes in reactive power not only in steady-state, but also in starting modes. To do this, it is necessary to have a calculation programme that allows determines the law of change in the reactive power consumed by the engine, and, accordingly, the capacitance of capacitors, with high reliability and speed, which allow for real-time control [11]. Individual compensation of the reactive power of asynchronous motors under various engine operating modes, in particular, during start-up, can be carried out using a capacitor bank with thyristor-controlled stages [12]. Another technical solution aimed at reducing the consumption of reactive power by AM is the use of active power filters that are switched on in parallel with the AM [13]. In [14], it is proposed to apply individual compensation of reactive power of AM implemented by connecting a three-phase capacitor bank of constant capacity and a three-phase regulated reactor in parallel to the motor stator winding.

The considered technical solutions allow reducing reactive power flows in the microgrid between the power source and the AM, but do not affect the energy efficiency of the AM itself.

To reduce the consumption of reactive power asynchronous motors and increase their energy efficiency, it is proposed to use AM, in the slots of the stator of which two three-phase windings are laid [15]. One of these windings, the so-called working one, is connected to a power source, and the other, the so-called compensation one, is closed to a three-phase capacitor of a certain capacity. The operating and compensation windings of the stator can be connected to several three-phase power sources, connected to each other in different ways. The parameters of the windings and the capacitance of the capacitor are determined when designing the electromagnetic system of such motors according to the method based on the modification and analysis of the AM replacement scheme [16; 17]. Another approach to reducing the magnetisation current, and therefore, the reactive power consumption of AM, is to use two stator windings isolated from each other. One of them is connected by a "star" and connected to a power source, and the other is connected by a "triangle" or "star" and capacitors are connected to it according to various schemes. In this case, the number of turns of these windings can be either the same or different [18; 19]. However, the use of the proposed technical solutions only allows compensating for the reactive power consumed by the engine. As a result, the AM power factor increases, but the compensation winding is only a carrier of reactive power, which does not allow fully unlocking the potential for improving the energy efficiency of the motor.

Other equipment used to improve the energy performance of an asynchronous electric drive during start-up includes devices that allow adjusting the voltage at the motor terminals, and, accordingly, controlling the start and stop of the drive, and provide energy savings by reducing the voltage on an underloaded motor [20-22].

The purpose of the study is to substantiate the value of the compensatory capacity of a compensated asynchronous motor (CAM), which is necessary to reduce the consumption of reactive power ad from the power supply network and create prerequisites for controlling the energy efficiency of electrical complexes with compensated asynchronous motors. The originality of the study consists in determining the need to change the compensation capacity of the CAM to improve its energy efficiency, depending on the operating mode, in particular, in the mode of repeated short-term starts.

MATERIALS AND METHODS

The compensated asynchronous motor is manufactured on the basis of a three-phase asynchronous motor with a short-circuited rotor. The effect of internal capacitive reactive power compensation is achieved by separating the phase zone 60o stator windings into two identical parts, spatially shifted together in the grooves by an angle θ=30° connected according to the scheme of a rotary autotransformer (AT) to a capacitor C_Δ [8].

Stator windings (CAM), which are an integral part of the AT, are functionally combined, compensating for reactive power relative to the voltage of the microgrid and operating for active power, and interconnected mutually inductively by the main magnetic flux.

The mathematical model of electromagnetic and electromechanical processes of a compensated asynchronous motor is represented by a system of equations of electrical equilibrium of the stator and rotor circuits, equations of electromagnetic moment of the motor and drive motion [8].

It is convenient to calculate the characteristics of electromechanical symmetric modes for one phase according to the scheme Fig. 1a. The calculation equations are a system of equations for the electrical equilibrium of the stator and rotor circuits. In this case, both stator windings that are part of the rotary at are mutually inductively connected to all other windings by the main magnetic flux. In the scattering field, they are connected as two half-windings of a single phase winding of the base motor. In this case, the single winding of the base AM is assumed to consist of two identical coaxial parallel branches with common parameters of the single winding [8]: R_{10}, X_{10} – active resistance and inductive phase dissipation resistance of a single stator winding; x_m – its main reactance and equal resistance of mutual induction between the same windings of the stator and rotor of the AM under study. When dividing a single winding of the base AM into two identical parallel branches with the same number of turns in each branch as in a single winding, but with twice the cross-section of the conductor, the active resistance of the branch will be equal to r_1=2R_{10}, a reactive x_m, x_1 with the same number of turns, they remain unchanged in each branch as in a single winding. But considering their division into two identical parallel branches, a mutually inductive connection is manifested between the branches of the phase winding as in the main field with resistance x_m, and over the scattering field within the phase with resistance x_1. If the phase windings are spatially displaced relative to each other, the mutual scattering resistance between them will be equal to $x_1 cos\theta$. Other changes in the parameters of the CAM windings, in particular, by doubling the number of phases, are ignored. Rotor resistance at r_2, x_2 when switching from base AM to CAM, is assumed to be unchanged.

$$
\begin{cases}
e_A = i_{1A}(r_1 + r_{1d} + r_{LA}) + (L_S + L_{1d} + L_{LA})\dfrac{di_{1A}}{dt} - i_{\Delta A}r_{LA} - L_{LA}\dfrac{di_{\Delta A}}{dt} + M\dfrac{di'_a}{dt} + U_0 + \\
+\dfrac{2\sqrt{3}}{3}kM\dfrac{d}{dt}[i_{\Delta A}\cos(\theta + 30^0) + i_{\Delta B}\cos(\theta + 90^0)]; \\
e_B = i_{1B}(r_1 + r_{LB}) + (L_S + L_{LB})\dfrac{di_{1B}}{dt} - i_{\Delta B}r_{LB} - L_{LB}\dfrac{di_{\Delta B}}{dt} + M\dfrac{di'_b}{dt} + U_0 + \\
+\dfrac{2\sqrt{3}}{3}kM\dfrac{d}{dt}[i_{\Delta A}\cos(\theta - 90^0) + i_{\Delta B}\cos(\theta - 30^0)]; \\
-e_C = (i_{1A} + i_{1B})(r_1 + r_{LC}) - (i_{\Delta A} + i_{\Delta B})r_{LC} + (L_S + L_{LC})\dfrac{d(i_{1A} + i_{1B})}{dt} - L_{LC}\dfrac{d(i_{\Delta A} + i_{\Delta B})}{dt} + \\
+M\dfrac{d(i'_a + i'_b)}{dt} - U_0 - \dfrac{2\sqrt{3}}{3}kM\dfrac{d}{dt}[i_{\Delta A}\cos(\theta + 150^0) + i_{\Delta B}\cos(\theta - 150^0)];
\end{cases}
$$

$$
\begin{cases}
0 = \sqrt{3}\omega_p M i_{1A} + M\dfrac{di_{1A}}{dt} + \sqrt{3}\omega_p M i_{1B} - M\dfrac{di_{1B}}{dt} + 2kM\omega_p\cos(\theta - 30^0)\cdot i_{\Delta A} + \\
+2kM\cos(\theta + 60^0)\dfrac{di_{\Delta A}}{dt} + 2kM\omega_p\cos(\theta + 30^0)\cdot i_{\Delta B} + 2kM\cos(\theta + 120^0)\cdot\dfrac{di_{\Delta B}}{dt} + \\
+\overline{i_a}(r_2 + \sqrt{3}\omega_p L_p) + L_p\dfrac{di'_a}{dt} - i'_b(r_2 - \sqrt{3}\omega_p L_p) - L_p\dfrac{di'_b}{dt}; \\
0 = -\sqrt{3}\omega_p M i_{1A} + M\dfrac{di_{1A}}{dt} + 2M\dfrac{di_{1B}}{dt} - 2kM\omega_p\cos(\theta + 30^0)\cdot i_{\Delta A} + 2kM\cos(\theta - 60^0)\dfrac{di_{\Delta A}}{dt} - \\
-2kM\omega_p\cos(\theta + 90^0)\cdot i_{\Delta B} + 2kM\cos\theta\dfrac{di_{\Delta B}}{dt} + \overline{i_a}(r_2 - \sqrt{3}\omega_p L_p) + L_p\dfrac{di'_a}{dt} + i'_b\cdot 2r_2 + 2L_p\dfrac{di'_b}{dt};
\end{cases}
$$

Equation (1), Continued

$$\begin{cases} e_A - e_B = i_{1A}r_{LA} + [2kM\cos(\delta + 120^0) + L_{LA}]\dfrac{di_{1A}}{dt} - i_{1B}r_{LB} - [2kM\cos(\theta + 60^0) - L_{LB}]\dfrac{di_{1B}}{dt} - \\ \quad -i_{\Delta A}(r_\Delta + r_{\Delta d} + r_{LA}) - (L_{S\Delta} + L_{\Delta d} + L_{LA})\dfrac{di_{\Delta A}}{dt} - \dfrac{1}{C_A}\displaystyle\int i_{\Delta A}dt + i_{\Delta B}(r_\Delta + r_{LB}) + (L_{S\Delta} + L_{LB})\dfrac{di_{\Delta B}}{dt} + \\ + \dfrac{1}{C_B}\displaystyle\int i_{\Delta B}dt + 2kM\cos(\theta + 120^0)\dfrac{di'_a}{dt} + 2kM\cos(\theta + 60^0)\dfrac{di'_b}{dt}; \\ e_B - e_C = i_{1A}r_{LC} - [2kM\cos(\theta + 60^0) - L_{LC}]\dfrac{di_{1A}}{dt} + i_{1B}(r_{LC} + r_{LB}) - [2kM\cos\theta - L_{LC} - L_{LB}]\dfrac{di_{1B}}{dt} - \\ \quad -i_{\Delta A}(r_\Delta + r_{LC}) - (L_{S\Delta} + L_{LC})\dfrac{di_{\Delta A}}{dt} - \dfrac{1}{C_C}\displaystyle\int i_{\Delta A}dt - i_{\Delta B}(2r_\Delta + r_{LC} + r_{LB}) - (2L_{S\Delta} + L_{LC} + L_{LB})\dfrac{di_{\Delta B}}{dt} - \\ - \left(\dfrac{1}{C_B} + \dfrac{1}{C_C}\right)\displaystyle\int i_{\Delta B}dt - 2kM\cos(\theta + 60^0)\dfrac{di'_a}{dt} - 2kM\cos\theta\dfrac{di'_b}{dt}. \end{cases} \tag{1}$$

$$M_E = \frac{-pM}{\sqrt{3}}[(i_{1A} + ki'_{\Delta A})(i'_b - i'_c) + (i_{1B} + ki'_{\Delta B})(i'_c - i'_a) + (i_{1C} + ki'_{\Delta C})(i'_a - i'_b)]$$

$$M_E = M_C + J\frac{d\omega}{dt}$$

where e_A, e_B, e_C – EMF, respectively, of phases A, B and C of the power source; i_{1A}, i_{1B}, i_{1C} – currents of the main windings, respectively, of phases A, B, and C of the CAM; r_{1d} – additional active resistance introduced into the circuit of the main winding of phase A; r_{LA} , r_{LB}, r_{LC} – active resistances, respectively, of phases A, B and C of the power supply network; L_{LA} , L_{LB}, L_{LC} – inductances, respectively, of phases A, B and C of the power supply network; L_S – total inductance of the main winding of the stator phase; L_{1d} – inductance of the additional resistance introduced into the circuit of the main winding of phase A; t – time; $i_{\Delta A}$, $i_{\Delta B}$, $i_{\Delta C}$ – currents of the additional windings, respectively, of phases A, B and C of the CAM; M – the main self-inductance of the windings of the CAM; i'_a, i'_b, i'_c – rotor currents, respectively, of phases A, B, and C of the CAM; U_0 – zero-sequence voltage between the zero point of the motor and the power source, which occurs in asymmetric modes and in transient processes; k – the ratio of the number of turns of the main and additional windings of the stator phases of the CAM; θ – angle of shift between the axes of the main and additional windings of the stator phases of the CAM; ω_p – speed of rotation of the rotor; r_Δ – active resistance of the additional winding of the stator phase of the CAM; $r_{\Delta d}$ – additional active resistance introduced into the circuit of the additional winding of phase A; $L_{S\Delta}$ – total inductance of the additional winding of the stator phase; $L_{\Delta d}$ – inductance of the additional resistance introduced into the circuit of the additional winding of phase A; C_A, C_B, C_C – capacities of capacitors connected, respectively, in phases A, B and C of the CAM; M_E – electromagnetic moment of the CAM; p – the number of pairs of poles of the CAM; $i'_{\Delta A}$, $i'_{\Delta B}$, $i'_{\Delta C}$ – currents of the additional windings, respectively, in phases A, B and C of the CAM reduced to the axis of the main winding of the CAM; M_c – moment of static load on the motor shaft; J – moment of inertia of the rotating masses of the drive, reduced to the shaft of the CAM; ω – rotor speed.

Magnetisation circuit resistance x_m for the motor mode, where the EMF of the windings is balanced by the microgrid voltage, is assumed $x_m \approx (1.1...1.3)x_{m0}$, in start-up mode $x_m \approx (1.6...1.7)x_{m0}$, where x_{m0} – the nominal resistance of the magnetisation circuit at idle speed of the machine and the main EMF of the winding, which is equal to the nominal voltage.

Variables that are arbitrarily defined in system (1) are the input (external) parameters of the CAM – angle θ between the stator windings in the rotary at and the value of the capacitive resistance $x_{C\Delta} = \dfrac{1}{\omega_0 C_\Delta}$ at the output of AT, and sliding s, which characterises the operating mode of the engine when the speed of rotation of its shaft changes in the range $0 \leqslant s \leqslant 1$.

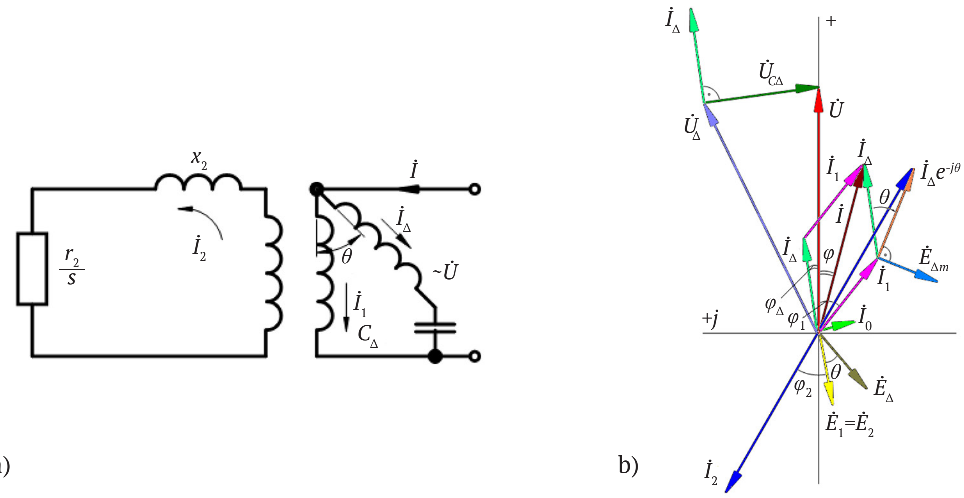

a) b)

Figure 1. Electrical replacement diagram (a) and vector diagram (b) of the CAM in the starting mode

Note: (r_2 – active rotor resistance, s – sliding, $\dot{I}_2$ – rotor current, θ – shear angle between the axes of the main and additional stator windings, $\dot{I}$ – current consumed by the CAM from the power supply network, $\dot{I}_1$ – current of the main winding of the CAM, $\dot{I}_\Delta$ – current of the additional winding of the CAM, $\dot{I}_1$ – magnetisation current of the CAM, C_Δ – capacitor capacity, $\dot{U}$– power supply voltage, $\dot{U}_{C\Delta}$ – voltage across the capacitor, $\dot{U}_\Delta$ – voltage on the additional winding, $\dot{E}_1$ – EMF of the main winding of the stator CAM, $\dot{E}_2$ – EMF of the additional stator winding CAM, $\dot{E}_{\Delta m}$ – additional EMF of the CAM caused by the spatial displacement of the main and additional windings, φ – angle between the supply voltage and current vectors of the CAM, φ_1 – angle between the supply voltage and current vectors of the main winding of the CAM, φ_Δ – angle between the supply voltage and current vectors of the additional winding of the CAM, φ_2 – the angle between the EMF and rotor current vectors of the CAM)

For the objectivity of the results obtained, the same machine is used as a calculation model and object of research, both base (AM 4A71B2) and compensated on its basis, with the same eigenvalues of the two stator windings r_1=20 ohm, x_1= 4.72 ohm in each branch; rotor windings with r_2=5.91 ohm, x_2=7.2 ohm, with the resistance of the magnetising circuit at idle x_m=250 ohm [8], in operating mode x_m=300 ohm, in the start-up mode s=1, x_m=400 ohm.

RESULTS AND DISCUSSION

In contrast to the base AM, where the current of a single stator winding has an active-inductive character both in the starting and operating modes, the stator winding of the CAM has two operating branches, the current $\dot{I}_1$ from one of which (the main one) retains an active-inductive character, and the current $\dot{I}_\Delta$ of additional capacitive load of the AT is capacitive-active. As in normal AM inrush current $\dot{I}_1$ the main winding exceeds the nominal value by 5-6 times (but with a larger $cos\varphi_1$ internal capacitive compensation), and the current $\dot{I}_\Delta$ depends not only on the start-up conditions (s=1), but also on the value of the capacitance of the capacitor C_Δ. At a certain capacity, it exceeds its nominal value and, as a capacitive one, increases the voltage $\dot{U}_\Delta=-\dot{E}_\Delta+\dot{I}_\Delta z_\Delta+jx_1\cos\theta\cdot\dot{I}_1$ on the winding of the secondary branch of AT. And the voltage at the output of the return AT, which is equal to $\dot{U}_{C\Delta}=\dot{U}-\dot{U}_\Delta$, at constant voltage $\dot{U}$power supply networks, increases $\dot{U}_{C\Delta}$, changes its phase, and the magnitude and phase of the capacitive current $\dot{I}_\Delta=\dfrac{\dot{U}_{C\Delta}}{-jx_{C\Delta}}$ (Fig. 1b). Current $\dot{I}_\Delta e^{-j\theta}$ as it is brought to the axis of the main winding, it is partially involved in the creation of the magnetisation current $\dot{I}_0=\dot{I}_1+_\Delta e^{-j\theta}+\dot{I}_2$ and create an additional EMF $\dot{E}_{\Delta m}=-jx_m\dot{I}_\Delta e^{-j\theta}$, which is close in phase to the EMF $\dot{E}_1=\dot{E}_2$ and $\dot{E}_\Delta$ and increases them. An increase in the EMF along the magnetisation curve requires an increase in the magnetisation current, which is performed by $\dot{I}_\Delta e^{-j\theta}$, replacing part of the inductive component in it reduces its value with an equivalent increase in the magnetisation current in general. Reduction of the inductive component of the magnetisation current due to the magnetisation action of a capacitive spatially biased current $\dot{I}_\Delta e^{-j\theta}$ leads to a decrease in the share of consumption from the reactive power network Q_0 to create the main magnetic flux. This manifests itself in the electromagnetic effect of current $\dot{I}_\Delta$ in the scheme of the rotary AT. The electrical action of this current leads to a direct exchange of reactive energy between the consumer (CAM) and the reactive power source (capacitors with capacitance C_Δ), increasing the power factor of the system at the total current $\dot{I}=\dot{I}_1+\dot{I}_\Delta$

The CAM has the possibility of introducing an additional EMF into the short-circuited rotor circuit $\dot{E}_{\Delta m}=-jx_m\dot{I}_\Delta e^{-j\theta}$, as a result of the effect of a spatially biased capacitive current of the return AT. This additional EMF increases the main EMF of the stator and rotor, $\dot{E}_1=\dot{E}_2$. During the start-up of the CAM, this leads to an increase in the starting current of the rotor, and, accordingly, the starting torque.

CAM start mode at the selected angle θ=30° significantly depends on the size of the capacity C_Δ ($x_{C\Delta}$) at the output of the rotary AT (Fig. 2). As the capacitance of the capacitor C_Δ increases (by reducing $x_{C\Delta}$) the value and phase of the voltage $\dot{U}_{C\Delta}$ at the output of AT changes, the current of the additional winding increases $\dot{I}_{\Delta}$, its phase also changes in the direction of coinciding with the phase of the supply voltage. Electromagnetic coupling between currents through magnetisation current $\dot{I}_0=\dot{I}_1+\dot{I}_{\Delta}e^{-j\theta}+\dot{I}_2$ changes the current $\dot{I}_1$ of the main winding and increases its power factor $cos\varphi_1$.

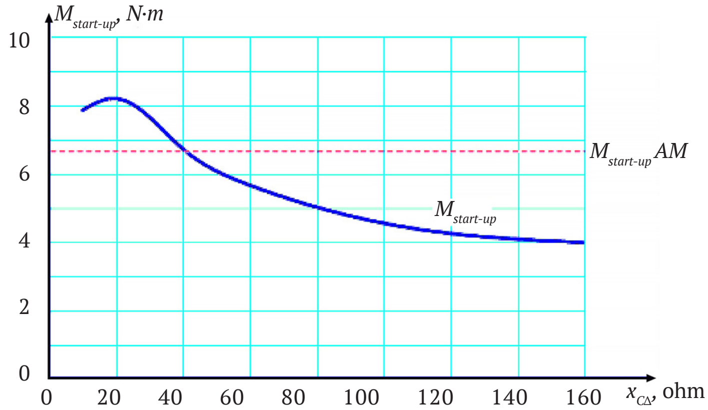

Figure 2. Dependence of the starting torque of the CAM on the resistance of the compensating capacitance $x_{C\Delta}$
Note: ($M_{start-up}$ – starting torque of the CAM, $M_{start-up}AM$ – starting torque of the base AM)

According to the mathematical model of CAM (1), the currents of the main and additional windings were determined $\dot{I}_1$, $\dot{I}_{\Delta}$ when s=1 (start-up) and a wide range of changes C_{Δ}=20...200 μF ($x_{C\Delta}$≈16 ... 160 ohm) (Fig. 3a). At the same time, with capacity C_{Δ}=147 μF (X_{SD}=21.75 ohm) the curves of the currents of the half-windings of the stator phases intersect, determining the equality of the values of the inrush currents of the main and additional windings $\dot{I}_1=\dot{I}_{\Delta}$, and, accordingly, their same thermal regime. However, the main feature of this point is that it satisfies the condition for creating the maximum starting torque of the CAM, which exceeds the starting torque of the base AM by 22.5% with a lower starting current of the stator CAM compared to the base motor. In this example, the maximum starting torque of the CAM is 8.26 N·m with an inrush current of 10.75 A.

Graphs of currents of the main and additional windings of the CAM at nominal load (M_n=3.75 N·m) also intersect, but in terms of capacity C_{Δ}, which is 5 times less than the starting point (Fig. 3b). At this point, the currents of the coils $\dot{I}_1=\dot{I}_{\Delta}$ are the same in size and have minimal values, which ensures a minimum of power losses in the CAM windings.

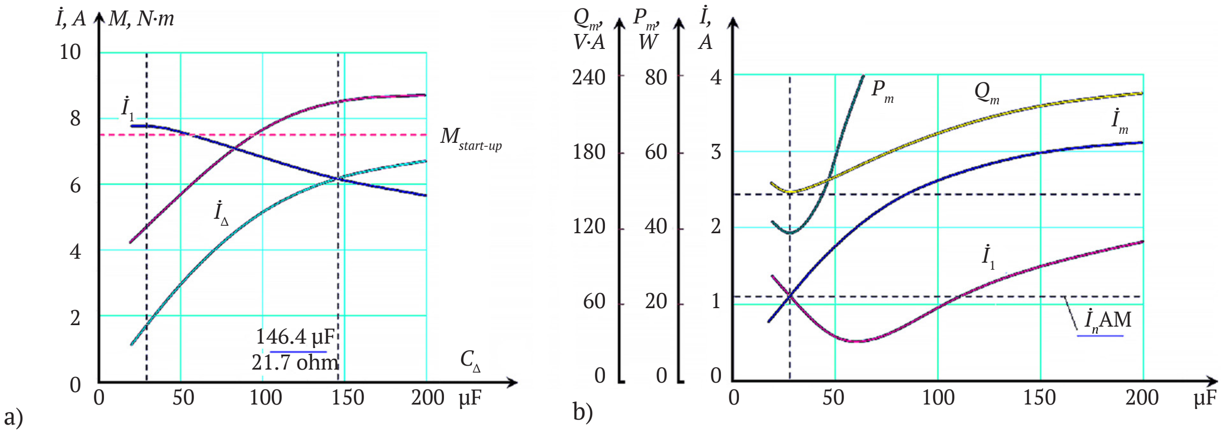

Figure 3. Characteristics of the starting (a) and nominal (b) CAM modes when the capacitive excitation changes(C_{Δ}=*var*)
Note: (M – moment CAM, $M_{start-up}$ – starting torque of the CAM, $\dot{I}_1$ – current of the main winding of the CAM, $\dot{I}_{\Delta}$ – current of the additional winding of the CAM, $\dot{I}_n$ – nominal current of the base AM, C_{Δ} – capacitor capacity, Q_m – reactive power consumption of the CAM, P_m – electrical losses in the stator windings of the CAM)

Intersection point of the dependence of the currents of the stator windings of the CAM on the capacitance value C_{Δ} at the output of the rotary AT of the stator windings determines the mode of normal excitation of the CAM. The normal excitation mode is the most favourable both during start-up and in other modes of operation of the CAM, since this case provides a minimum of power losses in the windings, a minimum of reactive power consumption by the motor, and an increase in its power factor. The set of these indicators shows the conditions for increasing the efficiency of the CAM during start-up in comparison with the serial base AM (Table 1).

Table 1. Comparative data of the starting mode of the base AM 4A71B2 and the CAM made on its

No.	Value	AM	CAM, C_Δ=147 μF
1	$\dot{I}$, A	11.24	10.75
2	$\dot{I}_1$, A	5.62	5.45
3	$\dot{I}_\Delta$, A	5.62	5.45
4	$\dot{I}_2$, A	10.93	12.1
5	M, N·m	6.74	8.26
6	Q, V·A	+j1,500	+j1,455
7	S, VA	2,470	2,539
8	ΣP_m, W	1,970	1,911
9	$cos\varphi$	0.796	0.867

To ensure a positive effect during the entire process of starting, accelerating and normal operation of the CAM, it is recommended to start it at one value of the compensation capacity, which provides an increased starting torque (in this case, C_Δ=147 μF) and during acceleration during sliding $s\approx0,1...0,2$ to reduce the amount of compensation capacity to C_Δ=29 μF (Fig. 4).

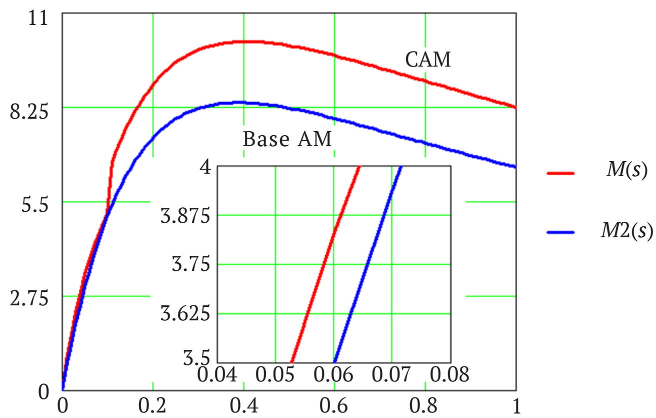

Figure 4. Mechanical characteristics of the base AM and CAM with switching of the starting capacity C_Δ=147 μF per nominal value C_Δ=29 μF when sliding s≈0.1 is reached

The obtained results allow substantiating the value of the compensation capacity for CAM at different nominal capacities and synchronous rotation speeds and provide conditions for improving the energy efficiency of power consumption systems with CAM. The use of internal capacitive reactive power compensation (ICRPC) of the CAM ensures a normal excitation mode and reduces its consumption of reactive power and the current that it consumes from the power supply network. This, in turn, would lead to a reduction in losses both in the motor itself (by reducing the currents of the main and additional stator phase windings) and in the power supply network. At the same time, under the influence of increased starting torque, the acceleration process of the CAM increases. The compensated asynchronous motor achieves a more rigid mechanical characteristic with the characteristic of the base AM.

In contrast to technical solutions aimed at improving the energy efficiency of AM by limiting reactive power flows between the power supply network and the motor, which cause a decrease in inrush currents and an increase in its power factor, but do not change the characteristics of AM [7; 9; 12; 23]. The use of ICRPC AM allows influencing the characteristics of the CAM, changing the spatial and tem-poral orientation of the currents of the main and additional windings of the phases of the stator and rotor of the CAM, ensuring the mode of normal excitation during start-up, minimising power losses in the windings and reactive power consumption.

To assess the effectiveness of the use of CAM, it is necessary to consider the amount of current reduction of specific motors, changes in the energy parameters of the power supply network, the number of repeated short-term starts and the duration of operation of electric drives with such engine modes in the design period.

CONCLUSIONS

The developed mathematical model of the CAM allows investigating both transient and steady-state processes, considering the spatial and temporal orientation of the currents of the half-windings of the stator and rotor phases.

It is proved that advanced asynchronous motors with a short-circuited rotor based on the use of ICRPC can provide a normal excitation mode and thus avoid additional reactive power flows between the motor and the power supply network, which reduces the consumption of electrical energy by the asynchronous motor. This is where additional opportunities lie for managing the energy efficiency of micro-energy networks.

The value of the compensation capacity for the CAM must be determined considering its nominal power and synchronous engine speed, ensuring the mode of normal excitation from s=1 to s_n. As the numerical experiment showed, the compensation capacity of the CAM in the starting mode should be almost 5 times greater than in the nominal slip: for an experimental machine, these indicators are 147 μF and 29 μF, respectively. Based on the results obtained, it can be argued that if the normal excitation mode of the CAM made on the basis of AM 4A71B2 motor is observed, electricity consumption will decrease by 3.5%.

Further substantiation of the regulation of the value of the compensation capacity of the CAM depending on the slip change and the study of the operating modes of micro-energy networks with CAM to control their energy efficiency are relevant. Problematic issues remain the specifics of using the internal capacitive compensation method for asynchronous motors of different nominal power and modes with sharply variable loads in the technological electric drives in which they operate.

REFERENCES

[1] Myshin, V.I. (2009). The effect of internal capacitive compensation of reactive power in asynchronous motors. *Electrical Engineering*, 8, 30-36.

[2] Yatsun, M.A. (2011). *Electric machines*. Lviv: Publishing House of Lviv Polytechnic.

[3] Voldek, A.I. (1976). *Electric machines*. Leningrad: Energy.

[4] Katsman, M.M. (2013). *Electric machines*. Moscow: Publishing Center "Akademiya".

[5] Kopylov, I.P. (2002). *Electric machines*. Moscow: Higher School.

[6] Ivanov-Smolensky, A.V. (2006). *Electric machines*. (3rd ed.; Vol. 1). Moscow: MEI Publishing House.

[7] Popovych, O.M. (2015). *Mathematical models, parameters, and characteristics of asynchronous motors of electromechanotronic systems* (Doctoral thesis, Institute of Electrodynamics of the National Academy of Sciences of Ukraine, Kyiv, Ukraine).

[8] Mishin, V.I., Kaplun, V.V., Chuyenko, R.M., Makarevych, S.S., & Gavrylyuk, V.V. (2012). *Compensated asynchronous machines*. Kyiv: KNUTD.

[9] Somgan, O.V., Rovinskyi, V.A., & Wozniak, O.S. (2005). Study of modes of reactive power consumption by asynchronous motors with variable load. *Promelectro*, 5, 33-38.

[10] Saodah, S., Kastawan, I.M.W., Yusuf, E., Manunggal, B.P., & Maryanti, M. (2021). Simulation of effects of using capacitor for reactive power (VAR) compensation on electrical power supply quality. *Atlantis Highlights in Engineering*, 9, 168-174.

[11] Malyar, V.S. (2013). Compensation of reactive power in asynchronous. *Electrical Engineering and Electromechanics*, 5, 36-38.

[12] Panfilov, D.I., Elgebaly, A.E., Astashev, M.G., & Rozhkov, A.N. (2019). Performance analysis of thyristors switched capacitors used for reactive power compensation of induction motor. *ASTES Journal*, 4(4), 58-64.

[13] Karaman, Ö.A., Gundoğdu, A., & Cebeci, M. (2020). Performing reactive power compensation of three-phase induction motor by using parallel active power filter. *International Advanced Researches and Engineering Journal*, 4(3), 239-248.

[14] Zakis, J., Rankis, I., & Zhiravetska, A. (2006). Investigation of an active system of reactive power compensation for induction motors. *Electronics and Electrical Engineering*, 70(6), 11-14.

[15] Popovych, O.M., & Smaglyuk, M.O. (2014). Research and design of asynchronous motors with internal compensation using simulation and structural modelling. *Bulletin of NTUU "KPI"*, 25, 14-25.

[16] Murgalimov, R.G., & Murgalymova, A.R. (2007). Towards the design of an energy-saving asynchronous motor with individual reactive power compensation. In *Electrotechnical and electromechanical energy converters and controlled electromechanical systems* (pp. 77-80). Yekaterinburg: Ural State Mining University.

[17] Murgalimov, R.G., Kosmatov, V.I., & Murgalymova, A.R. (2010). Method and algorithm for designing a compensated energy-saving asynchronous motor. *Bulletin of the Tula State University. Technical sciences*, 3, 281-284.

[18] Beljaev, E.F., Tashkinov, A.A., & Tsylev, P.N. (2013). Three-phase asynchronous motor (Patent of the Russian Federation No. 2478249). Perm National Research Polytechnic University. Retrieved from https://patentimages.storage.googleapis.com/1a/0d/66/ad7b48ac4c968c/RU2478249C1.pdf.

[19] Jimoh, A.A., & Nicolae, D.V. (2006). Performance analysis of a three-phase induction motor with capacitance injection. In *OPTIM, 10th international conference on optimization of electrical and electronic equipments* (pp. 1-6). Brasov: Transilvania University of Brașov.

[20] Zhurikhin, R.O., & Nekrasov, A.V. (2017). Method of frequency starting of an asynchronous motor with power supply from stabilized current source (Patent of the Ukraine No. 117283). Kremenchuk Mykhailo Ostrohradskyi National University. Retrieved from http://uapatents.com/5-117283-sposib-chastotnogo-pusku-asinkhronnogo-dviguna-z-zhivlennyam-vid-stabilizovanogo-dzherela-strumu.html.

[21] Chen, H., & Bi, C. (2021). Optimal starting frequency of three-phase induction motor. *IET Electric Power Applications*, 16(3), 362-369.
[22] Cao, Z., Shi, J., & Fan, B. (2021). Induction motor pre-excitation starting based on vector control with flux linkage deviation decoupling. *Journal of Vibroengineering*, 23(3), 728-743.
[23] Bigan, Z., Derechkei, P., Mazur, V., & Pop, O. (2022). Study of the cross-section for the 122Te(γ, n)121Te reaction by the activation method. *Scientific Herald of Uzhhorod University. Series "Physics"*, 51, 18-23.

Віктор Володимирович Каплун, Роман Миколайович Чуєнко, Світлана Сергіївна Макаревич

Національний університет біоресурсів і природокористування України
03041, вул. Героїв Оборони, 15, м. Київ, Україна

Дослідження енергетичних параметрів компенсованого асинхронного двигуна у режимі повторно-короткочасних пусків

Анотація. Стаття присвячена управлінню енергоефективністю асинхронних двигунів з короткозамкненим ротором малої та середньої потужності і є продовженням розвитку теорії компенсованих асинхронних двигунів. Мета дослідження – обґрунтування впливу величини ємності внутрішньої ємнісної компенсації реактивної потужності асинхронного двигуна в пусковому режимі. Виконане математичне моделювання компенсованого асинхронного двигуна дало можливість дослідити квазіперехідні електромагнітні процеси з урахуванням просторово-часової орієнтації струмів основної та додаткової обмоток фаз статора і ротора компенсованого асинхронного двигуна. Досягнення поставленої мети базується на встановленні закономірностей впливу величини компенсувальної ємності на енергетичні характеристики компенсованого асинхронного двигуна під з час його пуску та досягненні номінального електромагнітного моменту на валу ротора. Числове моделювання виконане при куті просторового зсуву фазних осей основної та додаткової обмоток фаз статора компенсованого асинхронного двигуна 30 °С. Цим забезпечується умова дотримання рівності величини струмів основної та додаткової обмоток статора компенсованого асинхронного двигуна. Як показав числовий експеримент, зміна величини компенсувальної ємності дає уявлення про умови забезпечення режиму нормального збудження такої електричної машини. Забезпечення нормального збудження під час пуску компенсованого асинхронного двигуна призводить до зміни енергетичних параметрів машини – мінімізації втрат потужності в обмотках і споживання двигуном реактивної потужності та підвищення його коефіцієнта потужності. Встановлено, що величина компенсувальної ємності, яка необхідна для забезпечення режиму нормального збудження під час пуску та усталеного нормального режиму компенсованого асинхронного двигуна відрізняються. Внаслідок моделювання встановлено, що для забезпечення енергоефективного пускового режиму і розгону до номінального ковзання величина компенсувальної ємності компенсованого асинхронного двигуна повинна бути майже в 5 разів більшою, ніж для усталеного номінального режиму. Результати цих досліджень можуть бути корисними для підвищення енергоефективності мікроенергетичних мереж, у складі яких працюють асинхронні двигуни малої та середньої потужності

Ключові слова: енергоефективність, двигуни середньої потужності, реактивна потужність, внутрішня ємнісна компенсація, компенсувальна ємність, пусковий режим

Machinery & Energetics
Vol. 13, No. 3. 2022

Journal homepage:
https://technicalscience.com.ua/en

UDC 539.3:539.42:624.012
DOI: 10.31548/machenergy.13(3).2022.34-42

Anastasiia Kutsenko[1*], Oleksii Kutsenko[2]

[1]National University of Life and Environmental Sciences of Ukraine
03041, 15 Heroiv Oborony Str., Kyiv, Ukraine

[2]Taras Shevchenko National University of Kyiv
01033, 60 Volodymyrska Str., Kyiv, Ukraine

Effect of Reinforcement on the Crack Resistance of Concrete Slabs

Abstract. A preliminary analysis of the available publications devoted to the study of crack resistance of reinforced concrete structures showed the absence of established general patterns of influence of important geometric parameters inherent in reinforced concrete elements on the distribution of the characteristics of fracture mechanics along the crack front. Based on the analysis, the purpose of the study was formulated: to establish these regularities for a concrete slab reinforced with a system of longitudinal steel rods. When conducting the research, a linear and elastic model of concrete was used, and the stress intensity factor was considered as a characteristic of the fracture mechanics. A surface crack of constant depth located in the cross-section of the slab was postulated. It was assumed that its faces completely cover the cross-section of reinforcing rods. The crack depth, the depth of reinforcing rods, their diameter, and the distance between adjacent rods were chosen as dimensionless geometric parameters relative to the thickness of the slab. The slab was loaded with two types of loads applied to its ends: constant tensile stresses (pure tension) and linearly variable axial stresses (pure bending). The problem of determining the stress intensity coefficient depending on geometric parameters was reduced to the boundary problem of elasticity theory. The CalculiX finite element analysis package was used to solve it and obtain the stress-strain state of the slab. More than four hundred finite element models were constructed for various combinations of parameters. Based on the known displacements of the crack face points, the values of the stress intensity factor along the crack front were calculated using the relation obtained in the study. It is established that its values significantly depend on the diameter of the reinforcement, and therefore, when conducting practical calculations, it is not recommended to replace the action of reinforcement on concrete with concentrated force. Polynomial approximations with a relative error of 10% are obtained for extreme values of the stress intensity factor. The materials of the study can be useful in the design of reinforced concrete structures, and when studying or teaching a course in fracture mechanics

Keywords: fracture mechanics, stress intensity factor, reinforced concrete structures, finite element method, CalculiX package

Article's History: Received: 04.03.2022; Revised: 29.06.2022; Accepted: 11.08.2022

INTRODUCTION

Issues of crack resistance of reinforced concrete structures (RCS) have been relevant for almost as long as the RCSs themselves exist, that is, for more than a century and a half. Such an insatiable interest in this topic is explained by its direct attitude to ensuring the safe operation of residential, public, and industrial constructions, because almost every modern construction includes reinforced concrete elements. Disregard for the rules and regulations of operation of such facilities is unacceptable and can lead to serious consequences. In this context, it is enough to recall only the case of the "worn-out" Shuliavsky bridge in Kyiv [1], when, under a favourable set of circumstances, there were no human casualties.

Historically, most of the publications devoted to the crack resistance of RCSs are experimental in nature. This circumstance is explained by the relative simplicity of manufacturing experimental samples and the guaranteed reliability of the results of field experiments. Theoretical studies of the crack resistance of RCSs for a long time remained at

Suggested Citation:
Kutsenko, A., & Kutsenko, O. (2022). Effect of reinforcement on the crack resistance of concrete slabs. *Machinery & Energetics,* 13(3), 34-42.

*Corresponding author

the level of model representations and were of little use for direct practical application. The situation began to change in the last two decades, when the development of – programme codes, primarily finite element analysis software, and computer technology allowed modelling the complex structure of RCSs with sufficient discreteness, capable of reproducing an adequate picture of the stress-strain state (SSS) of the reinforced concrete elements under study.

It is worth noting that concrete is generally a physically nonlinear material [2]. Therefore, many concepts of nonlinear fracture mechanics have emerged and/or found their further development in the study on crack resistance of concrete structures. Among them, it is worth noting the two-parameter criterion of local destruction, which in Ukrainian literature is usually referred to as the Leonov-Panasyuk-Dugdale model [3]. Other concepts used in the study of crack resistance of concrete elements include: the pre-destruction zone, the law of sample thickness, the fracture resistance curve (R-curve), etc. A fairly complete overview of the corresponding models is given in [4].

Despite the physical nonlinearity of concrete, the results of many studies [5-7] indicate the possibility of using linear fracture mechanics (LFM) methods to assess the state of cracks in concrete structures. One of the circumstances that facilitate this is the relatively large size of these structures, and the condition for the legality of using LFM is the small plastic zone in the vicinity of the crack vertex compared to the crack length [8]. The length of the macro-crack by definition should be commensurate with the characteristic size of the body in which it is located (otherwise, it refers to micro-cracks, the growth patterns of which are studied by methods of fatigue theory). Consequently, with given mechanical properties of the material, an increase in the size of the body increases the legality of using LFM in the study of its crack resistance. Based on the above, it can be argued that determining the characteristics of LFM in RCSs is of theoretical and practical interest. A significant amount of work is devoted to the investigation of the effect of reinforcement on the distribution of the values of the stress intensity factor (SIF), which is the main characteristic of LFM, along the crack front. The study will briefly consider papers that have a similar object of research.

The study [9] considered a reinforced concrete rod having an edge crack of constant depth located in some of its cross-section. Under assumption that the rod is in a deformable state of bending two approaches to determining the SIF of such a crack, are proposed: analytical and based on finite element modelling. According to the analytical approach, the stress state in the cross-section of the crack location was approached as the stress state of the rod, the cross-section height of which is less than the cross-section height of the original rod by the crack length. The nonlinear relationship between stresses and deformations inherent in concrete was also considered. From the condition of compatibility of deformations of concrete and reinforcement and Hooke's law, the stresses acting in the reinforcement were determined. In the future, the effect of reinforcement on the stress state of concrete was modelled by a concentrated force equal to the equivalent of the specified stresses, that is, their product on the cross-sectional area of reinforcement. The estimated stresses obtained in this way in the vicinity of the crack vertex were considered, in fact, as nominal load stresses in the Griffiths crack problem, and the SIF value itself was established based on the Griffiths formula. The numerical solution, which was based on classical linear fracture mechanics and the finite element method, was implemented using standard tools of the ANSYS software suite. The methods were compared for a single set of geometric and mechanical parameters. The discrepancy in the SIF values obtained by analytical and numerical methods was 1.3% for a certain value of the external bending moment. However, it increased rapidly with a slight increase in bending moment. Thus, with an increase in the moment by one and a half times, the discrepancy increased by an order of magnitude. The authors explain this by the fact that, unlike the numerical value of SIF, the analytical value does not depend linearly on the external moment.

The study [10] also considered a reinforced concrete rod having an edge crack of constant depth located in its cross-section. It is indicated that the simulation was performed using the ANSYS finite element analysis software suite. However, no geometric parameters indicating the relative position of the crack and reinforcement are reflected in the model description. The main conclusion made in the above paper is the significant dependence of the rod stiffness and the stress intensity factor on the rod width. This conclusion was also made on models with slightly variable geometric parameters: only the width of the rod changed within 50%.

In [11] the effect on the crack resistance of a concrete sample of a system of steel reinforcing bars located in it in a plane perpendicular to the external bending moment as a vector was investigated. In this case, some of these rods passed through the faces of a flat edge crack, which was postulated in the cross-section of the sample. As in the above studies, the effect of reinforcement on the stress state of concrete was modelled by concentrated forces. Although the paper provides an expression for SIF for the crack under study, which is based on the assumption of the flat nature of the problem and the superposition principle, the main attention in analysing the results is focused on the dependence of the stiffness of a reinforced concrete sample on the geometric and mechanical properties of its components.

Obviously, this review does not claim to be complete, but it reflects the main trends of such studies: the characteristics of LFM, if calculated, are only for very limited variations in the parameters of the concrete-reinforcement system. This restriction does not provide general conclusions about the criticality of a particular RCSs defect, depending on its size and the parameters of the reinforcement frame. Therefore, the purpose of this study is to determine the stress intensity factor depending on the geometric characteristics of a reinforced concrete element with a crack: the depth of the crack, the thickness of reinforcing rods and the parameters of their location. The originality of the study is explained by the lack of similar results in available papers, and its relevance is explained by the need to create a handbook of RCS defects that can help quickly assess the danger of defects in practice. The presence of these dependencies also allows analysing the fatigue growth of cracks. A separate goal of the study is to evaluate the validity of modelling the effect of reinforcement on the stress state of concrete with concentrated force, which is often used in theoretical studies, based on numerical results.

MATERIALS AND METHODS

The analysis of the influence of reinforcement on the crack resistance of RCSs will be carried out on the example of a reinforced concrete plates (slabs). Reinforced concrete slabs (RCPs) are one of the most commonly used structural elements in construction. The floor overlaps of most multistorey constructions, the walls of panel houses, the foundations of low-rise buildings – all these components are made in the form of RCPs [12]. As a result, this structural element is very variable in its size, shape, and configuration of reinforcement frames. Therefore, to assess their crack resistance, it is necessary to investigate the patterns of the influence of reinforcement on the distribution of SIF along the front of hypothetical cracks that may occur in RCP.

Problem statement. The study considers a concrete rectangular slab of length L, width W, and thickness h, reinforced with longitudinal steel rods in increments $2s$ by the width of the slab (Fig. 1a). The axes of the reinforcement bars are located at a distance of a from the lower surface of the slab, and their diameter is equal to d. It is assumed that in such a slab, in some of its cross-section, an edge crack of constant depth l has occurred, which is greater than the depth of the reinforcement: $l>a+d/2$. In other words, the face of the crack completely covers the reinforcing rods in the cross-section of its location.

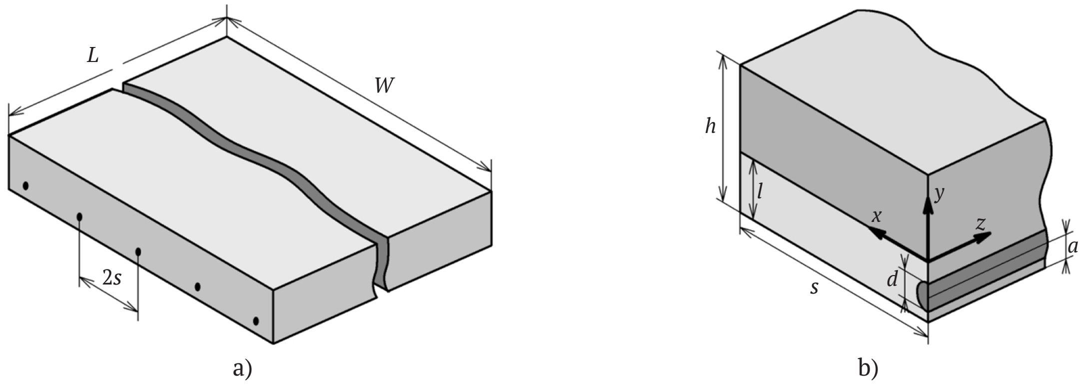

Figure 1. Geometry of the problem: a) general view of RCP; b) half-period of RCP

As an external load, the longitudinal stresses applied to the ends of the slab are considered: constant tensile stresses p (Fig. 2a) and linearly distributed stresses of maximum intensity p (Fig. 2b). The first type of load corresponds to the pure tension of the slab, and therefore, the results associated with it will be denoted by index N. The second type of load determines the pure bend ing of the slab, and therefore, the corresponding results will be denoted by index M. Due to the immutability of the load along the width of the slab, its stress-strain state will have a periodic character along the transverse direction. Therefore, to find it, it is enough to consider only a strip of width s – one half-period of the slab, which is shown in Fig. 1b. A coordinate system associated with a half-period is introduced: its axis x is directed along the crack front, axis y is directed vertically upwards and intersects the axis of the reinforcement rod, and the axis z is directed along the rod, which is shown in Figure 1b in dark grey. In this case, the area of the crack edge shown in Fig. 1b is highlighted in a light gray shade, set by the conditions $z=0$ and $y<0$. It will be also assumed that the plane of the crack location is located at a sufficiently large distance from plate end compared to s. In this case, the influence of edge effects on the stress distribution near the crack front can be ignored and it is assumed that it is symmetric with respect to the plane xy, and therefore, it is enough to consider the SSS of only one half of the slab period, for example, $z>0$.

Figure 2. Plate load: a) σ_{zN} (tension); a) σ_{zM} (bending)

Thus, the following problem is obtained: it is necessary to find the stress-strain state of an elastic body in the form of a rectangular parallelepiped, shown in Fig. 1b, if its surface is free of tangential stresses, and: the side surfaces $y=-l$ and $y=h-l$ and the surface of the crack face ($z=0$ and $y\leq 0$ except for the cross-section of the reinforcement) are also free from normal stresses, on the rest of the end face $z=0$ ($y>0$ without the cross-section of the reinforcement) are free of normal stresses; rest of end $z=0$ and two sides $x=0$ and $x=s$ because of symmetry conditions are of normal displacements; and at the far end $z=D$ ($D \gg h$) normal stresses are prescribed as:

$$\sigma_{zN}=p=const \quad \text{or} \quad \sigma_{zM}=2p(h/2-l-y)/h. \tag{1}$$

The problem statement is completed by setting the elastic properties of the material. Elastic modulus E and the Poisson's ratio v of concrete will be considered equal to 24 GPa and 0.2, respectively, which corresponds to the design values of concrete class C20/25 [13].

Note that, according to the statement, the problem contains 4 dimensionless geometric parameters. The following are selected as independent ones:

$$\bar{s}=s/h,\ \bar{l}=l/h,\ \bar{a}=a/h,\ \bar{d}=d/h. \tag{2}$$

As a method for solving this problem, the study will use the finite element method (FEM) implemented in the CalculiX packege. This packege determines SSS in solid deformable bodies of various rheological nature under the action of force and temperature loads [14]. Despite the fact that CalculiX is a free-access software suite, its capabilities are not much inferior to many similar commercial products, and in some aspects, due to the openness of its code, even surpass them. This packege also allows solving problems of fracture mechanics, even in a nonlinear formulation [15]. Fig. 3 shows a general view of the CalculiX finite-element model and its separate part in the vicinity of the reinforcement rod outlet to the crack face at $\bar{s}$=1, $\bar{l}$=0.3, $\bar{a}$=0.1, $\bar{d}$=0.1. The model is formed using 20- and 15-node quadratic elements of type C3D20 and C3D15, respectively.

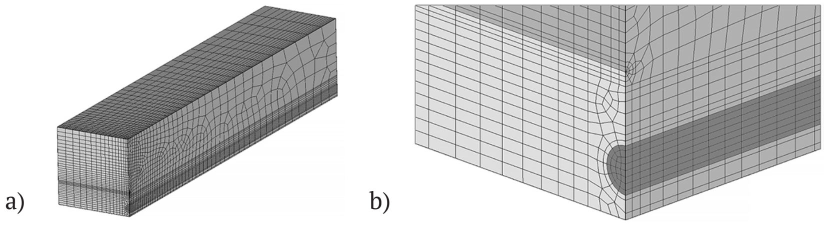

Figure 3. Finite element model for $\bar{s}$=1, $\bar{l}$=0.3, $\bar{a}$=0.1, $\bar{d}$=0.1: a) general view; b) crack face near reinforced rod

Since CalculiX does not have its own SSF estimation tool, it was implemented using additional code. The idea of determining the SIF from pre-calculated SSS is to approximate the field of normal displacements of the points of the crack edges u with an expression $(A++B\rho)\sqrt{\rho}$, where ρ – distance from the displacement determination point to the crack front. Thus, to determine the constans A and B, it is enough to know the displacements u_1 and u_2 at two points near the crack front located at a distance of ρ_1 and ρ_2, respectively. Indeed, substituting the pair of values (ρ_1, u_1) and (ρ_2, u_2) in the expression $u=(A+B\rho)\sqrt{\rho}$, a system of two linear equations is obtained with respect to constants A and B. The field of normal displacements of the crack edges of a normal fracture in the case of plane deformation (the case of the problem formulated) in accordance with the asymptotics of the Westerhard's solution is given by the relation [8; 16]:

$$u=\frac{4(1-v^2)}{E\sqrt{2\pi}}K\sqrt{\rho},\ \rho\to 0, \tag{3}$$

where the constant K is the stress intensity factor. Comparing expressions $(A+B\rho)\sqrt{\rho}$ and (3), we can conclude that K is proportional to the constant A. Therefore, based on the above relations, the expression for SIF is obtained:

$$K=\frac{E\sqrt{2\pi}}{4(1-v^2)}\frac{u_1\sqrt{\rho_2^3}-u_2\sqrt{\rho_1^3}}{\sqrt{\rho_1\rho_2}(\rho_2-\rho_1)}. \tag{4}$$

Equation (4) is the basis for determining the SIF from the known SSS.

To reduce the error in determining the fields in the vicinity of the crack front, it is necessary to move the middle nodes closest to it by a quarter of the length of the corresponding edge of the finite element (FE) towards the corner node lying on the crack front. The specified nodes are circled in Fig. 4a. With this arrangement, the approximations of the stresses fields in the FE near the front will have a root singularity, i.e., they will increase inversely proportional to $\sqrt{\rho}$. Approximations of displacements will decrease to zero proportionally to $\sqrt{\rho}$. This nature of approximations corresponds to the asymptotic solution of the problem of elasticity theory, and therefore, provides greater accuracy of the numerical solution. Similar shift must be made for the middle nodes near the concrete-reinforcement interface line on the crack face (Fig. 4b).

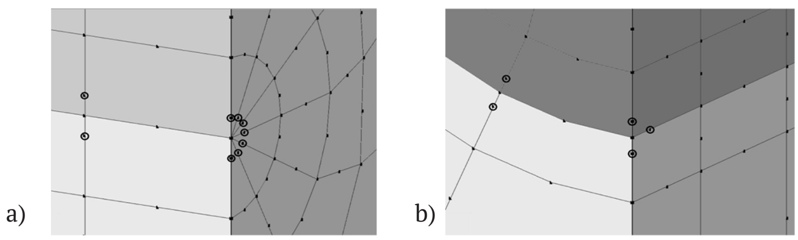

Figure 4. Shift of middle nodes: a) near the front; b) near the interface line on the crack face

Evidently from Figure 3a, a decrease in the dimension of the resolution system was achieved by increasing the FE size in the regions of the period farthest from the crack. The sufficiency of the discreteness of the finite element grid of models was checked by halving the FE size. The relative change in the numerical values of SSF did not exceed 1%.

RESULTS AND DISCUSSION

Using the developed FE models, a large number of calculations of the stresses fields and displacements of the RCP half-period with a crack were performed, based on which the SIF distributions along the crack front were determined. More than 800 SIF distributions were obtained – two for each model (for loads σ_{zN} and σ_{zM}). Figure 5 shows the distribution of normal displacements and normal stresses in the cross-section of the crack edge in the vicinity of the reinforcement rod obtained using the model shown in Fig. 3. The displacements distribution is given for the load case σ_{zN}, and the stresses distribution is for the case of load σ_{zM}. The positive direction of normal displacements is determined by the external normal to the crack face, i.e., in the negative direction of the axis z. The values are given in basic units of the SI system (displacement – in m, stresses – in Pa). The fields are calculated at p=100 MPA and h=0.12 m.

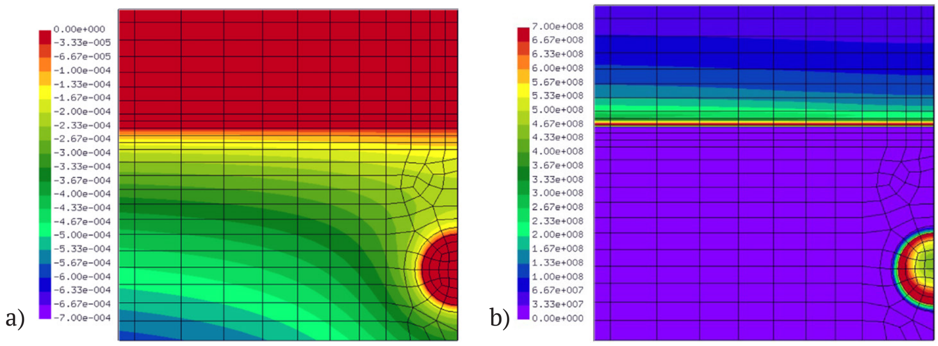

Figure 5. Distribution of fields for $\bar{s}$=1, $\bar{l}$=0.3, $\bar{a}$=$\bar{d}$=0.1:
a) normal displacements field for the load σ_{zN}; b) normal stresses field for the load σ_{zM}

A total of four values of the relative width of the half-period $\bar{s}$: 1, 2, 3, and 5 and three values of the dimensionless diameter of the reinforcement rod $\bar{d}$: 0.05, 0.1, and 0.15 were considered. Dimensionless crack depth $\bar{l}$ varied from 0.05 to 0.7 in increments ranging from 0.25 to 1. The depth of the reinforcement rod $\bar{a}$ axis also varied. At the same time, the obvious conditions for the correctness of the model construction were monitored: a $\bar{a}$>$\bar{d}$/2 and $\bar{a}$+$\bar{d}$/2<l. Fig. 6 and 7 show some of the SIF distributions along the front. A dimensionless coordinate is plotted along the abscissa axis of the corresponding graphs $\bar{x}$=x/s, and along the ordinate axis – the value of the dimensionless SIF $\bar{K}$=K/($p\sqrt{l}$). The lower index in the SIF designation, as already mentioned, is responsible for the type of load. The numbers in the circles correspond to the parameter $\bar{s}$ values, for which the corresponding distribution was constructed. The value of this parameter for those curves where there are no marks can be determined by analogy. Fig. 6 shows SIF graphs for crack with depth $\bar{l}$=0.3, Fig. 7 – with depth $\bar{l}$=0.7. The dotted lines correspond to the rod diameter $\bar{d}$=0,05, and dashed lines – with a diameter of $\bar{d}$=0.15. The depth of the reinforcement rod axis for all curves was determined by the condition $\bar{a}$=0".025"+$\bar{d}$/2, that is, for all curves, the depth of the reinforcement point closest to the crack front was fixed.

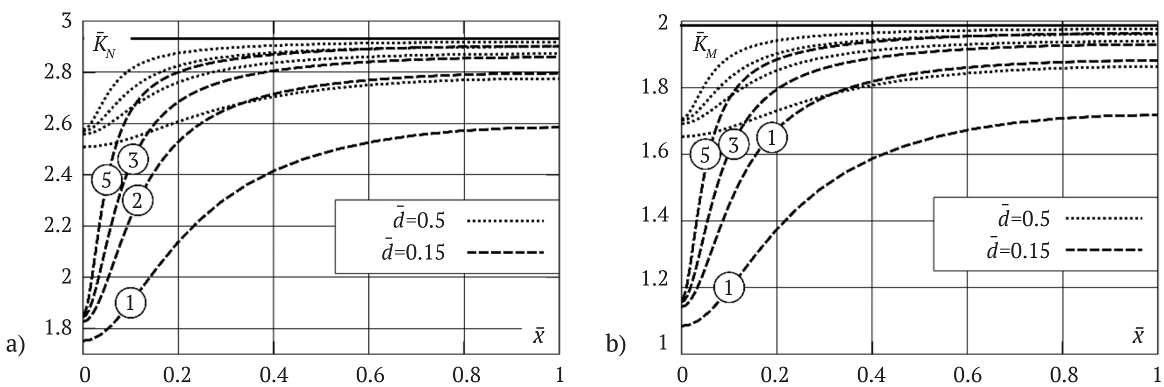

Figure 6. SIF distribution for crack with depth $\bar{l}$=0.3 for loading:
a) σ_{zN}; b) σ_{zM}

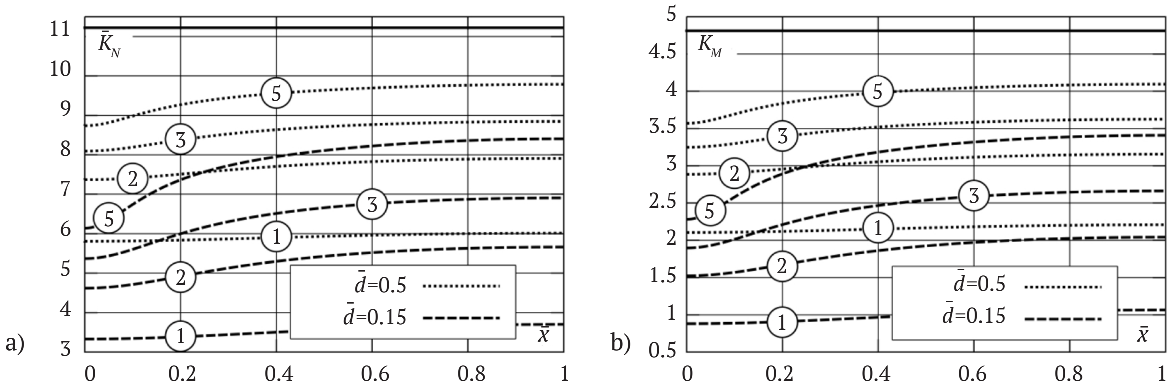

Figure 7. SIF distribution for crack with depth $\bar{l}$=0.7 for loading:
a) σ_{zN}; b) σ_{zM}

In addition to dotted and dashed lines, each of the graphs has a solid horizontal straight line that corresponds to the SIF value in the absence of reinforcement. These values were compared with known in the literature, which are calculated from solutions to the corresponding plane problems. Corresponding exact SIF approximations for tension and bending loads as a function of the only parameter $\bar{l}$ which remains in this case can be represented as [16]:

$$\bar{K}_N = \left(1{,}11 + 5\bar{l}^4\right)\left(1-\bar{l}\right)^{-1}\sqrt{\pi},$$
$$\bar{K}_M = 0{,}7\bar{l}^{-2}\sqrt{\left(1-\bar{l}\right)^{-3} - \left(1-\bar{l}\right)^{3}} \qquad (5)$$

The deviation of the calculated values from (5) does not exceed 1% and 4%, respectively.

Analysing the graphs shown in Figs. 6 and 7, it can be noted that all of them monotonically increase from the minimum value $\bar{K}_{min}=\bar{K}|_{\bar{x}=0}$ near the rod to its maximum value $\bar{K}_{max}=\bar{K}|_{\bar{x}=1}$. The rate of this growth varies. It is largest in the middle part of the front closer to the rod. However, at the neighbourhood of reinforced rod, and at the opposite end of the front, it decreases to zero (the velocity is the derivative, and the derivative is zero at the extreme points). The growth rate in the middle section significantly depends on the diameter of the reinforcement rod: the larger it is, the higher the growth rate, although the values themselves are significantly lower. This conclusion is important in the context of determining the adequacy of replacing the valve action with concentrated force.

Another important conclusion that can be drawn from Figs. 6 and 7, there is a locality of reinforcement action for small cracks. So for a crack with depth $\bar{l}$=0.3, the difference between the maximum and current SIF values is reduced by half at a distance of less than a third of the slab thickness. At the same time, $\bar{K}_{max}$ are much closer to SIF for a flat crack, that is, in the absence of reinforcement. The minimum SIF values, regardless of the crack depth, significantly depend on the reinforcement thickness. In case of a deep crack $\bar{l}$=0.3 they do not depend much on the length of the half-period $\bar{s}$ and already for $\bar{s}\geq 2$ they can be considered constant. For cracks with depth $\bar{l}$=0.7, the minimum SIF values significantly depend on both the rod diameter and the width of the half-period.

Thus, the general conclusion that can be drawn on the basis of the analysis performed is that it is incorrect to replace the arming action with concentrated force during practical calculations. To understand why this is the case, it is necessary to refer to the basic concepts of concentrated force in the mechanics of continuum in general and in elasticity theory in particular. From the course of elasticity theory, it is known [17] that the fields of displacements and stresses in Kelvin, problem, Boussinesq problem and similar three-dimensional problems of elasticity theory have a singularity of the type ρ^{-1} and ρ^{-2}, respectively. Here ρ – distance from the observation point to the point of application of a concentrated force. That is, both take infinite values at the point of application of the concentrated force. According to the solution, looks like the concentrated force "pins out" the point of its application to infinity, which does not correspond to reality. The key to the correct practical use of these singular solutions of elasticity theory lies in the Saint-Venan's principle [17-19]: replacing the system of external forces with a statically equivalent one has little effect on SSS at remote points. In this case, points located at a distance of at least five characteristic sizes of the area of application of forces are considered remote. In our case, the characteristic size of this area is the diameter of the reinforcement rod. That is, to adequately replace the action of the reinforcement with a concentrated force, it is necessary that the reinforcement rod is at least five of its diameters away from both the crack front and the edge of the slab. Obviously, such conditions cannot be implemented in practice in any way. Therefore, replacing the action of arming with a concentrated force can only be used to explain qualitative behaviour, and not to obtain quantitative results.

For each specific set of parameters (2), a fairly complete picture of the SIF distribution along the crack front can be obtained by knowing two values: $\bar{K}_{min}$ and $\bar{K}_{max}$. Therefore, it is important to be able to find their approximate values using simple relations. To do this, the results obtained were processed using the least squares method. A polynomial approximation of the specified extreme values of SIF as functions of parameters (2) was found. It turned out that the linear approximation is quite rough and allows a relative error (the ratio of the maximum deviation to the maximum value) of up to 25%. The trade-off between the accuracy and complexity of an expression can be considered an approximation in the form of second-order polynomials. Their relative error for all four values is about 10%. In general, this approximation can be represented as

$$\bar{K}_{ext} = \sum_{i=1}^{4}\sum_{j=i}^{4}\alpha_{ij}r_i r_j + \sum_{i=1}^{4}\beta_i r_i + \gamma, \qquad (6)$$

where *ext* takes one of four values: *Nmin*, *Nmax*, *Mmin*, or *Mmax*; $r_1=\bar{s}$, $r_2=\bar{l}$, $r_3=\bar{a}$, $r_4=\bar{d}$ – indexed geometric parameters (2). The approximation coefficients (6) are shown in Table 1.

Table 1. Approximation coefficients of extreme SIF values

Coefficients	Extreme values of SIF			
	$\bar{K}_{Nmin}$	$\bar{K}_{Nmax}$	$\bar{K}_{Mmin}$	$\bar{K}_{Mmax}$
α_{11}	-8.035×10^{-2}	-1.206×10^{-1}	-4.228×10^{-2}	-6.399×10^{-2}
α_{12}	1.557	2.309	7.727×10^{-1}	1.133
α_{13}	-7.622×10^{-1}	−1.013	-4.148×10^{-1}	-5.643×10^{-1}
α_{14}	9.476×10^{-1}	4.075	5.382×10^{-1}	2.221
α_{22}	9.924	1.680×10	-6.923×10^{-1}	3.291
α_{23}	2.526×10	1.624×10	1.364×10	7.825
α_{24}	-1.100×10^{2}	-1.134×10^{2}	-4.261×10	-5.394×10
α_{33}	-1.107×10	5.066	−4.810	2.301
α_{34}	-5.077×10	3.323×10	-2.014×10	1.933×10
α_{44}	2.548×10^{2}	1.052×10^{2}	1.300×10^{2}	5.129×10
β_1	2.590×10^{-2}	-6.800×10^{-2}	3.867×10^{-2}	1.472×10^{-2}
β_2	−1.868	−8.774	1.299	−2.534
β_3	−5.022	−7.455	−3.386	−3.217
β_4	4.746	1.520×10	−7.413	4.572
γ	2.171	3.873	1.499	2.312

Based on the values in Table 1 and equation (6), it is possible to quickly restore the overall qualitative picture of SIF distributions as a function of geometric parameters. Having distribution data and critical SIF values in concrete, it is possible to quickly give an answer about the degree of danger of a particular defect. In addition, they allow investigating the rate of growth of defects based on the Paris formula [8; 16].

CONCLUSIONS

The problem of crack resistance of RCP was reduced to the problem of linear elasticity theory, which was solved using the CalculiX finite element analysis package for variable values of geometric parameters of the system. In processing the obtained numerical results, general regularities of the dependence of the SIF on the geometric parameters of the RCP are established, namely:

– for all values of geometric parameters, SIF is a periodic and monotonous function on the half-period of the plate width, taking the minimum value near the reinforcing rods, and the maximum value in the middle between them;

– the maximum growth rate of the SIF corresponds to an interval close to its minimum;

– for shallow cracks, the effect of reinforcement is local: the minimum SIF value weakly depends on the length of the slab period, and the SIF itself quickly increases to its maximum value;

– as the rod diameter increases, the difference between the minimum and maximum SIF values increases;

The paper also provides a reasonable warning regarding the modelling of the action of reinforcement on concrete with concentrated force during practical calculations. Instead, it is proposed to use polynomial approximations of extreme SIF values given in the paper and obtained as a result of processing a large array of numerical data to estimate the stress state in the vicinity of the crack front.

Since for real diameters of reinforcing rods, the SIF varies significantly along the front of a flat crack, in order to correctly calculate the crack configuration during its subsidence, this study should be extended to the case of cracks of other configurations, for example, semi-elliptical.

ACKNOWLEDGEMENTS

The authors consider it their duty to express their sincere gratitude to the developers of the CalculiX packege [14] Guido Dhondt and Klaus Wittig for their tremendous and selfless work, the results of which allow researchers around the world to conduct numerical modelling in the field of mechanics free of charge.

REFERENCES

[1] Photo of the day: Shulyavsky bridge collapsed in Kyiv. (2017). Retrieved from https://ukranews.com/ua/news/482055-u-kyyevi-obvalyvsya-shulyavskyy-mist.

[2] Yafei, L., Tao, Z., Jie, Y., Tao, J., Qingfang, Z., & Hexuan, H. (2021). A simplified uniaxial stress-strain curve of concrete and its application in numerical simulation. *E3S Web of Conferences*, 283, article number 01045. doi: 10.1051/e3sconf/202128301045.

[3] Panasyuk, V. (2019). Development of investigations on fracture mechanics of materials and structural integrity: Achievements and perspectives (review). *Procedia Structural Integrity*, 16, 3-10. doi: 10.1016/j.prostr.2019.07.015.

[4] Akram, A. (2021). The overview of fracture mechanics models for concrete. *ACEE*, 14(1), 47-57. doi: 10.21307/acee-2021-005.

[5] Chauhan, D., Tewani, H., & Kalyana Rama, J. (2018). Application of principles of linear elastic fracture mechanics for concrete structures: A numerical study. *Applied Mechanics and Materials*, 877, 282-288. doi: 10.4028/www.scientific.net/AMM.877.282.

[6] Dong, W., Li, J., Zhang, X., & Zhang, B. (2019). Evolutions of SIFs of concrete under sustained loading by considering the effects of stress relaxations. *Journal of Materials in Civil Engineering*, 31(12), article number 04019287. doi: 10.1061/(ASCE)MT.1943-5533.0002949.

[7] Polyakova, I., & Imambayeva, R. (2021). Comparison of the stress-strain state reinforced concrete structures (columns and trusses) with linear and nonlinear statements of the deformation law. *E3S Web of Conferences*, 281, article number 01032. doi: 10.1051/e3sconf/202128101032.

[8] Anderson, T. (2017). *Fracture mechanics: Fundamentals and applications* (4th ed.). London: CRC Press. doi: 10.1201/9781315370293.

[9] Nuguzhinov, Z., Bakirov, Z., Vatin, N., Bakirov, M., Kurokhtina, I., Tokanov, D., & Khabidolda, O. (2021). Stress intensity factor of reinforced concrete beams. *Buildings*, 11(7), article number 287. doi: 10.3390/buildings11070287.

[10] Malipatil, K., & Itti, S. (2019). Stress intensity factor and damage index of reinforced concrete beam. In *Fatigue, durability, and fracture mechanics* (pp. 305-316). Belagavi: Visvesvaraya Technological University. doi: 10.1007/978-981-15-4779-9_19.

[11] Accornero, F., Rubino, A., & Carpinteri, A. (2020). Ductile-to-brittle transition in fibre-reinforced concrete beams: Scale and fibre volume fraction effects. *Material Design & Processing Communications*, 2(6), article number e127. doi: 10.1002/mdp2.127.

[12] Kulikov, P., Ploskyi, V., & Getun, G. (2021). *Constructions of buildings and structures. Book 1*. Kyiv: Lira-K.

[13] DBN V.2.6-98:2009. Constructions of buildings and structures. Concrete and reinforced concrete structures. (2011). Kyiv: Ministry of Regional Construction of Ukraine.

[14] CalculiX: A free software three-dimensional structural finite element program. (2021). Retrieved from http://www.calculix.de.

[15] Bulgakov, V., Aboltins, A., Kutsenko, O., Ivanovs, S., & Pascuzzi, S. (2021). Approximate approach of research and assessment of crack resistance of cylindrical housings. *Engineering for Rural Development*, 20, 1541-1547.

[16] Zrazhevsky, G., Kepich, T., & Kutsenko, O. (2005). *Basics of the theory of strength, deformation and fracture mechanics*. Kyiv: LOGOS.

[17] Sadd, M. (2020). *Elasticity: Theory, applications and numerics* (4th ed.). London: Academic Press.

[18] Ostanin, V. (2022). Effects of repulsion and attraction between rotating cylinders in fluids. *Scientific Herald of Uzhhorod University. Series "Physics"*, 51, 39-47.

[19] Shynkariuk, Y. (2022). Alternative representation of space and time: Geometric solution of problems of relativity theory. *Scientific Herald of Uzhhorod University. Series "Physics"*, 51, 74-82.

Анастасія Григорівна Куценко[1], Олексій Григорович Куценко[2]

[1]Національний університет біоресурсів і природокористування України
03041, вул. Героїв Оборони, 15, м. Київ, Україна

[2]Київський національний університет імені Тараса Шевченка
01601, вул. Володимирська, 64/13, м. Київ, Україна

Вплив армування на тріщиностійкість бетонних плит

Анотація. Попередній аналіз наявних літературних джерел, присвячених дослідженню тріщиностійкості залізобетонних конструкцій, показав відсутність встановлених загальних закономірностей впливу важливих геометричних параметрів, властивих залізобетонним елементам, на розподіл характеристик механіки руйнування вздовж фронту тріщини. На основі проведеного аналізу було сформульовано мету дослідження: встановлення зазначених закономірностей для бетонної плити, укріпленої системою поздовжніх арматурних стрижнів. При проведенні досліджень використовувалася лінійно-пружна модель бетону, а у якості характеристики механіки руйнування розглядався коефіцієнт інтенсивності напружень. Постулювалася поверхнева тріщина постійної глибини, розташована в поперечному перерізі плити. Передбачалося, що її береги повність покривають поперечний переріз арматурних стрижнів. У якості безрозмірних геометричних параметрів були обрані віднесені до товщини плити глибина тріщини, глибина залягання арматурних стрижнів, їх діаметр та відстань між сусідніми стрижнями. Плита навантажувалася двома типами навантаження, прикладеними до її торців: постійними розтягуючими напруженнями (чистий розтяг) та лінійно-змінними осьовими напруженнями (чистий згин). Задача визначення коефіцієнта інтенсивності напружень залежно від геометричних параметрів була зведена до граничної задачі теорії пружності. Для її розв'язання і отримання напружено-деформівного стану плити використовувався скінченно-елементний пакет CalculiX. Для різних комбінацій параметрів було побудовано більше чотирьохсот скінченно-елементних моделей. За відомими зміщеннями точок берега тріщини за допомогою співвідношення, отриманого в роботі, розраховувалися значення коефіцієнта інтенсивності напружень вздовж фронту тріщини. Встановлено, що його значення суттєво залежать від діаметра арматури, а тому при проведенні практичних розрахунків дію арматури на бетон не рекомендовано замінювати зосередженою силою. Для екстремальних значень коефіцієнта інтенсивності напружень отримано поліноміальні апроксимації з відносною похибкою в межах 10 %. Матеріали роботи можуть бути корисними при проектуванні залізобетонних конструкцій, а також при вивченні чи викладанні курсу механіки руйнування

Ключові слова: енергоефективність, двигуни середньої потужності, реактивна потужність, внутрішня ємнісна компенсація, компенсувальна ємність, пусковий режим

Machinery & Energetics
Vol. 13, No. 3. 2022

Journal homepage:
https://technicalscience.com.ua/en

UDC 621.87
DOI: 10.31548/machenergy.13(3).2022.43-52

Viatcheslav Loveikin[1*], Yuriy Romasevych[1], Lubov Shymko[1], Yuriy Loveikin[2]

[1]National University of Life and Environmental Sciences of Ukraine
03041, 15 Heroiv Oborony, Kyiv, Ukraine

[2]Taras Shevchenko National University of Kyiv
01033, 60 Volodymyrska Str., Kyiv, Ukraine

Minimisation of the Driving Torque of the Derricking Mechanism of a Tower Crane during Steady Load Hoisting

Abstract. Efficient use of a tower crane often requires combining various operations, such as hoisting load and derricking. In the case when the load is hoisted at a steady speed, the problem of optimal control of the trolley movement mechanism arises, which goes beyond engineering calculations and is a scientific and applied problem. Its relevance is related to improving the controllability of crane mechanisms, increasing the capacity and reliability of the crane, and improving the energy efficiency of its drive mechanisms. These indicators are related to the choice of optimisation criteria. Thus, the purpose of the study is to optimise the starting mode of the derricking mechanism according to the criterion of the RMS value of the driving moment during a steady load hoisting. To achieve this goal, the following methods were applied: dynamics of machines and mechanisms, mathematical modelling, integral and differential calculus, and the ME-D-PSO method. For the boundary conditions, parameters are selected that eliminate load oscillations on the flexible suspension when the derricking mechanism slews to the steady-state driving mode. Based on the results of optimisation of the joint movement of mechanisms for derricking and load hoisting, graphical dependences of kinematic, dynamic, and energy characteristics of the start-up transition process are constructed and their analysis is carried out. The obtained dependences reveal the conditions for eliminating load oscillations on a flexible suspension during steady-state movement and reducing dynamic loads and energy losses during the start-up of the derricking mechanism. To implement the optimal start mode of the derricking mechanism during steady load hoisting, it is recommended to use optimal control of the drive mechanisms. The results obtained should be applied to the development of new and modernisation of existing motion control systems for tower crane mechanisms

Keywords: optimal control, optimisation criteria, load oscillations, joined operations

Article's History: Received:28.03.2022; Revised: 08.07.2022; Accepted: 11.08.2022

INTRODUCTION

When operating tower cranes, it is quite common to combine the operations of movement of mechanisms. There are cases when one of the mechanisms performs a steady movement, and at this time another mechanism is switched on. The operation of mechanisms in this mode leads to an increase in dynamic loads caused by high-frequency oscillations of the links of drive mechanisms and the metal structure of the crane, and low-frequency oscillations of the load on a flexible suspension.

The most common case is the operation of crane mechanisms, when the load hoisting mechanism performs a steady movement with the process of starting or braking the derricking mechanism. Due to the significant dynamic loads in the mechanisms during such movements, there is a need to reduce them. Therefore, there is a need to choose such a mode of movement of the derricking mechanism, in which its driving torque would be minimal.

The review of scientific studies on this topic indicated the relevance and significant interest of the world scientific community in research aimed at improving the reliability and efficiency of loading and unloading processes, including by optimising the operating modes of modern

Suggested Citation:
Loveikin, V., Romasevych, Yu., Shymko, L., & Loveikin, Yu. (2022). Minimisation of the driving torque of the derricking mechanism of a tower crane during steady load hoisting. *Machinery & Energetics,* 13(3), 43-52.

*Corresponding author

crane mechanisms, which complies with safe conditions and provides trouble-free operation of hoisting and transport machines.

During the operation of tower cranes (and not only tower cranes), the payload performs a complex movement, in which a number of mechanisms work simultaneously, the operation of which has both mutual and general effects on the crane system [1; 2]. This feature requires the operator to be precise in choosing the operating modes of crane mechanisms, since the error can have dramatic consequences. Therefore, scientific investigation is often aimed precisely at improving the efficiency of controlling hoisting processes. Thus, in the study [3], a comprehensive review of crane control strategies is performed, where, along with a thorough analysis of control schemes for various types of crane systems that have been performed since 2000, an overview of modelling single - and double-lever crane systems is provided. A valuable contribution to the development of the theory of control of crane systems is the classification of strategies for the development and improvement of means of controlling the working processes of crane mechanisms, which systematises the scientific search that aims to optimise operating modes.

A typical line of scientific research is an attempt to improve the reliability and trouble-free operation of all mechanisms of crane systems. With the development of automation tools, first analogue and then digital, researchers focused their efforts on the development of theoretical foundations and practical research of the operating modes of a very wide arsenal of crane mechanisms: from conventional controllers [4] to neural networks, technical vision systems, and artificial intelligence [5-7]. This thesis also applies to specific crane manipulators [8]. The increase in requirements for the quality of loading and unloading processes has caused the expansion of the methodological tools of researchers in the construction of mathematical models of crane systems. At the same time, as noted in the study [9], the large-scale, fast, and modular development of tower cranes has brought significant problems of construction safety in difficult working conditions. The study simulates changes in the rotation angle. The obtained data should be used to improve control systems.

The purpose of [10] is to investigate the dynamic indicators of crane system mechanisms during crane operation and develop computer training methods to improve the quality of crane operator training. The researchers implemented a powerful visualisation interface for displaying the dynamic behaviour of the crane. The study results allow developing an effective programme for training operators of construction tower cranes.

The method of reducing oscillations for fast crane operation is substantiated in [11]. Researchers from the Faculty of Civil Engineering of the National Taiwan University conducted analytical studies to test the three-stage control method proposed by the authors, which aims to reduce the angles of oscillation during the operation of a tower crane at high speed. The method is based on the physical laws of motion of a double pendulum and uses fixed values of acceleration and deceleration to reduce the oscillation angle and frequency. Checking the mathematical model showed that the working cycle time is proportional to the square root of the working distance at a constant oscillation angle and no oscillation.

The evolution of information technologies and computer graphics has contributed to the development of automated methods for modelling loading and unloading processes. Virtual models allow investigating and predicting possible dangerous or inefficient actions of crane mechanisms. In the study [12], the authors focused on developing a mathematical model to support modelling and visualisation of cranes as the most important equipment in terms of project control. The researchers proposed a mathematical model that can more accurately represent the detailed activity of the crane. The computer programme developed by the researchers simulates and visualises the operation of crane mechanisms in real time. The created animation provides interactive functions.

The development of mathematical models is a special aspect of experimental research in the field of engineering. Thus, in studies [13] and [14], mathematical models are constructed, and a system of second-order linear differential equations describing the dynamics of transverse displacement of the centre of mass is obtained.

Slovak researchers conducted experiments using a three-dimensional laboratory model suitable for research in the field of mechanism control. Their study [15] is devoted to the identification of a dynamic model and the development of a trolley position controller along the boom of a tower crane, and damping load oscillations.

In [16], a mathematical model of a jib crane is proposed, which considers the degrees of freedom that characterise the selected type of system. The researchers developed a nonlinear control law that uses all states of the model. Verification of simulation results with real physical parameters shows the effectiveness of the proposed control scheme even in the presence of wind disturbances.

In the study [17], the author formulated optimisation criteria in the form of quadratic functionals for each tower crane mechanism. Minimisation of functionals allowed the researcher to obtain a set of optimal parameters of crane mechanisms, in which their interaction should be effective. An innovative feature of the presented solution is an integrated approach to optimising multi-drive systems, aimed at reducing the oscillations of a load suspended on a flexible suspension and minimising the forces acting on the rope. This approach, combined with the method of selective analysis of mechanism structures, can be developed as a method for synthesising globally optimal configurations of interacting mechanisms [17].

Based on the materials of the review of research on this topic, it was concluded that the scientific community focuses a lot on the problems of optimising the parameters of crane mechanisms and ensuring the reliability and safety of loading and unloading processes. At the same time, various programmes and methods of experimental research are used. However, showing special interest, this study will focus on the provisions and experience of using the metaheuristic optimisation method in these problems – the Particle Swarm Optimisation method (PSO) [18].

First of all, PSO is identified with an evolutionary algorithm, which is applied with considerable success to solving various engineering and technological problems [19; 20]. Since its first publication in 1995 [21], the algorithm has been constantly modified. It seems that at present there is not a single scientific field where various variants of PSO did not have their application for solving a wide range of optimisation problems. This is evidenced by the study by F. Marini and B. Walczak [22], where the researchers emphasise the importance of choosing the right PSO metaparameters. E. Hussain et al. [23] note that due to their flexibility, these algorithms can solve various optimisation problems in various fields, especially in engineering and computer science. The researchers summarised and analysed some of the most influential and diverse developments in various aspects of the PSO algorithm since its initial formulation. A comprehensive study [24], which was conducted by a team of researchers who are representatives of various scientific fields, revealed positive aspects and weaknesses in PSO algorithms. However, the researchers agree that PSO is a promising candidate for optimising a wide range of real-world optimisation problems. Eight potential research areas were identified to further improve the efficiency of PSO optimisation. One example of improving the effectiveness of PSO can be the study [25]. The problem of limited optimisation was considered to study PSO. The optimal set of parameters determined by sensitivity analysis was verified by comparison with other metaheuristic methods. In [26], a modified metaeuristic ME-PSO particle swarm method is also used to solve the nonlinear optimisation problem.

The purpose of this study is to solve the problem of minimising the driving torque of the drive mechanism for derricking when working together with the load hoisting mechanism by selecting the driving mode of the drive mechanisms.

The originality of the study consists in solving the scientific and applied problem of optimising the movement control of the derricking mechanism of a tower crane, provided that the load is hoisted at a steady speed. A special feature of this problem is the methodology for solving it, which consists in reducing it to the problem of unconstrained minimisation of a complex function, the minimum of which is found by the modified particle swarm method.

MATERIALS AND METHODS

To achieve this goal, the following methods were applied: dynamics of machines and mechanisms, mathematical modelling, integral and differential calculus, and ME-D-PSO.

The jib system of a tower crane (Fig. 1) is presented as a holonomic mechanical system consisting of absolutely solid bodies, except for the traction rope of the trolley movement, which has elastic properties.

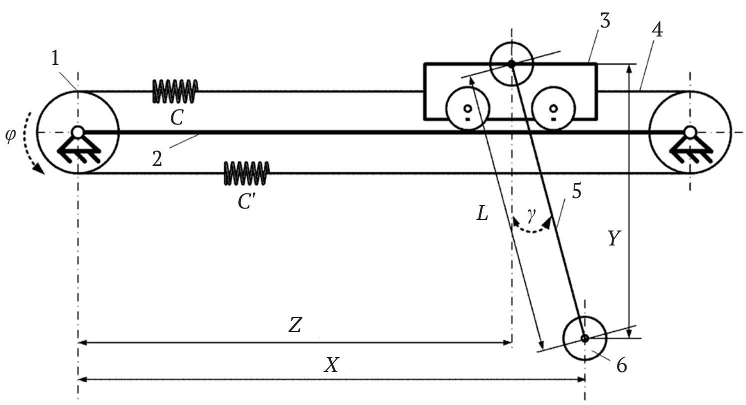

Figure 1. Dynamic model of joint movement of mechanisms for derricking and load hoisting: 1 – drive drum of the trolley; 2 – saddle jib; 3 – trolley; 4 – traction rope; 5 – flexible load suspension; 6 – load

The elastic properties of the rope are represented by the stiffness coefficient C or C' depending on the direction of movement of the trolley, and the flexible suspension of the load, which oscillates in the plane of trolley movement mechanism.

In the accepted dynamic model, the linear coordinates of the trolley's centre of mass are used as generalised coordinates z, and load x, and the angular coordinates of rotation of the trolley drive drum φ. Deviation of the load rope from the vertical is carried out in the plane of trolley movement mechanism by an angle v. At the same time, the length of the flexible load suspension l changes at a constant rate V and is expressed by the following dependence:

$$l=l_0+Vt, \tag{1}$$

where t – time; l_0 – initial length of load suspension.

To create equations of motion of the accepted dynamic model of the boom system (Fig. 1) the second order Lagrange equations are used:

$$\begin{cases} \dfrac{d}{dt}\dfrac{\partial T}{\partial \dot{\varphi}}-\dfrac{\partial T}{\partial \varphi}=M-\dfrac{\partial \Pi}{\partial \varphi}; \\ \dfrac{d}{dt}\dfrac{\partial T}{\partial \dot{z}}-\dfrac{\partial T}{\partial z}=-W-\dfrac{\partial \Pi}{\partial z}; \\ \dfrac{d}{dt}\dfrac{\partial T}{\partial \dot{x}}-\dfrac{\partial T}{\partial x}=-\dfrac{\partial \Pi}{\partial x}, \end{cases} \tag{2}$$

where T, Π – kinematic and potential energy of the system, respectively; M – driving torque on the shaft of the electric motor of the derricking mechanism, reduced to the axis of rotation of the drive drum; W – resistance force to trolley movement.

The vertical component of the movement of the centre of mass of the load is determined by the dependence:

$$y = (l_0 + Vt)\cos\nu = (l_0 + Vt)\cos\left(\frac{x-z}{l_0 - Vt}\right). \tag{3}$$

Taking the time derivative of equation (3), the vertical component of the velocity of the centre of mass of the load is found:

$$\dot{y} = V\cos\left(\frac{x-z}{l_0+Vt}\right) - (l_0+Vt)\sin\left(\frac{x-z}{l_0+Vt}\right)\left(\frac{(\dot{x}-\dot{z})(l_0+Vt) - V(x-z)}{(l_0+Vt)^2}\right). \tag{4}$$

Since the first component of equation (4) is more than an order of magnitude larger than the second component, so in further calculations only the first component will be used, i.e.:

$$\dot{y} = V\cos\left(\frac{x-z}{l_0+Vt}\right). \tag{5}$$

Then the kinetic energy of the mechanical system of joint movement of mechanisms for derricking and load hoisting is presented in the following form:

$$T = \tfrac{1}{2}I_1\dot{\varphi}^2 + \tfrac{1}{2}m_3\dot{z}^2 + \tfrac{1}{2}m[\dot{x}^2 + \dot{y}^2] = \\ = \tfrac{1}{2}I_1\dot{\varphi}^2 + \tfrac{1}{2}m_3\dot{z}^2 + \tfrac{1}{2}m\left[\dot{x}^2 + +V^2\cos^2\left(\tfrac{x-z}{l_0+Vt}\right)\right]. \tag{6}$$

In this case, the potential energy of the same system, considering the equation (3), is determined by the dependence:

$$\Pi = \frac{1}{2}C(\varphi r - z)^2 - mg(l_0+Vt)\cos\left(\frac{x-z}{l_0+Vt}\right). \tag{7}$$

where I_1 – the moment of inertia of the drive of the derricking mechanism is reduced to the axis of the drive drum; m_3, m – according to the weight of the trolley and load; r – radius of the drive drum of the derricking mechanism; g – gravity acceleration.

Next, the study finds derivatives of equations (6) and (7), which are necessary for system (2):

$$\begin{cases} \dfrac{\partial T}{\partial \varphi} = 0;\ \dfrac{\partial T}{\partial x} = -mV^2\cos\left(\dfrac{x-z}{l_0+Vt}\right)\cdot\sin\left(\dfrac{x-z}{l_0+Vt}\right)\cdot\dfrac{1}{l_0+Vt}; \\ \dfrac{\partial T}{\partial z} = mV^2\cos\left(\dfrac{x-z}{l_0+Vt}\right)\cdot\sin\left(\dfrac{x-z}{l_0+Vt}\right)\cdot\dfrac{1}{l_0+Vt}; \end{cases} \tag{8}$$

$$\frac{\partial T}{\partial \dot{\varphi}} = I_1\dot{\varphi};\ \frac{\partial T}{\partial \dot{z}} = m_3\dot{z};\ \frac{\partial T}{\partial \dot{x}} = m\dot{x}; \\ \frac{d}{dt}\frac{\partial T}{\partial \dot{\varphi}} = I_1\ddot{\varphi};\ \frac{d}{dt}\frac{\partial T}{\partial \dot{z}} = m_3\ddot{z};\ \frac{d}{dt}\frac{\partial T}{\partial \dot{x}} = m\ddot{x}; \tag{9}$$

$$\frac{\partial \Pi}{\partial \varphi} = cr(\varphi r - z); \tag{10}$$

$$\begin{cases} \dfrac{\partial \Pi}{\partial z} = -c(\varphi r - z) + mg\sin\left(\dfrac{x-z}{l_0+Vt}\right); \\ \dfrac{\partial \Pi}{\partial x} = -mg\sin\left(\dfrac{x-z}{l_0+Vt}\right). \end{cases} \tag{11}$$

Given that the angular coordinate $\nu = \dfrac{(x-z)}{l_0+Vt}$ does not exceed 12°, then it is taken in equations (8) and (11) $\sin\nu \approx \nu$, and $\cos\nu \approx 1$; dependencies (8) and (11) will have the form:

$$\frac{\partial T}{\partial \varphi} = 0;\ \frac{\partial T}{\partial z} = mV^2\frac{x-z}{(l_0+Vt)^2};\ \frac{\partial T}{\partial x} = -mV^2\frac{x-z}{(l_0+Vt)^2}; \tag{12}$$

$$\frac{\partial \Pi}{\partial z} = -C(\varphi r - z) - mg\sin\left(\frac{x-z}{l_0+Vt}\right);\ \frac{\partial \Pi}{\partial x} = mg\frac{x-z}{l_0+Vt}. \tag{13}$$

After substituting equations (9), (10), (12), and (13) in (2) a system of differential equations of the mechanical system of joint movement of mechanisms for derricking and load hoisting is obtained:

$$\begin{cases} I_1\ddot{\varphi} = M - Cr(\varphi r - z); \\ m_3\ddot{z} - mV^2\dfrac{x-z}{(l_0+Vt)^2} = -W + C(\varphi r - z) + mg\dfrac{x-z}{l_0+Vt} \\ \ddot{x} + V^2\dfrac{x-z}{(l_0+Vt)^2} = -g\dfrac{x-z}{l_0+Vt}. \end{cases} \tag{14}$$

From the last equation of system (14), the coordinate of the trolley's centre of mass is expressed:

$$x - z = -\frac{l_0+Vt}{g + \dfrac{V^2}{(l_0+Vt)}}\ddot{x}. \tag{15}$$

From equation (15):

$$z = x + \ddot{x}P \tag{16}$$

where P – transfer function determined by the dependency:

$$P = \frac{l_0+Vt}{g + \dfrac{V^2}{(l_0+Vt)}}. \tag{17}$$

Now, the time derivatives of equation (16) are taken and the speed and acceleration of the trolley are determined, including the third and fourth derivatives, which will be used in further studies:

$$\dot{z} = \dot{x} + \dddot{x}P + \ddot{x}\dot{P}; \tag{18}$$

$$\ddot{z} = \ddot{x}(\ddot{P}+1) + 2\dddot{x}\dot{P} + x^{IV}P; \tag{19}$$

$$\dddot{z} = \ddot{x}\dddot{P} + \dddot{x}(3\ddot{P}+1) + 3x^{IV}\dot{P} + x^{V}P; \tag{20}$$

$$z^{IV} = \ddot{x}P^{IV} + 4\dddot{x}\dddot{P} + x^{IV}(6\ddot{P}+1) + 4x^{V}\dot{p} + x^{IV}P. \tag{21}$$

The time derivatives of the transfer function (17) used in equation (18)-(21):

$$\dot{P} = V\frac{g + \dfrac{2V^2}{(l_0+Vt)}}{\left[g + \dfrac{V^2}{(l_0+Vt)}\right]^2}; \tag{22}$$

$$\dddot{P} = \frac{2V^6}{(l_0 + Vt)^3 \left[g + \frac{V^2}{(l_0 + Vt)}\right]^3}; \quad (23)$$

$$\ddddot{P} = -\frac{6V^7 g}{(l_0 + Vt)^4 \left[g + \frac{V^2}{(l_0 + Vt)}\right]^4}; \quad (24)$$

$$P^{IV} = \frac{24V^8 g^2}{(l_0 + Vt)^5 \left[g + \frac{V^2}{(l_0 + Vt)}\right]^5}. \quad (25)$$

From the second equation of system (14), the equation of the angular coordinate of the drum of the trolley movement mechanism is found using the relation (15). As a result, the following is obtained:

$$\varphi = \frac{1}{r}\left[z + \frac{1}{C}(m_3\ddot{z} + m\ddot{x} + W)\right]; \quad (26)$$

$$\dot{\varphi} = \frac{1}{r}\left[\dot{z} + \frac{1}{C}(m_3\dddot{z} + m\dddot{x})\right]; \quad (27)$$

$$\ddot{\varphi} = \frac{1}{r}\left[\ddot{z} + \frac{1}{C}(m_3 z^{IV} + m x^{IV})\right]. \quad (28)$$

After substituting (26) and (28) into the first equation of system (14), the dependence of the driving moment of the drive of the derricking mechanism on the horizontal coordinate of the centre of mass of the load and its time derivatives are obtained:

$$M = \frac{I_1}{r}\left[\begin{array}{l}\ddot{z} + \frac{1}{c}(m x^{IV} + m_3 z^{IV}) + \\ +(m_3\ddot{z} + m\ddot{x} + W)r\end{array}\right]. \quad (29)$$

Substituting expressions (19 and 21) in dependence (29):

$$M = \left(\frac{I_1}{r} + m_3 r\right)\ddot{z} + \\ + \frac{I_1}{cr}(m_3 z^{IV} + m x^{IV}) + (m\ddot{x} + W)r. \quad (30)$$

To reduce dynamic loads in the jib crane during the joint movement of the mechanisms for derricking and load hoisting, the movement mode of the derricking mechanism will be optimised. Since the purpose of the study is to minimise the driving moment of the derricking mechanism, therefore, its RMS value is taken as a criterion for optimising the movement mode of the jig system (M_{RMS}) at start:

$$M_{RMS} = \left[\frac{1}{t_1}\int_0^{t_1} M^2 dt\right]^{1/2} \to min, \quad (31)$$

where t – time; t_1 – duration of starting the derricking mechanism.

The selected optimisation criterion reflects the effect of loads on the drive elements and structures of the boom system, so it must be minimised. During the movement of the derricking mechanism on the start-up section with a steady load hoisting, it is necessary to provide boundary conditions that eliminate oscillations in the load on the flexible suspension when switching to a steady mode of movement of both mechanisms:

$$\left[\begin{array}{l} t = 0:\ x = z_0, \dot{x} = 0,\ z = z_0,\ \dot{z} = 0,\ \varphi = z_0/r,\ \dot{\varphi} = 0; \\ t = t_1:\ x = z_0 + \frac{V_y t_1}{2},\ \dot{x} = V_y, z = z_1,\ \dot{z} = V_y,\ \varphi = z_1/r, \dot{\varphi} = V_y/r. \end{array}\right. \quad (32)$$

The boundary conditions (32) are presented as dependences of the horizontal coordinate of the centre of mass of the load and its time derivatives up to and including the fifth order:

$$\left[\begin{array}{l} t = 0:\ x = z_0, \dot{x} = 0,\ \ddot{x} = 0,\ \dddot{x} = 0,\ x^{IV} = -\frac{W\left(g + \frac{V^2}{l_0}\right)}{m_3 l_0};\ x^V = 3\frac{W \cdot V\left(g + \frac{2V^2}{l_0}\right)}{m_3 l_0^2}; \\ t = t_1:\ x = z_1 = z_0 + \frac{V_y t_1}{2},\ \dot{x} = V_y, \ddot{x} = 0,\ \dddot{x} = 0,\ x^{IV} = -\frac{W}{m_3}\cdot\frac{g + \frac{V^2}{(l_0 + Vt_1)}}{l_0 + Vt_1}, \\ x^V = 3\frac{W \cdot V}{m_3}\cdot\frac{g + 2V^2/(l_0 + Vt_1)}{(l_0 + Vt_1)^2}. \end{array}\right. \quad (33)$$

The proposed optimisation problem (31), (33), considering the expression of the driving moment (30) for the dependences of the transfer function (17) and its time derivatives (22),..., (25), cannot be solved by analytical methods. Therefore, an approximate solution to this optimisation problem is used. The essence of the approximate method for solving problems (31), (33) is reduced to the problem of a class of multiparametric functions that satisfy the boundary conditions (33) and provide a minimum of the integral function (31). The class of multiparametric functions on which the solution of the optimisation problem is located is defined as the solution of the following boundary value problem:

$$\begin{cases} L(x) = 0; \\ \begin{cases} t = 0:\ x = z_0, \dot{x} = 0,\ \ddot{x} = 0,\ \dddot{x} = 0,\ x^{IV} = -\dfrac{W(g + V^2/l_0)}{m_3 l_0};\ x^{V} = 3\dfrac{W \cdot V(g + 2V^2/l_0)}{m_3 l_0^2}; \\ t = \dfrac{t_1}{2}: x = x_{t_1/2}, \dot{x} = \dot{x}_{t_1/2}, \\ t = t_1:\ x = z_0 + \dfrac{V_y t_1}{2},\ \dot{x} = V_y, \ddot{x} = 0,\ \dddot{x} = 0,\ x^{IV} = -\dfrac{W}{m_3} \cdot \dfrac{g + V^2/(l_0 + Vt_1)}{l_0 + Vt_1}, \\ x^{V} = 3\dfrac{W \cdot V}{m_3} \cdot \dfrac{[g + 2V^2/(l_0 + Vt_1)]}{(l_0 + Vt_1)^2}. \end{cases} \end{cases} \tag{34}$$

where $L(x)$ – an operator that depends on the function $x(t)$ and its time derivatives.

The solution of the boundary value problem (34) has two unknown parameters $x_{t_1/2}$ and $\dot{x}_{t_1/2}$. Operator $L(x)$ for the set optimisation problem is taken as a fourteenth-order differential equation, i.e.: $L(x)=x^{XIV}(t)$. As a result of solving the boundary value problem (34), the expression of the functional (31) is formed:

$$C_r = C_r(x_{t_1/2}, \dot{x}_{t_1/2}, t_1), \tag{35}$$

Which is a nonlinear function of unknown arguments $x_{t_1/2}, \dot{x}_{t_1/2}$ and t_1. To find the following values $x_{t_1/2}$ and $\dot{x}_{t_1/2}$ in which the functional (31) acquires a minimum value, a ME-D-PSO was used [27]. Its use does not require continuity and differentiation of criterion (35) and does not impose strict requirements on the optimisation problem. After constructing the functional dependency (35), it is possible to apply the ME-D-PSO method and find the optimal values of unknown parameters $x_{t_1/2}$ and $\dot{x}_{t_1/2}$. When solving the optimisation problem, the following parameters of the method are used: the rate of reduction of the criterion AR = 0.005; the number of particles (swarm population) is 50; the number of iterations is 40. The given parameters of the method allow effectively using computational resources when solving the optimisation problem of determining the desired driving mode of the drive mechanism.

For calculations, the jig system of a tower crane with a jig saddle with the following parameters was used: m=5000 kg; m_3=300 kg; I_1=50,16 kg·m²; r=0,15 m; z_0=10,0 m; l_0=16,0 m; C=7,24·10⁵ N·m; g=9,81 m/s; W=5500 N; V=0,85 m/s; t_1=5,0 s.

RESULTS AND DISCUSSION

As a result of solving the optimisation problem, graphical dependencies of kinematic parameters (Figs. 2 and 3), power (Fig. 4), and energy characteristics (Figs. 8 and 9) of the derricking mechanism during the start-up process are constructed.

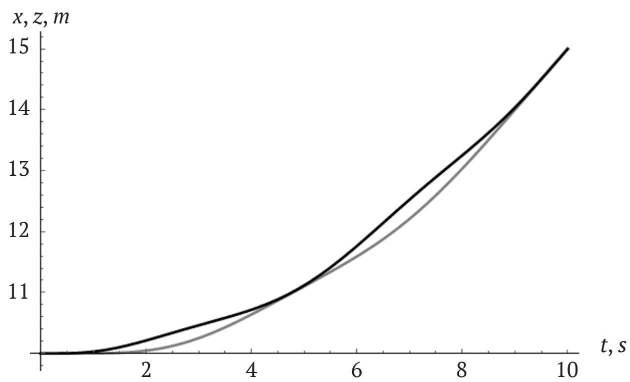

Figure 2. Graphs of horizontal movement of trolley and load

In Figures 2-4, the dark curve shows the characteristics of the trolley, and the light curve shows the characteristics of the load. Fig. 2 shows that at the beginning and end of the start, the movements of the trolley and load coincide. At the same time, during the start-up process, there are deviations in the movements of the trolley and load, which indicates the presence of oscillations of the load on the flexible suspension relative to the trolley. The change in the movement of the load is smoother compared to the movement of the trolley.

Figure 2 shows graphical dependences of changes in the speed of the trolley and load during the start-up process of the derricking mechanism, which indicate that oscillations in the speed of both the trolley and the load are observed during movement. These oscillations are caused by the swinging of the load on the flexible suspension and the elastic properties of the traction body of the trolley.

At the end of the start-up process, the speeds of the trolley and load coincide, and the movements of the trolley and load coincide at this point in time (Fig. 2). This indicates that after the trolley movement mechanism is released, there will be no oscillations in the load on the flexible suspension.

Figure 4 shows that during the start-up of the mechanism, changes in the trolley movement of the acceleration of the trolley and load have an oscillatory character with a significant amplitude of oscillations.

With an average trolley and load acceleration of 0.11 m/s² the maximum acceleration value of the trolley is 0.27 m/s², and the trolley – 0.21 m/s². At the beginning and end of the start-up process, the acceleration of the trolley and load takes zero values, which contributes to the smooth movement of the trolley and load in the area of stable movement of the derricking mechanism.

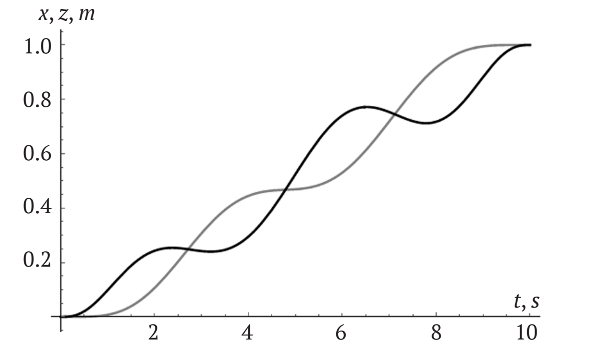

Figure 3. Graphs of horizontal speeds of trolley and load

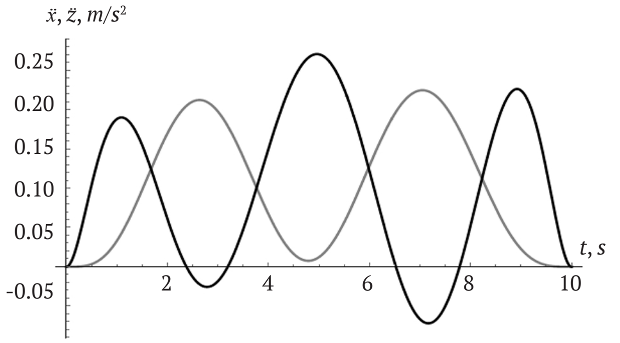

Figure 4. Graphs of horizontal accelerations of trolley and load

From a flat phase trajectory of load oscillations relative to the trolley (Fig. 5) it can be seen that during the start-up of the mechanism, changes in the trolley movement of oscillations fade out during two periods of oscillations. At the same time, the maximum deviation of the trolley and load movements is 0.32 m, and the maximum deviation of the trolley and load speeds reaches 0.21 m/s.

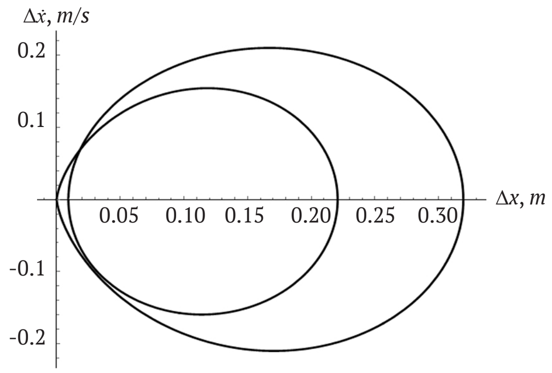

Figure 5. Phase trajectory of load oscillations relative to the trolley

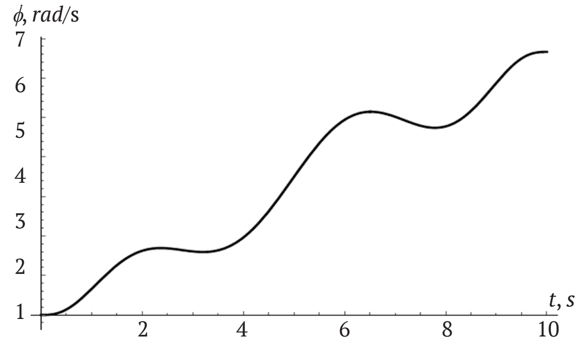

Figure 6. Graph of the angular velocity of the trolley drive drum

Angular velocity of the trolley drive drum (Fig. 6) changes from zero to a steady-state value if there are oscillations during the start-up process. The presence of oscillations of the drive drum is caused by oscillations of the trolley and load on the flexible suspension.

Figure 7 shows that the acceleration of the drive drum also has an oscillatory character. At the same time, in the middle of the start-up, it takes the maximum value, which is 1.8 rad/s², and at the end of the start-up reaches zero. This contributes to the normal operation of the drive drum during the steady movement of the derricking mechanism.

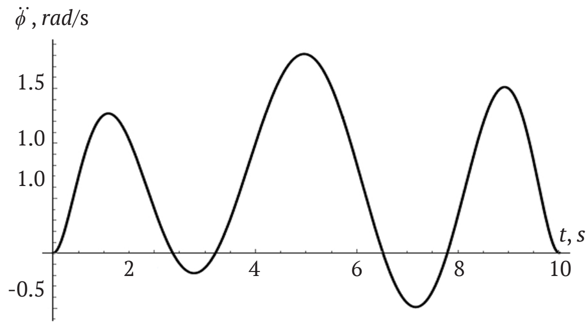

Figure 7. Graph of angular acceleration of the trolley drive drum

Figure 8 shows that at the beginning of start-up, the driving moment of the drive mechanism for derricking from the moment of static resistance forces to the movement of the trolley changes smoothly to a stable value, where moment oscillations are observed caused by the oscillations of the load on the flexible suspension. At the end of the start-up process, the driving moment gradually decreases to the value of the moment of static resistance forces. In the area of steady-state movement, in the absence of oscillations of the trolley and the load on the flexible suspension, the driving torque of the drive takes a steady-state value corresponding to the moment of static resistance forces to the movement of the trolley. Drive power of the derricking mechanism (Fig. 9) during the start-up process, it changes from zero to a steady-state value in the presence of oscillations. These oscillations in the nature of the change are close to oscillations in the angular velocity of the drive drum of the derricking mechanism (Fig. 6).

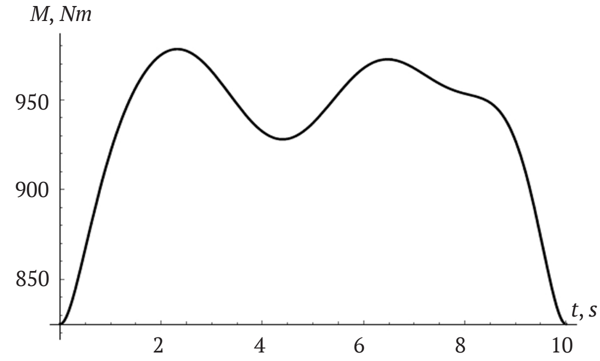

Figure 8. Graph of the driving torque of the derricking mechanism drive

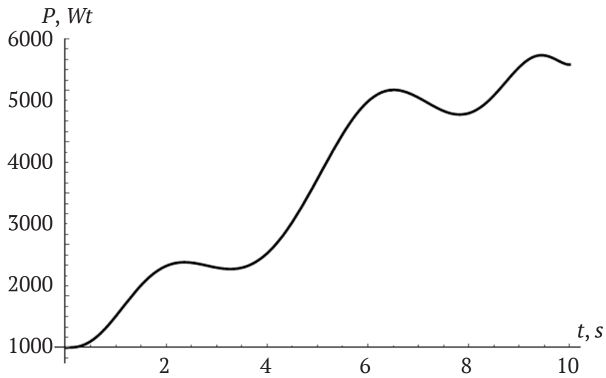

Figure 9. Power graph for the derricking actuator

Comparing the results obtained with well-known studies, it is worth noting a significant variety of methods for solving problems similar to the one that was solved in this study. For example, in [5], the apparatus of artificial neural networks was used. As a result, it was possible to almost completely eliminate the pendulum oscillations of the load on the flexible suspension. However, such control actions of the system in a strict sense are not optimal. In [11], the authors obtained an optimal method for controlling the movement of the crane movement mechanism in terms of speed. At the same time, it was assumed that the length of the flexible suspension of the load is constant, which distinguishes [11] from this study. In [16], the problem of eliminating the pendulum oscillations of the load is set quite broadly – five degrees of freedom of the system are considered, two of which correspond to the pendulum oscillations of the load. The results of the above study also allowed the authors to obtain a control corresponding to the absence of load oscillations in the tangential and radial directions at the end of acceleration. However, such control is also not optimal. The type of control is also different – it is a function of the phase coordinates of the system (the control obtained in this study is a function of time). In [17], the optimisation problem is presented in a variational formulation, similar to this study. The range of issues considered is quite wide, which allowed the author to improve the dynamic and energy performance of the crane and minimise the pendulum oscillations of the load. This makes the above study similar to this one. All calculations are given for a crane whose reach is changed by hoisting/lowering the beam, although the method is quite general and therefore, can obviously be used for other types of tower cranes.

CONCLUSIONS

In the conducted research, the problem of minimising the driving torque of the drive mechanism for derricking during a steady load hoisting is set and solved by selecting the driving mode of the drive.

A mathematical model of the dynamics of the movement of the derricking mechanism of a tower crane with a steady movement of the load hoisting mechanism is constructed, which considers the main movement of the drive mechanisms and oscillations of links with elastic properties. The model is a system of second-order nonlinear differential equations that is reduced to a single sixth-order differential equation.

To optimise the starting mode of the derricking mechanism during the steady-state movement of the hoisting mechanism, an integral dynamic criterion was reasonably chosen, which is presented in the form of the RMS value of the driving torque of the drive during the start-up process. To solve the nonlinear optimisation problem of selecting the mode of movement of the drive of the derricking mechanism during steady-state movement of the load hoisting mechanism, a modified metaheuristic method of a swarm of particles is used.

The results of optimisation of the driving mechanism mode showed that minimising the value of the driving torque led to a reduction in dynamic loads acting on the elements of crane mechanisms, and the elimination of oscillations of the trolley and load during the transition from the start-up process to the steady-state movement of the derricking mechanism. At the same time, oscillations of the trolley and load on a flexible suspension are observed at the start-up site.

Prospects for further study in this area are to consider other factors of the process of joint movement of mechanisms (for example, wind effects on load and trolley, the action of centrifugal force when the crane slews, etc.). The reasonable choice of a multiparameter function, on which an approximate solution of the problem is sought, also remains an open question. In addition, in subsequent studies, a transition will be made from a single (similar to (31)) to complex optimisation criteria that could reflect several undesirable indicators, which would allow the authors to more fully consider the requirements for the mode of movement of mechanisms.

REFERENCES

[1] Abdel-Rahman, E.M., Nayfeh, A.H., & Masoud, Z.N. (2003). Dynamics and control of cranes: A review. *Journal of Vibration and Control*, 9.7, 863-908.

[2] Romasevych, Y., Shymko, L., Ohiienko, M., Duczmal, W., Potwora, W., Titova, L., & Rogovskii, I. (2020). *Agrotronics and optimal control of cranes and hoisting machines*. Opole: The Academy of Management and Administration in Opole.

[3] Ramli, L., Mohamed, Z., Abdullahi, A.M., Jaafar, H.I., & Lazim, I.M. (2017). Control strategies for crane systems: A comprehensive review. *Mechanical Systems and Signal Processing*, 95, 1-23. doi: 10.1016/j.ymssp.2017.03.015.

[4] Singer, N., Singhose, W., & Kriikku, E. (1997). An input shaping controller enabling cranes to move without sway. In *American nuclear society topical meeting on robotics and remote systems* (pp. 12-14). Augusta: Paine College. doi: 10.2172/491559.

[5] Fasih, S.M., Mohamed, Z., Husain, A.R., Ramli, L., Abdullahi, A.M., Anjum, W. (2020). Payload swing control of a tower crane using a neural network-based input shaper. *Measurement & Control*, 53(7-8), 1171-1182. doi: 10.1177%2F0020294020920895.

[6] Qian, Y., Hu, D., Chen, Y., Fang, Y., & Hu, Y. (2022). Adaptive neural network-based tracking control of underactuated offshore ship-to-ship crane systems subject to unknown wave motions disturbances. *IEEE Transactions on Systems, Man, and Cybernetics: Systems*, 52(6), 3626-3637. doi: 10.1109/TSMC.2021.3071546.

[7] Jordan, M.I. (2019). Artificial intelligence – the revolution hasn't happened yet. *Harvard Data Science Review,* 1(1), 1-8. doi: 10.1162/99608f92.f06c6e61.

[8] Stepanov, M.A., & Ilukhin, P.A. (2018). Features and perspectives of automatized construction crane-manipulators. *IOP Conference Series: Materials Science and Engineering*, 317(1), article number 012039. doi: 10.1088/1757-899X/317/1/012039.

[9] Liu, F., Yang, J., Wang, J., & Liu, C. (2021). Swing characteristics and vibration feature of tower cranes under compound working condition. *Shock and Vibration*, 2021, article number 8997396. doi: 10.1155/2021/8997396.

[10] Kang, S.C., & Miranda, E. (2004). Physics based model for simulating the dynamics of tower cranes. In *Proceeding of Xth international conference on computing in civil and building engineering* (pp. 1-8). Weimar: Bauhaus-Universität Weimar. doi: 10.25643/bauhaus-universitaet.240.

[11] Kuo, T., Chiang, Y.-C., Cheng, S.-Y., & Jessy Kang, S.-C. (2015). Oscillation reduction method for fast crane operation. *Modular and Offsite Construction Summit Proceedings*, 1, 388-395. doi: 10.29173/mocs159.

[12] Shih-Chung, K., & Miranda, E. (2009). Numerical methods to simulate and visualize detailed crane activities. *Computer-Aided Civil and Infrastructure Engineering*, 24.3, 169-185. doi: 10.1111/j.1467-8667.2008.00579.x.

[13] Olt, J., Bulgakov, V., Beloev, H., Nadykto, V., Ihnatiev, Ye., Dubrovina, O., Arak, M., Bondar, M., & Kutsenko, A. (2022). A mathematical model of the rear-trailed top harvester and an evaluation of its motion stability. *Agronomy Research*, 20(2), 371-388 doi: 10.15159/ar.21.162.

[14] Mykhailov, Y., Zadosna, N., Postnikova, M., Pedchenko, G., Khmelovskyi, V., Bondar, M., Ionichev, A., Kozdęba, M., & Tomaszewska-Górecka, W. (2021). Energy assessment of the pneumatic sieve separator for agricultural crops. *Agricultural Engineering*, 25, 147-156. doi: 10.2478/agriceng-2021-0012.

[15] Čápková, R., & Kozáková, A. (2019). Experimental modelling and control of a tower crane. In *22nd international conference on process control* (pp. 97-101). Strbske Pleso: Hotel Toliar. doi: 10.1109/PC.2019.8815327.

[16] Ambrosino, M., Berneman, M., Carbone, G., Crépin, R., Dawans, A., & Garone, E. (2021). Modelling and control of 5-dof boom crane. *International Symposium on Automation and Robotics in Construction*, 2, 1-8. doi: 10.48550/arXiv.2103.02454.

[17] Chwastek, S. (2020). Optimization of crane mechanisms to reduce vibration. *Automation in Construction*, 119, article number 103335. doi: 10.1016/j.autcon.2020.103335.

[18] Romasevych, Yu., Loveikin, V., Ohiienko, M., Shymko, L., & Łukawiecki, K. (2021). *Innovation management in agriculture. Agrotronics and design of optimal controllers based on new modifications of particle swarm optimization*. Opole: Publishing House WSZiA

[19] Chopard, B., & Tomassini, M. (2018). Particle swarm optimization. In *An introduction to metaheuristics for optimization* (pp. 97-102). Cham: Springer. doi: 10.1007/978-3-319-93073-2_6.

[20] Piotrowski, A.P., Napiorkowski, J.J., & Piotrowska, A.E. (2020). Population size in particle swarm optimization. *Swarm and Evolutionary Computation*, 58, article number 100718. doi: 10.1016/j.swevo.2020.100718.

[21] Kennedy, J., & Eberhart, R. (1995). Particle swarm optimization. In *Proceedings of International Conference on Neural Networks*, 4, 1942-1948. doi: 10.1109/ICNN.1995.488968.

[22] Marini, F., & Walczak, B. (2015). Particle swarm optimization (PSO). A tutorial. *Chemometrics and Intelligent Laboratory Systems*, 149(B), 153-165. doi: 10.1016/j.chemolab.2015.08.020.

[23] Houssein, E.H., Gad, A.G., Hussain, K., & Suganthan, P.N. (2021). Major advances in particle swarm optimization: Theory, analysis, and application. *Swarm and Evolutionary Computation*, 63, article number 100868. doi: 10.1016/j.swevo.2021.100868.

[24] Shami, T.M. (2022). Particle swarm optimization: A comprehensive survey. *IEEE Access*, 10, 10031-10061. doi: 10.1109/ACCESS.2022.3142859.
[25] Isiet, M., & Gadala, M. (2020). Sensitivity analysis of control parameters in particle swarm optimization. *Journal of Computational Science*, 41, article number 101086. doi: 10.1016/j.jocs.2020.101086.
[26] Loveikin, V., Romasevich, Y., Shymko, L., Loveikin, Y., & Pochka, K. (2022). The dynamic analysis of the joint trolley movement and hoisting mechanism in the tower crane. *Strength of Materials and Theory of Structures*, 108, 267-282.
[27] Romasevych, Yu., Loveikin, V., & Makarets, V. (2020). Optimal constrained tuning of pi-controllers via a new pso-based technique. *International Journal of Swarm Intelligence Research*, 11(4), 87-105. doi: 10.4018/IJSIR.2020100104.

Вячеслав Сергійович Ловейкін[1], Юрій Олександрович Ромасевич[1], Любов Сергіївна Шимко[1], Юрій Вячеславович Ловейкін[2]

[1]Національний університет біоресурсів і природокористування України
03041, вул. Героїв Оборони, 15, м. Київ, Україна

[2]Київський національний університет імені Тараса Шевченка
01033, вул. Володимирська, 60, Київ, Україна

Мінімізація рушійного моменту приводу механізму зміни вильоту баштового крана при усталеному підйомі вантажу

Анотація. Ефективне використання баштового крана досить часто вимагає суміщення різних операцій, наприклад, підйому вантажу та зміни вильоту. У випадку коли вантаж піднімається при усталеній швидкості виникає задача оптимального керування механізмом переміщення візка, яка виходить за рамки інженерних розрахунків і представляє собою науково-прикладну задачу. Її актуальність пов’язана із покращенням керованості кранових механізмів, підвищення продуктивності та надійності роботи крана, покращенні енергоефективності його приводних механізмів. Вказані показники пов’язані з вибором критерію оптимізації. Отже, метою статті є оптимізація режиму пуску механізму зміни вильоту за критерієм середньоквадратичного значення рушійного моменту при усталеному підйомі вантажу. Для досягнення цієї мети були використані методи: динаміки машин і механізмів, математичного моделювання, інтегрального і диференціального числення, модифікований метод рою часточок ME-D-PSO. За крайові умови руху обрано параметри, які усувають коливання вантажу на гнучкому підвісі при виході механізму зміни вильоту на усталений режим руху. За результатами оптимізації сумісного руху механізмів зміни вильоту та підйому вантажу побудовані графічні залежності кінематичних, динамічних та енергетичних характеристик перехідного процесу пуску і проведено їхній аналіз. З отриманих залежностей виявлено умови усунення коливань вантажу на гнучкому підвісі при усталеному русі та зменшення динамічних навантажень та енергетичних витрат в процесі пуску механізму зміни вильоту. Для реалізації оптимального режиму пуску механізму зміни вильоту при усталеному підйомі вантажу рекомендовано використовувати оптимальне керування приводними механізмами. Отримані результати доцільно застосовувати для розробки нових і модернізації існуючих систем керування рухом механізмами баштових кранів

Ключові слова: оптимальне керування, критерій оптимізації, коливання вантажу, суміщення операцій

Machinery & Energetics
Vol. 13, No. 3. 2022

Journal homepage:
https://technicalscience.com.ua/en

UDC 681.5.013:664
DOI: 10.31548/machenergy.13(3).2022.53-61

Nataliia Lutska[1*], Lidiia Vlasenko[2], Anatoliy Ladanyuk[1], Nataliia Zaiets[3], Igor Korobiichuk[4]

[1]National University of Food Technologies
01601, 68 Volodymyrska Str., Kyiv, Ukraine

[2]State University of Trade and Economics
02156, 19 Kyoto Str., Kyiv, Ukraine

[3]National University of Life and Environmental Sciences of Ukraine
03041, 15 Heroiv Oborony Str., Kyiv, Ukraine

[4]Warsaw University of Technology
02-525, 1 Politechnika Sq., Warsaw, Poland

Ontological Support System of Managerial Decision-Making of Production Tasks for a Food Enterprise

Abstract. Resource and energy efficiency of industrial production, in particular, food production, is a defining requirement that will ensure its functioning without loss of quality and quantity of final products. This is achieved by observing the requirements for the operational parameters of the company's technological processes and their operational changes. Given the complexity of the functioning of the energy component of the world and Ukraine due to military operations and their consequences, the issue of quality/cost ratio has become more acute. Therefore, for large manufacturing enterprises, the development of systems for supporting management decision-making in accordance with the Industry 4.0 concept becomes relevant. This will contribute to improving the production and economic indicators of the enterprise through coordinated actions of all links of production activities by structuring and processing large amounts of heterogeneous information. The purpose of the study is to develop a decision support system for the task of choosing the structure of an automated control system based on an ontological knowledge base. The developed application ontology uses descriptive logic and is interpreted as part of a digital production double implemented by a single ontological knowledge base and ontological repository. Considering existing international standards, the OWL2 language was chosen for the implementation of the ontological knowledge base. The ontology system architecture contains an ontology server, a Node-Red application, and a user form. A project decision support system that issues recommendations based on requests for the structure of the control system for a technological facility with uncertainties, considering the requirements and restrictions set for each technological process of a food enterprise, reduces the time to choose the appropriate structures, schemes, and methods. Thus, the designer receives the necessary information, supported by knowledge from the subject area, for the synthesis of an effective automated control system. It is also assumed that the ontological system will be expanded by connecting new created applied ontologies that implement related tasks of an industrial enterprise

Keywords: control system, technology object, robust controller, applied ontology, mathematical model, subject area, decision support system

Article's History: Received: 01.04.2022; Revised: 04.07.022; Accepted: 11.08.2022

INTRODUCTION

Industry 4.0 technologies provide for the use of the latest methods and approaches to support decision-making by production operations of an industrial enterprise aimed at improving energy and resource efficiency, and production quality. Such systems must use heterogeneous production data and knowledge from different domains. In addition, such a system should be part of the enterprise's Digital Twin or easily integrated with it [1; 2]. Therefore, it is ontological models that are an indispensable single tool that will provide: integration of a variety of large amounts of information (data and knowledge) of the entire industrial

Suggested Citation:
Lutska, N., Vlasenko, L., Ladanyuk, A., Zaiets, N., & Korobiichuk, I. (2022). Ontological support system of managerial decision-making of production tasks for a food enterprise. *Machinery & Energetics,* 13(3), 53-61.

*Corresponding author

enterprise; unification of the industrial thesaurus; use of a single enterprise model (Digital Twin), which essentially describes "everything" (all aspects of the behaviour of the system and its parts) from different positions. The latter is intended for use for various purposes, including for the tasks of managing the production operations of an industrial enterprise.

As an example, the problem of designing a control system for a technological object in the food industry, which periodically occurs due to the uncertainties under which the object operates, is considered. Therefore, a significant proportion of technological processes require the use of robust synthesis methods, in which the structure and/or parameters of the regulator are calculated by H2/H∞ criterion. The choice of synthesis method is influenced by a number of objective and subjective factors. In particular, the requirements for the control system that are formulated by the designer and clarified during the synthesis process. It also affects the mathematical model of the control object and its accuracy, and the features of the technological process itself.

At the first stage, it is necessary to choose the structure of the system and the method of synthesising its parameters. Usually, typical structures of automatic systems are considered, taking into account complexity, uncertainty, multi-connectivity, the presence of delays, etc. In this regard, the task of automated selection of the system structure and methods for synthesising its parameters is urgent. This task is vague, so the paper suggests using data and knowledge of the subject area, which is established based on an ontological decision support system.

To solve problems of varying complexity in the context of operating and working with heterogeneous information, the use of ontologies is becoming more and more relevant. The significant advantages of building ontological systems are not only working with heterogeneous information, but also establishing relationships between different data that provide new accurate results. Nowadays, ontologies are well established in search engines, such as, for example, Wikipedia [3], Wikidata [4]. Moreover, Wikidata is based on a taxonomy and uses various principles and methods of classification and nomenclature of complex hierarchical systems that include manufacturing enterprises. Ontological systems have found the greatest practical and successful application in the medical field [5; 6] and genetic engineering [7; 8]. The successful results of creating ontological systems of these areas prompted similar work in other areas. However, when working on creating appropriate systems, there are a number of obstacles, in particular, the lack of standardised and complete conceptual libraries in various fields. Specialists in various fields [9], including production, are actively working on this. Today Wikidata is, if not a benchmark, then an extremely illustrative example of the successful implementation of an ontological search engine. In addition to Wikidata, there are other ontological knowledge bases, such as DBpedia, Freebase, OpenCyc, and YAGO [10].

LITERATURE REVIEW

Information is the main component of the Industry 4.0 concept, which provides information and automated components of the production operations management system of an industrial enterprise. At the same time, a well-known problem is an overabundance of information. Well-known search engines do not provide a sufficient level of search for specific complete data, and especially enterprise knowledge. This was the impetus for the use of Semantic Web technologies in industrial databases and knowledge of information search engines, including logical integration into the industrial Internet of Things (IIoT). It is the ontologies focused on the organisation and implementation of IIoT that meet new challenges in industry [11] and are currently relevant. In addition, ontological knowledge bases can be used for industrial design tasks in distributed systems and on the Web. In this case, the ontology is used to form a knowledge base containing the main concept of the subject area, which is a mandatory part of the intelligent decision support system. The ontological concept is implemented by various models of knowledge representation, for example, in the form of frame or semantic networks. Considering the development of international standards in the field of ontological engineering, a subset of descriptive logic and dialects of the OWL2 language [12; 13] become part of the de facto standard when building and working with the subject area. Built-in ontology description tools provide storage, validation, editing, transmission, and integration into a single enterprise ontology system.

The development of a unified information model of production based on ontologies, as a rule, involves the choice of a hierarchical structure and a top-level ontology [14]. Depending on the complexity of the problem being solved, the goals set, and the degree of detail, the ontology structure, in particular, the number of levels, is selected during development. Traditionally, a three-level or four-level ontology is used. The three-level system consists of Top-level Ontology, Domain Ontology, and Application Ontology; the four-level system contains Top-level Ontology, Core Ontology, Domain Ontology, and Application Ontology. At the same time, there is a need for harmonisation in systems that meet different needs at different hierarchical levels by using several models and connecting several existing ontologies [15].

When working with ontologies, it is essential to be able to use and connect already developed ontologies from a set of existing and often open ontologies. In particular, a number of ontologies have been developed for the top level, which differ mainly in their structure. Most commonly used are Basic Formal Ontology (BFO), Descriptive Ontology for Linguistic and Cognitive Engineering (DOLCHE), Suggested Upper Merged Ontology (SUMO) [16], etc.

Nowadays, the most popular top-level ontology is BFO [17], which has also found its place in the international standard ISO/IEC. BFO is a top-level ontology consisting of thirty-six classes. It is designed to support the integration, search, and analysis of information in all areas of scientific research and is undergoing a standardisation stage [18]. Its advantage is that it does not contain terms specific to individual material areas, but includes general conceptual forms.

At the next level of ontology – the domain level, the conceptual framework is conceptualised. With the advent of the semantic web, the field of domain ontology engineering is actively developing, and many ontologies appear for various subject areas [19]. A separate area is the development of environments for constructing and evaluating domain ontology [20].

Applied ontology clarifies the domain ontology, reveals its concepts and classes, describes concepts, and contains the most specific information in the form of a combination of concepts from the subject area ontologies and domain ontologies. As a rule, it contains extensions and clarifications for the methods and tasks under consideration. There are a large number of successful application solutions based on constructed application ontologies. The construction of ontologies has acquired a special meaning in connection with the development of Industry 4.0 concepts and the introduction of cyber-physical systems [21].

Methods of synthesis of control systems, including robust ones, are thoroughly considered in [22; 23], and the results of successful implementation of the latest control systems for technological objects of the food industry are investigated in [24-26].

The purpose of the study is to develop an ontological knowledge base for the decision support system for choosing an automatic control system for a technological object with uncertainties for the food industry, which is based on the axioms of applied ontology and issues a number of recommendations on criteria, structures of the control system and methods for configuring their parameters in accordance with the selected requirements. Such an ontological system is part of the ontological model of production. For the first time, the paper uses an ontological subsystem for supporting management decision-making for the design of automated process control systems.

MATERIALS AND METHODS

Building hierarchical ontological knowledge bases, including for decision support subsystems, is a building block of Smart Manufacture, which considers the concept of Industry 4.0 and is relevant. The implementation of this system would significantly reduce the time for re-designing technological object management systems, reduce decision-making time, increase profits, and ensure the resource and energy efficiency of the enterprise, which is an extremely important problem today.

A three-level ontology was developed when solving this problem. At the top level, BFO is used, as it will be standardised in the near future. At the Domain Ontology level, the main concepts and attitudes for the developed management decision support system were defined. At the lower level – Application Ontology, concepts were disclosed in the form of corresponding classes and subclasses, instances, relationships between them, Data Property, Object Property, axioms and rules. Figure 1 shows a fragment of a three-level ontology for the developed system.

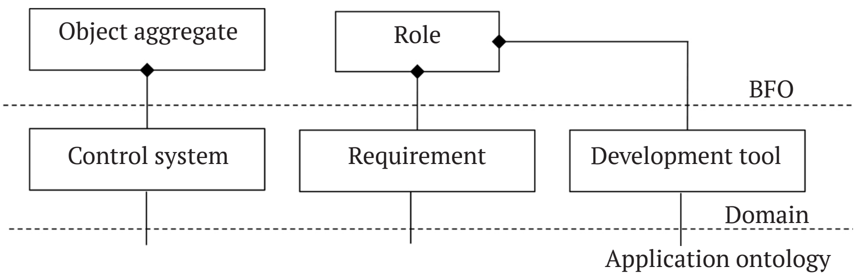

Figure 1. Domain ontology fragment used for Application ontology

Figure 2 presents the general structure of the ontological system for supporting managerial decision-making for production tasks of a food enterprise. Conventionally, the ontological system can be divided into four components. The Ontological manufacture model contains information about the selected structural hierarchy of a three-level ontology. Linking external ontologies displays a list of external ontologies that are connected to the ontology system. In particular, BFO describes fundamental categories [27]; QUDT – quantities, units of measurement, dimension vectors, and datatypes; OWL-Time – time intervals and time instants; Org – organisations, posts, roles. Semantic Design provides a division into levels and classes of ontology and the relationship between them. The Architecture part is used to describe the designed general structure of an ontological system and its implementation at the hardware and physical levels. This level has a wide range of opportunities and depends on the tasks being solved, the financial capabilities of the customer and the experience of the designer. A special feature of the architecture component is that it is not actually tied to a specific subject area and can be adapted for any ontological management decision support system. In this case, the developed system uses cloud technologies.

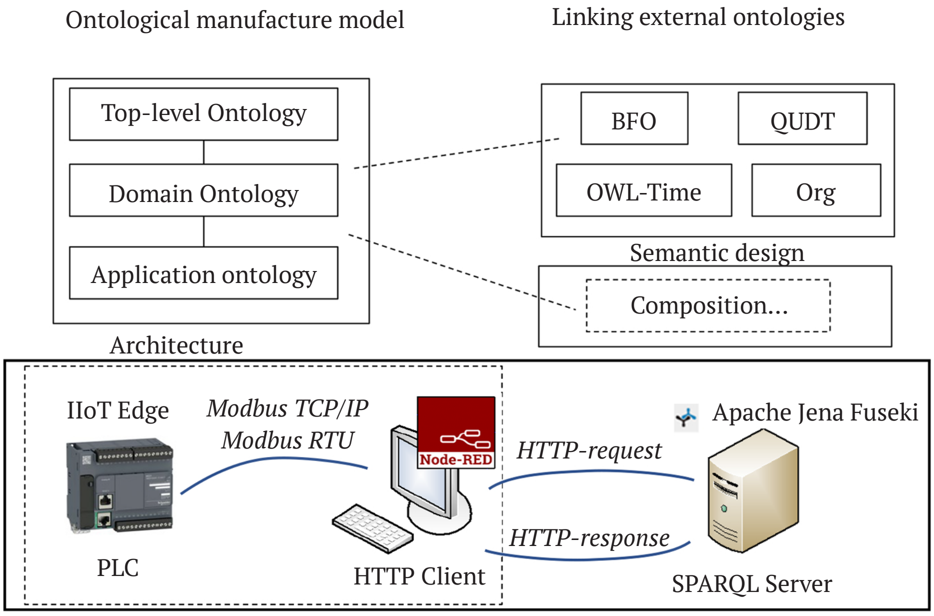

Figure 2. General structure of the ontological management decision support system

In the work, the effectiveness of the design solutions of the automated control system was evaluated based on the defined non-functional and functional requirements, considering the criteria of economic efficiency and the hierarchical relationship of the management level. Thus, the main attributes of the requirements of the automated control system include: requirements for the flexibility of the control system (flexibility), which determine the degree of flexibility of the system from the standpoint of the process operator; requirements for the quality of transients or frequency characteristics of the system (adjustmentAccuracy, adjustmentSpeed); requirements for the reliability of the system, which characterise the reliability of the developed system and depend on the probability of loss of stability of the system (levelFuncReability); general economic requirements for the control system, which determine the degree of total development costs (commonEconomic).

The problem area is also affected by the attributes of the process object and mathematical model. The first category includes: capacity (hasReceptivity), self-alignment (hasselfalignment), inertia (hasinertia), type of process variable (typeTechnVariable), and disturbance measurement (hasMeasurDisturb). To the second: the presence of a model and its type – linear, nonlinear, nonlinear with the possibility of linearisation (hasNonlin); the degree of uncertainty (hasuncertainy) and the type of its structure(structUncertainy); the presence of delay (hasDelay); multidimensional (hasMultidim). The peculiarity of the uncertainty of a technological object of the food industry is that this is explained as a set of states of the object during its functioning. The uncertainty of the mathematical model should consider the inaccuracy of the model, including changes in the process object and external environment during operation. Then, uncertainty describes the correctness of the forecast of the mathematical model at the time of control, and the degree of compliance with the actual object.

Thus, the structure of the applied ontology for automated selection of a control system for complex technological processes in the food industry is formed, which is shown in the UML class diagram notations in Figure 3. The ontology consists of three classes (Development_Requirement, Technological_Object, and Mathematical_Model) that contain instances with a number of attributes. They form the basis for the development of the management system. These same instances belong to the CS_Criteria, CS_Structure, and CS_Method classes, respectively, which, in turn, contain the necessary information used to synthesise the automatic control system. The division into these classes is based on the axioms of descriptive logic. Then the answer is the alternative solutions provided by the applied ontology – a set of criteria, methods, and structures of the control system. In the future, the designer synthesises the proposed control systems and calculates qualitative estimates of the forecast of each solution by testing the options proposed by the system on models. At the last stage, the proposed recommendations are sorted according to the selected estimates, from which the designer selects the final version of the system.

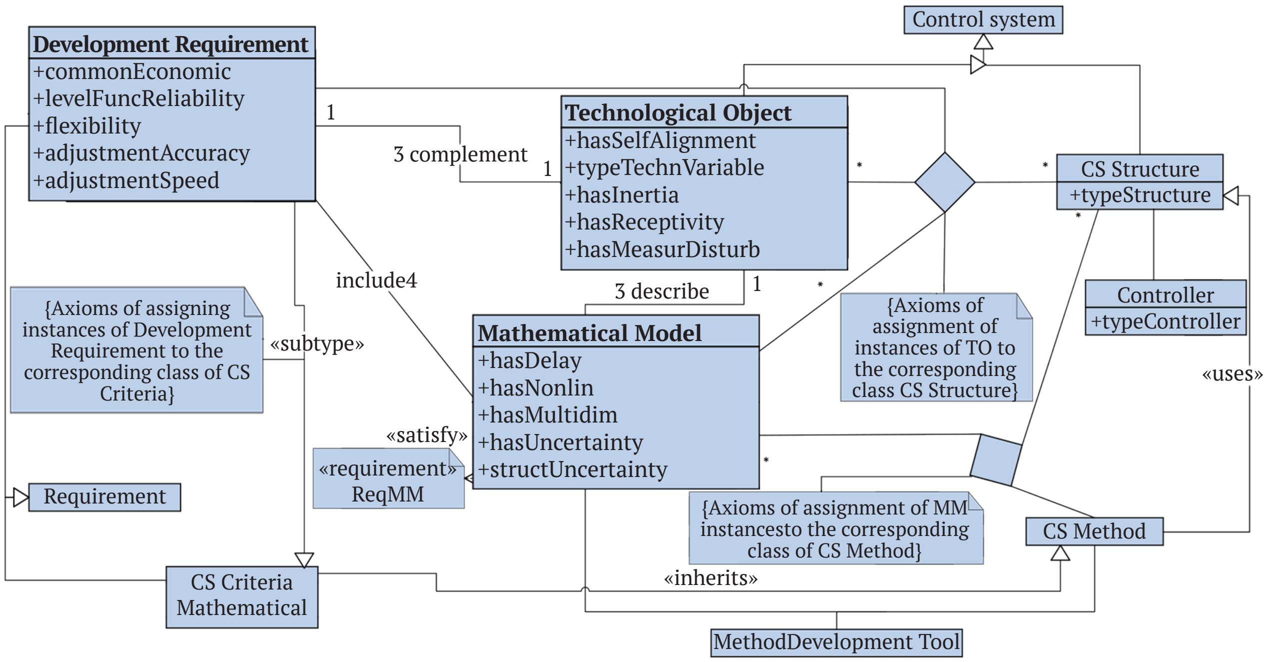

Figure 3. Structure of an applied ontology in UML notations

The Protege 5.5 editor was used to implement the application ontology, which supports descriptive logic in the OWL language. The ontology contains information in the form of knowledge about instances of the Development_Requirement, Technological_Object, and Mathematical_Model classes. Management system development entities are identified based on relationships between instances. Figure 4 shows a fragment of a VOWL graph that illustrates Class and Object Property. Instances of the Development_Requirement, Technological_Object, and Mathematical_Model classes contain data properties that are converted to the corresponding XSD data types. Some Data Property are ranked on a qualitative scale.

Axioms have been developed to assign instances of the Development_Requirement, Technological_Object, and Mathematical_Model classes to the corresponding CS_Criteria, CS_Structure, and CS_Method subclasses. The template for the corresponding axioms is as follows: if an instance of Technological_Object (has the appropriate attributes) and (is supplemented by an instance of Development_Requirement, which (has the appropriate attributes)) and (is described by an instance of Mathematical_Model, which (has the appropriate attributes)), then the instance Technological_Object belongs to the corresponding CS_Structure subclass.

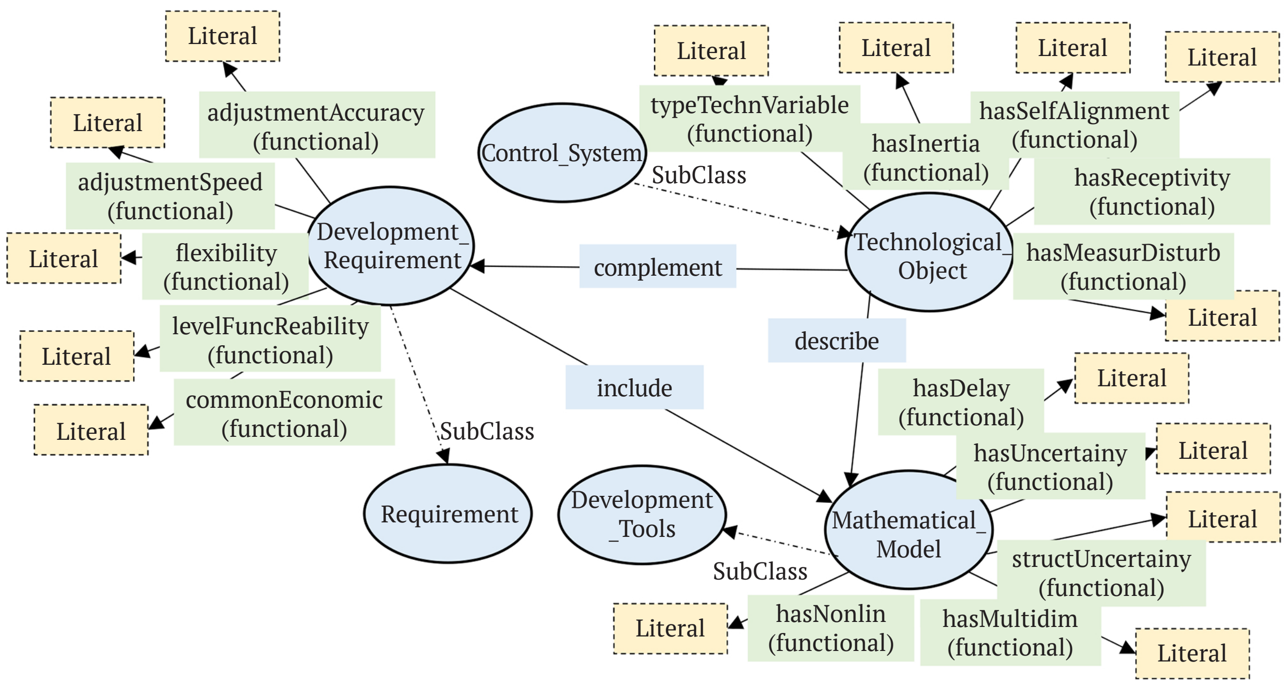

Figure 4. Fragment of the VOWL graph of the applied ontology

The constructed application ontology based on instances and attributes of the Development_Requirement, Technological_Object, and Mathematical_Model classes provides recommendations containing synthesis methods, criteria, and structures used to synthesise automated control systems for undefined food processing operations.

RESULTS AND DISCUSSION

Classical approaches to ontology verification are known in the literature, which contain the following estimates of criteria [28]: consistency, completeness, classification, brevity, and sensitivity. The test performed according to these criteria confirmed the reasonableness of the constructed ontology. The complexity and formality of the structure were also checked, observing three main levels: vocabulary level, taxonomy level, and non-taxonomic level [29]. The purpose of the assessment is to evaluate the internal maturity level of ontologies, which uses metrics to measure the complexity of an ontology at both the class and ontological levels using combinations of measurable characteristics. Considering industrial use, these metrics include:

– size of vocabulary (*SOV*) – total number of created classes *C* and properties in the ontology P:

$$SOV=|C|+|P|; \quad (1)$$

– edge node ratio (*ENR*) – connection density, which increases proportionally with increasing number of edges *E* between nodes (classes):

$$ENR=|E|/|C|; \quad (2)$$

– tree impurity (*TIP*) – used to determine how much the inheritance hierarchy of an ontology deviates from the tree:

$$TIP=|E|-|C|+1; \quad (3)$$

– entropy of ontology graph (*EOG*) – shows the complexity of the graph:

$$EOG = -\sum_{i=1}^{n} p(i)\log_2 p(i), \quad (4)$$

where *p*(*i*) represents the mass function of the probability that the concept has an i relation.

Then, the obtained metrics are usually compared with the "gold standard", which is considered an example [30]. The metric values are shown in Figure 5. *SOV* Domain ontology does not exceed 200 components, consisting of an impressive set of concepts, parameters, events, etc., grouped according to Industry 4.0 standards. Value of the edge node coefficient (*ENR*) is below normal, which means that this ontology is uncomplicated and well-grouped. *TIP* is a rational indicator of how well an ontology is organised through inheritance relationships. Total value *TIP* for each ontology, the average is higher, which means that this inheritance hierarchy deviated from the conventional tree form, i.e., it is quite complex. Indicator *EOG* is low, so ontologies have a relatively good structure (interpretation of small ones *EOG* indicates a less complex ontology in terms of relationship distribution).

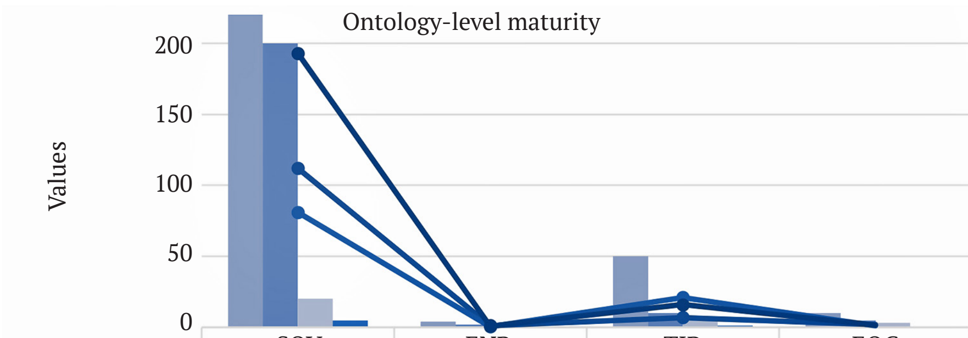

	SOV	ENR	TIP	EOG
Very high	500	4	50	10
Moderate	200	2	10	5
Low	20	1	5	3
Very low	5	0	1	0
Domain_Onto	112	1.2	7	2.1
Appl_Onto	81	0.5	21	1.3
Domain+Appl	193	0.8	16	1.7

Figure 5. Ontology-level maturity of ontology

The proposed applied ontology can be used for scientific and practical activities, analysis of instances of the knowledge base by classes or attributes. It was tested on a set of test instances of HermiT classes, and typical DL- and SPARQL- queries.

Node-RED is used as a programming tool for combining hardware devices, APIs, and online services, which ensures the implementation of the Industrial Internet of Things (IIoT) concept. Integration of information from Node-RED and the ontology server is implemented over the HTTP protocol and is used as a development and execution tool for Edge devices. An example of the architecture is shown in Figure 2. The SPARQL- query is generated in the sent URL, and the response is received in html format and contains data from the ontological server. The SPARQL-endpoint is accessible on top of HTTP, so the Fuseki server provides REST-style interaction with RDF ontology data. The developed software was tested to verify the operation of the entire proposed architecture, including the operation of the rezoner. As a result, many control system methods, structures, and criteria for system synthesis were obtained. This allowed making recommendations for a specific technological process and relevant requirements.

CONCLUSIONS

The paper proposes a system for supporting project decision-making, which recommends effective management system structures and methods for configuring their parameters. It is based on the axioms of applied ontology, which are developed in accordance with the subject areas of production automation, technological processes, and methods of synthesising automated systems under conditions of uncertainty.

Given that the proposed solutions are WEB-oriented, the decision support system presented in this paper is cost-effective, since it can be implemented in the cloud. This is confirmed by an increase in the efficiency of decisions made, an increase in the validity of management actions, an increase in the efficiency of the technological component, and a reduction in the risks of loss of stability of the automated process control system.

The level of correctness of the application of the proposed architecture and the corresponding algorithmic and software tools indicates the possibility of its use and implementation in the food industry.

This system meets international standards in the field of industrial production, in particular, the functions and tasks of designing a control system. It can also be interpreted as part of a digital representation of production models.

REFERENCES

[1] Digital twins for industrial applications white paper. (2018). Retrieved from https://hub.iiconsortium.org/portal/Whitepapers/5e95c68a34c8fe0012e7d91b.

[2] Qi, Q., & Tao, F. (2018). Digital twin and big data towards smart manufacturing and industry 4.0: 360 degree comparison. *Ieee Access*, 6, 3585-3593. doi: 10.1109/ACCESS.2018.2793265.

[3] Wikipedia. (n.d.). Retrieved from https://en.wikipedia.org/wiki/Main_Page.

[4] Wikidata. (n.d.). Retrieved from https://www.wikidata.org.

[5] Turki, H., Shafee, T., Taieb, M.A.H., Aouicha, M.B., Vrandečić, D., Das, D., & Hamdi, H. (2019). Wikidata: A large-scale collaborative ontological medical database. *Journal of Biomedical Informatics*, 99, article number 103292. doi: 10.1016/j.jbi.2019.103292.

[6] Pfundner, A., Schönberg, T., Horn, J., Boyce, R.D., & Samwald M. (2015). Utilizing the Wikidata system to improve the quality of medical content in Wikipedia in diverse languages: A pilot study. *Journal of Medical Internet Research*, 17(5), article number 4163. doi: 10.2196/jmir.4163.

[7] Putman, T.E., Lelong, S., Burgstaller-Muehlbacher, S., Waagmeester, A., Diesh C., Dunn, N., & Good, B.M. (2017). WikiGenomes: An open web application for community consumption and curation of gene annotation data in Wikidata. *Database*, 2017, 1-9. doi: 10.1093/database/bax025.

[8] Andra, W., Stupp, G., Sebastian, B.M., Good, B.M., Malachi, G., Griffith, O.L., & Su, A.I. (2020). Wikidata as a knowledge graph for the life sciences. In *eLife. Computational and Systems Biology*, 9, article number e52614. doi: 10.7554/eLife.52614.

[9] Shafee, T., Mietchen, D., & Su, A.I. (2017). Academics can help shape Wikipedia. *Science*, 357(6351), 557-558. doi: 10.1126/science.aao0462.

[10] Färber, M., Bartscherer, F., Menne, C., & Rettinger, A. (2018). Linked data quality of dbpedia, freebase, opencyc, wikidata, and yago. *Semantic Web*, 9(1), 77-129. doi: 10.3233/SW-170275.

[11] Ocker, F., Paredis, C., & Vogel-Heuser, B. (2019). Applying knowledge bases to make factories smarter. *Automatisierungstechnik*, 67(6), 504-517. doi: 10.1515/auto-2018-0138.

[12] Baader, F., Horrocks, I., Lutz, C., & Sattler, U. (2017). *Introduction to description logic*. Cambridge: Cambridge University Press.

[13] OWL 2. Web ontology language. Structural specification and functional-style syntax. W3C Recommendation. (2012). Retrieved from https://www.w3.org/TR/2012/REC-owl2-syntax-20121211/.

[14] Jindal, R., Seeja, K.R., & Jain, S. (2020). Construction of domain ontology utilizing formal concept analysis and social media analytics. *International Journal of Cognitive Computing in Engineering*, 1, 62-69. doi: 10.1016/j.ijcce.2020.11.003.

[15] Jiang, L., Shi, J., & Wang, C. (2022). Multi-ontology fusion and rule development to facilitate automated code compliance checking using BIM and rule-based reasoning. *Advanced Engineering Informatic*, 51, article number 101449. doi: 10.1016/j.aei.2021.101449.

[16] Schmidt, D., Trojahn, C., & Vieira, R. (2019). Matching BFO, DOLCE, GFO and SUMO: An evaluation of OAEI 2018 matching systems. *Ontology Matching Between Domain and Top-Level Ontologies*, 2519, article number 7.

[17] International Organization for Standardization. ISO/IEC 21838-2. Information technology – top-level ontologies. Part 2: Basic Formal Ontology. (2019). Retrieved from https://www.iso.org/standard/74572.html.

[18] Otte, J.N., Beverley, J., & Ruttenberg, A. (2022). BFO: Basic formal ontology. *Applied Ontology*, 17(1), 17-43. doi: 10.3233/AO-220262.

[19] Zouaq, A., & Nkambou, R. (2010). A survey of domain ontology engineering: Methods and tools. *Advances in Intelligent Tutoring Systems*, SCI 308, 103-119. doi: 10.1007/978-3-642-14363-2_6.

[20] Diamantini, C., Potena, D., & Storti, E. (2016). SemPI: A semantic framework for the collaborative construction and maintenance of a shared dictionary of performance indicators. *Future Generation Computer Systems*, 54, 352-365. doi: 10.1007/3-540-48005-6_6.

[21] Hildebrandt, C., Köcher, A., Küstner, C., López-Enríquez, C.M., Müller, A.W., Caesar, B., & Fay, A. (2020). Ontology building for cyber-physical systems: Application in the manufacturing domain. *IEEE Transactions on Automation Science and Engineering*, 17(3), 1266-1282. doi: 10.1109/TASE.2020.2991777.

[22] Bennett, S. (2017). *Robust Control: Systems, theory and analysis*. New York: Nova.

[23] Apkarian, P., & Noll, D. (2019). Optimization-based control design techniques and tools. In *Encyclopedia of Systems and Control* (pp. 1-9). London: Springer. doi:10.1007/978-1-4471-5102-9_144-2.

[24] Lutska, N.M. (2021). Robust optimal control systems for complex technological objects of food industry (Doctoral thesis, National University of Life and Environmental Sciences of Ukraine, Kyiv, Ukraine).

[25] Lutska, N.M., Zaiets, N.A., Vlasenko, L.O., Shtepa, V.M., & Savchuk, O.V. (2021). Forecasting the efficiency of the control system of the technological object on the basis of neural networks. *IEEE 20th international conference on modern electrical and energy systems (MEES)*, 2021, 1-6. doi: 10.1109/MEES52427.2021.9598540.

[26] Zaiets, N., Kondratenko, I., Lutskaya, N., Zhyltsov, A., & Usenko, S. (2020). Modeling and robust optimization of the technological mode of electrotechnological complexes with the renewable energy systems of heat. *E3S Web of Conferences*, 154(04006), 254-272. doi: 10.1051/e3sconf/202015404006.

[27] ISO/IEC 21838-2:2021. (2021). Information technology – top-level ontologies (TLO) – Part 2: Basic formal ontology (BFO). Retrieved from https://www.iso.org/standard/74572.html.

[28] Wilson, R., Goonetillake, J., Ginige, A., & Indika, W. (2021). Analysis of ontology quality dimensions, criteria and metrics. *International Conference on Computational Science and its Applications*, 2021, 320-337. doi: 10.1007/978-3-030-86970-0_23.

[29] Zakaria, N.H., Hassan, R., Othman, R.M., & Asmuni, H. (2015). Maturity-based analysis of lightweight ontology from the aspect of extensibility, reusability and evolutionary. *International Journal of Advances in Soft Computing and its Application*, 7, 55-74.

[30] Brank, J., Mladenic, D., & Grobelnik, M. (2006). Gold standard-based ontology evaluation using instance assignment. *Evaluation of Ontologies for the Web (EON 2006)*, 2006, 1-5.

Наталія Миколаївна Луцька[1], Лідія Олександрівна Власенко[2], Анатолій Петрович Ладанюк[1], Наталія Анатоліївна Заєць[3], Ігор Вацлавович Коробійчук[4]

[1]Національний університет харчових технологій
01601, вул. Володимирська, 68, м. Київ, Україна

[2]Державний торговельно-економічний університет
02156, вул. Кіото, 19, м. Київ, Україна

[3]Національний університет біоресурсів і природокористування України
03041, вул. Героїв Оборони, 15, м. Київ, Україна

[4]Варшавський технологічний університет
02-525, пл. Політехніки, 1, м. Варшава, Польща

Онтологічна система підтримки прийняття управлінських рішень виробничих задач харчового підприємства

Анотація. Ресурсо- та енергоефективність промислового виробництва, зокрема харчового, є визначальною вимогою, що забезпечить його функціонування без втрат якості та кількості кінцевої продукції. Це досягається дотриманням вимог до режимних параметрів технологічних процесів підприємства та оперативних їх змін. З огляду на ускладнення функціонування енергетичної складової Світу та України в зв'язку з військовими діями та їх наслідками, загострилося питання співвідношення якості та собівартості. Тому для великих виробничих підприємств актуальним стає розробка систем підстем підтримки прийняття управлінських рішень відповідно до концепції Ідустрії 4.0. Це сприятиме підвищенню виробничих та економічних показників підприємства за рахунок скоординованих дій всіх ланок виробничої діяльності шляхом структурування та обробки великих масивів різнорідної інформації. Метою статті є розробка системи підтримки прийняття рішень для задачі вибору структури автоматизованої системи керування на основі онтологічної бази знань. Розроблена прикладна онтологія використовує описову логіку та інтерпретується як частина цифрового двійника виробництва, що реалізується єдиною онтологічною базою знань та онтологічним сховищем. Враховуючи існуючі міжнародні стандарти для реалізація онтологічної бази знань обрана мова OWL2. Архітектура онтологічної системи містить онтологічний сервер, Node-Red-застосунок та форму користувача. Система підтримки прийняття проєктних рішень, яка видає рекомендації на основі запитів щодо структури системи керування для технологічного об'єкта з невизначеностями, з урахуванням поставлених вимог і обмежень для кожного технологічного процесу харчового підприємства скорочує час на вибір відповідних структур, схем та методів. Таким чином, проєктант отримує необхідну інформацію, що підкріплена знаннями з предметної області, для синтезу ефективної автоматизованої системи керування. Також передбачається, що онтологічна система буде розширена шляхом підключення нових створених прикладних онтологій, що реалізують суміжні задачі промислового підприємства

Ключові слова: система керування, технологічний об'єкт, робастний регулятор, прикладна онтологія, математична модель, предметна область, система підтримки прийняття рішень

Machinery & Energetics
Vol. 13, No. 3. 2022

Journal homepage:
https://technicalscience.com.ua/en

UDC 631.331
DOI: 10.31548/machenergy.13(3).2022.62-72

Victor Melnik*, **Alexei Zelensky, Andrew Zelensky**

State Biotechnological University
61002, 44 Alchevskikh Str., Kharkiv, Ukraine

Numerical Simulation of Gas-Dynamic Processes in the Centrifugal Radial Fan of Seeding Machines

Abstract. Increasing the efficiency of crop production, where a significant place is occupied by row crops (such as corn, sunflower, soy, sorghum, sugar beet, etc.), is inextricably linked with the introduction of energy- and resource-saving technologies to ensure high-quality and timely implementation of production processes. Sowing is an important technological process. To increase the speed, as a consequence, productivity and, most importantly, the quality of field work, precision seed drills with pneumatic systems with improved characteristics of vacuum generators are currently used. At the same time, the vacuum systems of such seeding machines are most often based on the use of a radial centrifugal fan. Therefore, an important task is to design the fan, considering the harmonisation of its parameters with the parameters of the seed drill in general, which requires a large number of tests and inspections. The use of full-scale models (test tables) requires significant time and resource costs. Based on numerical modelling of gas-dynamic processes, it becomes possible to significantly reduce the number of field experiments, and rather determine the rational form of a centrifugal radial fan. The purpose of this study is to consider the method of applying numerical modelling of gas-dynamic processes in a centrifugal radial fan using computer-aided engineering (CAE) packages. Application of computational fluid dynamics (CFD) methods for discretisation of solutions of differential equations taking into account Euler equations and Navier-Stokes equations. Numerical turbulence modelling based on k-ε models, k-ω models and Shear Stress Transport (SST) models. The results of calculating the three-dimensional field of velocities and pressures in the working area of the fan are presented, rational geometric characteristics and aerodynamic characteristics (dependence of the differential pressure on air flow) are determined. This approach to designing a centrifugal fan allows significantly harmonising its parameters at the development stage and reducing the time for implementing new projects

Keywords: numerical modelling, k-ε model, k-ω model, SST model, finite element method (FEM), finite volume method (FVM), CAD editor

Article's History: Received: 23.02.2022; Revised: 30.06.2022; Accepted: 11.08.2022

INTRODUCTION

Nowadays, high-pressure centrifugal radial fans (CRF) are widely used in agricultural machinery. They are one of the most important components of the pneumatic system of modern precision seeders. Often CRFs operate in a wide range of air flow values, which affects their productivity and, accordingly, the stability of pneumatic seed drill systems in general. In the end, all this affects the quality of work and productivity of seeding machines and, consequently, the speed and quality of sowing operations.

The use of innovative design solutions on seed drills allows achieving stable sowing quality, which leads to the establishment of the most favourable conditions for sown seeds and, as a result, to uniform germination. The latter, in turn, provides an increase in yield while minimising costs. The modern pneumatic seed drill system meets a wide range of requirements and, in particular, allows working in a precision farming system. Modern precision seed drills provide the possibility of flexible section-by-section adjustment of all seeding processes, in particular, they allow fine-tuning and accurately maintaining the seeding rate. The creation of a reliable and efficient CRF, as the basis of the pneumatic system of the seed drill, will further improve the quality indicators of its operation. This requires a detailed investigation and a deep understanding of the workflow that occurs between the interblade channels of the CRF. Applying the

Suggested Citation:
Melnik, V., Zelensky, A., & Zelensky, A. (2022). Numerical simulation of gas-dynamic processes in the centrifugal radial fan of seeding machines. *Machinery & Energetics,* 13(3), 62-72.

*Corresponding author

acquired knowledge in the design of CRF will allow avoiding mistakes, which will lead to an increase in gas-dynamic stability, performance facilitation, and overall efficiency of the developed fans.

As a result of the development of new promising pneumatic systems, the main source of obtaining the characteristics of a new fan was previously an experiment, which was unnecessarily expensive. A full-scale experiment requires the production of a large number of experimental parts of various, sometimes very complex geometries, and this, in turn, involves the use of high-tech equipment with a significant amount of time. At the same time, it is not possible to obtain comprehensive information about the flow parameters at all points of the studied region of the interblade channel [1-3]. All this affects the quality of the design and the cost of finishing the CRF.

Due to the growing progress in computer technology, flow studies using computational gas dynamics methods have become more promising methods for calculating the processes occurring in the flow part of the fan. Most often, such methods are based on the numerical solution of systems of Navier-Stokes equations [4].

The main advantages of numerical methods are:

– low cost (no need to create a test table for conducting experiments, which means that the need for appropriate special equipment, personnel training, etc. is eliminated);

– high information content of the simulated process, obtaining comprehensive information about all parameters at all points of the analysed flow area;

– safety of research processes;

– reducing the number of experiments to finalise CRF parts, which has a positive effect on the time and cost of developing the final product.

Considering the CRF as an aggregate in the pneumatic system of the seed drill, then the proposed methodology is presented for numerical modelling of gas-dynamic processes occurring in the interblade channels of the fan, and the determination of its optimal design and characteristics.

The process of development of seed drills shows the change of seeding machines that operate on a mechanical principle with the help of gravity forces to machines that use air flow. Long-term use of machines that use air flow during seeding [5] show an increase in the quality of seeding, an increase in the yield of agricultural crops with a decrease in technological and operating costs during their production. The quality of sowing seeds of row and grain crops can be implemented by improving the quality of the pneumatic system. These topics were considered by V.P. Chebotarev [6], V.V. Alt [7], S.G. Yasir [8] et al. The pneumatic system of the precision seed drill consists of a pneumatic seed drill, pneumatic pipes, and a fan. One of the main tasks is to ensure the quality of operation of the pneumatic system, in most cases, the vacuum system, and, in particular, to increase the stability of the CRF.

To solve this problem, much attention is usually paid to the development of an energy-efficient design and workflow of the pneumatic system. But at the same time, systematic studies show that the methodology for designing the CRF as an aggregate in the context of a pneumatic system of seeding machines has not been sufficiently developed.

The purpose of the study is: to consider the application of the sequential design scheme of CRF; to consider the numerical investigation of fan models using modern computer-aided engineering (CAE) software suites using computational fluid dynamics (CFD) methods [9-11]; to create a solid-state and mesh model; application of the method for describing gas dynamic processes, and a method for solving problems of gas dynamics based on discretisation methods for solutions of Euler differential equations and Navier-Stokes equations [12].

MATERIALS AND METHODS

A typical process of CRF modelling sequence is shown in Figure 1 [9]. To achieve the goal of developing a new CRF model, it is necessary to complete the following steps:

– analysis of existing models of fans of pneumatic precision seeders;

– creation of a technical task for model development;

– mathematical statement of the design problem;

– determination of geometric parameters, creation of a geometric scheme and profile of the fan impeller;

– implementation of 3D modelling of the fan model under study;

– substantiation of the choice of a mathematical model describing air flows and the solution method;

– solving the equations of the selected mathematical model of air flow;

– analysis of the results obtained and optimisation of geometric shapes of the flow part of the projected CRF.

The study considers the processes occurring in the flow part of the CRF. The fan blades, which form a circular mesh, rotate the air located in its channels [1; 13]. Under the influence of the resulting centrifugal forces, the air becomes accelerated, its density, pressure, and temperature increase. In the diffuser, the air velocity decreases, and pressure and temperature increase due to a decrease in kinetic energy. Gas flow currents can acquire such modes as: laminar, turbulent, and mixed laminar-turbulent.

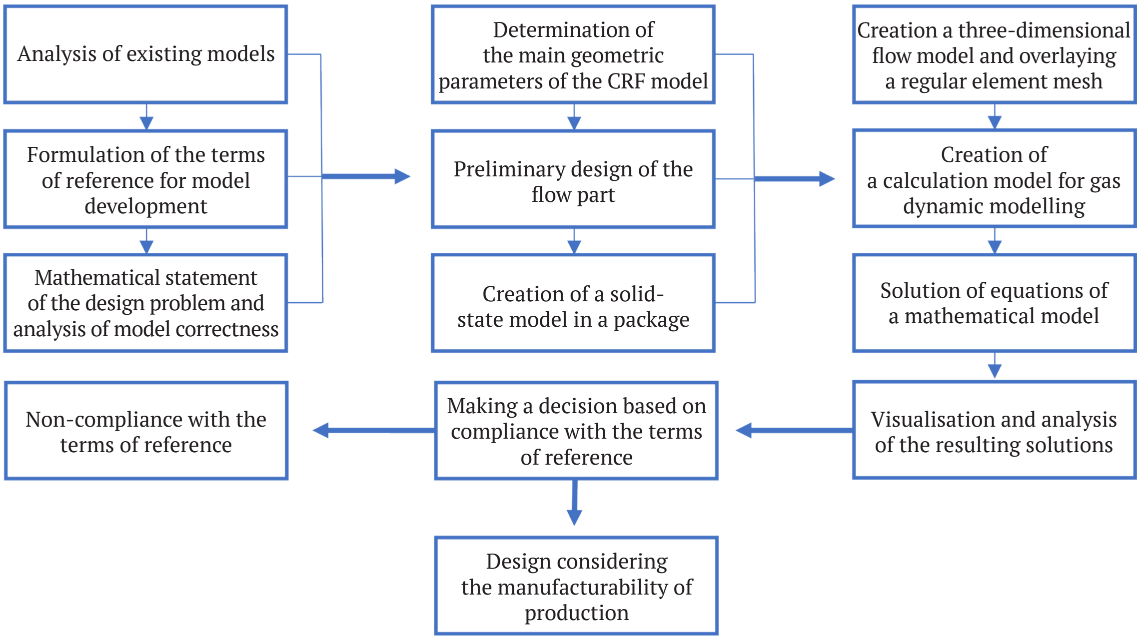

Figure 1. Modelling sequence of the process occurring in a centrifugal radial fan

The main difficulty in describing and calculating the air flow dynamics is to describe the turbulence of the flow. Turbulence is a three-dimensional non-stationary motion in which, due to the stretching of vortices, a continuous distribution of velocity ripples is created in the wavelength range from the minimum, determined by viscous forces, to the maximum, determined by the boundary flow conditions [4]. Under turbulence conditions, due to the intense mixing of air flows between different regions, the flow develops faster than laminar flow, the exchange of mass, momentum, and energy. In turn, part of the kinetic energy of the flow is converted into the kinetic energy of turbulent ripples, which then turns into heat, and these processes are irreversible [14]. Turbulence occurs in a continuous medium where small spatial fluctuations exceed the free path length of molecules.

The main difficulties in calculating the viscous incompressible flow are associated with a wide range of changes in the turbulence scale. When directly calculating the Navier-Stokes equations for a three-dimensional turbulent flow, large computational resources are required, and when calculating viscous flows, it becomes necessary to use a fine mesh with subsequent time step grinding, which also entails an increase in the computational resources used. Therefore, the main task is to select a method for solving gas dynamics equations that will reduce the necessary computational resources without losing accuracy in calculations.

Next, the study considers the process of modelling air flows on the CRF (Fig. 2). After creating a model of the processes occurring in the CRF and in the pipelines of the pneumatic system, a mesh approximation of the design area is performed. It is possible to create both an unstructured calculation mesh and a block-structured one. Then the model of a continuous medium is selected (in this case, air). The environment can be compressed or uncompressed. The boundary conditions are substantiated, in this case for moving and stationary elements, and also the wall flows of the model medium flow are described (the process of turbulence occurrence). During the execution of decisions, the accuracy is evaluated. At the same time, mathematical and physical estimates are made, the error during modelling is estimated, and the iterative solution is discretised. The results obtained for CRF are analysed. Such analysis can be graphical or numerical. The analysis is performed using the method of statistical analysis, correlation, variance, or factor. Based on them, conclusions can be drawn about further actions when designing the model: send it to production or refine it. Considering the gas flows that occur in a pneumatic system, there are two main approaches to modelling:

– direct numerical simulation of turbulent flows (DNS) consists in solving complete Navier-Stokes equations [15];

– modelling of flow using the Navier-Stokes mean equations over time (RANS), space (LES), and hybrid approaches (DES).

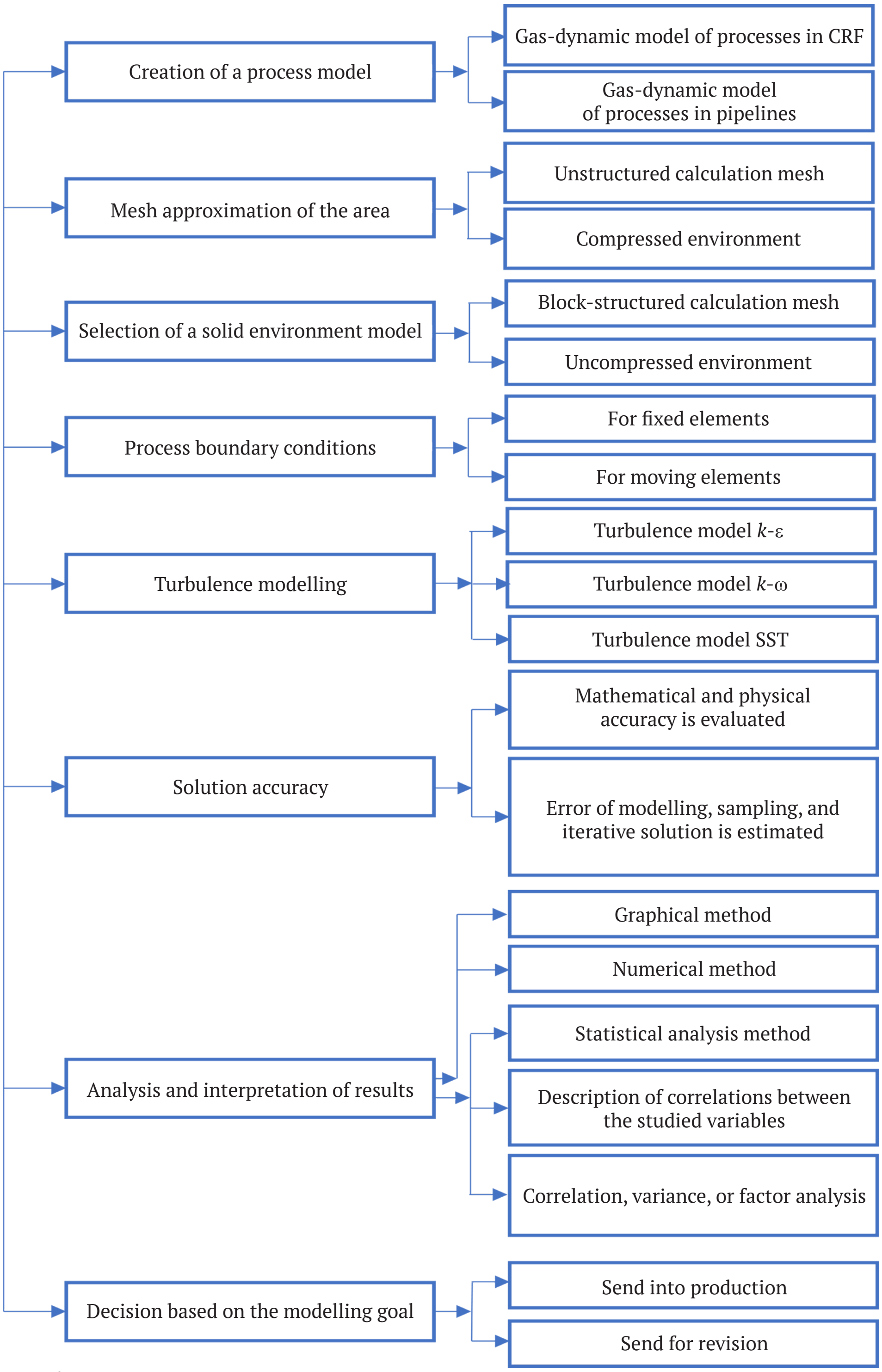

Figure 2. Modelling sequence of the process occurring in a centrifugal radial fan

Next, the study considers the pneumatic system of a precision seed drill (Fig. 3), consisting of CRF 1, a tree of pneumatic channels 2, and a group of seeding machines 3. Air enters CRF 1 through the inlet device 4, and goes outside through the outlet section 5 of the vacuum created by fan 1. Ambient air enters the channels 2 through the seeding machines 3, and then, in the form of a single flow, through the input device 4 it moves to the rotary part of the CRF 1 and then through the output section 5 (scroll housing) it is brought out again.

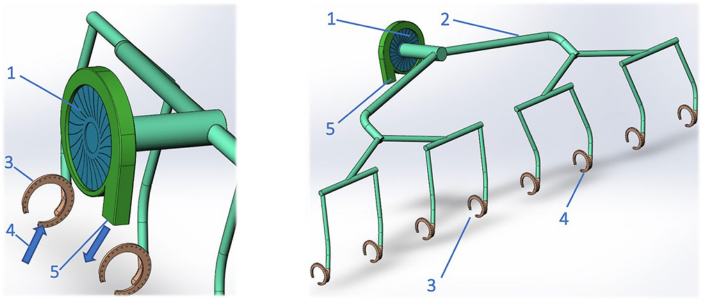

Figure 3. Design diagram of the pneumatic system of a precision seed drill with a centrifugal radial fan: 1 – fan; 2 – tree of pneumatic channels; 3 – seeding machines (air intake area); 4 and 5 – inlet device and outlet section of the fan

In the input device of the CRF, a laminar-turbulent transition is observed in wall currents. The boundary layer on the surface is a thin layer with a fast variable rate from zero to 99.5% of the incoming flow rate. In the boundary layer, due to the so-called Tollmin-Schlichting instability [4], transverse vortices are formed which undergo secondary instability and form Lambda structures downstream. In the future, they interact with each other and experience tertiary instability. Eventually, this leads to a loss of regular shape, and they become stochastic [4; 16; 17]. Another important feature of a turbulent boundary layer is the presence of a low-velocity jet stream that occurs due to the induction of Lambda structures. To numerically solve partial differential equations, the study used the finite element method (FEM). According to this method, the calculated area is divided into a set of finite sub-regions (elements) using a mesh. For each of these elements, the type of approximating function is reasonably chosen. In this case, outside of its element, the approximating function is equated to zero. The value of the function at the boundaries of elements (nodes) is obtained as a solution to the problem.

At the initial stage, when modelling the process occurring in the flow part of the projected CRF, such values are unknown in advance. Then, based on the tools of geometric design of the CAD package, a 2D model is formed, and then a 3D model (solid-state model) of the CRF (Fig. 4). Then, based on a three-dimensional solid-state model, using the operations of subtracting the volumes of the flow part and reducing insignificant parts and elements of the object under study, the area of air flow in the calculated CRF channel is distinguished (Fig. 5). In this case, the model under study is divided into several volumes (static and rotating sections of the calculated area). They will later be set by different boundary conditions. In this case: position 1 – the first input section, the volume that does not rotate; position 2 – the second section, the rotary part, the volume that rotates; position 3 – the third output section, the volume that does not rotate.

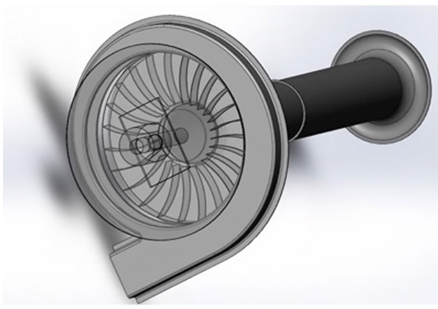

Figure 4. Solid-state model of centrifugal radial fan

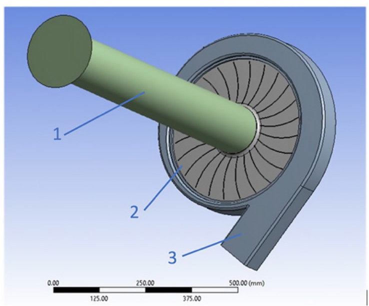

Figure 5. Air flow area of a centrifugal radial fan in the design channel: 1 –the inlet section is stationary (the first volume); 2 – the movable part (the second volume); 3 – the outlet area is stationary (the third volume)

Modelling a finite element mesh it is one of the most important stages of the computer engineering modelling process. It is used to divide the geometric area of calculation of the studied flow into elements, control volumes, etc., and also defines discrete points that correspond to the solution of partial differential equations. CAE packages offer two types of end-element mesh usage: structured and unstructured.

Structured elements are hexahedral elements, and unstructured elements are hexahedral, tetrahedral, or polyhedral elements. When dividing the study area into a calculated mesh in the regions of large velocity, pressure, and temperature gradients, a high-density mesh is used. In turn, the faces of the final volumes should be oriented by the flow lines of the flow under study.

In the sampling process, an approximation should be performed for the derived values at the nodal points (centres) of the control volumes of the resulting finite element mesh. This is because when considering internal flows for which the velocity components at the boundary are known and the pressure is unknown, it is easier to use unknowns at the centres of mass of elements. In this case, the number of points for calculating the pressure coincides with the number of points for calculating the velocity components. In addition, in the control volume centres, the values of the unknown function itself are not held, but only mediate the value of the control volume [3; 18; 19]. In turn: 1) the numerical solution obtained based on splitting the calculated space into discrete elements is approximate; 2) to improve the accuracy of the solution, it is broken down into smaller elements; 3 there is an accumulation of error; 4) the splitting method should ensure stability or convergence of the solution to the exact value when the splitting step decreases; 5) it is proposed to use the Neumann splitting method [4; 5; 20].

Next, for the three volumes under consideration, a mesh is created using the CAE package mesh generator. An automated algorithm is used to build a high-quality hexagonal mesh. After setting the parameters and requirements for the mesh, considering the requirements for probabilistic areas of turbulence, a three-dimensional finite element mesh is constructed: depending on the radius of curvature of the body; considering the number of given cells of elements, considering the thickening of the number of layers along the boundary layer and the size of cells, etc.

In turn, the current in the channels of the flow part of the model under study is conventionally divided into the region of the turbulent flow core and the region of the boundary layer. It significantly manifests friction forces, which is why it is characterised by a significant velocity gradient (the velocity varies from zero on the surface of the body's flow to the flow rate in the flow core) [3]. The thickness of the boundary layer usually corresponds to the distance from the wall, at which the flow rate will differ from the external flow rate by 1%.

In addition, the quality of the mesh affects the accuracy, convergence, and speed of obtaining a solution. The created mesh is pre-calculated, namely the number of elements and nodes. If necessary, considering the method of wall functions, a layer-by-layer reconstruction with an increase in the density of critical sections of the model. To investigate the operating modes of the CRF that significantly differ from the nominal (cruising) ones, the requirements for the quality of mesh breakdown are increased.

Having finally decided on the mesh parameters, a mesh model was obtained, which is shown in (Fig. 6).

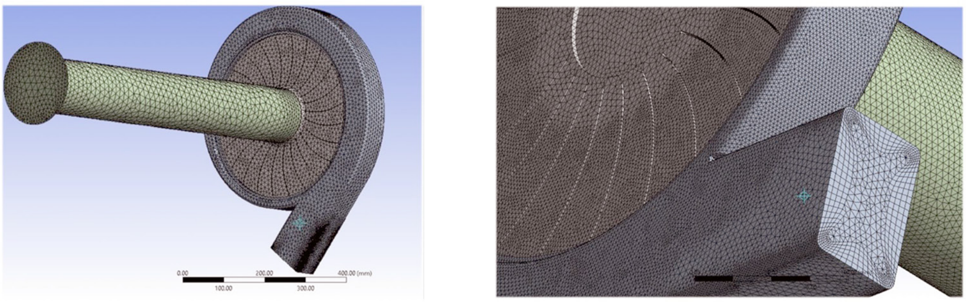

Figure 6. Mesh model of the flow part of a centrifugal radial fan

Setting calculation conditions. The calculation conditions, namely, the boundary conditions for the calculated meshes of elements of the flow part of the CRF model under study, in which it is necessary to calculate the air flow, are introduced into the processor of the PRE CAE package. At the same time, the calculated model under study consists of three areas [8; 14; 15].

Considering the fan model under study, it is assumed that, from a mathematical standpoint, the flow of the fan blade with air flow determines the system of Navier-Stokes equations [19]. It is recorded for the volume of air in question, which envelops the scapula after removing the volume of the scapula itself from it. The solution of this system gives the desired parameters of air flow in the area of interest.

During the simulation, 2 parametric turbulence models are used – k-ε (k – kinetic energy of turbulence, ε – dissipation) and SST (Shear Stress Transport). The latter is a combination of the k-ε and k-ω models of turbulence (ω –specific dissipation of turbulence), where the equation k-ε is used to calculate the flow in the free flow, and the equation k-ω of the model is used in the region near the walls [20]. The Reynolds Navier-Stokes equation (RANS) [12] are used to model turbulence with the Boussinesk approximation. The Businesk approximation (with the introduction of turbulent viscosity) consists of using Reynolds averaging of the Navier-Stokes equations. In the latter, the instantaneous velocity values are represented as the sum of the ripples of the mean over time, with the introduction of additional transfer equations for the characteristics of turbulence due to the turbulent kinetic energy *k* of the flow and its dissipation rate ε. In the end, 2 parametric RANS models *k*-ε and SST are chosen with turbulence models that are reliable, economical, and have acceptable accuracy for a wide range of turbulent flows with submodels for flow compressibility. In addition, the software products used implement a wide range of mathematical models that allow fully simulating the physical processes that often take place found in practice.

The following were chosen as the boundary conditions for the model under study: operating flow type – ideal gas; flow mode – steady state; flow without heat transfer; reference pressure 101,325 Pa; turbulence model *k*-ε or SST; rotor speed – 5,000 rpm.

As the boundary conditions at the inlet and outlet of the flow part: "Outlet pressure and mass air flow": outlet pressure (overpressure) – Free, i.e., 0 pa; air flow rate (Mass Flow Rate) – 0.494 KG/s [9]; Total Temperature – 288.15 K; combination of areas – select "on surfaces".

For further calculation, the appropriate surfaces were selected, set names for the calculated areas, and workflow parameters for the Inlet, Outlet sections, and the three areas marked: Hub – wall, Shroud – wall, and "Wall" – wall. The rotation was set for conditions of the "Wall" type (Figs. 7, 8).

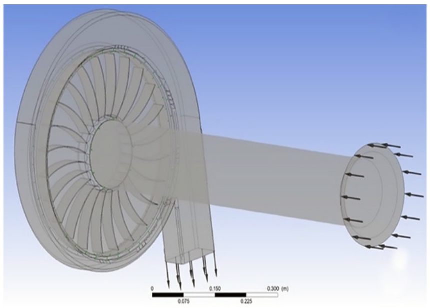

Figure 7. Calculation model with boundary conditions

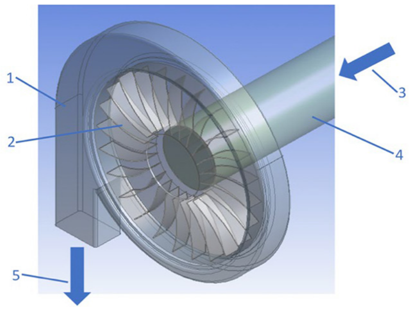

Figure 8. Setting of boundary conditions: 1 – air channel – fixed walls; 2 – impeller – movable walls; 3 – Inlet flow; 4 – air channel – fixed walls; 5 – outlet flow – mass flow rate

In addition, an important factor in gas-dynamic design is the reduction of pressure losses, uniformity of distribution, and the stabilisation of the values of the speed and flow rate of the gas flow in the channel [21-23]. When discretising the equations of a mathematical model, the weighted mismatch method was used. In this method, the solution is considered to converge with very small values of inconsistencies. The convergence criterion for solving a system of Reynolds equations is the value of the velocity values in each equation at the end of each iteration for a value less than RMS -1.0 E-6 (root-mean-square value).

RESULTS AND DISCUSSION

After all the boundary conditions have been set, the calculation requirements are set. Next, the process of numerical solution of the problem is started.

During calculations, a large array of calculated data was obtained (Fig. 9). Using them, the air flow in the flow part of the CRF is simulated. This allows seeing a characteristic picture of changes in gas-dynamic parameters, values of velocity, flow rate, pressure, and density of air flow distribution over the cross-sections of the study area.

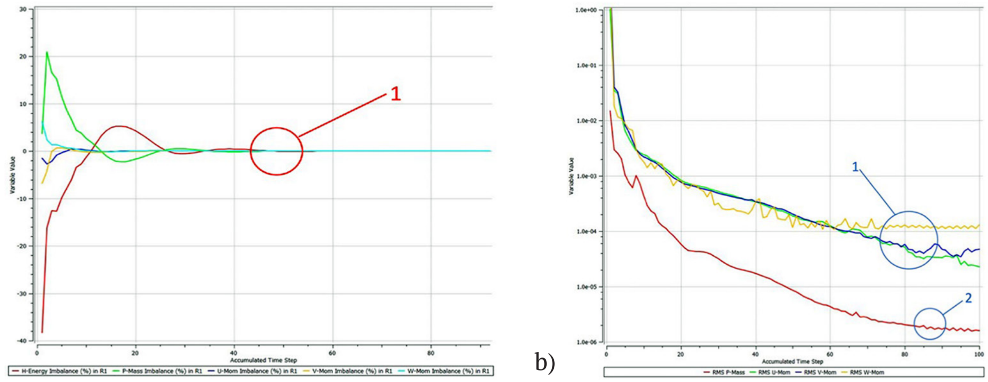
a) b)

Figure 9. Calculation results: a – calculation of a three-dimensional model of the air flow of a centrifugal radial fan (1 – an imbalance of solutions less than 1%); b – the root-mean-square value of the mass flow rate and moments

Since, when solving the equations of conservation of mass, momentum, energy, etc., the final solution must preserve these quantities, it should be borne in mind that for a numerical representation of a physical system, the imbalance of the CFD solution must be quite small, but it should not be zero. It is recommended that the desire for an imbalance in the solution should be less than 1% [24-26] (Fig. 9a). In Fig. 9b sections 1 and 2 of the non-coupling of integral parameters tend to be linearised, values oscillate, and the solution of moving convergence occurs. The solution is considered to converge when the values of the mean-square (RMS) inconsistencies are less than 1.0e-4...-1.0e-5. The convergence of solutions can be influenced by the turbulence model, the quality of the design mesh, wall functions, boundary conditions, air flow mode, etc. [27-29].

Analysing the obtained data, there is a possibility of determining the zones of disturbances (vortex generation) of the air flow, which negatively affects the nature of the flow in the channel, contributing to losses of velocity, pressure, and air flow (Fig. 10). Similar approaches were used in the design of CRF and analysis by G. Ronald, I.L. Lokshin [30-31]. Vortex generation zones and relative vortex regions were considered, which requires improvement and introduction of structural changes to the surfaces and a deeper study of these regions to improve the conditions of air flow. It is the use of numerical modelling of gas-dynamic processes in a centrifugal radial fan using CAE packages that facilitated a more thorough investigation of the processes that occur in the event of flow disturbances and turbulence.

Based on the obtained calculation results, the processes that take place in the flow part of the CRF are modelled. At the same time, the study relies on the data of changes in pressure, speed, and other parameters of interest along the flow part of the fan (Fig. 10, Fig. 11a) [2].

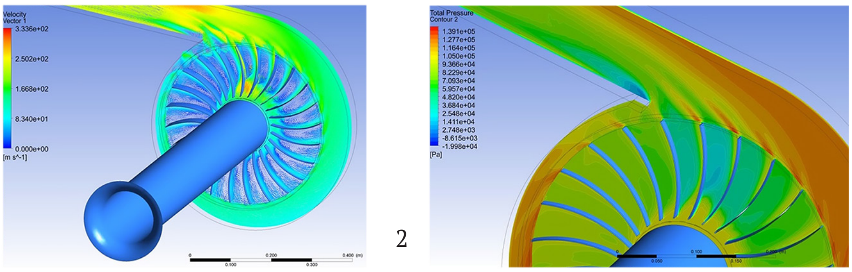
1 2

Figure 10. Picture of changes in the velocity and pressure vector of a centrifugal radial fan for the k-ε turbulence model 1 – separation loss and 2 – edge loss (shown in red circle)

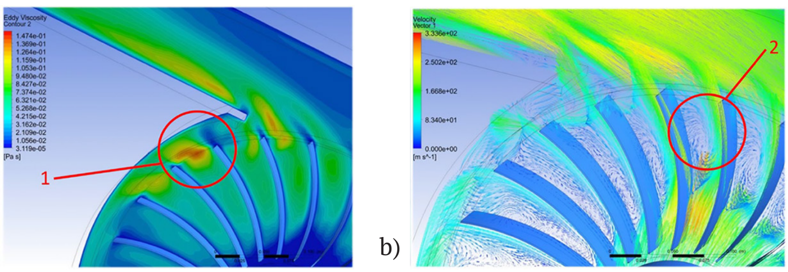
a) b)

Figure 11. Turbulent viscosity (a) and flow velocity vectors (b) in the flow part for a centrifugal radial fan (k-ε model) – the red circle shows the regions of relative vortices: 1 – the region of increased turbulent viscosity; 2 – the region of relative vortices

In addition, for example, the fields and velocity vectors along the flow part of the CRF can be considered in detail (Fig. 11b). Relative vortex (Fig. 11b) is formed in a rotating (ideal, according to the mathematical model) relative air flow in the interblade channel. Gas molecules cannot perform rotational movements in the interblade channel when flowing without friction. Therefore, they retain their direction in absolute space and during the rotation of the impeller, where each molecule moves in a circle.

Figure 11 shows that when the flow is closed in the interblade channel, a relative rotational motion is formed with the same angular velocity and the direction of rotation, the opposite direction of rotation of the impeller.

This is a relative vortex of gas molecules orbiting a calm core. Under the influence of an axial vortex, the circumferential component of the output velocity will decrease. Figure 12 shows the possible losses that occur in the fan in a systematic form, partially shown in (Fig. 10, 11).

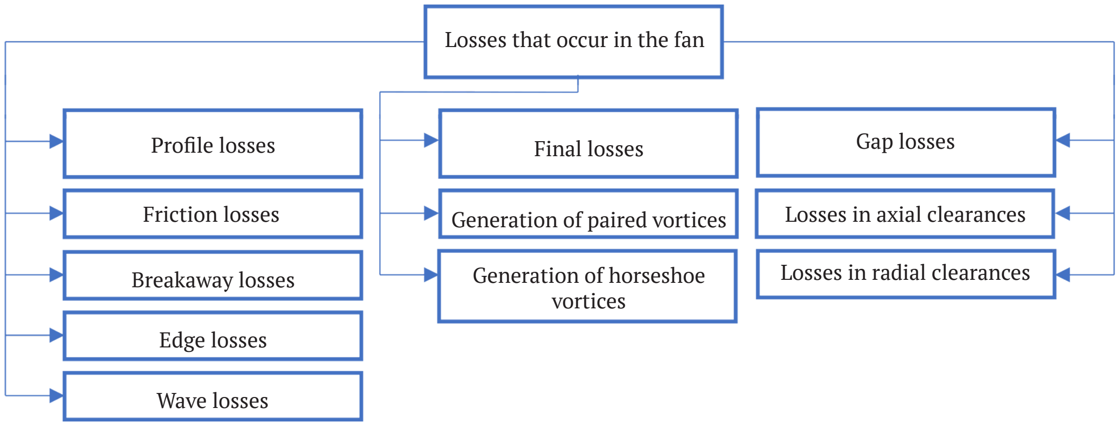

Figure 12. Losses that occur in a centrifugal radial fan

Fan losses can be divided into three groups: profile losses, end losses, and gap losses. Profile losses include losses that occur in a plane lattice: friction losses in the boundary layer, vortex losses when the flow breaks off on the profile, vortex losses behind the initial edge – edge losses; losses occur in compaction jumps – wave losses. Final losses are losses that occur in areas of the interblade channel adjacent to the end surfaces. As a result of flow in the convex surface at the top and bottom of the fan blade, at the junction with the end wall, local thickenings of the boundary layer occur. When interacting with the main flow, the thickened layers of the boundary layer begin to break off and form paired vortices rotating in the opposite direction. In addition, during turbulent separation, the air flow that forms the boundary layer twists and forms a vortex system, in which the ends bend down, taking a horseshoe shape. Losses in clearances include: losses in radial and axial clearances.

The results of the mathematical modelling of various fan models presented in Table 1 are obtained by multiple repetitions of calculations with different specified boundary conditions and subsequent mediation. To present the methodology for modelling the CRF workflow, there were no differences in the geometry and design features of the fans under study. The rotor speed is assumed to be 5,000 rpm, and the turbulence model is *k*-ε. By conducting research on a fan with counterclockwise curved blades model No. 01400Z24R, the lowest air consumption and low efficiency were obtained. When changing the direction of the blades (model No. 02400Z24LS), an increase in air consumption and efficiency was obtained. Improving the blade profile by changing the entry angle by 34° (model No. 03400Z24R50), the highest efficiency and highest air consumption were obtained. In model No. 04400Z24SB with straight blades and an entry angle of 44°, low air consumption and low efficiency were obtained.

Table 1. The result of gas-dynamic modelling at n-5,000 rpm and the turbulence model *k*-ε

Fan model	Air consumption, G_f, kg/s	Degree increased blood pressure, π_f	Efficiency, η
No. 01400Z24R	2.69	1.03	0.27
No. 02400Z24LS	2.81	1.05	0.57
No. 03400Z24R50	2.89	1.13	0.79
No. 04400Z24SB	2.55	1.04	0.423

A graphical interpretation of the relationships between the main parameters of the CRF (fan characteristic) is shown in (Fig. 13). Graphs allow analysing changes in the flow rate (Fig. 13a) and the pressure generated by the fan (Fig. 13b) in the middle section of the fan (Fig. 13: a – shows the change in velocity; b – shows the change in pressure along the cross-section of the interblade channel in the region of relative vortices) [21]. In Figure 13a, sphere 1 shows the place where the flow exits the braking area, and in Figure” 13b, the area between 1 and 2 shows the vortex generation area.

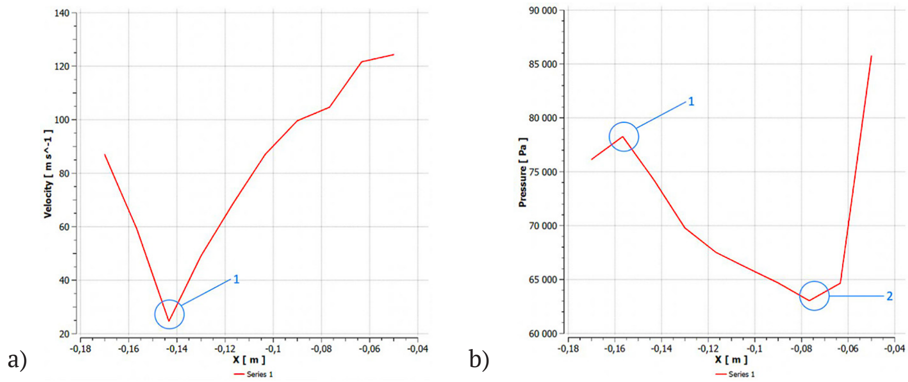

Figure 13. Area of occurrence of relative vortices:
a – distribution of flow velocity along the Section; b – distribution of flow pressure along the section

When considering the field of velocity vectors (Fig. 11b) there is an uneven flow along the height of the region of generation of reverse currents of axial vortices, which contributes to the generation of flow closure sites. All this suggests that it is necessary to deal more carefully with the profiling of the blades and the flow part of the CRF. Finding the optimal approach (changing the shape and size, angles of flow entry and exit in the fan crown) will allow minimising the total loss values.

CONCLUSIONS

Based on the presented methodology for calculating gas-dynamic parameters, it is possible to assess the nature of air flow in the flow part of the CRF, draw conclusions about the shape and size of pipelines, evaluate the design quality of the centrifugal wheel itself, that is, installation angles, dimensions, thickness, a number of blades, noise and safety factors.

Studies show that during design, achieving the desired air flow modes, high flow rates in the interblade channels of the CRF and, ultimately, acceptable values of the final parameters of the CRF can be achieved through careful profiling and the introduction of new design solutions.

The use of CAE software packages based on CFD methods in modelling the gas-dynamic characteristics of gas flow in the flow parts of CRF and pneumatic systems, in general, is very effective. This allows predicting the final parameters and significantly reducing the time and resources spent on fine-tuning such systems. In further research, when designing centrifugal radial fans, it is desirable to analyse the influence of various turbulence models on the quality of calculating air flow flows, adn conduct a comparative analysis with experimental data. This approach should be recommended for widespread use.

REFERENCES

[1] Kalinkevich, N.V., & Gusak, A.G. (2011). *Theory of turbochargers*. Sumy: SSU.

[2] Rathakrishnan, E. (2010). *Applied gas dynamics*. Hoboken: Wiley.

[3] Solodov, V.G. (2017). *Application of the ANSYS software package for solving fluid dynamics problems*. Kharkiv: Publishing house of KHNADU.

[4] Schlichting, H., & Gersten, K. (2017). *Boundary-Layer theory* (9th ed.). Berlin: Springer-Verlag.

[5] Precision seeder for row crops SCH-6M. (1972). Bucharest: Selanetoara.

[6] Chebotarev, V.P., Medvedev, A.L., Salapura, Yu.L., & Zubenko, D.V. (2012). Analysis of vertical switchgears of pneumatic seeders. *Mechanization and Electrification of the Rural State: Inter-Industrial Thematic Scientific Collection*, 96, 67-75.

[7] Alt, V.V., Shchukin, S.G., & Valkov, V.A. (2008). The concept of development of sowing machines. *Achievements of Science and Technology of the Agroindustrial Complex*, 9, 44-48.

[8] Yasir, S.H., Liao, Q., Yu, J., & He, D. (2012). Design and test of a pneumatic precision metering device for wheat. *Agricultural Engineering International: CIGR Journal*, 14(1), 16-25.

[9] Starodubtsev, Yu.V., & Solodov, V.G. (2005). Numerical model of viscous turbulent flow in one stage gas turbine. *Journal of Turbomachinery*, 128, 60-67.

[10] Babu, V. (2021). *Fundamentals of gas dynamics* (2nd ed.). Berlin: Springer.

[11] Anderson, J.D.Jr. (1995). *Computational fluid dynamics: The basics with applications*. New York: McGraw-Hill.

[12] Köhler, M. (2011). *Development and implementation of a method for solving the laminar boundary layer equations in airfoil flows*. Darmstadt: Technische Universitat Darmstadt SLA.

[13] Anderson, J.D.Jr. (2017). *Fundamentals of aerodynamics* (6th ed.). New York: McGraw-Hill Education.

[14] Cebeci, T. (2004). *Turbulence models and their applications*. Berlin: Springer.

[15] Chapman, D.R. (1980). Computational aerodynamics and prospects for its development. *Dryden Lecture. Rocket Technology and Cosmonautics*, 18(2), 3-30.
[16] Frank, M. (2016). *White fluid mechanics* (8th ed.). New York: McGraw-Hill Education.
[17] Chung, T.J. (2002). *Computational fluid dynamics*. Cambridge: Cambridge University Press.
[18] Menter, F., & Egorov, J. (2005). Turbulence models based on the length-scale equation. *Fourth International Symposium on Turbulence and Shear Flow Phenomena*, 4, 941-946.
[19] Frost, W., & Moulden, T. (Eds.). (1980). *Turbulence. Principles and applications*. Kyiv: Znannia.
[20] Hirsch, C. (2007). *Numerical computation of internal and external flows* (2nd ed.). Oxford: Published by John Wiley & Sons, Ltd.
[21] Reddy, J.N. (2006). *An introduction to the finite element method*. New York: McGraw-Hill.
[22] Hanlon, P.C. (2001). *Compressor handbook*. Washington: McGraw-Hill.
[23] Solodov, V.G. (2011). *Modeling of turbulence. Calculation of large vortices*. Kharkiv: KHNADU.
[24] ANSYS CFX – Solver theory guide. Release 15.0. (2013). Canonsburg: ANSYS Inc.
[25] Tokushev, M.Kh., & Martych, S.P. (2019). Classification of switchgears of pneumatic seeders. In *Seifullin readings – 15: Youth, science, technology – new ideas and perspectives: Scientific and theoretical conference* (pp. 208-211). Nur-Sultan: Kazakh Agrotechnical University. S. Seifullina.
[26] Prandtl, L. (1904). Über Flüssigkeitsbewegung bei sehr kleiner Reibung. Verhandl III. *Intern. Math. Kongr. Heidelberg*, 2, 484-491.
[27] Fletcher, A.J. (1988). *Computational techniques for fluid dynamics*. New York: Springer-Verlag: Berlin.
[28] Wilcox, D.C. (2006). *Turbulence modeling for CFD* (3rd ed.). La Cañada Flintridge: DCW Industries.
[29] Kornev, N. (2013). *Mathematical modeling of turbulent flows*. Rostock: University of Rostock.
[30] Ronald, H. (2000). *Aungier Centrifugal compressors a strategy for aerodynamic design and analysis*. New York: Asme press.
[31] Lokshin, I.L. (1959). Investigation of the flow behind the wheels of centrifugal fans in relative motion. *Industrial Aerodynamics*, 12, 2-153.

Віктор Іванович Мельник, Олексій Петрович Зеленський, Андрій Петрович Зеленський

Державний біотехнологічний університет
61002, вул. Алчевських, 44, м. Харків, Україна

Численне моделювання газодинамічних процесів у відцентровому радіальному вентиляторі посівних машин

Анотація. Підвищення ефективності рослинництва, де значне місце займають просапні культури (такі, як кукурудза, соняшник, соя, сорго, цукрові буряки та ін.), нерозривно пов’язане з впровадженням енерго- та ресурсозберігаючих технологій для забезпечення якісної та своєчасної реалізації технологічних процесів виробництва. Важливим технологічним процесом є посів. Для підвищення швидкості, як наслідок, продуктивності та, головне, якості проведення польових робіт в даний час застосовуються сівалки точного висіву з пневматичними системами з покращеними характеристиками генераторів вакууму. При цьому вакуумні системи таких посівних машин найчастіше базуються на використанні радіального відцентрового вентилятора. Тому важливим завданням є проектування вентилятора з урахуванням гармонізації його параметрів з параметрами сівалки в цілому вимагає проведення великої кількості випробувань та перевірок. При використанні тільки натурних моделей (стендів) необхідні дуже великі ресурсні та часові витрати. За рахунок чисельного моделювання газодинамічних процесів стає можливим суттєво скоротити кількість натурних експериментів, швидше визначити раціональний вигляд відцентрового радіального вентилятора. Мета даної роботи – розглянути методику застосування чисельного моделювання газодинамічних процесів у відцентровому радіальному вентиляторі за допомогою Computer-aided engineering (CAE) – пакетів. Застосування Computational fluid dynamics (CFD) – методів для дискретизації рішень диференціальних рівнянь з урахуванням рівнянь Ейлера та рівнянь Навье-Стокса. Для вивчення вихрових потоків, що виникають у міжлопаткових каналах вентилятора, використовується чисельне моделювання турбулентності на основі k-ε моделі, k-ω моделі та Shear Stress Transport (SST) моделі. Наведено результати розрахунку тривимірного поля швидкостей та тисків у робочій області вентилятора, визначено раціональні геометричні характеристики, аеродинамічна характеристика (залежність перепаду тиску від витрати повітря). Такий підхід проектування відцентрового вентилятора дає можливість суттєво гармонізувати його параметри на етапі розробки та скоротити час на реалізацію нових проектів

Ключові слова: числове моделювання, k-ε модель, k-ω модель, SST модель, метод кінцевих елементів, метод кінцевих об’ємів, CAD редактор

Machinery & Energetics
Vol. 13, No. 3. 2022

Journal homepage:
https://technicalscience.com.ua/en

UDC 631.312
DOI: 10.31548/machenergy.13(3).2022.73-80

Serhii Pylypaka[1*], Mykola Klendii[2]

[1]National University of Life and Environmental Sciences of Ukraine
03041, 15 Heroiv Oborony, Kyiv, Ukraine

[2]Separated Subdivision of National University of Life
and Environmental Sciences of Ukraine "Berezhany Agrotechnical Institute"
47501, 20 Academichna Str., Berezhany, Ternopil region, Ukraine

Transportation of a Material Particle by the Operating Mechanism of an Agricultural Machine in the form of a Vertical Screw Confined by a Coaxial Stationary Cylinder

Abstract. The use of vertical augers in screw conveyors significantly expands the operational capabilities of such mechanisation equipment for performing loading and unloading technological operations. However, the existing designs of vertical screws do not fully meet the operational requirements. Their main disadvantages are increased energy consumption, especially with their significant overall dimensions, which depend on the influence of friction of the process material on the conveyor surfaces. Therefore, the study considers the movement of a material particle by the operating mechanism of an agricultural machine in the form of a vertical screw confined by a coaxial stationary cylinder and establishes the dependence of the speed of transportation of a material particle on the influence of the particle friction coefficient on the surface of the screw and on the surface of the limiting cylinder. The purpose of the study is to determine the parameters of the movement of agricultural material particles when they interact with the helical surface of the operating mechanism of a vertical conveyor in the form of a screw that rotates around the axis and the surface of a coaxial fixed cylindrical casing. Mathematical modelling of the processes of movement of soil particles along the helical surface of the operating mechanism is described on the basis of general laws and principles of analytical and differential mathematics, theoretical and analytical mechanics. As a result of the study, the differential equations of movement of a particle of agricultural material on the helical surface of the screw, which rotates around its axis in a fixed cylinder, were compiled. The equation is solved using numerical methods and the trajectories of the relative motion of the particle along the helical line – the edge of the screw, which is common to the surface of the screw and the limiting cylinder are constructed. The friction forces of the material particle on the surfaces of the screw and casing are also considered. The limit value of the helical line lifting angle is found when the particle lifting becomes impossible at a given angular velocity of screw rotation. The influence of the friction angles and radius of the limiting cylinder on the particle lifting speed is estimated. Graphs of kinematic characteristics as a function of time are given. The materials of the study can be used by researchers for further investigation and by practitioners in the selection of conveyors for transporting agricultural materials

Keywords: conveyor, helical surface, angular and linear velocities, limiting casing, differential equations of motion, kinematic parameters

Article's History: Received: 15.04.2022; Revised: 21.07.2022; Accepted: 11.08.2022

INTRODUCTION

The helical surface in the form of a screw is a structural element of many transport and technological agricultural machines, which is widely used in screw conveyors for transporting technological agricultural material. Forces act between the particles of the material, but they can be ignored or neglected when the body is small in size, taking it as a material point [1] or in the case of moving the particle at a low speed, which occurs in lifting and transport machines [2]. It is also important to investigate the movement of material particles along helical surfaces that rotate around their axis. In [3], the movement of particles

Suggested Citation:
Pylypaka, S., & Klendii, M. (2022). Transportation of a material particle by the operating mechanism of an agricultural machine in the form of a vertical screw confined by a coaxial stationary cylinder. *Machinery & Energetics,* 13(3), 73-80.

*Corresponding author

by a vertical screw from the axis of rotation to the meeting with a cylindrical casing is studied. The particles move up after they meet the bounding cylinder. The paper investigates the movement of a particle of agricultural material, which interacts with two surfaces: the movable helical surface of the screw and the fixed surface of the cylinder.

The nature of material particles is quite broad. They can be not only mechanical particles, but also gas or liquid particles that interact with moving surfaces [4]. The movement of mechanical particles on the surface of a mobile tillage spherical disk is considered in [5], on the surface of a cylinder – in [6], on the surface of a cone – in [7]. Consideration of the movement of particles on helical surfaces is of practical importance, since such surfaces are used in screw conveyors [8; 9] and separators [10]. The use of a helical surface for calculating and manufacturing helical working elements is considered in [11; 12]. The theory of designing and constructing linear surfaces is highlighted in [13]. In [14], the practical possibility of using a screw operating mechanism for tillage is substantiated.

But today, the process of transporting a material particle by the operating mechanism of an agricultural machine remains rather neglected, in particular, the investigation of the interaction of material particles with a helical operating mechanism, the working surface of which is made in the form of a screw and a coaxial stationary cylinder, which are considered in the paper.

The purpose of the study is to theoretically investigate the movement of particles of agricultural materials when they interact with the helical surfaces of the operating mechanism of a vertical conveyor in the form of a screw and the surfaces of a stationary cylinder.

MATERIALS AND METHODS

Mathematical modelling of the movement of particles of agricultural materials is described based on general laws and principles of analytical and differential mathematics, theoretical and analytical mechanics, surface theory, and computer graphics systems. The results of the conducted theoretical studies are analysed using methods of numerical integration of differential equations to find primitive functions, using the *Simulink* package of the *MatLab* system.

In [3], it is shown that when a particle moves under its own weight along a helical surface, it moves away from its axis. This is conditioned by the fact that the particle moves along a curved trajectory, resulting in a centrifugal force that causes the particle to move to the periphery. If the screw rotates around the axis, then the particle of agricultural material performs a complex movement: sliding on the helical surface and rotating around the axis of the screw, which also causes it to move towards the cylindrical casing. The material particle slides along the helical surface, simultaneously contacting the surface of the screw and cylinder. Parametric equations of a helical line have the form:

$$x=R\cos\alpha;\ y=R\sin\alpha;\ z=R\alpha\,\mathrm{tg}\beta; \tag{1}$$

where R – cylinder radius – constant value; β – screw helical line lifting angle –constant value; α – angle of rotation of a point on a helical surface – independent variable.

The helical line (1) passes through two surfaces: the screw and the cylinder. When a particle comes into contact with these surfaces, reaction forces occur that are directed along the normal to them.

The helical surface is formed by rectilinear generatrix that are parallel to the horizontal plane, and one end of these generatrix runs along the helical line (1), and the other is directed to the axis of the helical surface (Fig. 1a). The parametric equations of the screw have the form:

$$\begin{aligned} X&=(R-u)\cos\alpha;\\ Y&=(R-u)\sin\alpha;\\ Z&=RR\alpha\,\mathrm{tg}\beta \end{aligned} \tag{2}$$

where u – value of a rectilinear helical forming surface – the second independent surface variable.

When the value of the value $u=R-r$, where r – radius of the screw shaft, the surface is confined by two helical lines (Fig. 1a). When $u=0$, the parametric equations of the screw helical line are obtained (1). To make the helical surface equations different from the helical line equations, they are denoted by lowercase letters for the line and uppercase letters for the surface.

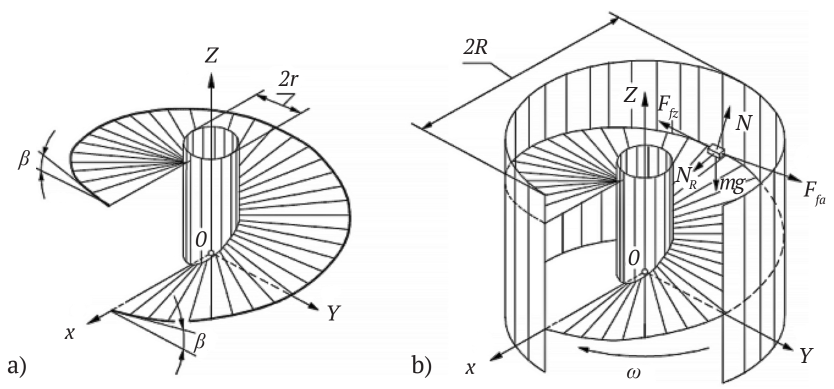

Figure 1. Scheme of transportation of a material particle by the screw:
a) turn of the helical surface of the screw, b) diagram of the forces applied to the particle

When rotating at angular velocity ω, a material particle located on the helical line (1) simultaneously contacts the movable helical surface and the fixed surface of the cylinder (Fig. 1b). The following forces are applied to the material particle: reaction N of screw surface, weight force, reaction N_R of cylinder, and friction force F_f (Fig. 1b). If the particle rises up in absolute motion, then the friction force on the helical surface F_{fa} is sent in the opposite direction of its sliding, and on the surface of the casing F_{fc} – in the opposite direction of movement (Fig. 1b).

The equation of motion of a material particle in the form $m\overline{a}=\overline{F}$ is created, and this equation is written in projections on the axis of the spatial coordinate system $OXYZ$.

The helical surface rotates around an axis at a certain angular velocity ω and over time t it will return at an angle that is equal to α_a=-ωt and will move in a helical line along a certain trajectory according to equations (1). The direction of rotation of the helical surface must be chosen so that the material particle can rise up in absolute motion. The helical line of the screw (1) is moved around the axis OZ on the corner α_a=-ωt:

$$\begin{aligned} x_a&=R\cos\alpha\cos(-\omega t)-R\sin\alpha\sin(-\omega t)=R\cos(\omega t-\alpha);\\ y_a&=R\cos\alpha\sin(-\omega t)-R\sin\alpha\cos(-\omega t)=R\sin(\omega t-\alpha);\\ z_a&=R\alpha\,\mathrm{tg}\beta. \end{aligned} \tag{3}$$

The obtained equations (3) consider rotation by angle $\alpha=\alpha(t)$ in the relative motion of the material particle and at an angle α_a=-ωt in figurative motion, therefore, they are equations of absolute motion.

Projections of the absolute velocity vector are obtained by differentiating equation (3) over time t:

$$\begin{aligned} x'_a&=-R(\omega-\alpha')\sin(\omega-t\alpha);\\ y'_a&=-R(\omega-\alpha')\cos(\omega-t\alpha);\\ z_a&=R\alpha'\,\mathrm{tg}\beta. \end{aligned} \tag{4}$$

The speed value is (4):

$$\begin{aligned} V_a&=\sqrt{x_a'^2+y_a'^2+z_a'^2}=\\ &=\frac{R}{\cos\beta}\sqrt{\omega(\omega-2\alpha')\cos^2\beta+\alpha'^2} \end{aligned} \tag{5}$$

The projection of a unit vector that sets the direction of the absolute velocity of a material particle is equal to:

$$\begin{aligned} T_{Vax}&=-\frac{(\omega-\alpha')\sin(\omega t-\alpha)\cos\beta}{A};\\ T_{Vay}&=-\frac{(\omega-\alpha')\cos(\omega t-\alpha)\cos\beta}{A};\\ T_{Vaz}&=\frac{\alpha'\sin\beta}{A}, \end{aligned} \tag{6}$$

where $A=\sqrt{\omega(\omega-2\alpha')\cos^2\beta+\alpha'^2}$.

Absolute acceleration w of particle is obtained by differentiating equation (4):

$$\begin{aligned} x''_a&=R''\alpha\sin(\omega t-\alpha)-R(\omega-\alpha')^2=\cos(\omega t-\alpha);\\ y''_a&=R''\alpha\cos(\omega t-\alpha)+R(\omega-\alpha')^2=\sin(\omega t-\alpha);\\ z''_a&=R\alpha''\mathrm{tg}\beta. \end{aligned} \tag{7}$$

Projections of the friction force vector F_{fa} are found by differentiating equations (1):

$$\begin{aligned} x'&=-R\alpha'\sin\alpha;\\ y'&=-R\alpha'\cos\alpha;\\ z'&=R\alpha'\mathrm{tg}\beta. \end{aligned} \tag{8}$$

The relative velocity of a material particle is equal to:

$$V=\sqrt{x'^2+y'^2+z'^2}=\frac{R\alpha'}{\cos\beta}. \tag{9}$$

The value of the projections of the unit vector of relative velocity is obtained by dividing the projections of this velocity by its absolute value:

$$T_{Vx}=-\cos\beta\sin\alpha;\ T_{Vy}=-\cos\beta\cos\alpha;\ T_{Vz}=-\sin\beta. \tag{10}$$

For the force F_{fa} to be applied at the point where the material particle is located, the projections of the unit vector of relative velocity should be rotated by the value (-ωt) around the axis Oz:

$$\{\cos\beta\sin(\omega t-\alpha);\ \cos\beta\cos(\omega t-\alpha);\ \sin\beta\}. \tag{11}$$

The vector of the normal to the helical surface is defined as the partial derivative of the screw equations (2) :

$$\begin{aligned} \frac{\partial X}{\partial\alpha}&=-(R-u)\sin\alpha; & \frac{\partial X}{\partial u}&=-\cos\alpha;\\ \frac{\partial Y}{\partial\alpha}&=(R-u)\cos\alpha; & \frac{\partial Y}{\partial u}&=-\sin\alpha; \end{aligned} \tag{12}$$

The vector product of the obtained vectors is defined (12):

$$\begin{aligned} &\begin{vmatrix} X & Y & Z\\ -(R-u)\sin\alpha & (R-u)\cos\alpha & R\,\mathrm{tg}\beta\\ -\cos\alpha & -\sin\alpha & 0 \end{vmatrix}=\\ &=\{R\,\mathrm{tg}\beta\sin\alpha;\quad R\,\mathrm{tg}\beta\cos\alpha;\quad R-u\} \end{aligned} \tag{13}$$

Vector (13) is not singular and its place on the surface is determined by coordinates: u and α. To find the normal to the screw surface, the vector (13) is substituted in the expression u=0 and its expression is reduced to a single one:

$$\{\sin\beta\sin\alpha;\ -\sin\beta\cos\alpha;\ \cos\beta\}. \tag{14}$$

The normal to the cylindrical casing is also found:

$$\{-\cos\alpha;\ -\sin\alpha;\ 0\}. \tag{15}$$

For the above reasons, the unit vectors (14), (15) are rotated by the angle (-ωt) and the expression of the unit vector of the normal to the helical surface at the particle placement point is written as:

$$\{\sin\beta\sin(\omega t-\alpha);\ -\sin\beta\cos(\omega t-\alpha);\ \cos\beta\}. \qquad (16)$$

The value of the unit vector of the normal to the cylindrical casing at the particle location takes the form:

$$\{-\cos(\omega t-\alpha);\ \sin(\omega t-\alpha);\ 0\}. \qquad (17)$$

Unit vector of particle weight force mg, which is directed downwards, is defined by projections:

$$\{0;\ 0;\ -1\}. \qquad (18)$$

The value of the friction forces F_{fa} and F_{fc} can be determined by the reaction values of the surface and the corresponding coefficient of friction: $F_{fa}=f_N$, $F_{fc}=f_R N_R$, where f and f_R – coefficients of friction of the material particle on the helical surface of the screw and the cylindrical casing, respectively.

Making up the equation of motion $m\overline{a}=\overline{F}$, it is written in projections on the axis of the spatial system, considering the directions (6), (11), (16), (17), and (18) of relevant forces $F_{fc}=f_R N_R$, $F_{fa}=f_N$, N, N_R and weight forces mg:

$$mx_a''=f_R N_R\frac{(\omega-\alpha')\sin(\omega t-\alpha)\cos\beta}{\sqrt{\omega(\omega-2\alpha')\cos^2\beta+\alpha'^2}}-fN\cos\beta\sin(\omega t-\alpha)-$$
$$-N\sin\beta\sin(\omega t-\alpha)-N_R\cos(\omega t-\alpha);$$
$$my_a''=f_R N_R\frac{(\omega-\alpha')\cos(\omega t-\alpha)\cos\beta}{\sqrt{\omega(\omega-2\alpha')\cos^2\beta+\alpha'^2}}-fN\cos\beta\cos(\omega t-\alpha)-$$
$$-N\sin\beta\cos(\omega t-\alpha)+N_R\sin(\omega t-\alpha);$$
$$mz_a''=-f_R N_R\frac{\alpha'\sin\beta}{\sqrt{\omega(\omega-2\alpha')\cos^2\beta+\alpha'^2}}-fN\sin\beta+N\cos\beta-mg. \qquad (19)$$

To obtain a system of equations with functions: $\alpha=\alpha(t)$, $N=N(t)$ and $N_R=N_R(t)$, the expressions for absolute acceleration from equation (7) are substituted in (19), and α'', N, N_R is defined:

$$\alpha''=f_R(\omega-\alpha')^2\cos\beta\frac{\omega\cos\beta(\cos\beta-f\sin\beta)-\alpha'}{\sqrt{\omega(\omega-2\alpha')\cos^2\beta+\alpha'^2}}-\frac{g\cos\beta}{R}(f\cos\beta+\sin\beta). \qquad (20)$$

$$N=m\cos\beta\left(g+\frac{f_R R\omega(\omega-\alpha')^2\sin\beta}{\sqrt{\omega(\omega-2\alpha')\cos^2\beta+\alpha'^2}}\right). \qquad (21)$$

$$N_R=mR(\omega-\alpha') \qquad (22)$$

To obtain solutions to differential equations, it is necessary to use numerical methods.

RESULTS AND DISCUSSION

The composite equations of motion of a material particle can only be solved by numerical methods. When $\beta=10^0$, R=0.1 m, $\omega=15\ s^{-1}$, $f=f_R=0.3$, obtain $\alpha'=2.1\ s^{-1}$. When $\beta=20^0$ and unchanged other parameters, obtain: $\alpha'=-0.5\ s^{-1}$. It is also obtained that when $\beta=10^0$ the particle is moving up (Fig. 2a), and when $\beta=20^0$ – on the contrary-down (Fig. 2b). When $\alpha'=0$ the particle "sticks" and rotates in absolute motion in a circle. Therefore, the corresponding angle β of lifting the auger line of the screw is found by equation:

$$\beta=\mathrm{Arctg}\frac{Rf_R\omega^2-fg}{Rf_R f\omega^2+g}. \qquad (23)$$

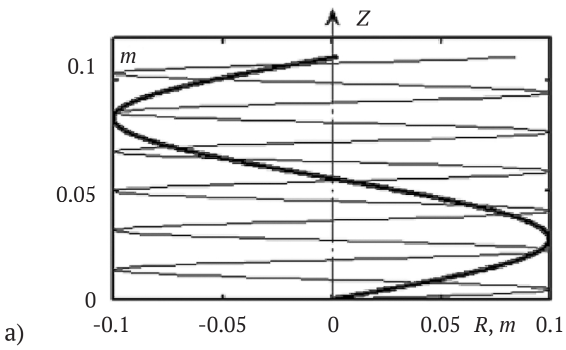

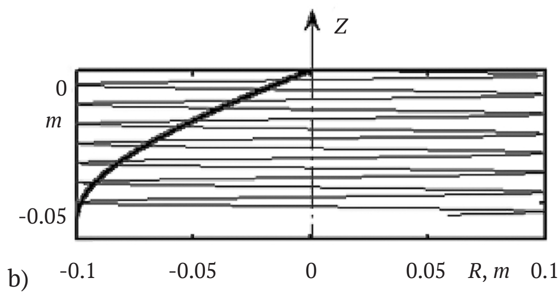

Figure 2. Trajectories of movement of a material particle at R=0.1 m, $\omega=15\ s^{-1}$, $f=f_R=0.3$
a) when $\beta=10^0$ – upward movement of the particle; b) when $\beta=20^0$ – downward movement of the particle

According to (23) for R=0.1 m, $\omega=15\ s^{-1}$ and $f=f_R=0{,}3$ the limit value of the helical line lifting angle is $\beta=17.8^0$. If $\beta\geq17.8^0$, then the rise of the particle at the specified parameters becomes impossible. As the angular velocity of rotation of the helical surface increases, the limit value of the angle β also grows, but up to a certain limit. Next, the study finds the limit to which equation (23) approaches with an unlimited increase in the angular velocity of rotation ω:

$$\lim_{\omega\to\infty}\mathrm{Arctg}\frac{Rf_R\omega^2-fg}{Rf_R f\omega^2+g}=\mathrm{Arcctg}\,f. \qquad (24)$$

Arctg f is the angle of friction of the particle on the surface of the screw and in this case, Arctg 0.3 =16.7^0. Lifting angle limit value β according to (24) is Arcctg 0.3=73.3^0, that is, these two angles add up to a right angle. When $\beta \geq 73.3^0$ lifting the particle up is not possible at any angular speeds of rotation of the helical surface.

If a specific angular velocity ω of screw rotation is set, then the limit value of the helical line lifting angle can be found by equation (23). At this interval (from zero to the limit value), there is a specific angle β, which provides the highest speed of particle transport up. The problem is reduced to finding the maximum value of the last expression in equations (4) or (8), since the vertical components of the relative and absolute velocities are equal.

Since equation (20) for a stationary process at α''=0 is necessary to solve by numerical methods to find the value of the angular velocity α' sliding of the particle, then finding the optimal angle β will be implemented in two stages. At the first stage, the value α' is found from equation (20) for the specified angles β from the acceptable range of their values. At the second stage, substituting the obtained values α' and corresponding angles β in the last expression in equations (4) or (8), the vertical component of the particle velocity is obtained. This data can be used to plot the dependency $z'=z'(\beta)$, from which the optimal angle value β is determined. The study provides a simplified version of the calculation for ω=15 s^{-1} (acceptable range of values of angle β=0…17.8^0):

$$\beta=50;\ \alpha'=3.53\ s^{-1};\ z'=0.03\ \text{m/s};$$
$$\beta=100;\ \alpha'=2.08\ s^{-1};\ z'=0.037\ \text{m/s};$$
$$\beta=150;\ \alpha'=0.73\ s^{-1};\ z'=0.02\ \text{m/s}.$$

From the results obtained, it can be seen that the highest rate of particle transport up is provided by the angle β=10^0. Using the same calculation method, the optimal angle value β is found at the value of the angular velocity ω=25 s^{-1}: β=20^0. In this case, the vertical component of the particle velocity is z'=0.29 m/s. Considering that the permissible interval of angle values for speed ω=25 s^{-1} makes up β=0…45.7^0, then it can be concluded that the optimal value of the angle β is close to the average value of the allowed interval. In [8], an equation for determining this angle is given for the case when the angular velocity of rotation of the screw increases indefinitely ($\omega \to \infty$):

$$\beta=45^0-0.5\text{Arctg}f \tag{25}$$

From (25) for f=0.3 obtain: β=36.65^0. This value is exactly two times less than the limit value (β=73.3^0), that is, it is exactly in the middle of the allowed interval.

Next, the study considers how the coefficients of friction f and fR affect the speed of lifting the particle. When the coefficient of friction f decreases, angular velocity α' of sliding of a material particle increases, and its maximum value is reached at the value of f=0, that is, for a completely smooth helical surface. Fig. 3a shows the graphical relationship $\alpha'=\alpha'(f)$ when R=0.1 m, ω=25 s^{-1}, f_R=0.3, β=20^0.

Reduction of the coefficient of friction f_R of the particle along the cylinder leads to a decrease in the angular velocity α' of movements of a material particle (Fig. 3b). Reduction of f_R leads to lowering of the material particle. The limit is the value of f_R when α'=0. By solving (23) with respect to f_R, the following is obtained:

$$f_R=\frac{g\left(f+\text{tg}\beta\right)}{R\omega^2\left(1-f\,\text{tg}\beta\right)}. \tag{26}$$

For the given data from (26), the limit value of the friction coefficient f_R: f_R=0.12 is found.

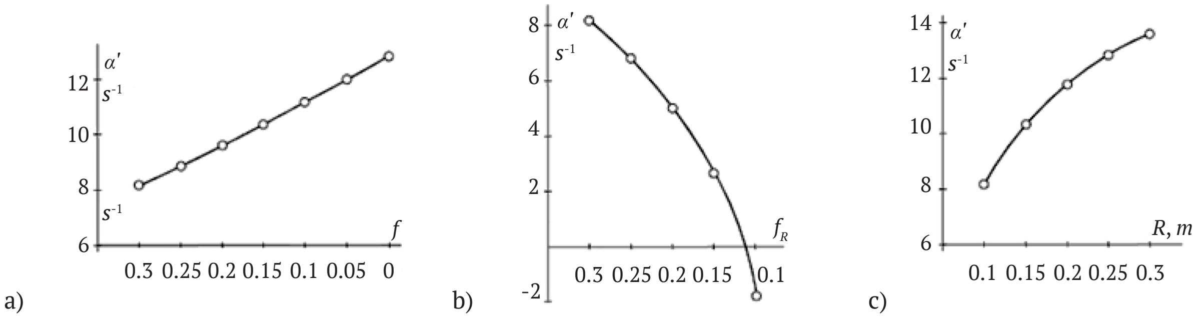

Figure 3. Graphical dependences of the angular velocity of a particle α' when ω=25 s^{-1}, β=20^0:
a) R=0.1 m, f_R=0.3;b) R=0.1 m, f=0.3; c) f=0.3, f_R=0.3

If the angular speed of rotation of the screw is increased, for example, to 30 s^{-1}, then the particle lift would be possible. The limit value of the coefficient of friction for this angular velocity is f_R=0.08. As the values of the angular velocity of rotation of the helical surface increase, the limit value of the coefficient decreases. Going to the boundary, the following is obtained:

$$\lim_{\omega\to\infty}\frac{g\left(f+\text{tg}\beta\right)}{R\omega^2\left(1-f\,\text{tg}\beta\right)}=0. \tag{27}$$

Thus, if the surface of the cylindrical casing is absolutely smooth, then the lifting of the particle becomes impossible for any angular speeds of screw rotation.

Figure 3c shows the graphical dependence $\alpha'=\alpha'(R)$, from which it follows that the increase in the radius value R leads to an increase in the lifting speed, but it has a certain limit.

If the angle value β is negative, the direction of winding the helical line changes, which means that with the same direction of the angular velocity of screw rotation, the particle on its surface will slide not up, but down. Transportation of the particle downwards has its own characteristics depending on the angle value β. If in equation (20) before the angle β the sign is changed, then one of the expressions in parentheses will be written: $f\cos\beta$-$\sin\beta$. If the angle β is equal to angular friction, i.e., f=tgβ, then this expression is converted to zero. To convert the entire equation (20) to zero, it is enough to equate another expression in parentheses to zero: ω-α'=0. The angular velocity of sliding of a material particle is equal to the angular velocity of rotation of the helical surface. Since they are directed in opposite directions, their sum is zero, that is, the particle in absolute motion does not rotate, but falls down in a straight line – the generating cylinder. Next, the study finds α' and z' for three angles: smaller, larger, and equal angular friction βf as with lifting the particle for R=0.1 m, ω=15 $s^{-1}$and f=f_R=0.3.

$\beta<\beta_f$: β=-10^0; α'=8.8 s^{-1}; z'=-0.16 m/s;
$\beta=\beta_f$: β=-Arctg$f$=-16.7^0; α'=15 s^{-1}; z'=-0.45 m/s;
$\beta>\beta_f$: β=-20^0; α'=20.4 s^{-1}; z'=-0.74 m/s.

Figure 4 shows the relative and absolute trajectories of the particle's motion for these cases. Frontal projections of trajectories are shown at different scales.

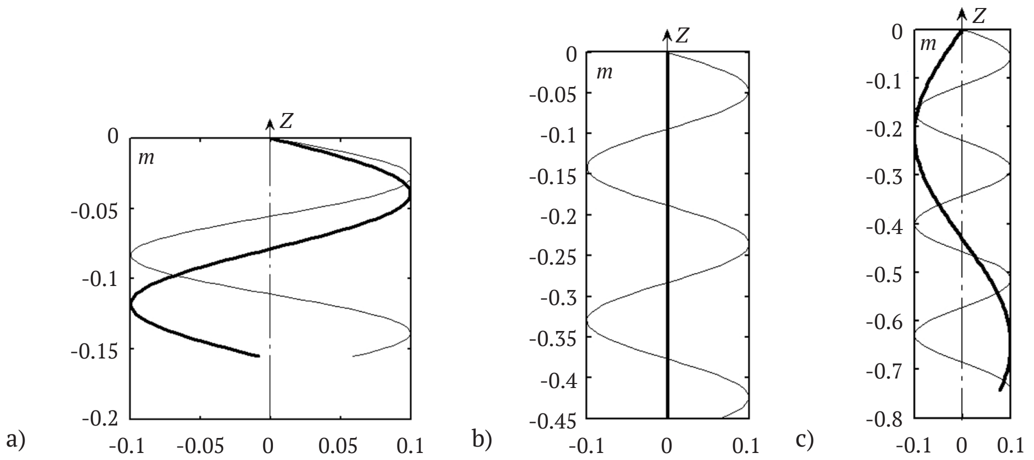

Figure 4. Trajectories of the particle's downwards movement at R=0.1 m, ω=15 s^{-1}, f=f_R=0.3 during the time t=1 s: a) β=-10^0; b) β=- Arctg$f$=-16.7^0; c) β=-20^0

By solving differential equation (20), the kinematic parameters of the motion of a material particle by numerical methods is found. Figure 5 shows graphical dependencies α'=$\alpha'(t)$ and z'=$z'(t)$, which show the motion of the particle for 1.5 seconds. The angular velocity and velocity reach the values obtained earlier.

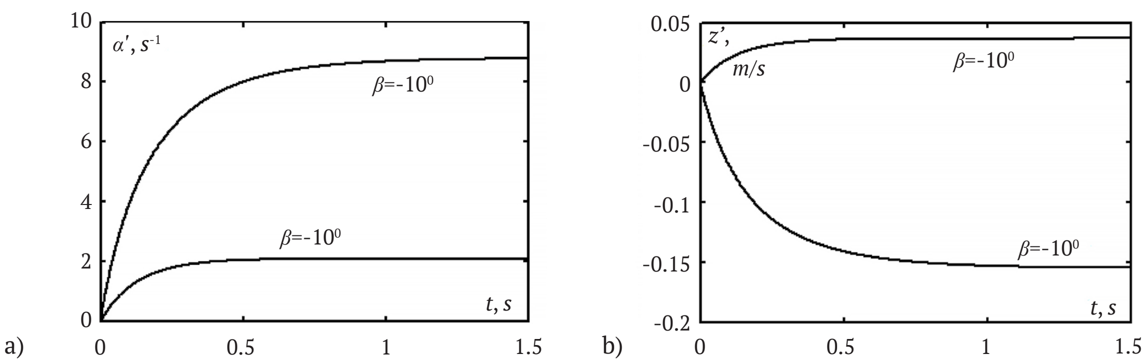

Figure 5. Graphical dependences of changes in the velocities of movement of a material particle at R=0.1 m, ω=15 s^{-1} and f=f_R=0.3: a) graphical dependency α'=$\alpha'(t)$; b) graphical dependency z'=$z'(t)$

The process of overloading the flow of loose material would differ from the movement of a single particle, but it can be assumed that the qualitative picture of overloading the material will be the same.

In [15], it is proved that a material particle can move at different velocities when moving up in the conveyor. In addition, studies [16; 17] show that at the same angular velocity of rotation of a helical surface, the velocity of movement of a material particle up z'_a will depend on the size of the tilt angle β of a helical line. In [18], it is proved that after stabilisation of the movement of a material particle, the speed of movement of the material particle up and the angular sliding velocity α' material particles are constant values, and therefore, the angular acceleration value $\alpha''=0$ is zero. The value α' can be determined with the specified parameters of the helical surface, the angular velocity of its rotation, and the coefficients of friction [19]. Having solved the equations of motion of a material particle compiled in this paper by numerical methods, the resultscorresponding to the results given in are obtained [20]. It was also established that there was a change in the direction of movement of the material particle [21].

CONCLUSIONS

As a result of the conducted theoretical studies, a mathematical model of the movement of a material particle by the working surface of a helical body, which is a screw and the surface of a limiting cylinder, is obtained.

As a result of solving differential equations by numerical integration, it is established that a particle falling on the surface of a vertical screw that moves around its axis is thrown back to a coaxial stationary limiting cylinder under the action of centrifugal force. Further movement of the particle occurs along the common line of these two surfaces – a helical line – with simultaneous sliding on both surfaces. The absolute movement of a material particle in the vertical direction occurs both up and down and depends on the angle β tilt of the helical line of the screw and its angular rotation speed. The limiting value of the angle β of inclination of the helical line, at which the lifting of the particle is impossible, and the value of the angle at which the value of the particle velocity is the greatest, is determined.

It is established that a decrease in the coefficient of friction of a particle on the helical surface leads to an increase in the speed of its movement up, and a decrease in the coefficient of friction of a material particle on the surface of the limiting cylinder leads to its decrease.

When changing the direction of winding the helical line, the particle can only be transported downwards at a much higher speed.

The prospect of this study is to establish the regularities of the movement of the material flow along the working surfaces of the helical body and the limiting cylinder and determine the energy and power parameters of transportation.

REFERENCES

[1] Bulgakov, V., Nikolaenko, S., Holovach, I., Adamchuk, V., Kiurchev, S., Ivanovs, S., & Olt, J. (2020). Theory of grain mixture particle motion during aspiration separation. *Agronomy Research*, 18(1), 18-37.

[2] Loveikin, V.S., & Romasevych, Yu.O. (2017). Dynamic optimization of a mine winder acceleration mode. *Naukovyi Visnyk Natsionalnoho Hirnychoho Universytetu*, 4, 81-87.

[3] Pylypaka, S.F., Klendii, M.B., & Klendii, O.M. (2017). Particle motion over the surface of a rotary vertical axis helicoid. *INMATEH – Agricultural Engineering*, 51(1), 15-28.

[4] Liaposchenko, O., Pavlenko, I., & Nastenko, O. (2017). The model of crossed movement and gas-liquid flow interaction with captured liquid film in the inertial-filtering separation channels. *Separation and Purification Technology*, 173, 240-243.

[5] Hevko, B.M., Hevko, R.B., Klendii, O.M., Buriak, M.V., Dzyadykevych, Y.V., & Rozum, R.I. (2018). Improvement of machine safety devices. *Acta Polytechnica*, 58(1), 17-25.

[6] Pylypaka, S., Klendii, M., Kremets, T., & Klendii, O. (2018). Particle motion over the surface of a cylinder, which performs translational oscillations in a vertical plane. *Engineering Journal*, 22(3), 83-92.

[7] Bulgakov, V., Adamchuk, V., & Kuvachev, V. (2021). Results of experimental studies of a block-modular agricultural unit. *Herald of Agrarian Science*, 99(7), 49-58.

[8] Hryhoryev, A.M. (1972). *Screw conveyors movement*. Moscow: Mashinostroenie.

[9] Evstratova, A.V. (2007). Mathematical description of the process of vertical screw transportation of a flow of bulk material. *Bulletin of Higher Educational Institutions. North Caucasus Region*, 6, 53-55.

[10] Anikin, M.F., Ivanov, V.D., & Pevzner, L.M. (1970). *Screw separators for beneficiation of ores*. Moscow: Nedra.

[11] Bulgakov, V., Holovach, I., Nadykto, V., Parakhin, O., Kaletnik, H., Shymko, L., & Olt, J. (2020). Motion stability estimation for modular traction vehicle-based combined unit. *Agronomy Research*, 18(4), 2340-2352.

[12] Bulgakov, V., Pascuzzi, S., Ivanovs, S., Kaletnik, G., & Yanovich, V. (2018). Angular oscillation model to predict the performance of a vibratory ball mill for the fine grinding of grain. *Biosystems Engineering*, 171, 155-164.

[13] Kresan, T., Pylypaka, S., Ruzhylo, Z., Rogovskii, I., & Trokhaniak, O. (2021). External rolling of a polygon on closed curvilinear profile. *Acta Polytechnica*, 61(1), 270-278.

[14] Hevko, B.M., Hevko, R.B., Klendii, O.M., Buriak, M.V., Dzyadykevych, Y.V., & Rozum, R.I. (2018). Improvement of machine safety devices. *Acta Polytechnica*, 58(1), 17-25.

[15] Hevko, R., Rohatynskyi, R., Hevko, M., Lyashuk, O., Trokhaniak, O. (2020). Investigation of sectional operating elements for conveying agricultural materials. *Research in Agricultural Engineering*, 66(1), 18-26.

[16] Hevko, R.B., Lyashuk, O.L., Dzyura, V.O., Dovbush, T.A., Trokhaniak, O.M., & Liashko, A.P. (2021). Experimental studies of the process of loose material transportation by a pneumatic-screw conveyor. *INMATEH – Agricultural Engineering*, 63(1), 479-487.
[17] Tkachenko, I., Hevko, R., Gandziuk, M., Synii, S., Trokhaniak, O. (2021). Substantiation of the parameters of a horizontal conveyer-cleaner of root crops. *Bulletin of the Transilvania University of Brasov*, 1, 213-222. doi: 10.31926/BUT.FWIAFE.2021.14.63.1.19.
[18] Hevko, R., Zalutskyi, S., Tkachenko, I., Lyashuk, O., & Trokhaniak, O. (2021). Design development and study of an elastic sectional screw operating tool. *Acta Polytechnica*, 61(5), 624-632. doi: 10.14311/AP.2021.61.0624.
[19] Kuvachov, V., Bulgakov, V., Adamchuk, V., Kaminskiy, V., Melnik, V., & Olt, J. (2021). Experimental research into new harrowing unit based on gantry agricultural implement carrier. *Agronomy Research*, 19(1), 126-135.
[20] Bulgakov, V., Trokhaniak, O., Adamchuk, V., Olt, J., & Ivanovs, S. (2022). Experimental studies of flexible sectional screw conveyor torque value. In *Engineering for rural development: Contents of proceedings of 21st international scientific conference* (pp. 472-477). Jelgava.
[21] Bulgakov, V., Olt, J., Ivanovs, S., Trokhaniak, O., Gadzalo, J., Adamchuk, V., Chernovol, M., Pascuzzi, S., Santoro, F., & Arak, M. (2022). Research of a contact stresses in swivel elements of flexible shaft in screw conveyor for transportation of agricultural materials. *Estonian Academic Agricultural Society*, 33(1), 1-7. doi: 10.15159/jas.22.12.

Сергій Федорович Пилипака[1], Микола Богданович Клендій[2]

Національний університет біоресурсів і природокористування України
03041, вул. Героїв Оборони, 15, м. Київ, Україна

[2]Відокремлений підрозділ національного університету біоресурсів і природокористування України «Бережанський агротехнічний інститут», Україна
47501, вул. Академічна, 20, м. Бережани, Тернопільська область, Україна

Транспортування частинки матеріалу робочим органом сільськогосподарської машини у вигляді вертикального шнека, обмеженого співвісним нерухомим циліндром

Анотація. Застосування в гвинтових конвеєрах вертикальних шнеків дозволяє суттєво розширити експлуатаційні можливості таких засобів механізації для виконання завантажувально-розвантажувальних технологічних операцій. Однак існуючі конструкції вертикальних шнеків не в повній мірі задовольняють експлуатаційні вимоги. Основними їх недоліками є підвищені енерговитрати, особливо при їх значних габаритних розмірах, які залежать від впливу тертя технологічного матеріалу по поверхнях конвеєра. Тому в статті розглянуто рух частинки матеріалу робочим органом сільськогосподарської машини у вигляді вертикального шнека, обмеженого співвісним нерухомим циліндром та встановлено залежність швидкості транспортування частинки матеріалу від впливу коефіцієнта тертя частинки по поверхні шнека та коефіцієнта тертя частинки по поверхні обмежуючого циліндра. Метою дослідження було визначення параметрів руху частинок сільськогосподарських матеріалів при їх взаємодії із гвинтовою поверхнею робочого органа вертикального конвеєра, виготовленого у вигляді шнека, який обертається навколо осі, та поверхнею співвісного нерухомого циліндричного кожуха. Математичне моделювання процесів руху частинок ґрунту по гвинтовій поверхні робочого органу описано на базі загальних законів і принципів аналітичної та диференціальної математики, теоретичної та аналітичної механіки. В результаті проведеного дослідження було складено диференціальні рівняння переміщення частинки сільськогосподарського матеріалу по гвинтовій поверхні шнека, який обертається навколо своєї осі у нерухомому циліндрі. Рівняння розв'язано за допомогою чисельних методів і побудовано траєкторії відносного руху частинки по гвинтовій лінії – крайці шнека, яка є спільною для поверхні шнека і обмежуючого циліндра. Також враховано сили тертя частинки матеріалу по поверхнях шнека і кожуха. Знайдено граничне значення кута підйому гвинтової лінії, коли підйом частинки стає неможливим при заданій кутовій швидкості обертання шнека. Виявлено вплив кутів тертя і радіуса обмежуючого циліндра на швидкість підйому частинки. Наведено графіки кінематичних характеристик у функції часу. Матеріали статті можуть бути використані науковцями для подальших досліджень та практиками у виборі конвеєрів для транспортування сільськогосподарських матеріалів

Ключові слова: конвеєр, гвинтова поверхня, кутова і лінійна швидкості, обмежуючий кожух, диференціальні рівняння руху, кінематичні параметри

Machinery & Energetics
Vol. 13, No. 3. 2022

Journal homepage:
https://technicalscience.com.ua/en

UDC 681.511;681.527
DOI: 10.31548/machenergy.13(3).2022.81-91

Viktor Trokhaniak*

National University of Life and Environmental Sciences of Ukraine
03041, 15 Heroiv Oborony, Kyiv, Ukraine

Investigation of the Lateral Ventilation System in a Poultry House Using CFD

Abstract. Maintaining a normalised microclimate in a poultry house is one of the main factors. It is the quality indicators of air parameters that ultimately determine the quality of product output. Keeping poultry requires considerable efforts and technological solutions. In this regard, the purpose of the study is to improve the microclimate system in the poultry house by installing ventilation equipment on the side wall. A powerful tool for predicting the air flow pattern in a poultry house is Computational Fluid Dynamics (CFD) modelling using ANSYS Fluent. This is an alternative to experimental research. CFD modelling results have shown that the valves operate most efficiently at 330 mm from the ceiling. The pressure drop of the supply valves is 45.85 Pa. The air velocity at the inlet of the supply valves is 9.17 m/s. The air velocity at a height of 0.7 m from the floor level varies within 0.57 m/s, the temperature – 9.91°C

Keywords: hinged screw sections, inactive zone between sections, material flight length, straight and curved routes, material departure angle

Article's History: Received: 30.03.2022; Revised: 07.07.2022; Accepted: 11.08.2022

INTRODUCTION

Evaluating the performance of new ventilation systems can be a difficult task, as it is time-consuming and rather expensive [1]. As an alternative to field measurements, Computational Fluid Dynamics (CFD) modelling is a powerful tool for predicting air flow patterns, particle and gas concentrations, and the thermal environment in livestock premises [2-4]. It was also used to evaluate the effectiveness of existing ventilation systems and new structures [5; 6].

In the study [7], three k-ε turbulence models were evaluated: standard k-ε, renormalisation group (RNG) k-ε, and realistic k-ε for estimating the internal environment of poultry based on temperature and air velocity measurements. The purpose of the study was to determine which turbulence model best reproduces experimental results using CFDs. Choosing a suitable turbulence model is important because it can significantly affect the results. In this study, the RNG k-3 model was best consistent with air velocity and temperature measurements, and therefore, its use and typical parameters were recommended for modelling the internal environment of poultry houses.

In [8], the design of air intake devices for this typical broiler room in a cold region under the condition of transverse ventilation was optimised based on two influencing factors: the length of the flow direction device and the air flow direction. Optimised air supply devices have helped improve air flow in the broiler room, thereby changing environmental factors such as internal temperature distribution, wind speed distribution, and carbon dioxide distribution. The ideal flow direction device should be approximately 1 m or 2 m long but no more.

The purpose of [9] is to create a 3D model using CFD that can reproduce real operating conditions inside the poultry housing. The improvement consists in integrating the main explicit and latent heat sources in accordance with the procedure described in [10], which was previously applied to a 2D CFD model. To investigate the typical cooling and heating processes observed in the poultry house, they were identified and considered for modelling. The results of the model were first tested on the basis of experimental data to evaluate the effectiveness of the model for predicting temperature and humidity gradients. The simulated field velocity was then used to calculate the ventilation intensity.

To maximise the benefits of weather conditions, the authors [11] analyse the influence of natural ventilation on the dynamics of the internal climate of the poultry house, with an emphasis on the role of external climatic parameters, in addition to wind direction. According to experimental data, seven periods with a stable wind direction of at least 4 hours were identified with a predominant

Suggested Citation:
Trokhaniak, V.I. (2022). Investigation of the lateral ventilation system in a poultry house using CFD. *Machinery & Energetics,* 13(3), 81-91.

*Corresponding author

north-easterly wind direction. Three of these periods were selected as typical examples and used to test a three-dimensional CFD model for integrating the main elements, internal climate: animal heat generation and water vapour, radiation heat transfer, and ventilation. The predictions of the three-dimensional CFD model were then analysed using the concept of air residence time to estimate the ventilation rate and to investigate explicit and latent heat exchange.

In the study [12], the authors developed a 3D CFD model for modelling air velocity, air temperature, humidity, and heat stress in a commercial laying hen house. The model was successfully confirmed by field measurements during the warm, transitional, and cold periods of the year. Heat stress was detected in 69.1%, 78.0%, and 18.4% of kindergartens in summer, autumn, and winter according to the temperature and humidity indicator at the incoming air temperature of 26.0°C, 15.0°C, and 2.5°C with ventilation intensity of 85.8, 15.5, and 11.7 air exchange per hour, respectively. As a continuation of the study [13], the authors developed a new ventilation system, an upward airflow displacement (UAD) ventilation system, which allows fresh air to enter the poultry house through air ducts located at the bottom of the cages, move upwards due to thermal buoyancy caused by chickens and the static pressure difference caused by exhaust fans, and eventually exit the housing through fans installed on the roof. The results showed that the UAD system resulted in a 46-129% increase in the efficiency of air exchange in cages and provided a more uniform thermal environment with 9.4% less heat stress in summer and 68% less cold stress in winter compared to the conventional system.

The paper [14] presents the results of a study of intelligent control systems for biotechnological objects on the example of a greenhouse. A measurement system has been developed to effectively study solar radiation and predict possible information violations. Neural networks were used as a mathematical tool for predicting temperature time series. Subsequently, in [15; 16], a software and hardware subsystem of phytomonitoring was created in a modern greenhouse building, which is provided using LabVIEW software and Arduino equipment, which is tested directly in production. To conduct experiments, the authors of [17] developed a mobile robot for monitoring the state of the atmosphere and phyto status in protected ground objects to form control strategies that maximise production profits. As the final stage, the authors [18] developed an energy-efficient control system for the electrical engineering complex of an industrial greenhouse. Evaluation of the quality of plant products based on the use of Harington desirability function. This allows determining the parameters of the microclimate (plant temperature, temperature, and humidity), maximising the profit of products. All these methods that were used to create, analyse, and predict the microclimate in greenhouses can be used to a large extent for poultry houses.

The authors [19; 20] conducted a study of modular poultry maintenance. The design of a module for raising poultry with an infrared heater has been developed. The proposed design is energy efficient and is recommended for installation in poultry houses. The microclimate in the module is analysed. The air temperature near the bird in the module reaches 18.6°C, and the average speed does not exceed 0.75 m/s.

This paper is a continuation of scientific and practical research on improving the aerodynamic characteristics of the air environment in poultry housing [21]. Thus, *the purpose of the study* is to improve the microclimate system in the air environment of the poultry house by installing exhaust fans on the side wall in a total of 8 units. The scientific component is the investigation of hydrodynamics and heat exchange processes in the air environment of the poultry house with the improvement of the location of exhaust ventilation equipment.

MATERIALS AND METHODS

According to the purpose of the study, the authors modify the location of exhaust fans. The bottom line is as follows: in the conventional design of the poultry housing (Figs. 1, 2) exhaust fans are mounted not on the rear end wall of the poultry house, but on the side (Fig. 3.). 4 units for each wall, a total of 8 units. Current indicators in the poultry house can be seen in Table 1.

Table 1. Current indicators in the poultry house premises

Current indicators	Livestock	Cross	Age/Weight, g	Density units/m^2	Density kg/m^2	External temperature, C	Internal humidity, %	External humidity, %
	57,971	Ross	18/707	24.15	15.46	2	72	92

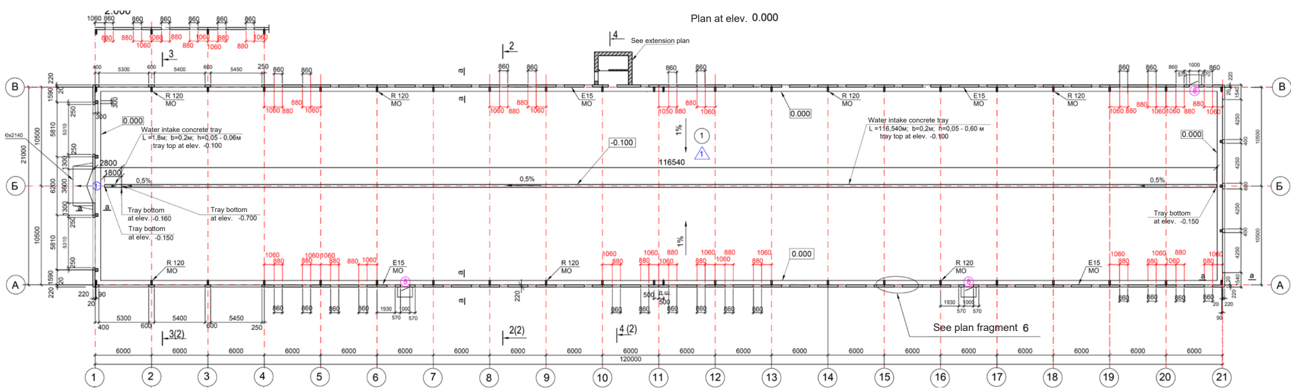

Figure 1. Valve arrangement plan

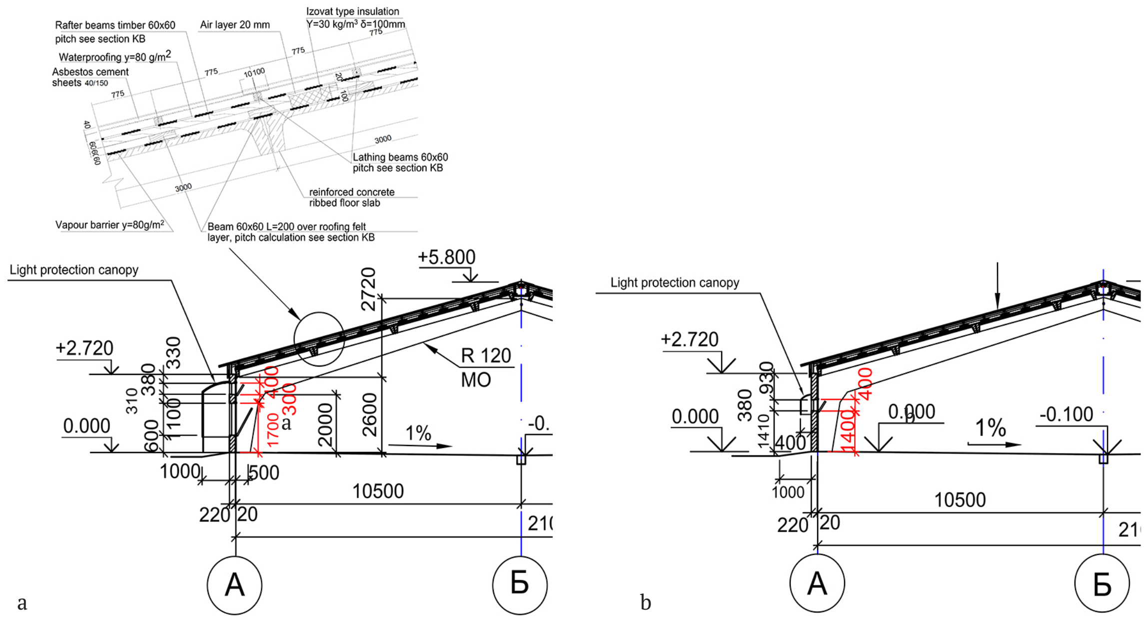

Figure 2. Fragment of a plan with side ventilation inlets: a – 1-6 valve, b – 7-40

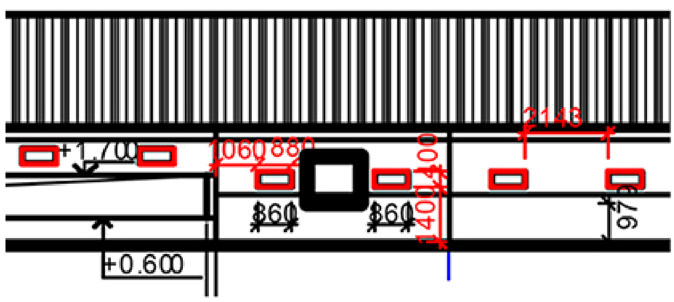

Figure 3. Location of the first exhaust fan on the side wall

Figure 4 shows the 3D geometry of a poultry house for CFD modelling made in 100% scale, but only half of the poultry house. The boundary condition "symmetry" is set in the centre of the poultry house. The remaining boundary conditions are shown in Figure 4a. These measures were carried out due to insufficient power of computer equipment. Figure 4b clearly shows concrete frame (stick).

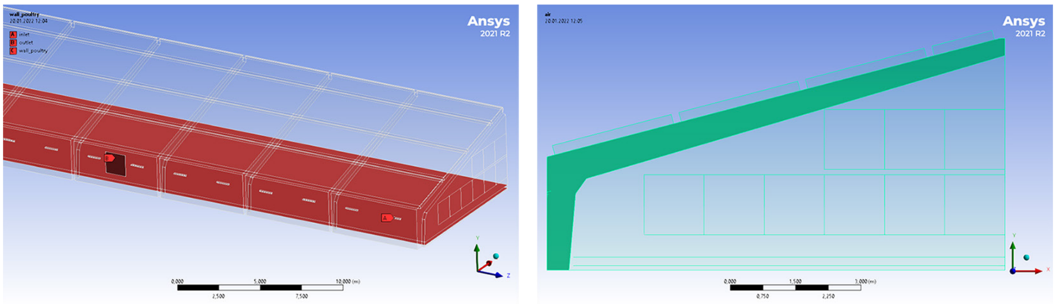

Figure 4. 3D poultry house geometry: a – with indication of boundary conditions; b – with selection of concrete frame

Figure 5a shows the constructed mesh in the air environment of the poultry house from the side. The openings of exhaust fans and supply valves are presented in a close-up form (Fig. 5b). In the openings of exhaust fans and supply valves, the mesh is reduced relative to the rest of the wall area. In addition near the floor where the bird was located, mesh grinding was performed for a more accurate calculation of hydrodynamics, and heat and mass transfer by numerical method.

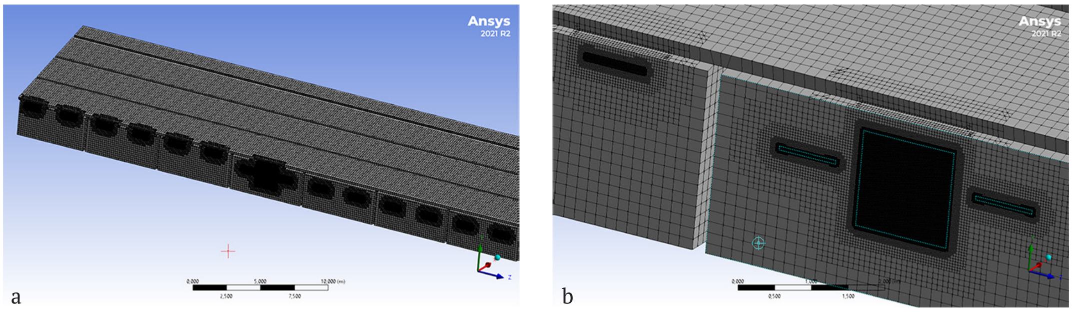

Figure 5. Mesh in the air environment of the poultry house: a – remotely, b – close

Table 2 shows the parameters for building a mesh in the air environment of a poultry house. Using the ANSYS Meshing software, a 3D calculation mesh is constructed using the 3D element method. The CutCell mesh construction method was applied. The number of elements reaches 4.3 million. The Orthogonal Quality mesh indicator is 0.22. The minimum size of the exhaust fan element on the side wall of the poultry house is 0.01 m. It is smaller than the size of the supply valve element by 0.03. This decision was made due to the fact that the authors of this study are more interested in the behaviour of air in exhaust fans. Air behaviour in supply valves has already been investigated [21].

Table 2. Parameters for building a mesh for a poultry room

Configuration options	Indicator	Size
Mesh quality indicator (orthogonal quality)	0.22	–
Number of elements	4,291,613	units
Number of nodes	4,849,379	units
Method	CutCell	–
Maximum face size	0.16	m
Minimum face size	0.04	m
Minimum size of the supply valve element	0.04	m
Minimum size of the exhaust fan element	0.01	m

Calculations were made at an air flow rate of 21.5 kg/s. The outside air temperature is assumed to be +2°C and the parameters of thermal radiation are entered. The walls are made of concrete and insulated with foam 35 kg/m^3 thickness, respectively: 60/100/60 mm. Insulated roof "Izovat" Y=30 kg/m^3, 100 mm. For more information, see Figure 2. The floor is insulated with expanded polystyrene 45 kg/m^3 with a thickness of 100 mm and a width of 2 m from the wall around the perimeter, the rest of the area is 50 mm. In poultry premises, poultry is a source of heat when kept on the floor and the temperature is +41°C. The heating system is not provided. For air removal, Munters EM50 1.5 Hp exhaust fans are used in the amount of 4 units. Wlotpowietrza 3000-VFG supply valves with a total number of 79 units. Spoilers are mounted above the valves at an angle of inclination from the vertical of 75°C. The remaining design parameters of the poultry house can be obtained from Figure 1-3.

The CFD model was performed using the Navier-Stokes equations for convective flows [22-24]. The calculations use the Spalart-Allmaras turbulence model [25; 26] and the Discrete Ordinates radiation model [9; 27].

RESULTS AND DISCUSSION

This section presents the results of the numerical modelling of a poultry house in 3D using ANSYS Fluent. This allows assessing the hydrodynamic air flows in the poultry house. To perform numerical modelling, a 3D grid is previously constructed using the 3D element method in ANSYS Meshing.

Figure 6-14 show the results of numerical modelling of the poultry house in three sections along the length of the room – 16.23 m, 50.78 m, and 85.25 m. The first section is the middle of the 6th supply valve. The second is the 2nd exhaust fan (between the 17th and 18th supply valves). The third section is located in the middle of the 29th supply valve. There are 40 supply valves along the length of the poultry house.

Figure 6 and 12 show the temperature field in different parts of the poultry house. At a constant air flow rate of 77,402 m^3/h and the inlet air temperature of +2°C. The upper layers of air near the ceiling and near the side wall are slightly higher in temperature. This is accompanied by the radiation of the sun and ranges from +22 to +24°C. Since the bird is a source of heat, and in combination with radiation, the air in the room is partially heated. In the centre of the room, the temperature reaches +16°C along the entire height. Cool air with a temperature of +2°C is directed to the centre of the room and washes the bird. In the area where the supply air is actively mixed with the air that is in the poultry house, the air temperature does not exceed +9.85°C (Fig. 6a, 6b). Figure 6b shows how the exhaust fan draws some of the heat from the bird. Which is unacceptable. The average air temperature on exhaust fans is +8.5349°C.

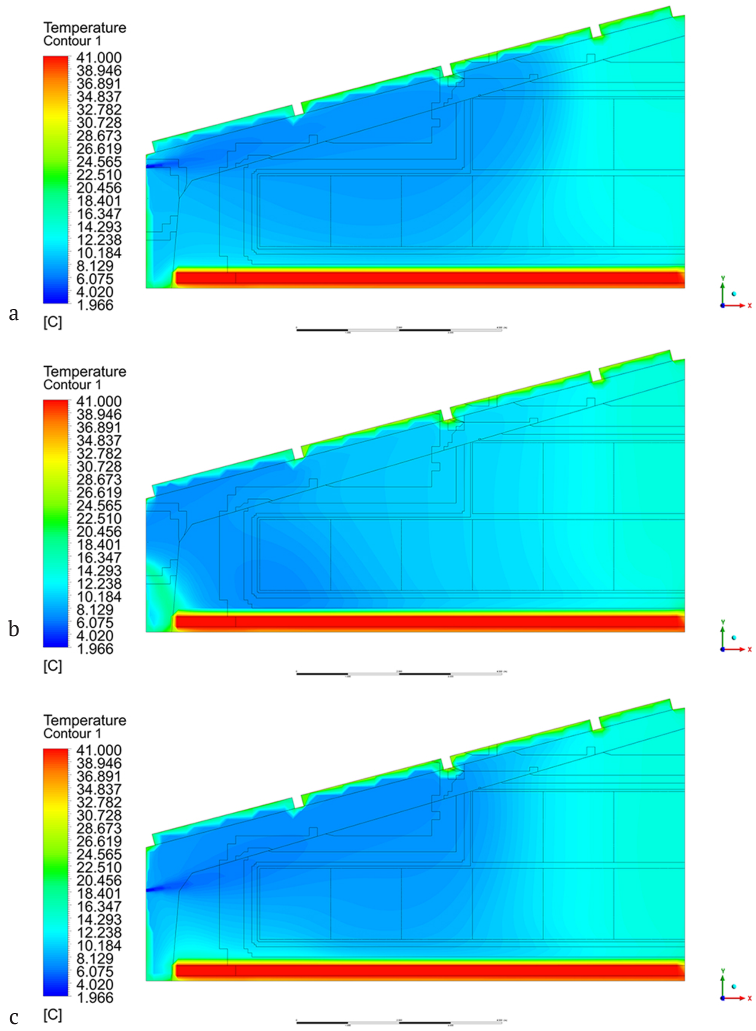

Figure 6. Mesh in the air environment of the poultry house: a – remotely, b – close

Figure 7 shows the pressure field in the poultry house. At the inlet on the supply valves, the pressure is 45.846271 Pa (Fig. 7a, 7b). On the exhaust fans, a certain vacuum is observed – -8.4171922 Pa (Fig. 7b). At certain points, the maximum pressure reaches 54.505 Pa.

Figure 8-9 show the hydrodynamics of air flow in the poultry house. As mentioned above, the air flow is directed upwards by supply valves. However, due to the low pressure and speed at the inlet, the air after passing a third of the room falls down. Only valves that are located at a height of 330 mm from the ceiling (Fig. 8a, 8b, Fig. 9a, 9b) pass smoothly near the ceiling surface. Air is partially retained due to the concrete protrusions of the ceiling (Fig. 2a). After that, it is sent to the centre of the room. But it reaches a third of the room. The average air velocity at the inlet of the supply valves is 9.166368 m/s. At certain points in the poultry house, the maximum speed can reach up to 9.871124 m/s. In the very centre, two vortices are formed along the length of the poultry house by 16.23 m (Fig. 9a). Due to disturbances near the exhaust fans, along the length of the poultry house by 50.78 m (Fig. 9b), stagnant zones occur near the ceiling. A vortex forms at a distance of 4.15 m from the side wall. This is conditioned by the low speed at the fan outlet. On the exhaust fan section, the average speed is 3.4614946 m/s (Fig. 8b, 9b). At a distance of 85.25 m from the front end wall of the poultry house (Fig. 8b, 9b) several vortices are formed. The air that is pumped through the supply valves at a height of 810 mm from the ceiling does not reach the centre of the room. They do not give a sufficient effect this can be caused by a disturbance that occurs due to large volumes of the room. It is also caused by low air velocity, low pressure on these supply valves, and protrusions in the concrete floor.

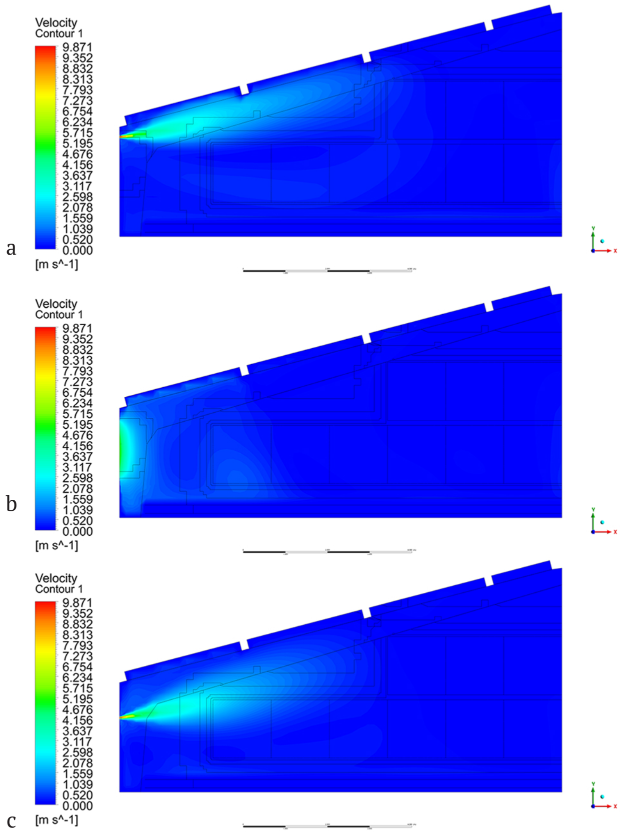

Figure 8. Velocity field (m/s) in the poultry house at a distance from the front end wall at: a – 16.23 m; b – 50.78 m; c – 85.25 m

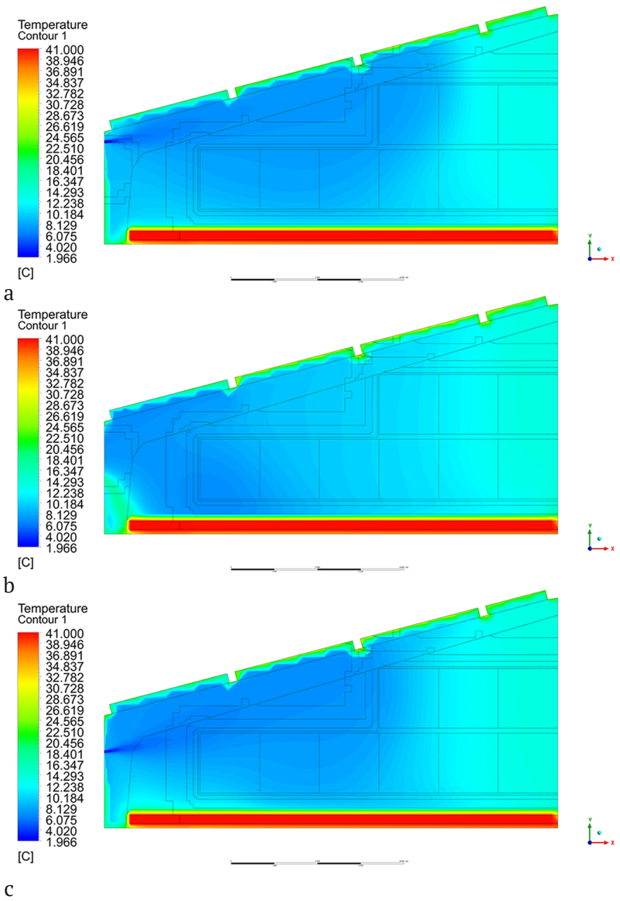

Figure 7. Pressure losses (Pa) in the poultry house at a distance from the front end wall at: a – 16.23 m; b – 50.78 m; c – 85.25 m

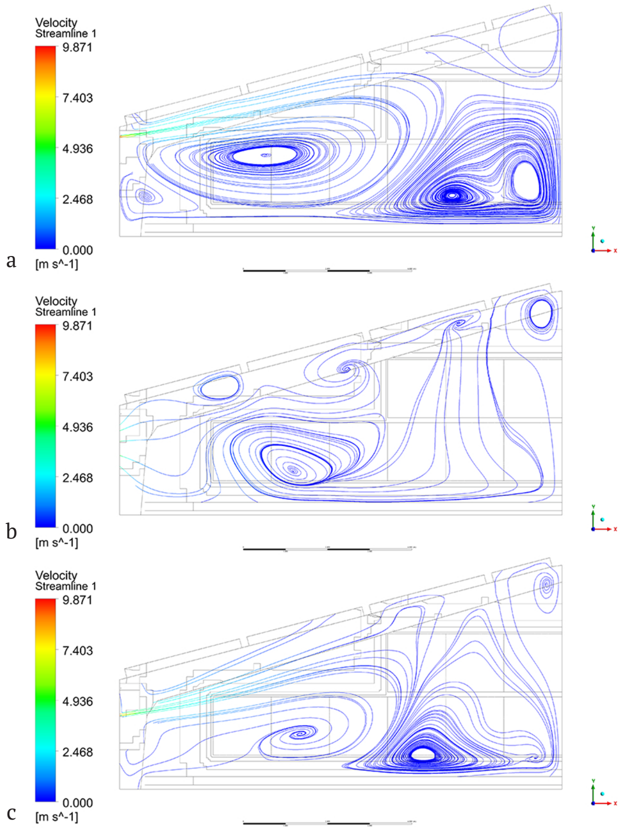

Figure 9. Current lines (m/s) in the poultry house at a distance from the front end wall at: a – 16.23 m; b – 50.78 m; c – 85.25 m

Figure 10 shows the field of velocities and temperatures along the room plane at a height of 0.7 m from the floor level. These results are the most interesting, which would help assess the hydrodynamics and heat exchange of air above the bird. The average air velocity is 0.57 m/s, the temperature is 9.91°C. Only at some points the speed is slightly higher than 2 m/s. The main array of birds will not experience any discomfort.

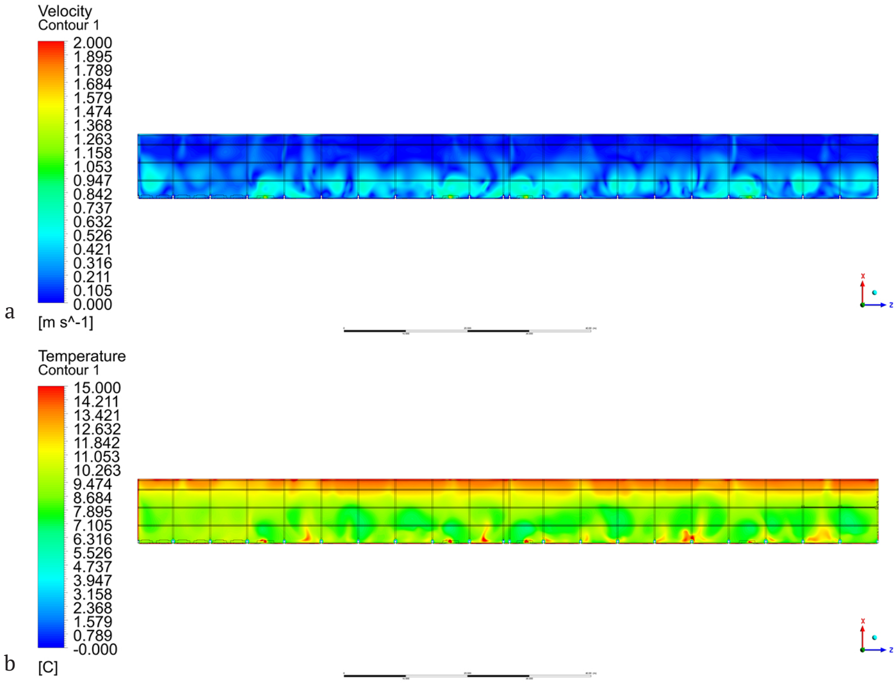

Figure 10. Velocity field, m/s (a), and temperature field, oC (b) in the poultry house at a height of 0.7 m from the floor level

Due to disturbances and stagnant zones in the centre of the poultry house, the air velocity reaches about 0.32156 m/s. It was indicated above that the temperature reaches +16°C over the entire altitude. In the study [28-29], exhaust fans are located on the upper line of the rear end wall. This arrangement accompanies the creation of a tunnel effect in the centre of the poultry house. In this regard, in the future, the authors suggest installing two exhaust fans on the rear end wall in addition to the existing ones. This would increase the air velocity in the centre of the poultry house.

Figure 11-14 show current lines and visualisation of the volume flow rate in the range from 0 to 2 m/s for a poultry house in 3D. The results show that the valves located at 810 mm from the ceiling do not work effectively. Valves located at 210 mm are slightly better. The first valves that are located to the right and left of the exhaust fans practically do not work. All air that enters through them immediately enters the exhaust fan. The authors suggest that these 8 valves should be closed and not used. Thus, there will not be such a large disturbance in certain areas of the poultry house. And also the speed of the remaining valves will rise to 0.1-0.2 m/s.

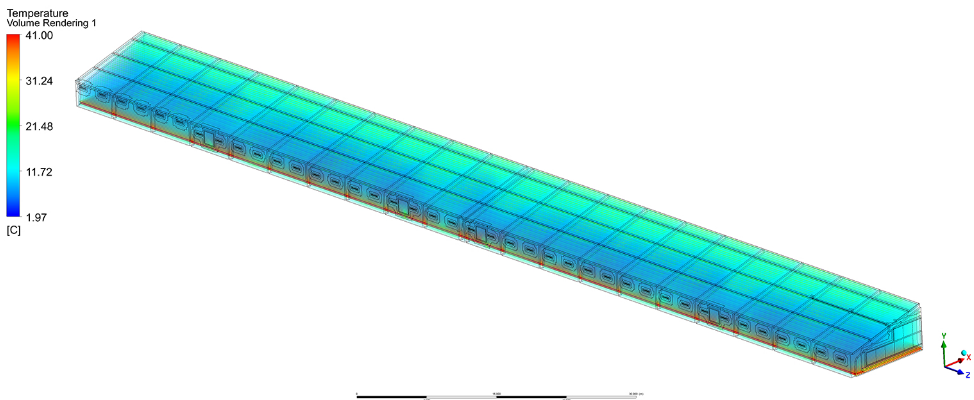

Figure 11. Visualisation of the volumetric temperature flow rate of the poultry house air environment, oC

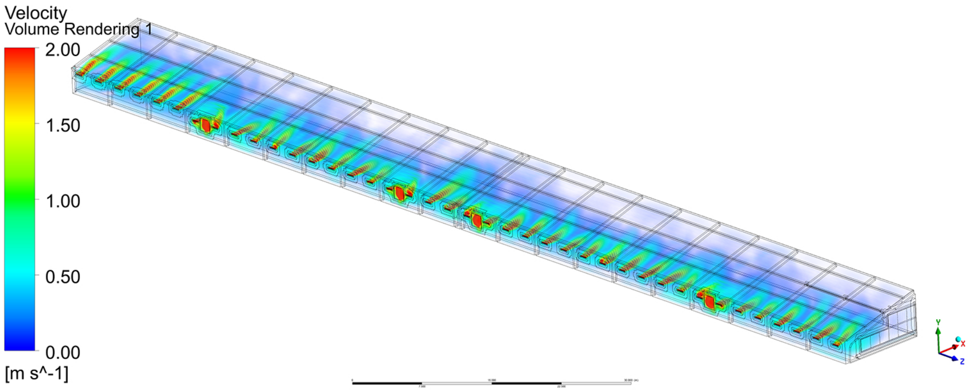

Figure 12. Visualisation of the volume air flow rate of the poultry house in the range from 0 to 2 m/s

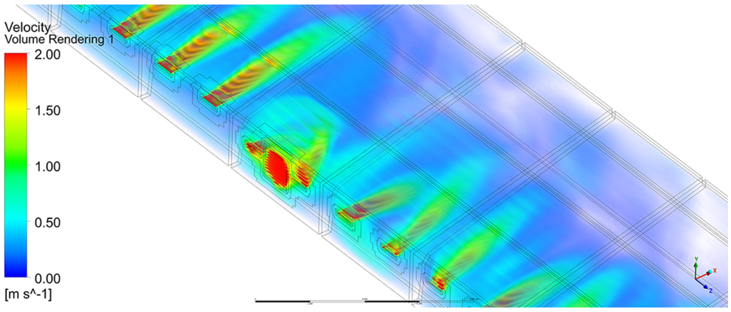

Figure 13. Visualisation of the volumetric air flow rate of the poultry house in the convergence of the first exhaust fan in the range from 0 to 2 m/s

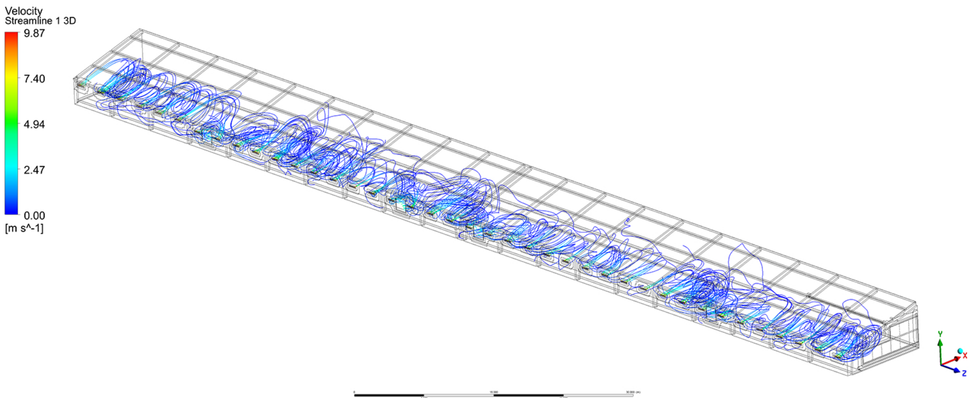

Figure 14. 3D current lines (m/s) in the poultry house

Detailed information on the average indicators of the air environment in the poultry house as a result of numerical modelling is presented in Table 3.

Table 3. Average indicators of the air environment in the poultry house

Parameter	Dimension	Supply valves (inlet)	Exhaust fans (outlet)
Inlet air consumption for half of the poultry house	kg/s	21.5	21.5
Inlet air consumption for half of the poultry house	m^3/h	77,402	77,402
Inlet air consumption for a full poultry house	m^3/h	154,804	154,804
Air pressure	Pa	45.846271	-8.4171922
Air temperature	°C	2.0757952	8.5349084
Air velocity	m/s	9.166368	3.4614946
Air density	kg/m^3	1.2816432	1.2532063
Coefficient of thermal conductivity of air	W/m·K	0.024559	0.025
Kinematic air viscosity	kg/m·s	$1.68137 \cdot 10^{-5}$	$1.71239 \cdot 10^{-5}$

With practical experience, raising poultry in conventional poultry houses is divided into 16 uniform zones in terms of output and meat quality. Along the perimeter of the area near the side walls of the poultry house, the quality of meat is much worse. In the centre of the poultry house, the output of product quality is much better. From the results of CFD modelling, it can be seen that due to lower speeds over the bird, and more uniform temperatures, the product quality, compared to the conventional location of exhaust fans, will be higher. However, the presented results have both positive and negative effects on the bird in general. The authors evaluated all the pros and cons of the proposed ventilation system and will continue to work on the elimination of shortcomings.

CONCLUSIONS

CFD modelling of heat and mass transfer in the poultry house premises was performed. For CFD modelling, a mesh was built by the method of volumetric elements of the air environment of the poultry house in 3D. The CutCell method is used to build a mesh in the ANSYS Meshing pre-processor. The maximum mesh face size is 0.16 m. The number of elements is about 4.3 million. The mesh quality index Orthogonal Quality is 0.22.

The results of numerical modelling have shown that the most efficient valves are those located at a height of 330 mm from the ceiling. The pressure drop of the supply valves is 45.85 Pa. The air velocity at the inlet of the supply valves is 9.17 m/s. The air velocity at a height of 0.7 m from the floor level varies within 0.57 m/s, the temperature – 9.91°C. The angle of inclination of the valve relative to the wall is 75°. Opening of the valve by 4 mm. However, with the proposed location of exhaust fans on the side wall of the poultry house, the ventilation system does not work efficiently enough. The authors recommend not using two supply valves (total 8 units) located to the right and left of the exhaust fans. This would increase the speed of the remaining valves to 0.1-0.2 m/s. In addition, two additional fans on the rear end wall of the house along the top line should be included. This would create a tunnel effect in the centre of the poultry house. And this is accompanied by an increase in air speed. At the same time, it reduces disturbances in the air environment of the poultry house.

ACKNOWLEDGEMENTS

The study was conducted with the support of topic 4/81 commissioned by the branch “Poultry Complex” of Vinnytsia Poultry Farm LLC and topic No. 110/1m-pr-2022 by Order of the Ministry of Education and Science of Ukraine.

REFERENCES

[1] Bjerg, B., Norton, T., Banhazi, T., Zhang, G., Bartzanas, T., Liberati, P., Casconeg, G., Leeh, I.-B., & Maruccii, A. (2013). Modelling of ammonia emissions from naturally ventilated livestock buildings. Part 1: Ammonia release modelling. *Biosystems Engineering*, 116(3), 232-245. doi: 10.1016/j.biosystemseng.2013.08.001.

[2] Bustamante, E., Garcıa-Diego, F.J., Calvet, S., Estelles, F., Beltran, P., Hospitaler, A., & Torres, A.G. (2013). Exploring ventilation efficiency in poultry buildings: The validation of computational fluid dynamics (CFD) in a cross-mechanically ventilated broiler farm. *Energies*, 6(5), 2605-2623. doi: 10.3390/en6052605.

[3] Kwon, K.S., Lee, I.B., Zhang, G.Q., & Ha, T. (2015). Computational fluid dynamics analysis of the thermal distribution of animal occupied zones using the jet-drop-distance concept in a mechanically ventilated broiler house. *Biosystems Engineering*, 136, 51-68. doi: 10.1016/j.biosystemseng.2015.05.008.

[4] Wang, K., Wang, X., & Wu, B. (2014). Assessment of hygrothermal conditions in a farrowing room with a wet-pad cooling system based on CFD simulation and field measurements. *Transactions of the ASABE*, 57(5), 1493-1500. doi: 10.13031/trans.57.10634.

[5] Manbeck, H.B., Hofstetter, D.W., Murphy, D.J., & Puri, V.M. (2016). Online design aid for evaluating manure pit ventilation systems to reduce entry risk. *Frontiers in Public Health*, 4(2), 1-16, doi: 10.3389/fpubh.2016.00108.

[6] Norton, T., Grant, J., Fallon, R., & Sun, D.W. (2010). Assessing the ventilation performance of a naturally ventilated livestock building with different eave opening conditions. *Computers and Electronics in Agriculture*, 71(1), 7-21. doi: 10.1016/j.compag.2009.11.003.

[7] Küçüktopcu, E., & Cemek, B. (2019). Evaluating the influence of turbulence models used in computational fluid dynamics for the prediction of airflows inside poultry houses. *Biosystems Engineering*, 183, 1-12. doi: 10.1016/j.biosystemseng.2019.04.009.

[8] Ma, Y.X., & Zou, H.F. (2020). Optimized design of air inlet devices based on environmental analysis of a broiler house model. *IOP Series: Materials Science and Engineering*, 789, article number 012036. doi: 10.1088/1757-899X/789/1/012036.

[9] ANSYS. Fluent theory guide. Release 2020 R1. (2020). Retrieved from https://d.shikey.com/down/Ansys.Products.2020.R1.x64/install_docs/Ansys.Products.PDF.Docs.2020R1/v201/ANSYS_Fluent_Theory_Guide.pdf.

[10] Rojano, F., Bournet, P.-E., Hassouna, M., Robin, P., Kacira, M., & Choi, C.Y. (2015). Modelling heat and mass transfer of a broiler house using computational fluid dynamics. *Biosystems Engineering*, 136, 25-38.

[11] Rojano, F., Bournet, P.-E., Hassouna, M., Robin, P., Kacira, M., & Choi, C.Y. (2016). Computational modelling of thermal and humidity gradients for a naturally ventilated poultry house. *Biosystems Engineering*, 151, 273-285. doi: 10.1016/j.biosystemseng.2016.09.012.

[12] Tong, X., Hong, S.-W., & Zhao, L. (2019). CFD modelling of airflow pattern and thermal environment in a commercial manure-belt layer house with tunnel ventilation. *Biosystems Engineering*, 178, 275-293. doi: 10.1016/j.biosystemseng.2018.08.008.

[13] Tong, X., Hong, S.-W., & Zhao, L. (2019). Using CFD simulations to develop an upward airflow displacement ventilation system for manure-belt layer houses to improve the indoor environment. *Biosystems Engineering*, 178, 294-308, doi: 10.1016/j.biosystemseng.2018.08.006.
[14] Dudnyk, A., Lysenko, V., Zaets, N., Komarchuk, D., Lendiel, T., & Yakymenko, I. (2019). Intelligent control system of biotechnological objects with fuzzy controller and noise filtration unit. *2018 International Scientific-Practical Conference on Problems of Infocommunications Science and Technology*, 3, 586-590. doi: 10.1109/INFOCOMMST.2018.8632007.
[15] Lendiel, T., Lysenko, V., & Nakonechna, K. (2021). Computer-integrated technologies for fitomonitoring in the greenhouse. *Lecture Notes on Data Engineering and Communications Technologies*, 48, 711-729. doi: 10.1007/978-3-030-43070-2_30.
[16] Lysenko, V., Zhyltsov, A., Bolbot, I., Lendiel, T., & Nalyvaiko, V. (2020). Phytomonitoring in the phytometrics of the plants. *E3S Web of Conferences*, 154, article number 07012. doi: 10.1051/e3sconf/202015407012.
[17] Lysenko, V.P., Bolbot, I.M., Lendiel, T.I., Nakonechna, K.V., Kovalskiy, V.P., Rysynets, N.O., Gromaszek, K., Amirgaliyev, Y., & Nurseitova, K. (2021). Mobile robot with optical sensors for remote assessment of plant conditions and atmospheric parameters in an industrial greenhouse. *International Society for Optical Engineering*, 12040, article number 120400D. doi: 10.1117/12.2613975.
[18] Lysenko, V., Bolbot, I., & Lendel, T. (2019). Energy efficient system of electrotechnological complex control in industrial greenhouse. *Technical Electrodynamics*, 2(2), 78-81. doi: 10.15407/techned2019.02.078.
[19] Spodyniuk, N., & Lis, A. (2020). Research of temperature regime in the module for poultry growing. *Lecture Notes in Civil Engineering*, 100, 451-458. doi: 10.1007/978-3-030-57340-9_55.
[20] Trokhaniak, V.I., Spodyniuk, N.A., Antypov, I.O., Shelimanova, O.V., Tarasenko, S.V., & Mishchenko, A.V. (2021). Experimental research and CFD modelling of modular poultry breeding. *INMATEH – Agricultural Engineering*, 65(3), 303-311. doi: 10.35633/inmateh-65-32.
[21] Trokhaniak, V.I., Rogovskii, I.L., Titova, L.L., Dziubata, Z.I., Luzan, P.H., & Popyk, P.S. (2020). Using CFD simulation to investigate the impact of fresh air valves on poultry house aerodynamics in case of a side ventilation system. *INMATEH – Agricultural Engineering*, 62(3), 155-164. doi: 10.35633/inmateh-62-16.
[22] Khmelnik, S.I. (2018). *Navier-Stokes equations. On the existence and the search method for global solutions*. Raleigh: Mathematics in Computers.
[23] Antypov, I.O. (2016). Development of means for intensification of heat exchange processes in heat accumulators based on accumulative phase transition materials. *Energy and Automation*, 2, 110-119.
[24] Marzouk, S.A., Abou, A.M.M., El-Fakharany, M.K., & El-Said, E.M.S. (2022). A comparative numerical study of shell and multi-tube heat exchanger performance with different baffles configurations. *International Journal of Thermal Sciences*, 179, article number 107655. doi: 10.1016/j.ijthermalsci.2022.107655.
[25] Allmaras, S.R., Johnson, F.T., & Spalart, P.R. (2012). Modifications and clarifications for the implementation of the Spalart-Allmaras Turbulence model. In *7th international conference on computational fluid dynamics* (pp. 9-13). Melbourne: Melbourne Institute of Technology.
[26] Nordanger, K., Holdahl, R., Kvamsdal, T., Kvarving, A.M., & Rasheed, A. (2015). Simulation of airflow past a 2D NACA0015 airfoil using an isogeometric incompressible Navier-Stokes solver with the Spalart-Allmaras turbulence model. *Computer Methods in Applied Mechanics and Engineering*, 290, 183-208. doi: 10.1016/j.cma.2015.02.030.
[27] Moreno, J., Casado, C., & Marugán, J. (2019). Improved discrete ordinate method for accurate simulation radiation transport using solar and LED light sources. *Chemical Engineering Science*, 205, 151-164. doi: 10.1016/j.ces.2019.04.034.
[28] Trokhaniak, V.I. (2020). Numerical simulation as method of research and improvement of side ventilation system in poultry house with conventional ranking of exhaust fans. *Machinery & Energetics*, 11(3), 121-128. doi: 10.31548/machenergy2020.03.121.
[29] Ostanin, V. (2022). Effects of repulsion and attraction between rotating cylinders in fluids. *Scientific Herald of Uzhhorod University. Series "Physics"*, 51, 39-47.

Віктор Іванович Троханяк

Національний університет біоресурсів і природокористування України
03041, вул. Героїв Оборони, 15, м. Київ, Україна

Дослідження бокової системи вентиляції в пташнику за допомогою CFD

Анотація. Підтримання нормованого мікроклімату у птахівничому приміщенні це один із основних факторів. Саме від якісних показників параметрів повітря в кінцевому результаті залежить якість виходу продукції. Птиця при її утриманні вимагає значних зусиль і технологічних рішень. В зв'язку з цим метою дослідження є вдосконалення системи мікроклімату у пташнику шляхом встановлення вентиляційного обладнання на боковій стінці. Потужним інструментом прогнозування схеми повітряного потоку в пташнику є моделювання обчислювальної гідродинаміки (Computational Fluid Dynamics (CFD)) за допомогою ANSYS Fluent. Це є як альтернатива експериментальним дослідженням. Результати CFD моделювання показали, як практичну цінність в тому, що най ефективніше клапани працюють які розташовані на висоті 330 мм. від перекриття. Перепад тиску у припливних клапанів становить 45,85 Па. Швидкість повітря на вході припливних клапанів 9,17 м/с. Швидкість повітря на висоті 0,7 м. від рівня підлоги коливається в межах 0,57 м/с, температура – 9,91 °C

Ключові слова: обчислювальна гідродинаміка, мікроклімат, аеродинаміка, птахівниче приміщення, припливні клапана

Machinery & Energetics
Vol. 13, No. 3. 2022

Journal homepage:
https://technicalscience.com.ua/en

UDC 633.63
DOI: 10.31548/machenergy.13(3).2022.92-98

Oleksandra Trokhaniak*

National University of Life and Environmental Sciences of Ukraine
03041, 15 Heroiv Oborony, Kyiv, Ukraine

Estimation of Eddy Currents and Power Losses in the Rotor of a Screw Electrothermomechanical Converter for Additive Manufacturing

Abstract. Screw conveyors are widely used in the movement of various loose and lump materials related to agricultural production, such as: seed granular materials, cereals, bran, chaff, turf, flakes, mixed feed, mineral fertiliser pellets, etc. However, the conventional flexible screw conveyor operating mechanisms do not fully meet the operational requirements for these types of conveyors. Screw operating mechanisms are characterised by the complexity of the design and manufacturing technology, high material consumption, which causes increased energy consumption, damage to the transported material and the inner surface of flexible sleeves. Therefore, the task of developing new designs of flexible sectional screw operating mechanisms with advanced technological capabilities is urgent. To increase the reliability of the flexible screw conveyor, it was proposed to make its operating mechanism from separate screw sections that are pivotally connected to each other. Therefore, the purpose of this study is to determine the rational parameters and operating modes of the developed operating mechanism, which would ensure stable transportation of loose and lump materials on various technological routes. The study was conducted using the methods of differential and integral calculus, the theory of mathematical and computer modelling, mathematical planning of the experiment. This paper shows the results of theoretical and experimental studies of the process of transporting loose or lump material in the inactive zone between the pivotally connected screw sections of a flexible screw conveyor. The results of comparison of the obtained results of theoretical and experimental studies are shown. This allows choosing rational design, kinematic and technological parameters of the developed sectional screw operating mechanism when moving loose or lump agricultural materials along curved routes, both in horizontal and inclined directions, and along curved routes

Keywords: hinged screw sections, inactive zone between sections, material flight length, straight and curved routes, material departure angle

Article's History: Received: 05.04.2022; Revised: 14.07.2022; Accepted: 11.08.2022

INTRODUCTION

Screw conveyors are widely used for moving a variety of loose and lump materials, mainly related to agricultural production, such as: seed granular materials, cereals, bran, chaff, turf, flakes, mixed feed, mineral fertiliser pellets, etc. The results of establishing the contact interaction of loose and lump materials with the working surfaces of screw conveyors are described in [1-3].

The study of the mechanical and technological properties of agricultural materials is given in [4]. As a rule, rigid screw operating mechanisms are used to transport bulk and lump materials, which can be placed at different angles. Flexible screw conveyors are also commonly used, the study of the parameters and operating modes of which is presented in [5-7].

Pneumatic conveyors that can transport various loads along curved routes are quite widely used. The main disadvantage of these types of conveyors is the significant energy consumption and price, which limits their use. Such types of conveyors and screw feeders for feeding loose materials are investigated in [8-10].

Combining technological operations, such as transportation and mixing of feed mixtures, is possible with the use of puck conveyors, which can operate on different routes, but only stationary ones. The results of studies of such conveyors are given in [11; 12].

However, existing screw flexible augers cannot fully meet the operational requirements that are put forward for these types of conveyors. The use of shaftless flexible spirals causes rapid destruction during the operation

Suggested Citation:
Trokhaniak, O.M. (2022). Study of the process of movement of loose materials using a flexible screw conveyor. *Machinery & Energetics,* 13(3), 92-98.

*Corresponding author

of the conveyor on curved tracks, due to the presence of alternating cyclic loads. The production of a screw in the form of a solid or sectional shaft, on which individual elements of screw blades are placed, causes a significant complication in the design of the screw, an increase in its material consumption, and this, in turn, leads to an increase in energy consumption and damage to moving materials.

Thus, the task of developing new designs and substantiating the parameters of screw flexible operating mechanisms of conveyors, the use of which would allow increasing the functional and operational indicators of the process of transporting loose and lump agricultural materials is relevant.

The purpose of this study is to improve the functional and operational characteristics of screw conveyors by developing and substantiating the parameters of flexible screw operating mechanisms, which are made on the basis of pivotally connected sections, for transporting loose agricultural materials.

The results of theoretical and experimental developments, which are described in this paper, are a continuation of previous studies [13-15] and are aimed at improving the efficiency of the process of operation of flexible screw conveyors, the operating mechanisms of which are made based on pivotally connected sections.

The paper presents the results of theoretical and experimental studies of the operating mechanism of a flexible screw conveyor made of separate sections that are pivotally connected to each other.

MATERIALS AND METHODS

In order to increase the reliability of the flexible screw conveyor, it was proposed to make its operating mechanism from separate screw sections that are pivotally connected to each other. The placement of the blades of adjacent sections is shown in Fig. 1a. In this case, screw blades 1 and 2 are placed in the axial direction with a gap δ (inactive zone). The hinge mechanism 3 connects screw sections to each other. It is made on the principle of a gimbal with separated axes placed mutually perpendicular. The edges of adjacent screw blades are offset by an angle α in the circular direction. The difference between the design of such a screw is that during the convergence of loose or lump material from the edge of the screw blade 1 to a distance δ it (particles of material) must fly by in a certain amount of time t_1. Moreover, the edge of the screw blade 2 is at least (the angle of departure of the material should also be considered) for the time t_2 it should turn a corner α, for the purpose of capturing the transported material.

Figure 1b provides a general view of the sections of the screw that is placed on the curved section and its individual sections.

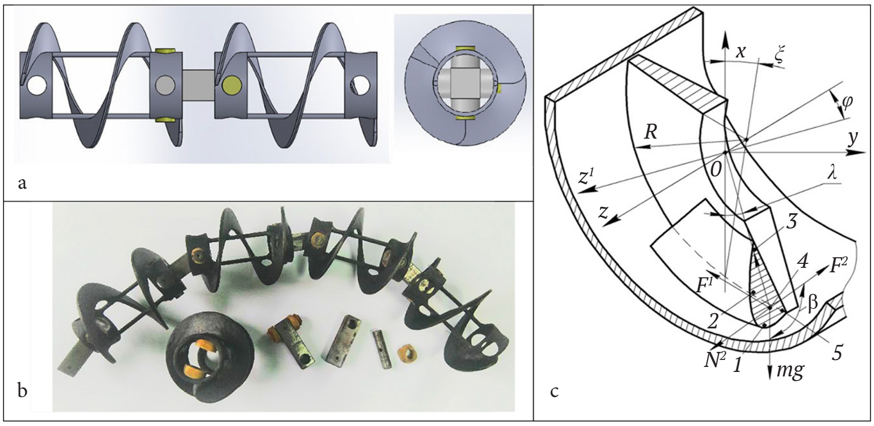

Figure 1. Design and calculation scheme of screw sections that are pivotally connected to each other: a – diagram of two sections; b – general view of the sections of the screw sectional mechanism, which is placed on the curved section and the view of individual elements of the sections; c – diagram for determining the forces acting on the elementary volume of loose material, which continuously moves in the casing

The study considers the movement of loose cargo along a fixed casing using the helical sector of the screw spiral. Its elementary volume is selected, which is simultaneously in contact with the fixed casing and the rotating section of the screw spiral. On the side of the casing, it is affected by a reaction directed perpendicular to the working surface and the friction force. The reaction from the chute side is equal to the vector sum of the forces that arise from the weight of the selected elementary volume and the centripetal force.

The elementary volume is also affected by the reaction from the surface of the screw blade, which is directed perpendicular at the point of contact to the surface of the operating mechanism, and the friction force also acts, respectively. Fig. 1b shows the forces acting on the elementary volume of loose material moving in the casing.

The equation of motion of a separate elementary volume of loose material that is not related to the flow has the form of a system of two differential equations

$$m(d^2z/dt^2)=N_1cos\xi-F_1sin\xi-F_2sin\beta-mg\ sin\beta; \quad (1)$$

$$mR(d^2\lambda/dt^2)=N_1sin\xi-F_1cos\xi-F_2cos\beta-mg\ sin\lambda cos\varphi, \quad (2)$$

where m – mass of the material particle; R – casing radius; N_1 – reaction that occurs in the screw to the material;

F_1 – friction force from the action of force N_1; N_2 – force generated in the screw from the material; F_2 – friction force from the reaction N_2; ξ – the angle of lifting of the screw helical line; φ – the angle of inclination of the axis of the screw section to the horizon; β – the angle of direction of movement of the material particle relative to the casing; λ – the angular position of the material particle in its rotational motion; z – longitudinal coordinate of the material particle along the casing axis.

Reaction N_2 is defined from the condition

$$N_2 = mg\cos\lambda\cos\varphi + mR\cdot(d\lambda/dt)^2. \quad (3)$$

The friction forces are determined accordingly

$$F_1 = f_1 N_1 \qquad F_2 = f_2 N_2, \quad (4)$$

where f_1 – coefficient of friction of the material on the surface of the screw blade; f_2 – coefficient of friction of the material on the surface of the casing.

Considering the directions of movement of the material particle and the geometry of the helical blade, when it rotates at an angular velocity ω, the following geometric dependencies can be set:

$$tg\beta = \dot{z}/R\dot{\lambda} \qquad tg\xi = \dot{z}/R(\omega - \dot{\lambda}). \quad (5)$$

Considering the movement of the selected material element in the flow, then the last term can be excluded from equation (2), since its weight force is compensated by the support of the loose material located below. The rest of the effort works as before. Then equation (2) will take the form

$$mR(d^2\lambda/dt^2) = N_1\sin\xi + F_1\cos\xi - F_2\cos\beta. \quad (6)$$

To solve the system of equations (1)-(5), transformations are used to reduce the unknown force from the equalities N_1 and output the parameters in terms of the angle value λ. Preliminary, this system will take the form:

$$m\ddot{z} = N_1(\cos\xi - f_1\sin\xi) - f_2(mg\cos\lambda\cos\phi + mR\dot{\lambda}^2)\sin\beta - mg\sin\phi; \quad (7)$$

$$mR\ddot{\lambda} = N_1(\sin\xi - f_1\cos\xi) - f_2(mg\cos\lambda\cos\phi + mR\dot{\lambda}^2)\cos\beta -$$

$$- mg\sin\lambda\cos\phi \quad (8)$$

Therefore, the differential equation of motion for the variable λ will have the form:

$$\ddot{\lambda} + \dot{\lambda}A + B_c\cos\lambda - B_s\sin\lambda - C = 0. \quad (9)$$

In this equation, the coefficients are determined by the following dependencies:

$$A = f_2[\cos(\beta+\xi) - f_1\sin(\beta+\xi)];$$
$$B = (f_2 g/R)\cdot[\cos(\beta+\xi) - f_1\sin(\beta+\xi)]\cos\phi\cos\xi;$$
$$B_s = (g/R)\cdot[\cos\xi - f_1\sin\xi)\cos\phi\cos\xi;$$
$$C = (g/R)\cdot(\sin\xi + f_1\cos\xi)\cos\phi\cos\xi. \quad (10)$$

In the case of flow movement, when applying equation (6), the coefficient of B_s=0.

When there is a movement of the material flow, it is necessary that the centripetal force is greater than the weight force. Otherwise, particles of loose or lump material will not be able to stay in continuous mode, which significantly distorts the picture of flow transportation. This can be achieved if $\dot{\lambda} > \sqrt{g/R}$.

An important moment of particle movement occurs when the flow particles separate from the spiral fin and their free flight inside the casing until they stop or until they come into contact with the screw blade of the next section.

The free movement of load particles along the surface of the casing during the occurrence of separation from the edge of the screw spiral is recorded using two second-order differential equations

$$m(d^2z/dt^2) = -F_2\sin\beta - mg\sin\phi; \quad (11)$$

$$mR(d^2\lambda/dt^2) = -F_2\cos\beta - mg\sin\lambda\cos\phi. \quad (12)$$

After the conversion,

$$m\ddot{z} = -f_2(mg\cos\lambda\cos\phi + mR\dot{\lambda}^2)\sin\beta - -mg\sin\phi; \quad (13)$$

$$mR\ddot{\lambda} = -f_2(mg\cos\lambda\cos\phi + mR\dot{\lambda}^2)\cos\beta - mg\sin\lambda\cos\phi. \quad (14)$$

The third stage of movement can be the free flight of flow particles when separated from the surface of the casing if the calculated value of the pressure force on the chute is N_2<0. Then the equations of motion of particles can be described by a system of three independent differential equations of motion along three mutually perpendicular axes x, y and z:

$$\ddot{x} = -g\cos\phi \qquad \ddot{y} = 0 \qquad \ddot{z} = -g\sin\phi. \quad (15)$$

The movement of the body in free fall will be completed if there is contact with the casing, that is, an unevenness is performed $x^2+y^2 \geqslant R^2$. The relationship of velocities in Cartesian and cylindrical coordinate systems when material particles are separated from the screw blade is written as

$$\dot{x} = R\dot{\lambda}\sin\lambda \qquad \dot{y} = -R\dot{\lambda}\cos\lambda. \quad (16)$$

When a material particle falls on the surface of the casing, the angular velocity of rotation is written as the sum of projections of velocity vectors on the tangent to the circle at the point of contact

$$\dot{\lambda} = (\dot{x}\sin\lambda - \dot{y}\cos\lambda)/R. \quad (17)$$

Equation (9) is a second-order nonlinear differential equation. Its analytical solution is impossible. In this case, the numerical method of integrating these equations is used – that is, the Runge-Kutta method.

Consider the flow movement of loose material at different points of its cross-section. The characteristic points of the cross-section of the flow are shown in Fig. 1b.

It is assumed that the friction forces between material particles (grains, corn, or other loose material) significantly exceed the friction forces on the surface of the screw and casing. This assumption makes allows considering the motion of particles as a whole with the same angular velocity. The actual movement of the material differs from the ideal one, so points 1 and 2, which are located at the edge of the loose material flow section, are slightly behind points 3, 4, and 5, which are located near the screw blade.

A significant lag will be observed only in the case of transportation of a material that has a low coefficient of friction between individual particles (grains). However, for the transport of grain material, the mutual mixing of individual particles is insignificant, the particles almost stick together and move in a continuous stream, especially at high speeds. This statement was experimentally confirmed in [2; 16; 17].

The speed of movement of point 1, which is located at the edge of the flow section, is maximum due to the maximum distance from the centre of the casing. The linear velocity of point 5 will also be similar. The velocity of points 2 and 4 decreases in proportion to the radius along which they move. The lowest speed is typical for point 3, which is located closest to the centre of rotation.

The presence of different linear velocities for individual points of cross-section of the material flow leads to different trajectories of their flight when separated from the screw blade. Linear particle separation rate

$$v_i=R_i\dot{\lambda}, \tag{18}$$

where R_i – rotation radius of i-th particle.

Speed v_i is directed tangentially to a circle of the corresponding radius and is directed along the vector that makes up the angle β_i with a circle in the XOY plane. It follows from (5) that:

$$tg\beta_i=\dot{z}/(R_i\dot{\lambda}). \tag{19}$$

Moreover, as a longitudinal (axial) $\dot{z}$, and angular velocity $\dot{\lambda}$ all elements of the cross-section are assumed to be the same. Analysis of equation (19) shows that particles at smaller radii have a larger departure angle β_i, and, accordingly, have a lower component of the circular velocity in the plane perpendicular to the axis Z.

In order to determine the maximum possible flight distance of particles from different cross-section points, the free movement of each of the particles is considered along a circle of the corresponding radius. It is assumed that individual particles interact with each other during free motion, that is, there are friction forces between them, and the movement of each of them occurs along a circle of the previous radius. This assumption is substantiated by the fact that the lower particles cannot rise up due to the presence of upper particles there. There is practically no lag or advance of the lower particles relative to the upper ones due to significant friction forces between them. Therefore, at short distances, the motion of particles can be considered as the motion of a connected mass.

The smaller the particle's rotation radius R_i, the lower the centripetal acceleration:

$$a_{ni}=R_i\dot{\lambda}^2. \tag{20}$$

If the angular velocity decreases due to braking, the centripetal acceleration will be less than the acceleration of gravity g and the particles begin to fall freely to the lower surface of the casing. The decline begins with the lower layers, gradually spreading to the upper layers.

The maximum flight length is considered to be this distance along the Z axis when the particle moves over the surface of the casing before it comes into contact with it. Such a study should be carried out for an arbitrary moment of separation of the particle from the edge ($0\leq\lambda\leq2\pi$) and from them, determine the shortest flight length. In this case, it is necessary to calculate the angular displacement of the particle in the direction of the angle λ to determine the coordinates of the point that the particle will reach at the maximum flight length. Knowing the corresponding final coordinate, it is possible to calculate the axial distance between the ends of adjacent screw blades δ and the required angular displacement α between them.

The motion of each particle is determined from equations (13) and (14), in which it is necessary to put the corresponding radii R_i, angles β_i, and coefficients of friction f_i.

When solving systems of differential equations (9), (13), (14), and (15), it is necessary that the final conditions in the previous step automatically become initial for the next one.

To analyse the motion of a particle in the flow and in the breakaway zone, a programme was created in the Delphi software environment using the Runge-Kutta method and the ability to graphically display the results.

The method of conducting experimental studies is as follows: the reloading pipe was adopted as the basis, the description of the structure and principle of operation of which is given in [18-20]. Grain with admixtures of plastic material granules of different colours was chosen as the loose material. Directly under the discharge pipe was a tray on which the material was unloaded and the range of flight of the loose material was set by means of filming, fixing the trajectory of multi-coloured pellets. The angle of departure of the material was fixed at the values of λ=90°, 180°, 270°. According to theoretical studies at an angle λ=270° length L of the flight of the material is minimal, and therefore, to ensure continuous movement of the material between adjacent screw sections, it is necessary to consider the most unfavourable option. Speed of rotation of the operating mechanism n and the angle of its inclination to the horizon φ, according to the results of theoretical studies, is chosen at the following values: n=450, 600, 750 rpm; φ=10°, 20°, 30°.

RESULTS AND DISCUSSION

The results of the calculations performed allowed constructing graphical dependencies (Fig. 2) of free flight lengths *L* of material particles from the rotation speed value n of screw operating mechanism *L=f(n)*, (Fig. 2a) and the angle of inclination φ of the axis of the screw section to the horizon *L=f*(φ), (Fig. 2b) for different angular positions of the material particle at the moment of its separation from the screw blade λ.

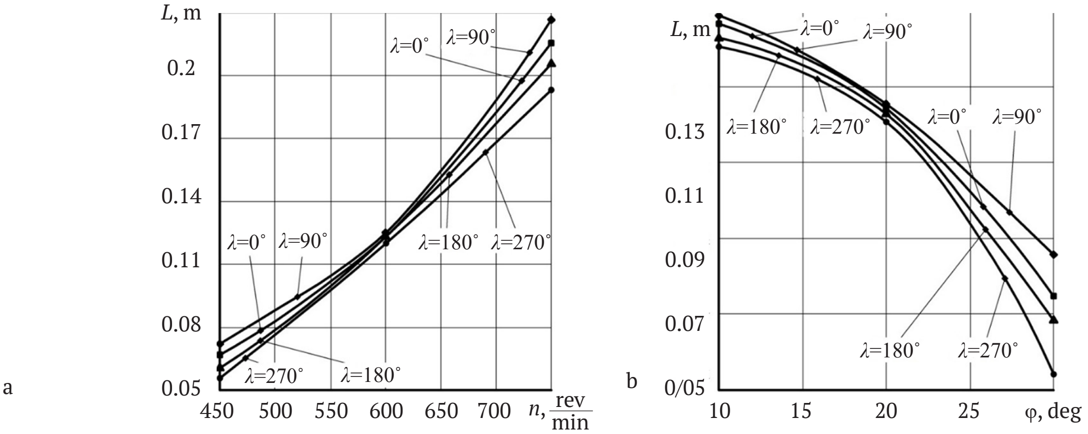

Figure 2. Graphical dependences of the free flight range of a material particle *L* on the speed of rotation of the screw operating mechanism *n*(a) and the angle of inclination φ of the axis of the screw section to the horizon (b) for different angular positions λ of the particle at the moment of separation from the screw blade to contact with the lower surface of the casing

When performing calculations and determining the effect of one of the parameters on the value L, others were taken as constants and the values of their parameters were: ξ=22.5°; ξ=20°; *R*= 52 mm; *n*=600 rpm.

From the analysis of graphical dependencies *L=f(n)* it is established that the maximum value L corresponds to the angle of separation of the material particle from the helical fin λ=90°, (λ=0° corresponds to the lower horizontal point of the casing) and will be *L*=0.226 m for *n*=750 rpm (Fig. 2a). Minimum value *L* will be *L*=0.191 m for λ=270°.

At *n*=450 rpm, the values of L for different values λ are within *L*=0.055...0.073 M, and at *n*=600 rpm, the minimum range of change of *L*=0.118 0 0.124 m for different values of λ is observed.

From the analysis of graphical dependencies *L=f*(φ) it is established that the maximum value L corresponds to the minimum angle φ=10° and will be *L*=0.144..0.148 m (Fig. 2b) at different values of λ. With increasing angle φ value *L* decreases, and at φ=30° is *L*=0.055...0.085 m.

As the lifting angle ξ increases, the range of values L also increases for different angular positions of λ at the moment of separation of the material particle from the screw blade.

A multi-factor experiment was also conducted. The factor field had the following range of parameter changes: 450≤*n*≤750 rpm; 0≤λ≤270° deg; 10°≤φ≤30°.

Based on the statistical processing, the regression equation to determine the change in *L* has the form

$$L=-0.06384+0.304\cdot 10^{-3}\cdot n+0.1783\cdot 10^{-2}\cdot \phi-0.1853\cdot \cdot 10^{-4})\cdot \lambda+0.715\cdot 10^{-7}\cdot n^2-0.377\cdot 10^{-5}\cdot n\cdot \phi-0.86\cdot 10^{-7}\cdot n\cdot \lambda- -0.455\cdot 10^{-4}\cdot \phi^2+0.194\cdot 10^{-5}\cdot \phi\cdot \lambda-0.48\cdot 10^{-7}\cdot \lambda^2. \quad (21)$$

When determining the influence of two factors on the value *L* , the third one is assumed to be unchanged with its average value. The average values of the factors are as follows: *n*=600 rpm; λ≤270°; 10°≤φ≤30°.

Response surfaces range of grain material particles *L* are shown in Figure 3.

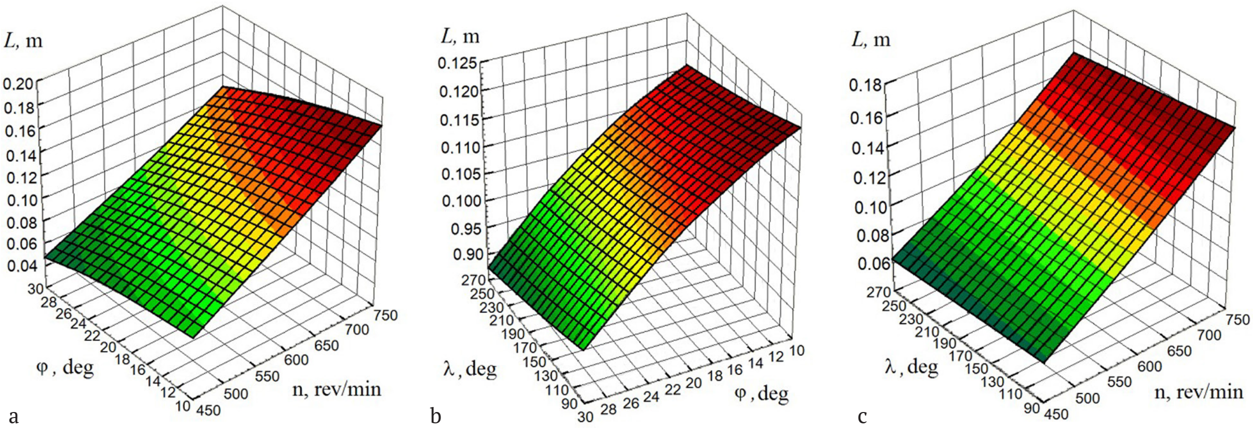

Figure 3. Response surfaces of the material's flight range *L*: a – *L=f*(φ; *n*); b – *L=f*(λ; φ); c – *L=f*(λ; φ)

Based on the analysis of the regression equation and response surfaces, it is established that the maximum effect on the value of *L* has a speed of rotation of the operating mechanism *n*. Thus, for the average values of λ and φ growth n from 450 to 750 rpm causes an increase in the value *L* by 0.092 m. The next most intense effect on the value *L* is an angle of inclination of the axis of the screw section to the horizon φ. Its increase from 10° to 30° at the average values of λ and n causes a decrease in the value *L* by 0.028 m. Minimal impact on the value *L* has an angle λ, the growth of which is from 90° to 270° at the average values of φ and n leads to a decrease in the value *L* by 0.009 m.

The obtained data must be considered when designing such a sectional screw operating mechanism. Based on the most unfavourable option in this range of parameter changes, the distance between the ends of adjacent screw blades δ the distance should not exceed 0.04 m.

In addition, experimental studies on determining the capacity for the process of transporting grain material have shown that for *n*=600 rpm with clearance δ=14 mm, the power is about N=1.2 kW; at δ=28 mm – N=1.7 kW; at δ=42 mm – N=3.2 kW. Therefore, it is rational to choose the gap value δ within 0.01...0.03 mm.

Comparison of the obtained results in theoretical and experimental studies, showed that for *n*=600 rpm; φ=20° and different values λ the difference between the obtained data is 3.7%...14.8%.

Therefore, the conducted theoretical studies can be applied to a wider range of changes in the design and kinematic parameters of the operating mechanism with a hinged connection of sections.

From the analysis of theoretical studies for the operating mechanisms of flexible screw conveyors [3; 6; 9], it can be concluded that the authors overwhelmingly deduced analytical dependencies to establish the functional, operational and design parameters of flexible screw operating mechanisms. At the same time, the issues of substantiating the parameters of screws that ensure their high functional and operational parameters with the minimum permissible weight of the operating mechanism are not resolved. This would significantly reduce energy costs for the movement process and the degree of damage to loose and lump agricultural material.

The results of experimental studies presented in this paper relate to screw spirals without the use of a flexible shaft. However, as practical studies have shown, during the transportation of material along a curved route (especially at small radii of curvature), due to the occurrence of cyclic alternating deformations, screw spirals are quickly destroyed, which sharply limits the use of such operating mechanisms due to non-compliance with operational requirements. In order to increase the reliability of the technological process, when developing and investigating operating mechanisms, it is necessary to use: a sectional method for manufacturing operating mechanisms (to eliminate alternating cyclic loads); increase the contact area between the torque transmission units, which would reduce internal stresses and forces in friction pairs by increasing the torque transmission arm.

CONCLUSIONS

The paper presents the results of theoretical and experimental studies of the operating mechanism of a flexible screw conveyor made of separate sections that are pivotally connected to each other.

Based on the derived equations of motion of loose material between separate adjacent helical sections, the dependences of the flight range of material particles L are established from the speed of rotation of the screw operating mechanism n, the angle of its inclination to the horizon φ, and the various angular positions of the particle λ, which moves in the material flow at the moment of its separation from the screw blade.

Based on the proposed method, experimental studies were conducted, according to the results of which it can be concluded that for the factor field of parameter changes: 450≤*n*≤750 rpm; 0°≤λ≤270°; 10°≤φ≤30° value L varies in the range from 0.042 to 0.188 mm.

Given the sharp increase in power costs for the material transportation process for δ>0.032, clearance value δ should be taken in the range of 0.01...0.03 mm.

Based on comparisons of the obtained results of theoretical and experimental studies at n=600 rpm; φ=20°, and different values of λ, their discrepancy is 3.7%...14.8%.

Based on a complex of theoretical and experimental studies, a competitive sectional screw operating mechanism has been created, which allows improving the functional and operational characteristics of screw conveyors for transporting loose and lump agricultural materials.

REFERENCES

[1] Baranovsky, V.M., Hevko, R.B., Dzyura, V.O., Klendii, O.M., Klendii, M.B., & Romanovsky, R.M. (2018). Justification of rational parameters of a pneumoconveyor screw feeder. *INMATEH: Agricultural Engineering*, 54(1), 15-24.

[2] Hevko, B.M., Hevko, R.B., Klendii, O.M., Buriak, M.V., Dzyadykevych, Y.V., & Rozum, R.I. (2018). Improvement of machine safety devices. *Acta Polytechnica, Journal of Advanced Engineering*, 58(1), 17-25.

[3] Hevko, R.B., Yazlyuk, B.O., Liubin, M.V., Tokarchuk, O.A., Klendii, O.M., & Pankiv, V.R. (2017). Feasibility study of mixture transportation and stirring process in continuous-flow conveyors. *INMATEH: Agricultural Engineering*, 51(1), 49-59.

[4] Hevko, R.B., Liubin, M.V., Tokarchuk, O.A., Lyashuk, O.L., Pohrishchuk, B.V., & Klendii, O.M. (2018). Determination of the parameters of transporting and mixing feed mixtures along the curvilinear paths of tubular conveyors. *INMATEH: Agricultural Engineering*, 55(2), 97-104.

[5] Lech, M. (2001). Mass flow rate measurement in vertical pneumatic conveying of solid. *Powder Technology*, 114, 55-58.

[6] Lyashuk, O.L., Rogatynska, O.R., & Serilko, D.L. (2015). Modelling of the vertical screw conveyer loading. *INMATEH Agricultural Engineering*, 45(1), 87-94.

[7] Pylypaka, S.F., Nesvidomin, V.M., Klendii, M.B., Rogovskii, I.L., Kresan, T.A., & Trokhaniak V.I. (2019). Conveyance of a particle by a vertical screw, which is limited by a coaxial fixed cylinder. *Bulletin of the Karaganda University. "Mathematics" Series*, 95(3), 129-139.
[8] Lyashuk, O.L., Sokil, M.B., Klendiy, V.M., Skyba, O.P., Tretiakov, O.L., Slobodian, L.M., & Slobodian, N.O. (2018). Mathematical model of bending vibrations of a horizontal feeder-mixer along the flow of grain mixture. *INMATEH Agricultural Engineering*, 55(2), 35-44.
[9] Lyashuk, O.L., Vovk, Y.Y., Sokil, M.B., Klendii, V.M, Ivasechko, R.R, & Dovbush, T.A. (2019). Mathematical model of a dynamic process of transporting loose material by means of a tube scraping conveyor. *Agricultural Engineering International: CIGR Journal*, 21(1), 74-81.
[10] Manjula, E.V.P.J., Hiromi, A.W.K., Ratnayake, C., & Melaaen, M.C. (2017). A review of CFD modelling studies on pneumatic conveying and challenges in modelling offshore drill cuttings transport. *Powder Technology*, 305, 782-793.
[11] Mondal, D. (2018). Study on filling factor of short length screw conveyor with flood-feeding condition. *Materials Today: Proceedings*, 5, 1286-1291.
[12] Tripathi, N., Sharma, A., Mallick, S.S., & Wypych, P.W. (2015). Energy loss at bends in the pneumatic conveying of fly ash. *Particuology*, 21, 65-73.
[13] Owen, P.J., & Cleary, P.W. (2010). Screw conveyor performance: comparison of discrete element modelling with laboratory experiments. *Progress in Computational Fluid Dynamics*, 10(5-6), 327-333.
[14] Qi, J., Meng, H., Kan, Z., Li, C., & Li, Y. (2017). Analysis and test of feeding performance of dual-spiral cow feeding device based on EDEM. *Transactions of the Chinese Society of Agricultural Engineering*, 33, 65-71.
[15] Tian, Y., Yuan, P., Yang, F., Gu, J., Chen, M., Tang, J., Su, Y., Ding, T., Zhang, K., & Cheng, Q. (2018). Research on the principle of a new flexible screw conveyor and its power consumption. *Applied Sciences*, 8(7), article number 1038.
[16] Tsarenko, O.M., Voityuk, L.M., & Shvayko, M.V. (2003). *Mechanical-technological properties of agricultural materials*. Kyiv: Meta.
[17] Roberts, A.W., & Bulk, S. (2015). Optimizing screw conveyors. *Chemical Engineering*, 122(2), 62-67.
[18] Yao, Y.P., Kou, Z.M., Meng, W.J., & Han, G. (2014). Overall performance evaluation of tubular scraper conveyors using a TOPSIS-based multiattribute decision-making method. *Scientific World Journal*, 2014, article number 753080.
[19] Wang, D.-X. (2012). Research on numerical analysis and optimal design of the screw conveyor. *Univ. Technol.*, 27, 32-36.
[20] Hevko, R.B., Klendii, M.B., & Klendii, O.M. (2016). Investigation of a transfer branch of a flexible screw conveyer. *INMATEH: Agricultural Engineering*, 48(1), 29-34.

Олександра Миколаївна Троханяк

Національний університет біоресурсів і природокористування України
03041, вул. Героїв Оборони, 15, м. Київ, Україна

Дослідження процесу переміщення сипкого матеріалу за допомогою гнучкого гвинтового конвеєра

Анотація. Гвинтові конвеєри знайшли широке використання під час переміщення різноманітних сипких та кускових матеріалів, які належать до сільськогосподарського виробництва, наприклад такі як: насіннєві гранульовані матеріали, зернові, висівки, полова, дерть, пластівці, комбікорми, гранули мінеральних добрив та ін. Але, загальновідомі гнучкі гвинтові робочі органи транспортерів не в повній мірі відповідають експлуатаційним вимогам, що висуваються до даних видів конвеєрів. Шнековим робочим органам характерна складність конструкції і технологія їх виготовлення, висока матеріаломісткість, що викликає підвищені енерговитрати, пошкодження транспортованого матеріалу та внутрішньої поверхні гнучких рукавів. Тому, актуальним є завдання розроблення нових конструкцій гнучких секційних гвинтових робочих органів із розширеними технологічними можливостями. Для підвищення надійності функціонування гвинтового гнучкого транспортера було запропоновано його робочий орган виконувати із окремих гвинтових секцій, що шарнірно з'єднані між собою. Отже, метою цих досліджень являється визначення раціональних параметрів та режимів роботи розробленого робочого органу, що дозволить забезпечити стабільне транспортування сипких та кускових матеріалів на різних технологічних трасах. Дослідження проведено із використанням методів диференціального та інтегрального числення, теорії математичного та комп'ютерного моделювання. методу математичного планування експерименту. У даній статті показані результати теоретичних та експериментальних досліджень процесу транспортування сипкого чи кускового матеріалу у неактивній зоні між шарнірно з'єднаними гвинтовими секціями гнучкого гвинтового конвеєра. Показано результати порівняння отриманих результатів теоретичних та експериментальних досліджень. Це дає змогу вибрати раціональні конструктивні, кінематичні та технологічні параметри розробленого секційного гвинтового робочого органу під час переміщення сипких чи кускових сільськогосподарських матеріалів по криволінійних трасах, як в горизонтальному та похилому напрямках, так і по криволінійних трасах

Ключові слова: шарнірно з'єднані гвинтові секції, неактивна зона між секціями, довжина польоту матеріалу, прямі та криволінійні траси, кут вильоту матеріалу

ТЕХНІКА ТА ЕНЕРГЕТИКА

Науковий журнал

Том 13, № 3. 2022

Заснований у 2010 р. Виходить чотири рази на рік

Оригінал-макет видання виготовлено у відділі науково-технічної інформації
Національного університету біоресурсів і природокористування України

Відповідальний редактор:
Г. Івченко

Редагування англомовних текстів:
С. Воровський, К. Касьянов

Комп'ютерна верстка:
К. Сосєдко

Підписано до друку 11 серпня 2022 р. Формат 60*84/8
Умов. друк. арк. 11,7
Наклад 50 прим.

Адреса видавництва:
Національний університет біоресурсів і природокористування України
вул. Героїв Оборони, 15, м. Київ, 03041, Україна
E-mail: info@technicalscience.com.ua
www: https://technicalscience.com.ua/uk

MACHINERY & ENERGETICS

Scientific Journal

Volume 13, No. 3. 2022

Founded in 2010. Published four times per year

The original layout of the publication is made in the Department of Scientific and Technical Information of National University of Life and Environmental Sciences of Ukraine

Managing Editor:
H. Ivchenko

Editing English-language texts:
S. Vorovsky, K. Kasianov

Desktop publishing:
K. Sosiedko

Signed for print of August 11, 2022. Format 60*84/8
Conventional printed pages 11.7
Circulation 50 copies

Editors Office Address:
National University of Life and Environmental Sciences of Ukraine
03041, 15 Heroiv Oborony, Kyiv, Ukraine
E-mail: info@technicalscience.com.ua
www: https://technicalscience.com.ua/en